NATIONAL AERONAUTICS AND SPACE ADMINISTRATION

*Technical Report 32-1526*

*Volume I*

# *The Deep Space Network*

*Progress Report*
*For November and December 1970*

JET PROPULSION LABORATORY
CALIFORNIA INSTITUTE OF TECHNOLOGY
PASADENA, CALIFORNIA

February 15, 1971

NATIONAL AERONAUTICS AND SPACE ADMINISTRATION

*Technical Report 32-1526*

*Volume I*

# *The Deep Space Network*

## *Progress Report*
## *For November and December 1970*

JET PROPULSION LABORATORY
CALIFORNIA INSTITUTE OF TECHNOLOGY
PASADENA, CALIFORNIA

February 15, 1971

Prepared Under Contract No. NAS 7-100
National Aeronautics and Space Administration

# Preface

This is the first issue of a new series of bimonthly progress reports describing work performed for the JPL/NASA Deep Space Network (DSN). Current work for the DSN was previously reported in Volume II of the now retired Space Programs Summary series of Laboratory bimonthly publications. The new report series is an uninterrupted follow-on to the Space Programs Summary, Volume II.

This report series presents progress on DSN supporting research and technology, advanced development and engineering, and implementation, and DSN operations which pertain to mission-independent or multiple-mission development as well as to support of flight projects. Each issue presents material in some, but not all, of the following categories in the order indicated.

Description of the DSN

Mission Support
- Interplanetary Flight Projects
- Planetary Flight Projects
- Manned Space Flight Project
- Advanced Flight Projects

Advanced Engineering
- Tracking and Navigational Accuracy Analysis
- Communications Systems Research
- Communications Elements Research
- Supporting Research and Technology

Development and Implementation
- Space Flight Operations Facility Development
- Ground Communications Facility Development
- Deep Space Instrumentation Facility Development
- DSN Project and System Development

Operations and Facilities
- DSN Operations
- Space Flight Operations Facility Operations
- Ground Communications Facility Operations
- Deep Space Instrumentation Facility Operations
- Facility Engineering

In each issue, the part entitled "Description of the DSN" describes the functions and facilities of the DSN and may report the current configuration of one of the six DSN systems (tracking, telemetry, command, monitoring, simulation, and operations control).

The work described in this report series is either performed or managed by the Tracking and Data Acquisition organization of JPL for NASA.

# Contents

## DESCRIPTION OF THE DSN



## MISSION SUPPORT

### Planetary Flight Projects



## ADVANCED ENGINEERING

### Tracking and Navigational Accuracy Analysis



### Communications Systems Research

# Contents (contd)

## Communications Elements Research



## Supporting Research and Technology



# DEVELOPMENT AND IMPLEMENTATION

## SFOF Development

## Contents (contd)

### GCF Development



## OPERATIONS AND FACILITIES

### SFOF Operations

# DSN Functions and Facilities

N. A. Renzetti
Mission Support Office

*The objectives, functions, and organization of the Deep Space Network are summarized. The Deep Space Instrumentation Facility, the Ground Communications Facility, and the Space Flight Operations Facility are described.*

The Deep Space Network (DSN), established by the NASA Office of Tracking and Data Acquisition under the system management and technical direction of JPL, is designed for two-way communications with unmanned spacecraft traveling approximately 16,000 km (10,000 mi) from earth to planetary distances. It supports, or has supported, the following NASA deep space exploration projects: *Ranger*, *Surveyor*, *Mariner* Venus 1962, *Mariner* Mars 1964, *Mariner* Venus 67, *Mariner* Mars 1969, *Mariner* Mars 1971 (JPL); *Lunar Orbiter* and *Viking* (Langley Research Center); *Pioneer* (Ames Research Center); *Helios* (West Germany); and *Apollo* (Manned Spacecraft Center), to supplement the Manned Space Flight Network (MSFN).

The DSN is distinct from other NASA networks such as the MSFN, which has primary responsibility for tracking the manned spacecraft of the *Apollo* Project, and the Space Tracking and Data Acquisition Network (STADAN), which tracks earth-orbiting scientific and communications satellites. With no future unmanned lunar spacecraft presently planned, the primary objective of the DSN is to continue its support of planetary and interplanetary flight projects.

To support flight projects, the DSN simultaneously performs advanced engineering on components and systems, integrates proven equipment and methods into the network,[1] and provides direct support of each project through that project's Tracking and Data System. This management element and the project's Mission Operations personnel are responsible for the design and operation of the data, software, and operations systems required for the conduct of flight operations. The organization and procedures necessary to carry out these activities are described in Ref. 1.

[1]When a new piece of equipment or new method has been accepted for integration into the network, it is classed as Goldstone duplicate standard (GSDS), thus standardizing the design and operation of identical items throughout the network.

By tracking the spacecraft, the DSN is involved in the following data types:

(1) *Radio Metric:* generate angles, one- and two-way doppler, and range.

(2) *Telemetry:* receive, record, and retransmit engineering and scientific data.

(3) *Command:* send coded signals to the spacecraft to activate equipment to initiate spacecraft functions.

The DSN operation is characterized by six DSN systems: (1) tracking, (2) telemetry, (3) command, (4) monitoring, (5) simulation, and (6) operations control.

The DSN can be characterized as being comprised of three facilities: the Deep Space Instrumentation Facility (DSIF), the Ground Communications Facility (GCF), and the Space Flight Operations Facility (SFOF).

## I. Deep Space Instrumentation Facility

### A. Tracking and Data Acquisition Facilities

A world-wide set of deep space stations (DSSs) with large antennas, low-noise phase-lock receiving systems, and high-power transmitters provide radio communications with spacecraft. The DSSs and the deep space communications complexes (DSCCs) they comprise are given in Table 1.

Radio contact with a spacecraft usually begins when the spacecraft is on the launch vehicle at Cape Kennedy, and it is maintained throughout the mission. The early part of the trajectory is covered by selected network stations of the Air Force Eastern Test Range (AFETR) and the MSFN of the Goddard Space Flight Center.[2] Normally, two-way communications are established between the spacecraft and the DSN within 30 min after the spacecraft has been injected into lunar, planetary, or interplanetary flight. A compatibility test station at Cape Kennedy (discussed later) monitors the spacecraft continuously during the launch phase until it passes over the local horizon. The deep space phase begins with acquisition by either DSS 51, 41, or 42. These and the remaining DSSs given in Table 1 provide radio communications to the end of the flight.

To enable continuous radio contact with spacecraft, the DSSs are located approximately 120 deg apart in longitude; thus, a spacecraft in deep space flight is always

[2]The 9-m (30-ft) diam antenna station established by the DSN on Ascension Island during 1965 to act in conjunction with the MSFN orbital support 9-m (30-ft) diam antenna station was transferred to the MSFN in July 1968.

**Table 1. Tracking and data acquisition stations of the DSN**

| DSCC | Location | DSS | DSS serial designation | Antenna | | Year of initial operation |
|---|---|---|---|---|---|---|
| | | | | Diameter, m (ft) | Type of mounting | |
| Goldstone | California | Pioneer | 11 | 26 (85) | Polar | 1958 |
| | | Echo | 12 | 26 (85) | Polar | 1962 |
| | | (Venus)[a] | 13 | 26 (85) | Az–El | 1962 |
| | | Mars | 14 | 64 (210) | Az–El | 1966 |
| — | Australia | Woomera[b] | 41 | 26 (85) | Polar | 1960 |
| Tidbinbilla | Australia | Weemala (formerly Tidbinbilla)[b] | 42 | 26 (85) | Polar | 1965 |
| | | Ballima[b] (formerly Booroomba) | 43 | 64 (210) | Az–El | Under construction |
| — | South Africa | Johannesburg[b] | 51 | 26 (85) | Polar | 1961 |
| Madrid | Spain | Robledo[b] | 61 | 26 (85) | Polar | 1965 |
| | | Cebreros[b] | 62 | 26 (85) | Polar | 1967 |
| | | Robledo | 63 | 64 (210) | Az–El | Under construction |

[a]A research-and-development facility used to demonstrate the feasibility of new equipment and methods to be integrated into the operational network. Besides the 26-m (85-ft) diam az–el-mounted antenna, DSS 13 has a 9-m (30-ft) diam az–el-mounted antenna that is used for testing the design of new equipment and support of ground-based radio science.

[b]Normally staffed and operated by government agencies of the respective countries (except for a temporary staff of the Madrid DSCC), with some assistance of U.S. support personnel.

within the field-of-view of at least one DSS, and for several hours each day may be seen by two DSSs. Furthermore, since most spacecraft on deep space missions travel within 30 deg of the equatorial plane, the DSSs are located within latitudes of 45 deg north or south of the equator. All DSSs operate at S-band frequencies: 2110–2120 MHz for earth-to-spacecraft transmission and 2290–2300 MHz for spacecraft-to-earth transmission.

To provide sufficient tracking capability to enable useful data returns from around the planets and from the edge of the solar system, a 64-m (210-ft) diam antenna network will be required. Two additional 64-m (210-ft) diam antenna DSSs are under construction at Madrid and Canberra, which will operate in conjunction with DSS 14 to provide this capability. These stations are scheduled to be operational by the middle of 1973.

### B. Compatibility Test Facilities

In 1959, a mobile L-band compatibility test station was established at Cape Kennedy to verify flight–spacecraft–DSN compatibility prior to the launch of the *Ranger* and *Mariner* Venus 1962 spacecraft. Experience revealed the need for a permanent facility at Cape Kennedy for this function. An S-band compatibility test station with a 1.2-m (4-ft) diam antenna became operational in 1965. In addition to supporting the preflight compatibility tests, this station monitors the spacecraft continuously during the launch phase until it passes over the local horizon.

Spacecraft telecommunications compatibility in the design and prototype development phases was formerly verified by tests at the Goldstone DSCC. To provide a more economical means for conducting such work and because of the increasing use of multiple-mission telemetry and command equipment by the DSN, a compatibility test area (CTA) was established at JPL in 1968. In all essential characteristics, the configuration of this facility is identical to that of the 26-m (85-ft) and 64-m (210-ft) diam antenna stations.

The JPL CTA is used during spacecraft system tests to establish the compatibility with the DSN of the proof test model and development models of spacecraft, and the Cape Kennedy compatibility test station is used for final flight spacecraft compatibility validation testing prior to launch.

## II. Ground Communications Facility

The GCF provides voice, high-speed data, wideband data, and teletype communications between the SFOF and the DSSs. In providing these capabilities, the GCF uses the facilities of the worldwide NASA Communications Network (NASCOM)[3] for all long distance circuits, except those between the SFOF and the Goldstone DSCC. Communications between the Goldstone DSCC and the SFOF are provided by a microwave link directly leased by the DSN from a common carrier.

Early missions were supported by voice and teletype circuits only, but increased data rates necessitated the use of high-speed circuits for all DSSs, plus wideband circuits for some stations.

## III. Space Flight Operations Facility

Network and mission control functions are performed at the SFOF at JPL. The SFOF receives data from all DSSs and processes that information required by the flight project to conduct mission operations. The following functions are carried out: (1) real-time processing and display of radio metric data; (2) real-time and non-real-time processing and display of telemetry data; (3) simulation of flight operations; (4) near-real-time evaluation of DSN performance; (5) operations control, and status and operational data display; and (6) general support such as internal communications by telephone, intercom, public address, closed-circuit TV, documentation, and reproduction of data packages. Master data records of science data received from spacecraft are generated. Technical areas are provided for flight project personnel who analyze spacecraft performance, trajectories, and generation of commands.

[3]Managed and directed by the Goddard Space Flight Center.

## Reference

1. *The Deep Space Network*, Space Programs Summary 37-50, Vol. II, pp. 15–17. Jet Propulsion Laboratory, Pasadena, Calif., Mar. 31, 1968.

# *Mariner* Mars 1971 Mission Support

R. P. Laeser
*Mission Support Office*

*The DSN support plans for the* Mariner *Mars 1971 mission have been modified by a move of the analog playback function from the SFOF media conversion center to the DSIF Compatibility Test Area, and by the DSN assumption of the responsibility for sequence of event generation computer software. Both of these new plans are discussed.*

## I. Introduction

Two major changes recently occurred in the DSN plans to support the *Mariner* Mars 1971 Project. First, all planned usage of the SFOF media conversion center (MCC) was diverted to the DSIF Compatibility Test Area (CTA 21). Secondly, the DSN assumed responsibility for the Sequence of Events Generation (SOEGEN) Program and is converting it to a multimission capability. Each of these changes will be discussed in detail.

## II. Analog Playback Facility

Until recently, the SFOF MCC was to operationally support *Mariner* Mars 1971 in two roles:

(1) Conversion of analog recordings of occultation data from DSSs 41 and 62 to a digital form in order to be computer compatible (Ref. 1).

(2) Playback of predemodulation analog telemetry recordings, through a subcarrier demodulation assembly (SDA), to produce digital recordings identical to the DSIF produced telemetry ODR (Ref. 2).

The MCC plan was to perform both functions using a PDP-7 computer and various special-purpose equipment.

The new plan takes advantage of existing equipment and operational software in CTA 21. This results in a significant cost saving—the primary reason for the change. The configuration for the analog playback capability, serving both the telemetry and occultation data requirements, is shown in Fig. 1. The FR 2000 analog record/playback device provides, with high time-base stability, an analog telemetry input to the subcarrier demodulator assembly (SDA). Subsequent telemetry processing is identical to the processing at any DSS; demodulation is performed by the SDA; symbol synchronization is performed by the symbol synchronization assembly (SSA); and an original data record (ODR) digital recording is written by the telemetry and command processor. Although not planned for operational usage, the data could be sent directly to the SFOF IBM 360/75 computer via high-speed (4800 bps) or wideband (50,000 bps) data lines. It should be mentioned at this point that predemodulation recordings cannot be replayed directly from the receiving

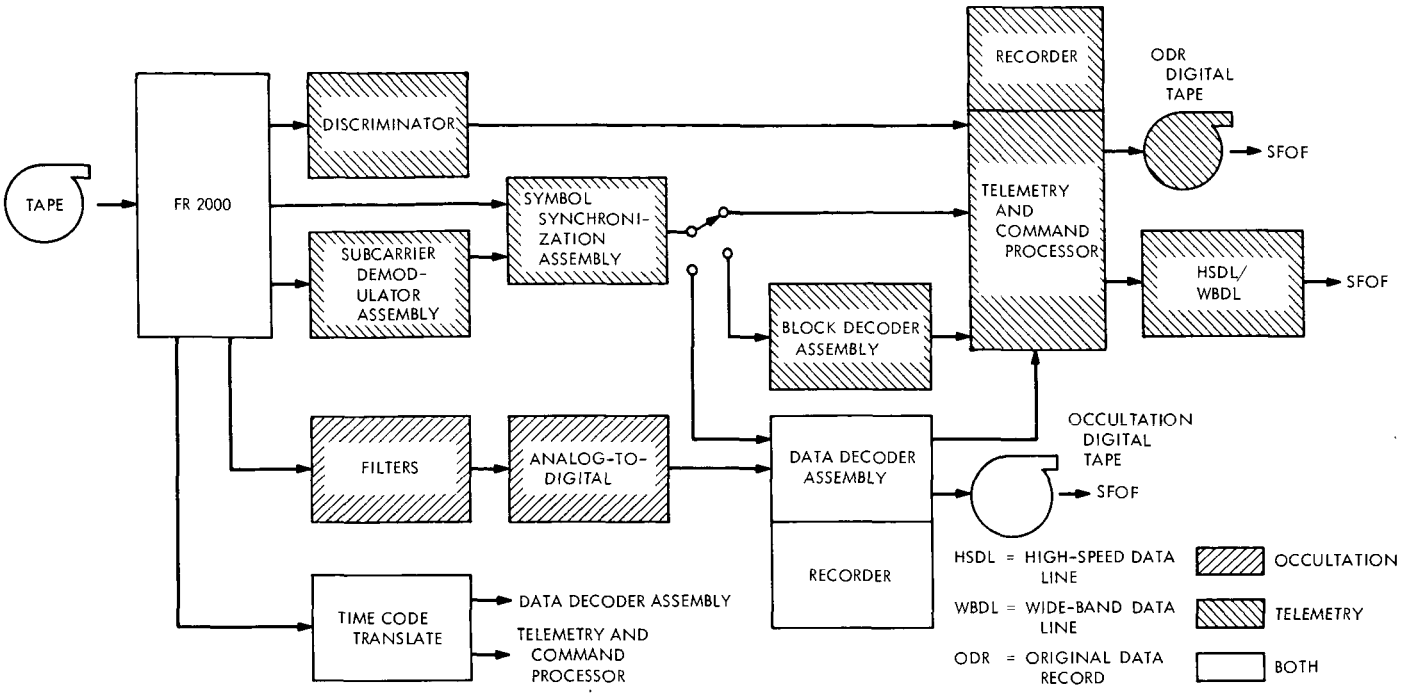


**Fig. 1. CTA 21 analog playback capability**

DSS as can postdemodulation recordings, because of a time-base stability problem; only DSS 14 and CTA 21 have the FR 2000 record/playback devices. It is planned to use this capability only when the SDA has failed and the data is required for the master data record.

The FR 2000 is also used to playback recordings of open-loop receiver data for the *Mariner* Mars 1971 occultation experiment. DSS 14 will have an on-site digitization capability, but DSSs 41 and 62 will not. Recorded data from the latter stations will be played into a minicomputer (the data decoder assembly [DDA], which is normally used for other purposes) after filtering and undergoing analog-to-digital conversion. The format of the DSS 14 and the CTA 21 recorded tapes will be identical.

## III. Sequence-of-events Generation

A sequence of events is necessary to both mission and DSN operations. In the past, sequences were printed from manually prepared punched cards and from makeshift computer programs, which likewise had manual inputs. The complexity of the *Mariner* Mars 1971 mission, with its 24-h adaptive operations cycle, obviates the need for a sequence-of-events generation capability which requires less manual labor to prepare, which can be executed in a short period of time, and which is as foolproof as possible.

The sequence which contains all events of interest to everyone is obviously operationally burdensome. For instance, the DSIF is not very interested in all the steps that the Command Team may be executing. In a mission of nearly continuous high activity, such as *Mariner* Mars 1971, the ability to generate subsequences of special interest becomes all the more important.

With these types of general requirements, the *Mariner* Mars 1971 mission operations system (MOS) undertook the specification of a sequence-of-events generation program. The implementation was split into two phases: Phase 1 for launch and cruise, and the more complex Phase 2 for orbital operations. Implementation was jointly funded by the DSN and *Mariner* Mars 1971 Project. Recently, it was decided that the capability should be multimission; therefore, the DSN accepted full responsibility for the program.

In general, the program will:

(1) Accept files of planned events versus time from various input sources, including other programs.

(2) Compile all inputs into a time-ordered sequence of events (SOE).

(3) For certain prespecified trigger events, compile predefined subsequences.

(4) Automatically validate the SOE with respect to predefined criteria.

(5) Display the completed sequences (total or extracted) in formats convenient to the various users.

(6) Output extracted sequences in a high-speed data block format.

There will be two types of inputs to the program: control inputs and sequence data inputs. The control inputs will be used to specify the mode of processing, file selection, and output formats. Sequence data inputs will include the event/time pair and reference time specifications. The reference time specification allows use of *launch minus, midcourse plus* and other such artificial time bases. Each time/event pair includes the time of occurrence of the event, in either GMT or one of the reference time systems, identification data and either a statement of the event or a trigger word which will cause a stored subsequence to be compiled. Inputs will be either manually entered via cards or keyboard, or transferred from another program. For *Mariner* Mars 1971, the COMGEN (command generation) program will supply spacecraft command information and the PREDICTS program will supply station rise and set times, and one two-way light time to the spacecraft. Actual scheduled station track times will be manually entered, although it is hoped to automate this interface in the future.

After a sequence is compiled, a validation process will be invoked. This process will check to assure that:

(1) For a given event, the sequence has necessary prerequisite events. For example, a DSS must be able to view the spacecraft before commanding it.

(2) For a given event, certain time-sensitive supporting future events are in the sequence.

(3) Time constraints do not prohibit an event from occurring at, before, or after the time of another event.

(4) Mutually exclusive events do not occur at the same time.

Failure to validate will result in an alarm message to the operator.

Three primary outputs will be available. The high-speed data output will be used to transmit sequences to remote sites, such as supporting DSSs. A text listing will provide tabular prints up to 128 characters wide, with heading information such as item number, mission time, absolute time, station identification, report by-to, action, and Mission A events, depending upon the user's needs. Finally, a bar chart format will be available which will include the following header information: view periods for three stations, a local time scale, and a GMT scale. The period of time covered by the bar chart will be variable. The remainder of the page will be divided into fields; events will be placed across the fields according to time.

Operation of the program will be a cooperative effort between the DSN and supported flight projects. Within necessary constraints, anyone will be able to build his own sequences and access other's sequences. In this way the DSN will be able to compile a time ordered sequence of DSN events for all projects being simultaneously supported.

## References


1. Laeser, R. P., "*Mariner* Mars 1971 Mission," in *The Deep Space Network*, Space Programs Summary 37-63, Vol. II, p. 11. Jet Propulsion Laboratory, Pasadena, Calif., May 31, 1970.

2. Laeser, R. P., and Gatz, E. C., "*Mariner* Mars Mission Support," in *The Deep Space Network*, Space Programs Summary, Vol. II, p. 7. Jet Propulsion Laboratory, Pasadena, Calif., May 31, 1970.

# *Viking* Mission Support

D. J. Mudgway
Mission Support Office

*The support provided to the* Viking *Project by the tracking and data system is discussed in the following areas: trajectory design factors, launch/arrival times, look angle between spacecraft, communication range and signal level, solar conjunction, and near-earth phase trajectories.*

## I. Introduction

In Space Programs Summaries 37-61, 37-62, and 37-63, Vol. II, the support provided by the tracking and data system (TDS) to the *Viking* Project was described with particular reference to management and organization; technical documentation; and TDS configurations for telemetry, command, and tracking.

The redirection of the Project from 1973 to 1975 has not materially affected these plans, but over the past few months, TDS support activity has been mainly directed toward achieving a better understanding of the influence of TDS capabilities and constraints on the design of the *Viking* 1975 Mission.

The capabilities of the Deep Space Network, as a significant factor in the design of *Viking* 1975 Mars Mission, will be described with reference to the following areas of interest:

(1) Trajectory design.

(2) Space vehicles.

(3) Telecommunications problems.

(4) Navigation accuracy.

(5) Science experiments.

(6) Mission operations.

## II. Trajectory Design Factors

Two types of earth-Mars trajectories, namely, the broken-plane type and Type II, are possible for the *Viking* mission after consideration of the 1975 launch opportunity, spacecraft weight, and launch vehicle (*Titan/Centaur*) capability.

Broken-plane trajectories bridge the gap between Type I[1] and Type II trajectories. Broken-plane trajectories permit earth–Mars transfers when it would otherwise be necessary to use single-plane trajectories that would be highly inclined to the ecliptic plane, requiring excessive energy. In the broken-plane trajectories, the spacecraft would make a plane change maneuver from a trajectory very nearly in the earth's orbital plane to a trajectory in Mars orbital plane.

[1]The earth–Mars heliocentric transfer angle is less than 180 deg in Type I trajectories and exceeds 180 deg in Type II trajectories.

By comparison with the broken-plane trajectories, Type II trajectories require fewer midcourse maneuvers and there is some loss of flexibility in launch period. Even though the flight time to Mars is about 1 mo more than the broken-plane trajectories, there is somewhat less risk involved because of the single-plane midcourse maneuvers associated with Type II trajectories.

From the TDS point of view there is no significant advantage of one type over the other, although a slightly longer mission was considered to be a less potential hazard than additional midcourse maneuvers.

In July 1970 these and other trajectory related factors were evaluated and a decision was made to adopt the Type II trajectory.

## III. Launch/Arrival Times

The span of launch and arrival dates resulting from this decision are as follows: The launch span would be from August 12 to September 19, 1975 (nominal); and the arrival span would be from July 18 to August 16, 1976 (nominal).

Current TDS planning indicates possible launch periods of November 1975 for *Helios B* and July 1976 for the Grand Tour Jupiter/Saturn/Pluto Mission, a situation which could fully extend the current TDS capabilities for network support (two 85-ft subnets and one 210-ft subnet).

## IV. Look Angle Between Spacecraft

The angular separation for two *Viking* spacecraft flying typical Type II trajectories to Mars is shown in Fig. 1 as a function of time from launch. The separation for broken-plane trajectories is similar.

Recognizing that the angular beamwidth of a 210-ft antenna is about 0.1 deg, it is apparent that both spacecraft do not appear in one antenna beam until 7 to 5 days before encounter. In a subsequent article on navigation accuracy it will be seen that several weeks of continuous tracking data are required on each spacecraft prior to Mars orbit insertion (MOI) to realize the desired insertion accuracy. In addition, the demands of the first orbiter and its lander are likely to fully engage each deep space station (DSS) during its view period. These two conflicting requirements preclude the possibility of a DSS time-sharing scheme between the two spacecraft.

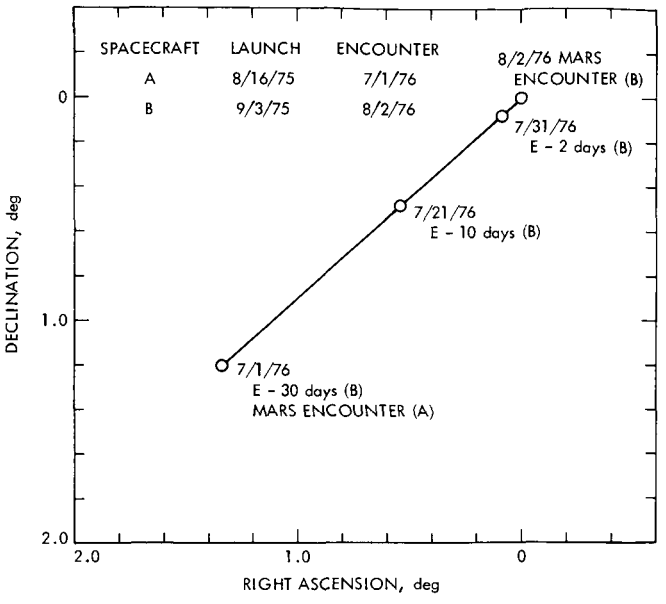


**Fig. 1. Relative angular separation of spacecraft B while spacecraft A is in Mars orbit**

At present, the navigation and orbital operations requirements are being studied in the hope that an optimum arrangement of separated arrival times and navigation and operations requirements can be found.

## V. Communication Range and Signal Level

A typical earth-to-Mars Type II trajectory is shown in Fig. 2, with the corresponding geocentric range and range rate in Fig. 3. The range at encounter is approximately $300 \times 10^6$ km and increases to $400 \times 10^6$ at maximum range. This has a profound effect in limiting the maximum data rates received by the DSN in comparison with past Mars missions, such as *Mariner* Mars 1969 and 1971. The maximum data rate for the orbiter block-coded telemetry channel is 4 kbps (nominal), while the maximum rate which can be supported by the communications link from the lander is about 250 bps.

## VI. Solar Conjunction

Consideration of the Type II earth–Mars orbits proposed for the *Viking* spacecraft shows that earth–Mars conjunction occurs a short time after encounter. A plot of sun–earth–Mars angle as a function of calendar date is shown in Fig. 4 with earth–Mars conjunction occurring on November 25, 1976. As a consequence of the proximity of the radio beam to the solar disk, both uplink and downlink suffer a degradation in performance. The two principal contributors to the degradation are increased system

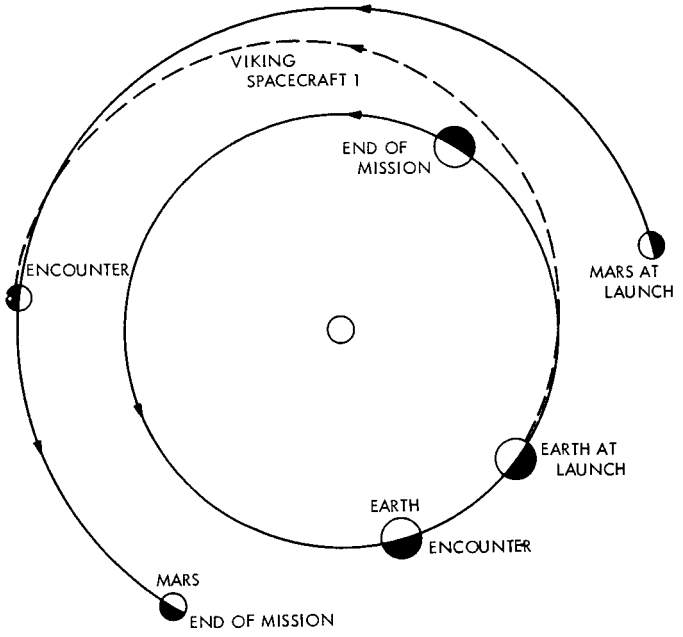


**Fig. 2. Typical earth–Mars orbital projection**

temperature and spreading of the telemetry modulation spectrum.

These effects first become significant about a month prior to conjunction when the sun–earth–Mars angle is about 8 to 9 deg. The way in which this affects the downlink telemetry link is discussed in detail in a subsequent article on the telecommunications problem.

## VII. Near-Earth Phase Trajectories

The *Viking* mission utilizes a parking orbit ascent (*Titan III*) and two *Centaur* burns to inject the spacecraft into a Type II transfer orbit to Mars. The parking orbit is a 100-nmi circular orbit with a launch azimuth sector from 90 to 115 deg. The parking-orbit coast time is variable with a maximum coast time of 30 min.

For any given day the launch azimuths are variable and progressively increase, becoming more southerly the later the vehicle is launched during the daily window. The earth tracks for several representative Type II launch trajectories are shown in Fig. 5.

TDS development and analysis of these trajectories has been tabulated in Ref. 1, where view periods and other related data for supporting stations of the Air Force Eastern Test Range, the Manned Space Flight Network, and DSN may be found. This material forms the basis for all TDS planning in the near-earth phase.

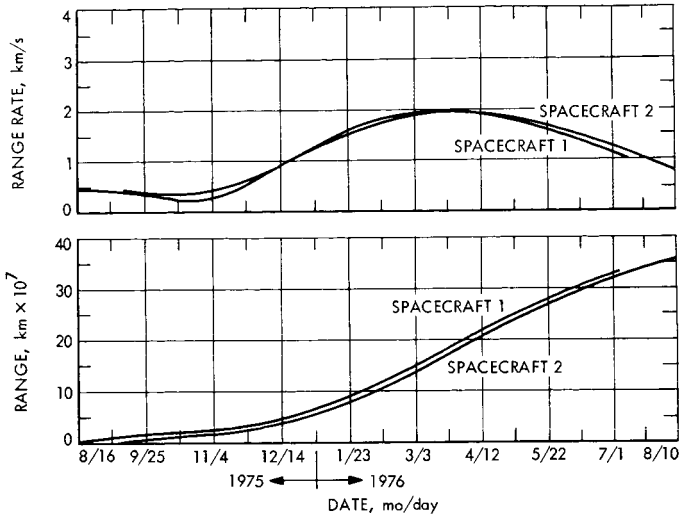


**Fig. 3. Typical geocentric range and range rate**

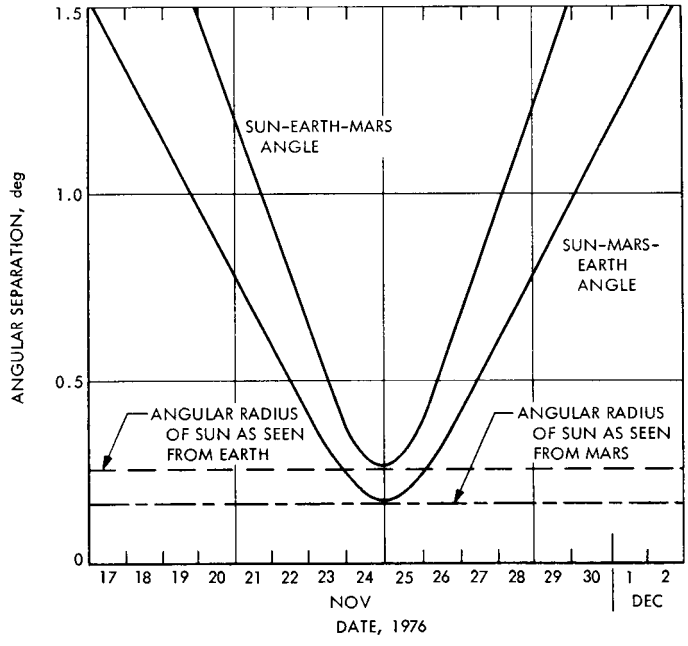


**Fig. 4. Earth–Mars conjunction, November 1976**

The problems facing the initial acquisition station of the DSN first become apparent as a result of these studies. Trade-offs are made between the need for good radiometric data at the earliest possible time after spacecraft separation, and the conflicting factors of high angle and doppler rates, and orbit uncertainties.

Depending on the parking orbit coast time for the actual trajectory selected at launch, either DSS 51 (short coast times) or DSS 42 (long coast times) will be used as the initial DSN acquisition station.

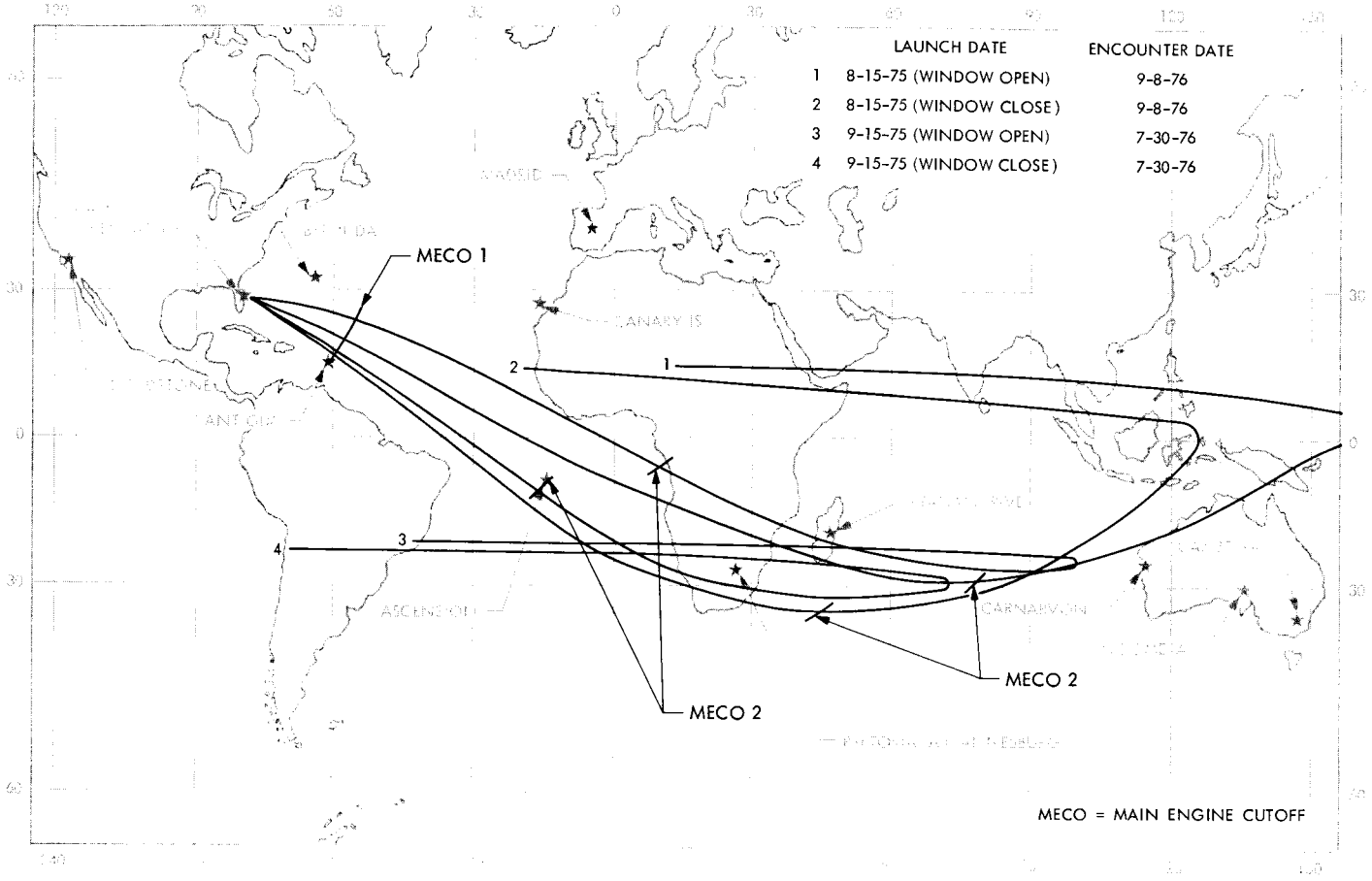


**Fig. 5. *Viking* Type II trajectory earth tracks**

## Reference

1. Levy, H. N., Jr., *Viking Preliminary Near-Earth Phase Characteristics and Station Viewperiods* (JPL internal document), Sept. 4, 1970.

# DSN Inherent Accuracy Project

*T. W. Hamilton*
*Mission Analysis Division*
*D. W. Trask*
*Tracking and Orbit Determination Section*

*The objectives and organization of the DSN Inherent Accuracy Project, and the technical work performed by the project, are described. Current work (reported in the three following articles) is introduced and summarized.*

## I. Description

The DSN Inherent Accuracy Project was formally established by the DSN Executive Committee in July 1965. The objectives of the project are:

(1) Determination (and verification) of the inherent accuracy of the DSN as a radio navigation instrument for lunar and planetary missions.

(2) Formulation of designs and plans for refining this accuracy to its practical limits.

Achievement of these goals is the joint responsibility of the Telecommunications and Mission Analysis Divisions of JPL. To this end, regular monthly meetings are held to coordinate and initiate relevant activities. The project leader and his assistant (from the Mission Analysis and Telecommunications Divisions, respectively) report to the DSN Executive Committee, and are authorized to task project members to (1) conduct analyses of proposed experiments, (2) prepare reports on current work, and (3) write descriptions of proposed experiments. The project is further authorized to deal directly with those flight projects using the DSN regarding data-gathering procedures that bear on inherent accuracy.

The various data types and tracking modes provided by the DSIF in support of lunar and planetary missions are discussed in Ref. 1. Technical work directly related to the Inherent Accuracy Project is presented in Ref. 2 and in subsequent Space Programs Summary (*The Deep Space Network*) volumes, and is continued in the three following articles.

For most upcoming planetary missions, such as *Mariner* Mars 1971, the tightest bounds on the allowable errors for a number of parameters arise from the navigational accuracy requirements during encounter support. In particular, encounter navigational accuracy is most sensitive to error sources that cause a diurnal signature on the radio tracking data (Ref. 3). These sources of error are of two classes: (1) those parameters that define the locations of the DSS in inertial space, and (2) those phenomena that directly affect the DSS tracking data. The first category includes the locations of the DSS with respect to earth's crust; Universal Time (UT1); polar motion (the motion of the earth's crust with respect to the spin axis); precession and nutation (orientation of the earth's spin axis with respect to inertial space); and the ephemerides of the

earth, moon, and target body. Of these, uncertainties in the first three are currently the major limitations to the encounter support of navigation accuracy.

The dominant sources of error in the second category are those affecting the tracking data directly. These include frequency system instability, electrical phase path variations (through both the spacecraft and the DSS), and the transmission media (the troposphere and the charged particles in the ionosphere and space plasma).

## II. Current Work

The three following articles are concerned with the effect of the transmission media on the radio metric data. The first article (MacDoran, et al) discusses an interesting result obtained with the differenced range versus integrated doppler (DRVID) technique during the *Mariner* Mars 1969 mission. This technique takes advantage of the fact that charged particles affect range increments obtained from the accumulated doppler count, and those obtained from differencing range measurements, by a nearly equal but opposite amount; i.e., the effect advances the phase velocity (doppler) and retards the group velocity (ranging). Thus, DRVID can be used to calibrate tracking data to obtain the effect of charged particles. DRVID was first tried during the *Lunar Orbiter* and *Mariner V* missions, and although these attempts were not successful in obtaining the desired calibration information for the tracking data, they did succeed in identifying problem areas that masked the effects of the charged particles. Subsequently, the recent effort during *Mariner* Mars 1969 (Refs. 4 and 5) has yielded encouraging results. In fact, not only has the calibration of radio metric data proved possible with DRVID, but as explained by MacDoran, et al, DRVID has been used to probe the solar corona during the superior conjunctions of the *Mariner VI* and *VII* spacecraft. It has been possible to establish a correspondence between plasma fluctuations in the radio raypath and McMath regions on the solar surface. Estimates of electron densities a factor of four larger than the normal ambient condition and scale sizes from $6 \times 10^4$ to $2 \times 10^6$ km have been made for plasma clouds transiting the radio path.

The next two articles (Miller, et al; Winn and Leavitt) discuss tropospheric refraction. Currently, doppler residuals at lower elevation angles generally show systematic behavior such that it has become common practice to delete all data taken below elevation angles of 10 or 15 deg from the orbit determination solutions. This is unfortunate, because there are indications (Ref. 3) that this low elevation data is particularly desirable for inclusion in the orbit determination process. It is felt that the systematic lower elevation angle doppler residuals are due to inadequacies in the ability to correct for the transmission media—in particular, the troposphere—and a serious effort is being made to correct this situation.

One approach is to use a separate exponential refractivity profile for both the wet and the dry component instead of the single profile model presently used. Further, instead of representing the ray trace results from these profiles by an empirical formula, they will be more accurately represented in the orbit determination software in tabular form. However, neither the wet nor the dry refractivity profile is invariant so the tropospheric calibration error caused by assuming a nominal refractivity profile, as opposed to the actual profile, was examined (Miller, et al). For reasonable profile variations, it was found that the error in the tropospheric range correction obtained by using the nominal profile will be less than 0.5 m down to a 5-deg elevation angle, which is within the acceptable limits for support of the *Mariner* Mars 1971 mission during real-time operations. This allows a table of tropospheric corrections versus elevation angle for a nominal refractivity profile to be stored in the orbit determination software, and the tropospheric corrections to the radio metric tracking data are obtained by scaling the contents of this table by the zenith tropospheric range correction. Consequently, a considerable simplification is realized over having to perform raypath tracings for each tracking pass during the *Mariner* Mars 1971 mission.

The scaling factor must still be determined for each tracking pass. Possible ways of doing this include the use of radiosonde data to compute the zenith range correction or including the scaling factor as a "solve for" parameter during the orbit determination process itself. An analytical investigation of this later technique was reported by Ondrasik (Ref. 6), while Winn and Leavitt attempt to accomplish this by processing tracking data obtained from *Surveyor* spacecraft after they had landed on the moon. This is a preliminary study and the charged particle corrections—notably, those due to the ionosphere which have a diurnal signature—have not been removed from the tracking data. Nevertheless, where systematic errors in the doppler residuals are visible below a 25-deg elevation angle, solving for the tropospheric scaling factor—on a tracking pass by tracking pass basis—removes the signature at elevation angles above 15 deg, and reduces the second moment of the doppler residuals by 80%.

## References


1. Trask, D. W., "DSIF Data Types and Tracking Modes," in *The Deep Space Network*, Space Programs Summary 37-39, Vol. III, pp. 6–7. Jet Propulsion Laboratory, Pasadena, Calif., May 31, 1966.

2. Trask, D. W., and Hamilton, T. W., "DSIF Two-Way Doppler Inherent Accuracy Limitations," and "Quality of Two-Way Doppler Tracking Data Obtained During the *Mariner IV* Mission," in *The Deep Space Network*, Space Programs Summary 37-38, Vol. III, pp. 8–20. Jet Propulsion Laboratory, Pasadena, Calif., Mar. 31, 1966.

3. Hamilton, T. W., and Melbourne, W. G., "Information Content of a Single Pass of Doppler Data from a Distant Spacecraft," in *The Deep Space Network*, Space Programs Summary 37-39, Vol. III, pp. 18–24. Jet Propulsion Laboratory, Pasadena, Calif., May 31, 1966.

4. MacDoran, P. F., and Wimberly, R. N., "Charged-Particle Calibrations From Differenced Range Versus Integrated Doppler—Preliminary Results From *Mariner* Mars 1969," in *The Deep Space Network*, Space Programs Summary 37-58, Vol. II, pp. 73–77. Jet Propulsion Laboratory, Pasadena, Calif., Jul. 31, 1969.

5. MacDoran, P. F., and Martin, W. L., "DRVID Charged-Particle Measurement With a Binary-Coded Sequential Acquisition Ranging System," in *The Deep Space Network*, Space Programs Summary 37-62, Vol. II, pp. 34–41. Jet Propulsion Laboratory, Pasadena, Calif., Mar. 31, 1970.

6. Ondrasik, V. J., "A Solution for the Tropospheric Zenith Range Correction Using a Single Pass of Differenced Doppler Data," in *The Deep Space Network*, Space Programs Summary 37-63, Vol. II, pp. 16–21. Jet Propulsion Laboratory, Pasadena, Calif., May 31, 1970.

# Probing the Solar Plasma With *Mariner* Radio Metric Data, Preliminary Results

*P. F. MacDoran and P. S. Callahan*
*Tracking and Orbit Determination Section*
*A. I. Zygielbaum*
*Communications Systems Research Section*

*A radio technique, exploiting the opposite changes of group and phase velocity in a dynamic plasma, was used to probe the solar corona during the superior conjunctions of the* Mariner VI *and* VII *spacecraft. From an analysis of range and doppler radio metric data generated by the DSN in tracking the spacecraft, it was possible to establish a correspondence between plasma fluctuations in the radio raypath and McMath sunspot regions on the solar surface. Estimates of 3000 electrons/cm$^3$ and scale sizes of $6 \times 10^4$ and $2 \times 10^6$ km were made for plasma clouds transiting the radio path when tracking within a few degrees of the sun.*

## I. Introduction

Shortly after their encounters with Mars in the summer of 1969, the *Mariner VI* and *VII* spacecraft entered an extended mission phase to take advantage of the continuing spacecraft life. With the advent of the *Mariner* Mars 1969 extended mission came a new ranging system, called fast acquisition ranging, using a sequential binary code (Ref. 1). This new system possesses 40 times the sensitivity of the ranging system used during the primary *Mariner* Mars 1969 mission. The increased sensitivity made it possible for the *Mariner VI* and *VII* spacecraft to be ranged around their entire orbit, particularly at 2.6 AU at their solar superior conjunctions. The range and doppler radio metric tracking close to the sun made it possible to measure the solar plasma dynamics.

The plasma dynamics were measured with a method known as differenced range versus integrated doppler (DRVID), which exploits the opposite change of group and phase velocity as the plasma density changes. The method is sensitive only to changes in the columnar electron content, not to the total content. The original purpose of DRVID (Ref. 2) was to provide charged particle calibrations for doppler data; however, it has proved useful in probing the solar plasma as well. Calibration of plasma-caused time delay in range data requires knowledge of the total electron columnar content; however, only the change in the columnar content is required to calibrate doppler data for charged particle effects. The DRVID technique is, therefore, ideally suited for doppler calibration.

Approximately 150 h of DRVID data suitable for calibration of doppler data and for studying the solar plasma were collected during the extended mission covering 4 months after the *Mariner VI* and *VII* superior conjunctions. From a preliminary study of this data, it was found that:

(1) Doppler phase-locked tracking is often valid even when the "receiver out of lock" indicator shows the data to be invalid.

(2) Solar plasma clouds with typical sizes of $6 \times 10^4$ and $2 \times 10^6$ km occur at heliocentric distances of 27 solar radii.

(3) Local electron density variations are at least a factor of four above steady-state predictions.

(4) A correspondence occurs between plasma fluctuations in the raypath and McMath sunspot regions on the solar surface.

## II. Operational DRVID Description

The DRVID method is based on the apparent path differences as measured by group and phase methods in a plasma. In a dynamic plasma, the group and phase velocities are not constant but vary such that for an increasing columnar electron content the phase velocity increases by the same amount that the group velocity decreases. Range code modulation is propagated at the group velocity while doppler information propagates at the phase velocity.

By comparing the path changes indicated by range differences against those found by integrating the velocity inferred from the doppler data, a remainder results that is proportional to the number of electrons which have entered or left the raypath during the interval of observation. Note that such a technique cancels out all common effects in the doppler and range such as the earth's troposphere and more importantly the tracking station–spacecraft relative motions. Even the less prosaic effects of general relativity and possible gravity waves are removed by this differencing technique.

As shown in Ref. 2, the DRVID function is given in meter-kilogram-second units by

$$\text{DRVID} = \frac{40.3}{f^2} \int_{t_1}^{t_2} \int_{\text{raypath}} \frac{d}{dt}\, n(s,t)\, ds\, dt$$

where

DRVID = two-way range change, m

$f$ = radio frequency, Hz

$n(s,t)$ = space and time variable electron density, electrons/m$^3$

$t_1, t_2$ = time limits of observation span

The columnar electron content is given by

$$I(t) = \int_{\text{raypath}} n(s,t)\, ds$$

so that the change in the columnar electron content is given by

$$\Delta I(t) = 6.007 \times 10^{16}\, \text{DRVID}(t), \text{ electrons/m}^2$$

for the case of S-band range and doppler tracking.

The validity of the DRVID technique, using the fast acquisition ranging system, was established in limiting cases in late 1969. In these tests with the *Mariner* spacecraft at an angular distance of 60 deg from the sun, the earth's ionosphere was measured by DRVID and independently verified by a VHF Faraday rotation method (Ref. 3). These method verification tests also established that ground equipment variations were less than 0.1 m/h.

For observations within a few degrees of the sun, independently determined solar plasma dynamics are unavailable to check the DRVID method to the required precision. Thus, an alternate, although less rigorous approach, had to be devised to test the internal consistency of the observations. The method involved eliminating the plasma contribution from the doppler data and examining the residuals for systematic effects. The internal consistency tests are valid since the solar plasma excursions are assumed uncorrelated with the inherently diurnal variations that normally occur in doppler tracking data. However, if the plasma dynamics were introduced by the earth's ionosphere, the effect would be diurnal in character and, therefore, would invalidate any doppler residual analysis to independently check the DRVID data.

## III. Autocorrelation Detection Plasma Transit

The simultaneous presence of an uplink and downlink in the medium between the earth and spacecraft offers an opportunity to measure the position of plasma intersections with the radio raypath. As plasma irregularities

transit the raypath, they will, in general, cause a particular signature in the DRVID data. As illustrated in Fig. 1, the plasma signature will arrive at the earth twice, first on the downlink and then again at a time $\tau^*$ when the uplink signature is received. Given a plasma stream which crosses the raypath at a particular point and persists for a time comparable to the length of the observations (several hours), an autocorrelation of the DRVID data should exhibit a correlation maximum at a time shift $\tau^*$. Inspection of Fig. 1 shows that the domain of physically significant autocorrelation time shifts extends from zero (at the spacecraft) to a round-trip light time (at the earth).

Although independently conceived by the authors, the autocorrelation technique applied to bi-static tracking was first proposed by Thiede and Lusignan (Ref. 4), in the context of phase excursions introduced into doppler data by refractive index variations. The DRVID data type differs somewhat from the proposed uses of Ref. 4 since DRVID has sensitivity to only the charged particle effects and no dependence on relative spacecraft motion and neutral atmospheric effects.

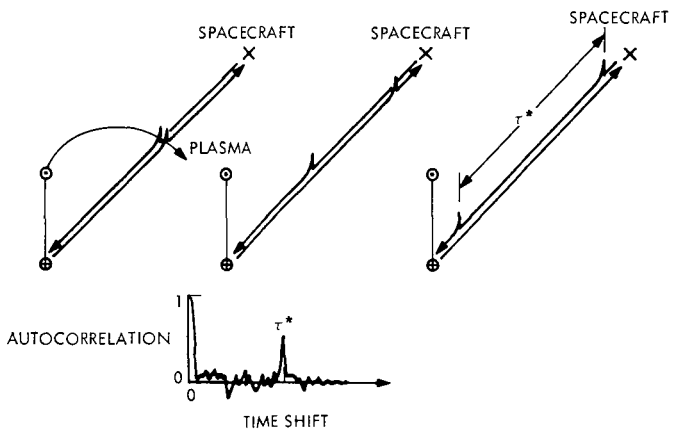


**Fig. 1. Autocorrelation for location of plasma transit**

## IV. Observations

Figure 2 shows columnar electron changes and the range change at S-band for an event of May 29, 1970 observed in *Mariner VII* DRVID data. The spacecraft range $\rho$ was 2.5 AU; the sun–earth–probe angle was 6 deg. The received ranging power was −190 dBm with a total uplink power of 200 kW from the 64-m tracking station at DSS 14. The curve fit to the data points is the result of a 15th-order least-squares power series. The event itself is rare because it apparently shows plasma entering and leaving the raypath. Most excursions observed were either of plasma entering or leaving but not both. The shape of

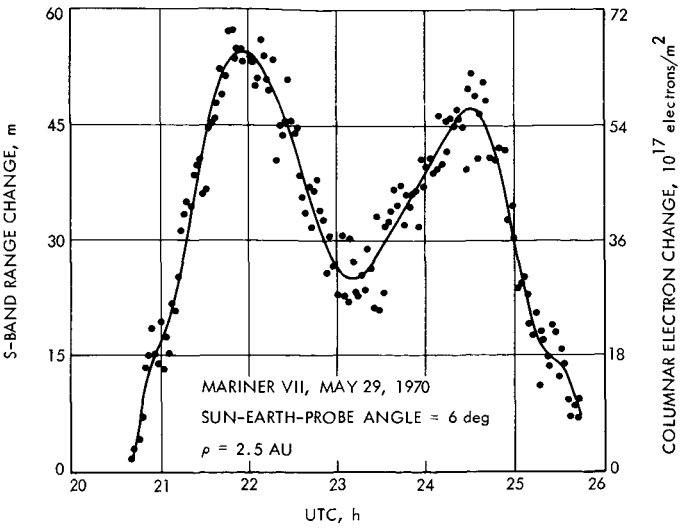


**Fig. 2. DRVID-measured solar plasma dynamics**

the excursion suggests the transit of two connected clouds. The change in the columnar electron content is approximately $65 \times 10^{17}$ electrons/m$^2$. Assuming that the excursion results from two similar plasma clouds, the duration of each is about 2½ h.

Figure 3 shows the result of the internal consistency test of the DRVID data to verify that it removes the apparent plasma effects from integrated doppler orbit residuals. "Receiver-out-of-lock" indications were so frequent that these doppler data would not normally be used. The

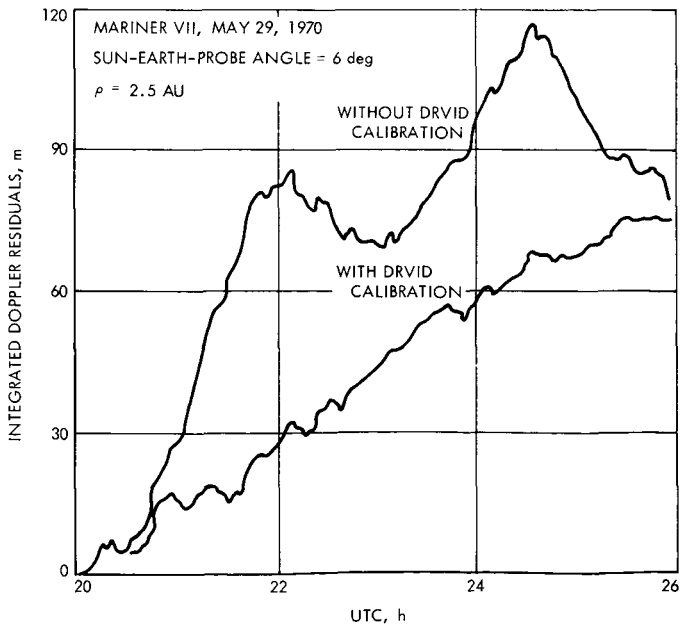


**Fig. 3. Integrated doppler residuals**

power series shown in Fig. 2 removes the double-humped excursion from the integrated doppler residuals. Since only a diurnal variation is left after the removal of DRVID, it is presumed that a real plasma excursion was observed and that sufficient doppler phase-lock was maintained. The diurnal signature results from using an approximate orbit to determine the doppler residuals.

Many similar events have been analyzed for data taken within a few degrees of the sun. Columnar content rates of change lasting several hours have been found up to $3 \times 10^{15}$ electrons/m$^2$/s. It is likely that there were even larger rates of change; however, the internal consistency test showed that there was a failure to maintain doppler phase-lock in such cases. Phase-lock failures were fortunately few, only about 5% for a month around superior conjunction. For comparison, columnar content rates in the earth's ionosphere rarely exceed $10^{14}$ electrons/m$^2$/s.

Figure 4 shows the result of autocorrelating the residuals of the individual DRVID samples from a 15th-order least-squares power series fit to the data of May 29, 1970. Relative correlation maxima occur at time shifts of 18, 24, and 36 min. The absolute significance of the autocorrelation function has been disturbed by the inability of the power series fit to adequately remove the long period (150 min) oscillation from the data.

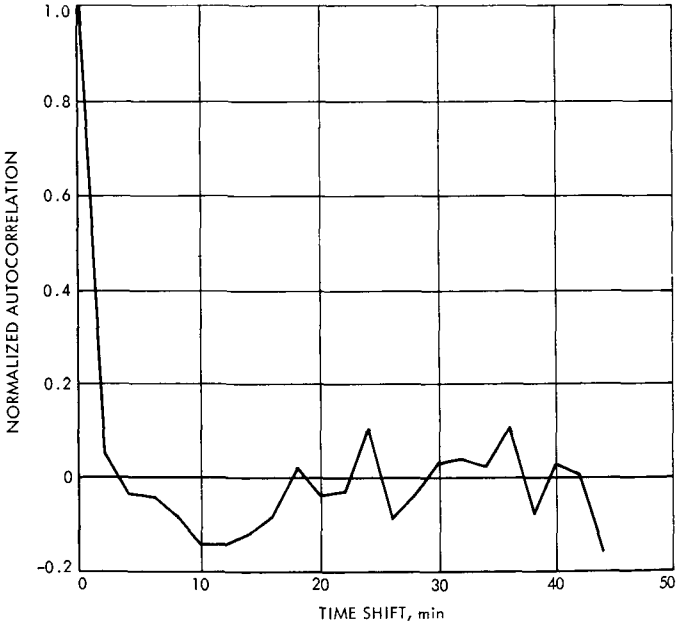


**Fig. 4. Normalized autocorrelation (*Mariner VII*, May 29, 1970)**

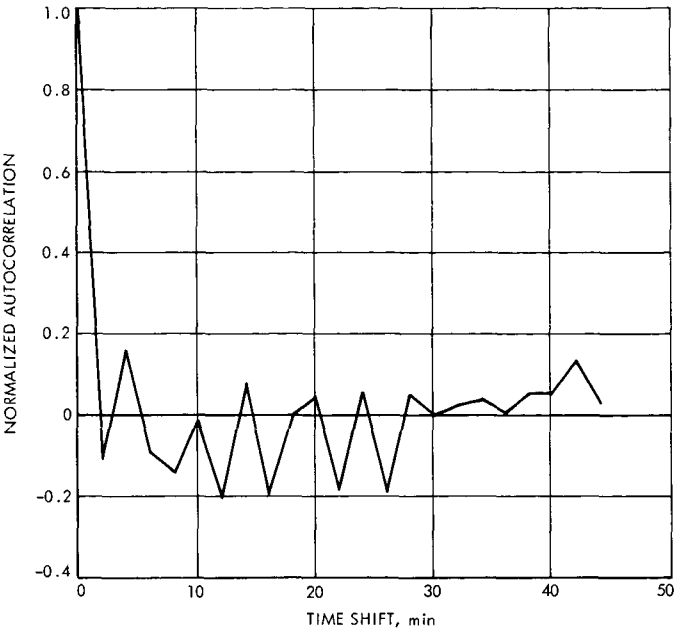


**Fig. 5. Normalized autocorrelation (*Mariner VI*, June 2, 1970)**

Figure 5 shows the results of autocorrelating the DRVID data from *Mariner VI* on June 2, 1970. The correlation reaches relative maxima at 4, 14, and 24 min. The round-trip light time was 43.1 min. Note the negative correlation spikes before and after each of the positive peaks. Also note the region of little fluctuation from 30 to 40 min.

## V. Solar Plasma Propagation Model/Solar Surface Disturbance Correspondence

The model is quite simple: The sun rotates with an angular rate of approximately 13.4 deg/day. Ignoring heliographic latitude dependence, material ejected from the surface travels radially at a speed between 300 and 350 km/s. These assumptions result in a simple spiral structure for the streaming material. A specific example, the data in Fig. 4 for *Mariner VII* on May 29, 1970, will be helpful in illustrating the use of the model.

The correlation $\tau^* = 24$ min implies that the plasma crossed the raypath 1440 s from the spacecraft or 1158 s from the earth since the earth/spacecraft round-trip light time was 2519 s. Both *Mariner VI* and *VII* are essentially in the ecliptic plane so plane geometry is adequate. Figure 6 shows the geometry of *Mariner VII* on May 29, 1970. The radial path from the sun to the raypath plasma intersection is 0.12 AU ($0.18 \times 10^8$ km). The plasma transit

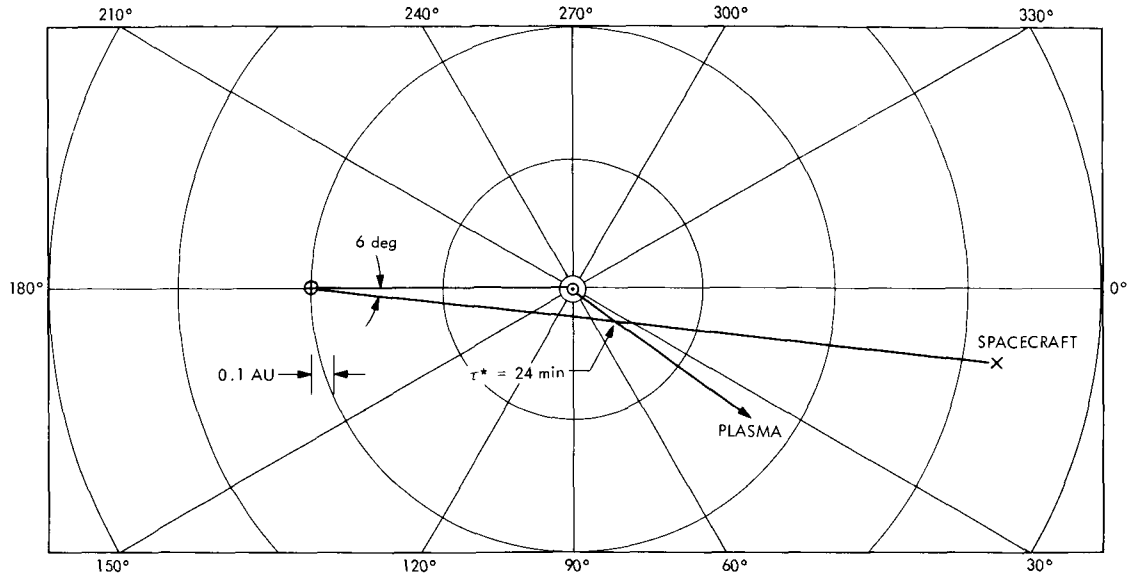


**Fig. 6. Ecliptic plane geometry (*Mariner VII*, May 29, 1970)**

is observed on day 149.9. Assuming an average velocity of 320 km/s, the material had to leave the solar surface on day 149.3. The assumed radial motion of the plasma requires it to have departed the sun's surface at a relative earth/sun longitude of 120°W. The question is now whether or not a solar surface disturbance is located at such a longitude at the required time. Since the relative longitude of 120°W is not visible from the earth on day 149.3, an indirect method is necessary.

The ESSA[1] Research Laboratories Solar-Geophysical Data (Prompt Reports) contain H$\alpha$ spectroheliograms taken daily. In the spectroheliogram for June 11 at 23:25, UT, McMath region 789 A-B extends over a range of longitudes from 45 to 80°E. Assuming a rotation rate of 13.4 deg/day, and assuming that the 789 complex remains substantially unchanged, on May 29.3 the complex will be located between longitudes 96 and 131°W. The calculated longitude of 120°W is in the center of region 789. McMath region 789 is not observed to make a west limb transit before it is detected in the raypath. However, projecting ahead to the expected time of east limb transit for the plasma emitter, region 789 appears at the predicted time. Thus, it appears possible to observe the development of active regions on the back of the sun with the autocorrelation technique.

The other autocorrelation peaks at 18 and 36 min, by an analysis similar to that above, correspond to McMath regions 740 and 759, respectively. Figure 7 illustrates the plasma crossing and the mapping to the sun.

Three important correlations were found in Fig. 5, *Mariner VI*, June 2, 1970, at 4, 14, and 24 min, and a conspicuous lack of correlations is seen between 30 and 40 min. Using a velocity of 300–350 km/s, the 4-, 14-, and 24-min correlations are found to correspond to McMath regions 774, 781 A-B, and 792, respectively. Region 781 A-B is a return of region 743 and region 774 is a return of region 740. Note that region 740 appeared in the analysis of *Mariner VII*, May 29, 1970, 3 days prior to these *Mariner VI* observations.

Consider the lack of correlation features between 30 and 40 min in Fig. 5. Because of the peculiar mapping involving the earth–spacecraft geometry, the plasma velocity, and the solar rotation, the correspondence between correlation time shifts are found and the sun's surface is not immediately obvious. Table 1 contains the relative longitudes and dates of ejection from the sun if

**Table 1. Correlation time shift $\tau^*$ mapping to longitude/time pairs on the sun's surface**

| Correlation time shift $\tau^*$, min | Relative longitude, °W | Day numbers |
|---|---|---|
| 30 | 32.6 | 152.2 |
| 32 | 19.9 | 151.6 |
| 34 | 12.6 | 151.1 |
| 36 | 7.9 | 150.5 |
| 38 | 4.8 | 149.9 |
| 40 | 2.5 | 149.3 |

[1]Environmental Science Services Administration.

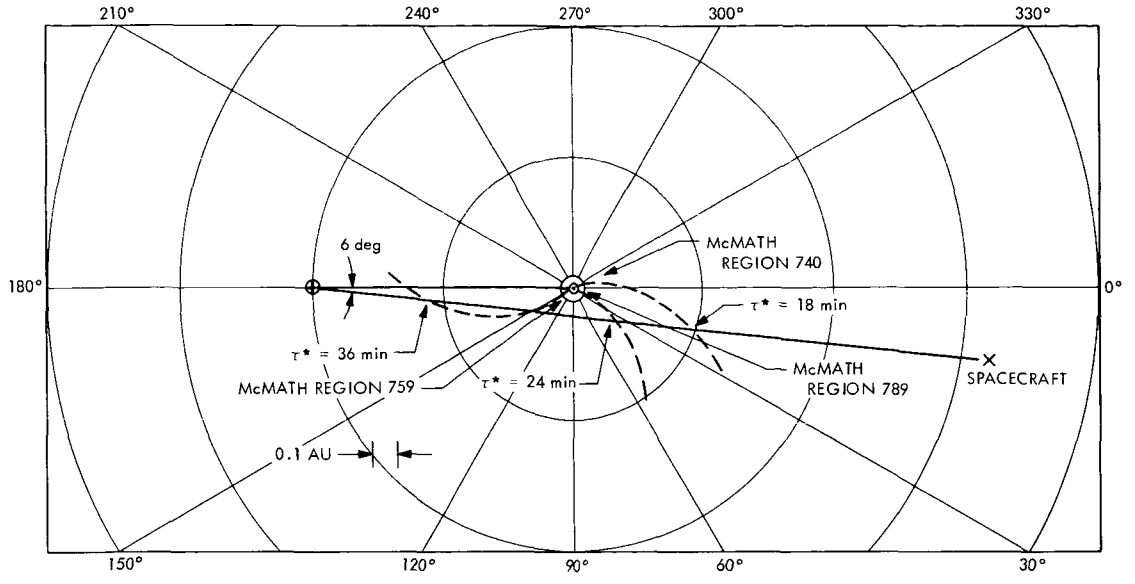


**Fig. 7. Plasma transit/McMath region correspondence (*Mariner VII*, May 29, 1970)**

material were to cause correlations at the specified time shifts. An examination of the ESSA data shows no active regions for the times and longitudes of Table 1. Therefore, not only do correlation maxima map to McMath sunspot regions, but regions on the sun without McMath regions produce a marked lack of autocorrelations in the DRVID data.

These examples are not isolated incidents. Many such correspondences have been made for both *Mariner* spacecraft in May and June of 1970. Over 90% of the correlation maxima found have been mapped to McMath regions in the manner described here. Several instances of long periods without correlations have been mapped to regions of no activity.

## VI. Plasma Cloud Properties

For the case of *Mariner VII* on May 29, 1970, the presence of three solar surface disturbances contributing to the columnar electron dynamics complicates the interpretation; however, an order of magnitude estimate of the parameters for the clouds causing the large changes is possible. For the purposes of estimation, let us assume that the large scale dynamics of the double cloud were contributed by the region with the smallest heliocentric distance to the raypath, McMath region 789. The velocity transverse to the raypath is smaller than the average velocity of 320 km/s by the dot product of the radial plasma velocity vector and the impact vector. Thus, the transverse velocity is $v_T = 260$ km/s, implying that the clouds have a transverse dimension of approximately $2.3 \times 10^6$ km. Assuming the longitudinal dimensions of the cloud to be comparable, an estimate can be made for the change in the average electron density. The columnar content is observed to increase by $65 \times 10^{17}$ electrons/m$^2$. Given a cloud of size $2 \times 10^6$ km, it follows that the average density must have changed by $\sim 3 \times 10^9$ electrons/m$^3$ (3000 electrons/cm$^3$). If one assumes that these plasma dynamics occurred at the position indicated by the 24-min correlation peak, then 3000-electron/cm$^3$ variations can occur at 0.12 AU (27 solar radii).

It is of interest to compare this variation with the steady-state electron density predictions for the solar corona. Various models for the solar corona (Refs. 5, 6, and 7) all predict substantially the same electron density at 0.12 AU, approximately 700 electrons/cm$^3$. A variation in density of 3000 electrons/cm$^3$ is rather unexpected. There is, of course, the possibility that the plasma dynamics resulted from one of the other two McMath regions, 740 or 759. The plasma from both those regions intersect the raypath at heliocentric distances of 0.4 and 0.6 AU, respectively. The implied cloud dimensions would be $0.6 \times 10^6$ km with an average electron density variation of $10^4$ electrons/cm$^3$. Since the steady-state electron density at 0.5 AU is expected to be between 50 and 100 electron/cm$^3$, a variation of $10^4$ electron/cm$^3$ seems hard to accept.

The DRVID autocorrelation peaks often appear to be preceded and/or followed by relative negative correlations, as can be seen in Figs. 4 and 5. These relative minima accompanying the maxima could be physically

interpreted as indicating that the plasma irregularities causing the correlations are of a compression/rarefaction nature. Determining the detailed structure of the irregularities is not possible because the data frequency is limited to 2 min/sample. The indications are, however, that the correlation width of the irregularities is approximately 4 min. If the irregularities have a simple rectangular electron density compression/rarefaction structure, their autocorrelation would have a triangular shape as shown in Fig. 8. Plasma compression associated with velocity waves has been observed by Neugebauer and Snyder (Ref. 8) in data from *Mariner II*. The deviations from the triangular pattern are possibly caused by data noise and the oversimplified model. The width of the correlation triangle is proportional to the irregularity size $w$ divided by the transverse velocity $v$. Using $v_T = 260$ km/s and a correlation time scale $\sim 240$ s, it is found that the irregularities have a typical size of $6 \times 10^4$ km. Because of the data sampling rate, the correlation time scale will always be about 240 s. If the apparent transverse velocity changes because of geometry, the correlation will be sensitive to a different size of plasma irregularity. The maximum size observable from the correlation is about $10^5$ km, while the minimum is about $2 \times 10^4$ km.

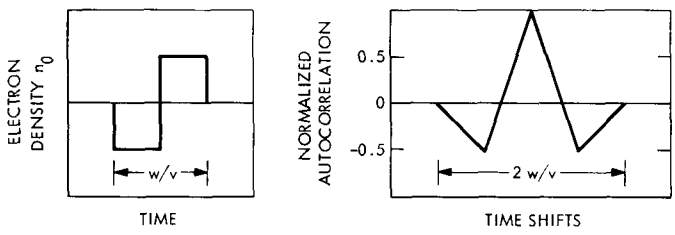


**Fig. 8. Autocorrelation of rectangular plasma density variation**

## VII. Conclusions

The radio metric data obtained during the superior conjunctions of *Mariner VI* and *VII* have provided a previously unavailable opportunity to investigate plasma effects near the sun. The effects were found to be larger than expected. In one special case, the size of the plasma cloud was estimated to be $2 \times 10^6$ km, and a density change was calculated to be at least 3000 electrons/cm$^3$, more than a factor of 4 times the predicted steady-state density.

The sizes of plasma clouds observed were in the range of $6 \times 10^4$ to $2 \times 10^6$ km. The latter is a deduction being dependent only on the plasma's transverse velocity. The smaller size is inferred from the width of autocorrelations in the data. Because the correlation technique is sensitive to different cloud sizes at different points along the raypath, it appears that with sufficient data the spectrum of sizes in the range $10^4$–$10^6$ km could be deduced.

Autocorrelating the data allows the range to plasma clouds that cross the raypath to be determined. The correlations have a structure which suggests that the electron density variations may be of a compression/rarefaction type. With a simple model of a rotating sun and radial material ejection at average velocities of 300–350 km/s, over 90% of the observed correlations can be mapped to active McMath regions on the sun's surface. McMath regions which develop on the backside of the sun are observed via the autocorrelation and their times of east limb transit are predicted to within less than ½ day. Furthermore, if the autocorrelation is observed to be particularly featureless, it is found that there are no active regions in the appropriate area of the sun's surface.

On the basis of the material discussed in this article, it would appear that DRVID can make meaningful contributions not only to doppler data calibration but also to scientific exploitation of radio metric data. From the evidence presented, there appears a probable correspondence between McMath sunspot regions and large solar wind variations. Given that McMath regions directly influence the raypath columnar electron content, it should be possible to establish weighting and selection criteria for orbit data processing based on ESSA H$\alpha$ spectroheliograms, even when DRVID data is unavailable.

## References


1. Martin, W. L., "Information Systems: A Binary-Coded Sequential Acquisition Ranging System," in *The Deep Space Network*, Space Programs Summary 37-57, Vol. II, pp. 72–81. Jet Propulsion Laboratory, Pasadena, Calif., May 31, 1969.

2. MacDoran, P. F., "A First Principles Derivation of the Differenced Range Versus Integrated Doppler (DRVID) Charged-Particle Calibration Method," in *The Deep Space Network*, Space Programs Summary 37-62, Vol. II, pp. 28–34. Jet Propulsion Laboratory, Pasadena, Calif., Mar. 31, 1970.

3. MacDoran, P. F., and Martin, W. L., "DRVID Charged-Particle Measurement With a Binary-Coded Sequential Acquisition Ranging System," in *The Deep Space Network*, Space Programs Summary 37-62, Vol. II, pp. 34–41. Jet Propulsion Laboratory, Pasadena, Calif., Mar. 31, 1970.

4. Thiede, E. C., and Lusigman, B. V., "A Technique to Study Randomly Varying Media," *IEEE Trans. Antennas and Propagation*, Vol. AP-18, No. 1, Jan. 1970.

5. Whang, T. C., and Chang, C. C., "An Inviscid Model of the Solar Wind," *J. Geophys. Res.*, Vol. 70, p. 4175, 1965.

6. Hartle, R. E., and Sturrock, P. A., "Two-Fluid Model of the Solar Wind," *Astrophys. J.*, Vol. 151, p. 1155, 1968.

7. Hundhausen, A. J., and Gentry, R. A., "Numerical Simulation of Flare-Generated Disturbances in the Solar Wind," *J. Geophys. Res.*, Vol 74, p. 2908, 1969.

8. Neugebauer, M., and Snyder, C. W., "Mariner 2 Observations of the Solar Wind, 1, Average Properties," *J. Geophys. Res.*, Vol. 71, p. 4469, 1966.

# A Cursory Examination of the Sensitivity of the Tropospheric Range and Doppler Effects to the Shape of the Refractivity Profile

L. F. Miller, V. J. Ondrasik, and C. C. Chao
Tracking and Orbit Determination Section

*The different shapes that refractivity profiles may assume during a year are grossly represented by 21 simple analytical expressions. By comparing the results obtained by using ray tracing techniques on these various profiles, it is possible to obtain an approximate bound on the error induced by mapping a tropospheric zenith range effect down to lower elevation angles with the wrong profile. For an elevation angle of 10 deg, these approximate error bounds are 1.3 and 2.6% in the range and doppler effect, respectively.*

## I. Introduction

One of the error sources which seriously degrades the quality of radio metric data generated by the DSN in tracking of spacecraft and used in determining the orbits of these spacecraft is the troposphere. In the past, attempts at reducing the tropospheric-induced errors used a tropospheric refractivity model which is independent of time. It has always been recognized that this model is only an approximation to the true physical situation and in the future will probably have to be improved. The present tropospheric model is deficient to such a degree at low elevation angles that it has become common practice to delete all data taken below elevation angles of 10 or 15 deg from the orbit determination solution. This is unfortunate because there are indications (Ref. 1) that this low elevation angle data is particularly desirable for inclusion in the orbit determination process.

A critical evaluation of this time-independent troposphere model divides rather naturally into the four areas listed below.

(1) An examination of the temporal behavior of the zenith tropospheric range effect.

(2) An examination of how sensitive the mapping of the zenith range effect down to lower elevation angles is to the shape of the refractivity profile, assuming the troposphere to be spherically symmetric with respect to (w.r.t.) the center of the earth.

(3) An examination of tropospheric inhomogeneities and asymmetries to determine how much their presence will contribute to the total tropospheric range effect.

(4) An examination of real tracking data to see if the observed minus computed data residuals may be improved if the above temporal variations are taken into account.

Studies of this type will not only assist in evaluating a time-independent troposphere model but may reveal phenomena which could be incorporated into an improved model.

An investigation of the temporal behavior of the zenith tropospheric range effect is under way and preliminary results of studying a year's worth of radiosonde balloon data were reported in Ref. 2. The most important of these results is that the zenith range effect remains within ±5% of its yearly average except for a few exceptional days.

This article gives the results of the initial attack on the second problem area listed above. To obtain some idea of how the mapping of the zenith range effects down to lower elevation angles is affected by the shape of the refractivity profiles, the following approach was adopted.

(1) Make a cursory examination of a year's worth of radiosonde balloon data to see how the refractivity profiles vary.

(2) Develop analytical functions which may approximate the various types of refractivity profiles.

(3) Develop ray tracing methods which will compute range effects at an arbitrary elevation angle for any of the above analytic refractivity profiles.

(4) Compare the results of mapping the zenith range effect to lower elevation angles for particular profiles with mappings which result from using a nominal profile.

The comparison in item (4) will give the desired measure of how sensitive the mapping of zenith range effect is to the actual shape of the refractivity profile.

## II. Tropospheric Range Effect

Electromagnetic signals entering the earth's atmosphere are bent and retarded due to the presence of a dielectric, the air. Liu (Ref. 3) presents the equations, obtained from variational principles, for this bending and retardation under the assumption that the earth's atmosphere is spherically symmetric w.r.t. the center of the earth. It is convenient to convert the time delay into the distance an electromagnetic signal would travel in that period. This

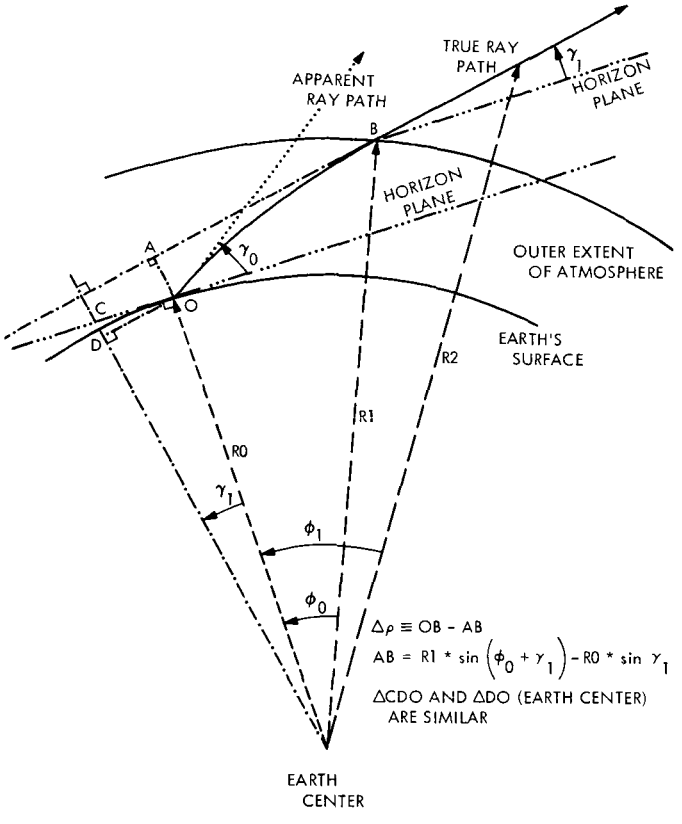


**Fig. 1. Bending geometry**

distance, known as the range effect $\Delta\rho$, is illustrated in Fig. 1, and may be expressed by the following equation if the troposphere starts at a radius $r_0$ from the center of the earth and terminates at a radius $r_1$.

$$\Delta\rho = \int_{r_0}^{r_1} \frac{n^2(r)\, r\, dr}{(n^2r^2 - n_0^2 r_0^2 \cos^2\gamma_0)^{1/2}} - AB \qquad (1)$$

where

$AB$ = the distance that the signal would travel in the troposphere if it were unrefracted

$n(r)$ = the index of refraction

$r$ = the distance of the signal from the earth's center at some instant

$\gamma$ = the signal's elevation angle w.r.t. the plane of the horizon

$n_0 \equiv n(r_0)$

$\gamma_0 \equiv \gamma(r_0)$

Another very useful quantity to calculate is the "unrefracted" elevation angle $\gamma_1$, which is shown in Fig. 1. This

angle is important because it is a function only of the time, the location of the station, and the ephemeris of the spacecraft. The difference between the elevation angle observed at the station $\gamma_0$ and the unrefracted elevation angle $\gamma_1$ is a function of the integral shown below.

$$\Delta\gamma = \gamma_0 - \gamma_1 = f\left[\phi = \int_{r_0}^{\infty} \frac{r_0 n_0 \cos\gamma_0\, dr}{r\,(n^2 r^2 - r_0^2 n_0^2 \cos^2\gamma_0)^{1/2}}\right] \tag{2}$$

Using Eqs. (1) and (2) in tandem, it is now possible, at least tabularly, to express the tropospheric range effect in terms of the unrefracted elevation angle once $n\,(r)$ is specified.

## III. Refractivity Profiles

Refractivity $N$ is defined as

$$N = (n - 1) \times 10^6 \tag{3}$$

To an accuracy of approximately 0.5% (Ref. 4), the refractivity may be computed:

$$N = 77.6\left(\frac{P}{T}\right) + 3.73 \times 10^5\left(\frac{P_{H_2O}}{T^2}\right), \qquad T \epsilon -50, 40^\circ\,\mathrm{C} \tag{4}$$

where

$P$ = pressure in millibars

$P_{H_2O}$ = partial pressure of the water vapor (mbar)

$T$ = temperature in °K

The first term in Eq. (4) is called the dry portion of the refractivity and the second term, which seldom exceeds 20% of the total, is called the wet portion. By using radiosonde balloon data, it is possible to obtain $P$, $P_{H_2O}$, $T$, and thereby $N$ as a function of height $h$ above the station. The curve representing $N\,(h)$ is called the refractivity profile.

A year's worth of refractivity profiles, obtained from Edwards Air Force Base (EAFB) 1967 radiosonde balloon data, was cursorily examined to see how the refractivity profiles may vary. It is common for the refractivity profiles $N\,(r)$ to vary daily and seasonally. This change may be one of scale or of type, and often there is an apparently random fluctuation about any simple functional representation of $n\,(r)$. Nevertheless, the 21 forms of $n\,(r)$ which were chosen for study encompass the gross tendencies of the Edwards meteorological data. These 21 different refractivity profiles are shown in Table 1 and are composed

**Table 1. Representative refractivity profiles**

| Group | Description | Number | $N_{dry}$ | $B_{dry}$ | $N_{wet}$ | $B_{wet}$ | $N_{max}$ | $d$ |
|---|---|---|---|---|---|---|---|---|
| 1a | Variations in $B_{dry}$ | 1 | 290 | 5 | 15 | 2 | | |
| | | 2 | 290 | 6 | 15 | 2 | | |
| | | 3 | 290 | 8 | 15 | 2 | | |
| | | 4 | 290 | 9 | 15 | 2 | | |
| 1b | Variations in $N_{dry}$ | 5 | 400 | 7 | 15 | 2 | | |
| | | 6 | 315 | 7 | 15 | 2 | | |
| | | 7 | 265 | 7 | 15 | 2 | | |
| | | 8 | 240 | 7 | 15 | 2 | | |
| | | 9 | 180 | 7 | 15 | 2 | | |
| 2a | Variations in $B_{wet}$ | 10 | 290 | 7 | 15 | 1 | | |
| | | 11 | 290 | 7 | 15 | 3 | | |
| 2b | Variations in $N_{wet}$ | 12 | 290 | 7 | 5 | 2 | | |
| | | 13 | 290 | 7 | 10 | 2 | | |
| | | 14 | 290 | 7 | 20 | 2 | | |
| | | 15 | 290 | 7 | 40 | 2 | | |
| 3a | Variations in $d$ | 16 | 290 | 7 | 15 | 2 | 20 | 5 |
| | | 17 | 290 | 7 | 15 | 2 | 20 | 1 |
| | | 18 | 290 | 7 | 15 | 2 | 20 | 2 |
| 3b | Variations in $N_{max}$ | 19 | 290 | 7 | 15 | 2 | 25 | 1 |
| | | 20 | 290 | 7 | 15 | 2 | 50 | 1 |
| | Nominal | | 290 | 7 | 15 | 2 | | |

of a dry and a wet term. Profiles 1 and 4 are, physically, very unlikely, but are included to obtain some idea of error bounds. In all cases, the dry term is assumed to be exponential in character, but the wet term is either purely exponential or increases parabolically for a time, then decreases exponentially. These two classes of refractivity profiles may be expressed by

$$N_I = N_{\text{dry}} \exp(-hB_{\text{dry}}) + N_{\text{wet}} \exp(-hB_{\text{wet}})$$

$$N_{II} = N_{\text{dry}} \exp(-hB_{\text{dry}}) + \begin{cases} N_{\max} - (N_{\max} - N_{\text{wet}})\left(h - \frac{d}{2}\right)^2 \frac{4}{d^2}, & h < d \\ N_{\text{wet}} \exp(-hB_{\text{wet}}), & h > d \end{cases}$$

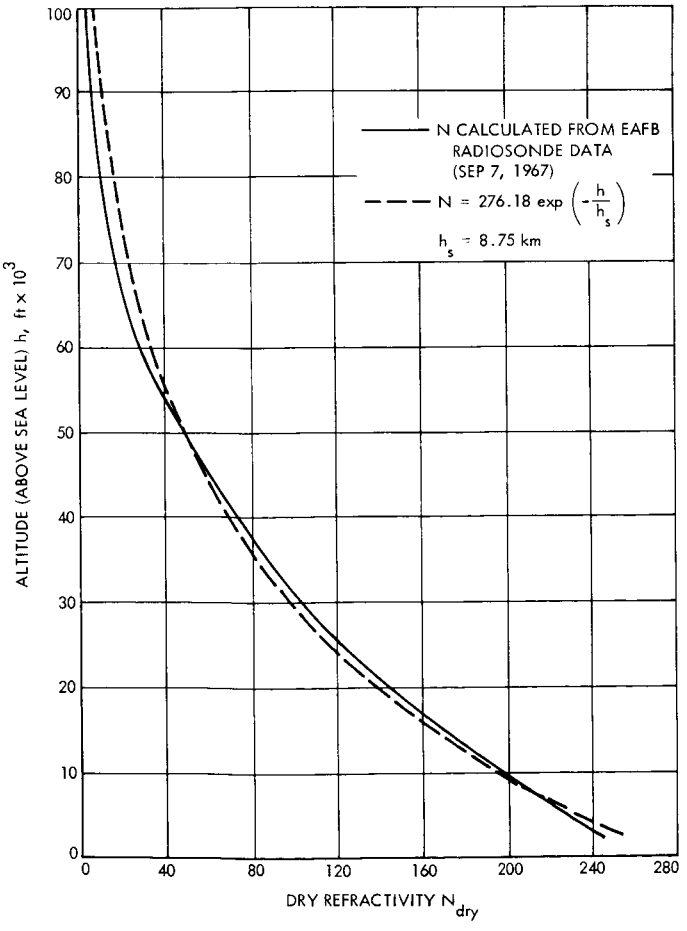


**Fig. 2. Comparison between real and approximated dry refractivity profiles**

where

$h$ = height above surface

$N_{\text{dry/wet}}$ = dry, wet surface refractivity

$B_{\text{dry/wet}}$ = dry, wet inverse scale heights

$N_{\max}$ = maximum wet refractivity

$d$ = thickness of the parabolic refractivity region

Examples of how the exponential dry term, the exponential wet term, and the parabolic–exponential wet term represent the actual refractivity profiles are given in Figs. 2 and 3.

To see how the shape of the profile affects the mapping of the zenith range effects down to lower elevation angles, a comparison will be made with the mapping which results from a nominal profile. Following the cursory examination of the 1967 data, mentioned above, it seemed reasonable to adopt a nominal refractivity profile which is biexponential in character and has the parameter values given in Table 1. The first 9 profiles in Table 1

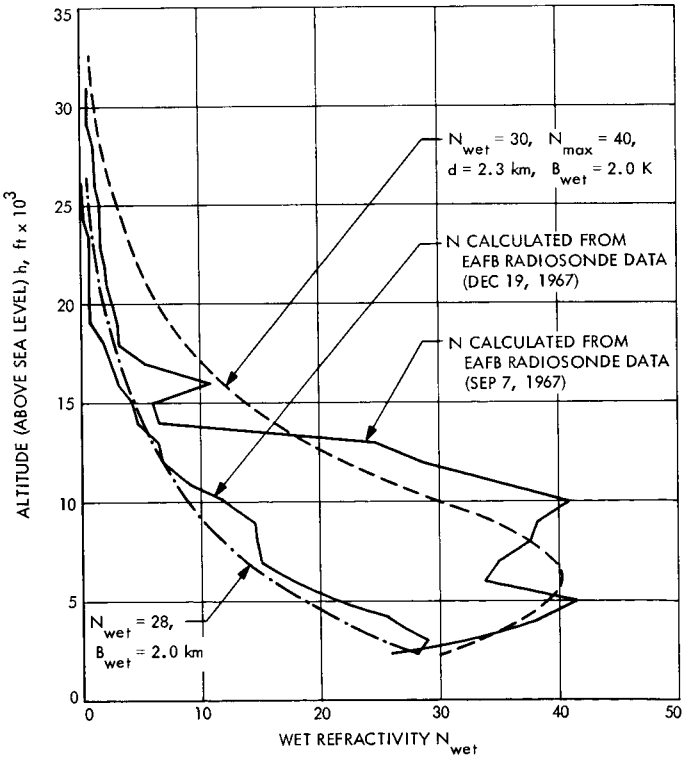


**Fig. 3. Comparison between real and approximated wet refractivity profiles**

differ from the nominal in the parameters of the dry portion, the next 6 differ from the nominal in the parameters of the wet portion, and the remaining 5 profiles differ from the nominal by having parabolic parameters.

## IV. Mapping the Zenith Range Effect to Lower Elevation Angles and the Associated Errors

The tropospheric range effect at any elevation angle produced by a particular refractivity profile is found by substituting the profile into Eq. (1) and then performing the integration numerically. This ray tracing procedure was carried out for all the refractivity profiles given in Table 1. For example, the tropospheric range effect as a function of elevation angle for the nominal profile is shown in Fig. 4.

The sensitivity of the range effect at a particular elevation angle to the shape of the profile may be examined by comparing the range effect produced by a number of arbitrary profiles with the range effect produced by the nominal profile. The most convenient comparison involves computing the following quantity:

$$\delta\rho(\gamma) = [\Delta\rho(\gamma, \text{arbitrary}) - \Delta\rho_c(\gamma, \text{nominal})] \times \frac{100}{\Delta\rho_c(\gamma, \text{nominal})}$$

where

$$\Delta\rho_c = \Delta\rho(\text{nominal})\,\Delta\rho_z(\text{arbitrary})/\Delta\rho_z(\text{nominal})$$

$$\Delta\rho_z = \text{zenith range effect}$$

This quantity will be called the range mapping error and represents the percentage of error which would result if a given zenith range effect was mapped down to a lower elevation angle, assuming the profile to be the nominal profile, and scaled by the indicated amount, instead of the correct profile. Table 2 gives the value of the range mapping error at several observed surface elevation angles for the 20 profiles given in Table 1. If the table was presented in terms of unrefracted elevation angles, the changes in the values of $\delta\rho(\gamma)$ would only be of second order.

Some idea of the bounds on the error, due to the spherical symmetry mapping of the zenith range effect down to lower elevation angles with the nominal profiles instead of the correct profile, may be obtained by adding the magnitudes of the largest range mapping error from each of the six groups of profiles in Table 2 for each elevation angle.

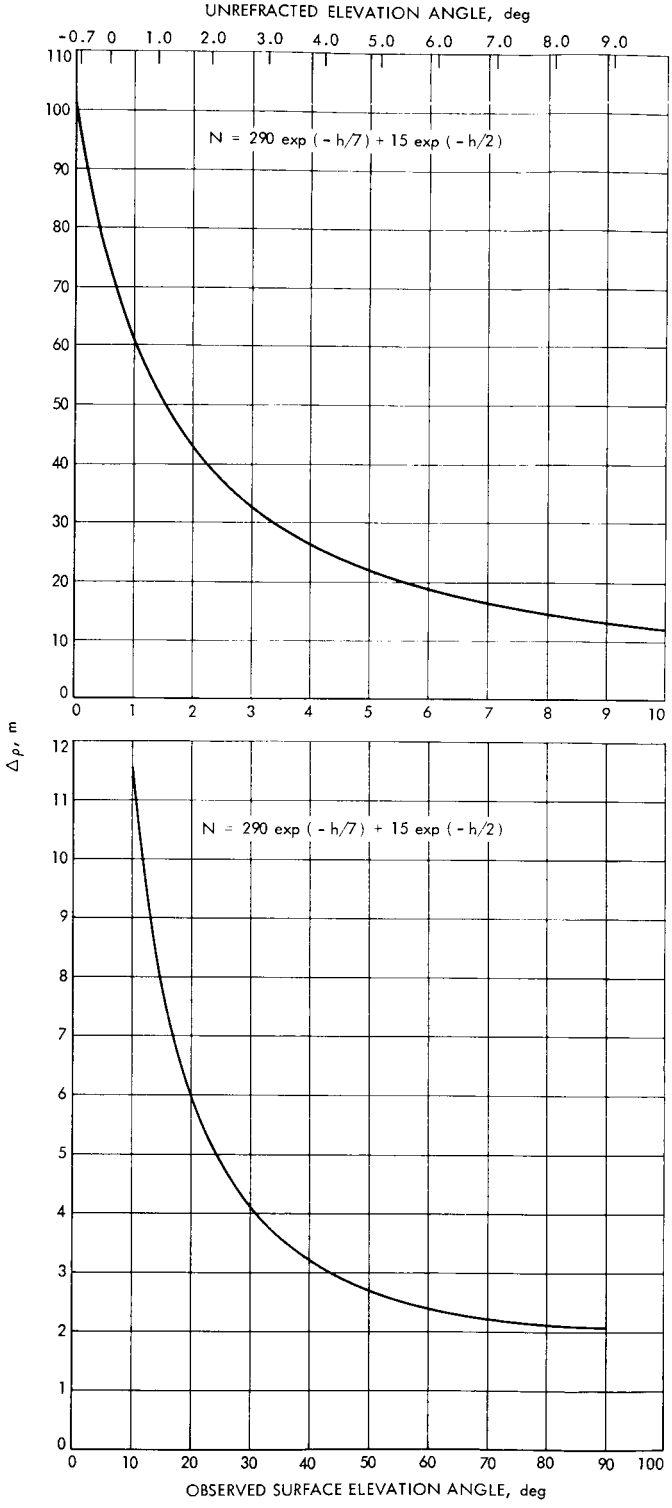


**Fig. 4. Tropospheric range effect**

If the somewhat unrealistic profiles 1 and 4 are ignored, this tentative error bound is 1.3% for elevation angles of 10 deg or higher, and only goes up to 3.0% for an elevation angle of 5 deg.

**Table 2. Range mapping error for various profiles and elevation angles**

| Profile group | Profile number | $\delta\rho$, % | | | | | |
|---|---|---|---|---|---|---|---|
| | | Observed surface elevation angle, deg | | | | | |
| | | 3 | 5 | 10 | 19 | 30 | 60 |
| 1a | 1 | 5.78 | 2.89 | 0.89 | 0.25 | 0.09 | 0.01 |
| | 2 | 2.72 | 1.40 | 0.44 | 0.13 | 0.05 | 0.005 |
| | 3 | −2.45 | −1.31 | −0.43 | −0.13 | −0.05 | −0.005 |
| | 4 | −4.68 | −2.55 | −0.85 | −0.25 | −0.09 | −0.01 |
| 1b | 5 | 1.68 | 0.79 | 0.23 | 0.07 | 0.02 | 0.002 |
| | 6 | 0.37 | 0.18 | 0.05 | 0.01 | 0.005 | 0.006 |
| | 7 | −0.36 | −0.17 | −0.05 | −0.01 | −0.005 | −0.006 |
| | 8 | −0.72 | −0.35 | −0.10 | −0.03 | −0.01 | −0.001 |
| | 9 | −1.52 | −0.74 | −0.22 | −0.06 | −0.02 | −0.002 |
| 2a | 10 | −0.05 | −0.03 | −0.01 | −0.003 | −0.001 | −0.0001 |
| | 11 | 0.0001 | 0.008 | 0.004 | 0.001 | 0.0005 | 0.00005 |
| 2b | 12 | −0.36 | −0.17 | −0.05 | −0.01 | −0.005 | −0.0005 |
| | 13 | −0.18 | −0.08 | −0.02 | −0.007 | −0.002 | −0.0003 |
| | 14 | 0.18 | 0.08 | 0.02 | 0.007 | 0.002 | 0.0003 |
| | 15 | 0.91 | 0.41 | 0.12 | 0.03 | 0.01 | 0.001 |
| 3a | 16 | 0.05 | 0.03 | 0.01 | 0.002 | 0.0008 | 0.0004 |
| | 17 | 0.08 | 0.05 | 0.02 | 0.004 | 0.002 | 0.0002 |
| | 18 | 0.13 | 0.08 | 0.03 | 0.008 | 0.003 | 0.0003 |
| 3b | 19 | 0.11 | 0.06 | 0.02 | 0.006 | 0.003 | 0.0002 |
| | 20 | 0.23 | 0.12 | 0.04 | 0.01 | 0.004 | 0.0004 |

The tropospheric doppler effect $\Delta\dot{\rho}$ is found by recognizing that the doppler data is actually differenced range. Thus, the tropospheric doppler effect at some time, with an associated elevation angle $\gamma$, is

$$\Delta\dot{\rho}\,[\gamma(t)] = \frac{1}{2T_c}\left\{\Delta\rho\left[\gamma\left(t+\frac{T_c}{2}-\tau\right)\right] + \Delta\rho\left[\gamma\left(t+\frac{T_c}{2}\right)\right] - \Delta\rho\left[\gamma\left(t-\frac{T_c}{2}-\tau\right)\right] - \Delta\rho\left[\gamma\left(t-\frac{T_c}{2}\right)\right]\right\}$$

where

$T_c$ = doppler averaging or count time

$\tau$ = round-trip light time

If the round-trip light time is ignored, as will be done here, the above equation reduces to the simpler form.

$$\Delta\dot{\rho}\,[\gamma(t)] = \frac{1}{T_c}\left\{\Delta\rho\left[\gamma\left(t+\frac{T_c}{2}\right)\right] - \Delta\rho\left[\gamma\left(t-\frac{T_c}{2}\right)\right]\right\}$$

Figure 5 shows $\Delta\dot{\rho}$ calculated from the nominal profile, as a function of refracted and unrefracted elevation angles under the assumption that the elevation angle changes by +1 deg in half of the doppler averaging time (for a station on the equator viewing a zero declination spacecraft, this corresponds to $T_c = 8$ min).

The sensitivity of the tropospheric doppler effect to the shape of the profile may be examined by considering the doppler mapping error $\delta\dot{\rho}$, defined by the

$$\delta\dot{\rho}\,[\gamma(t)] = \left\{\Delta\rho\left[\left(t+\frac{T_c}{2}\right), \text{arbitrary}\right] - \Delta\rho_c\left[\gamma\left(t+\frac{T_c}{2}\right), \text{nominal}\right] - \Delta\rho\left[\gamma\left(t-\frac{T_c}{2}\right), \text{arbitrary}\right] + \Delta\rho\left[\gamma\left(t-\frac{T_c}{2}\right), \text{nominal}\right]\right\} \times \left[\Delta\rho_c\left(\gamma+\frac{T_c}{2}\right) - \Delta\rho_c\left(\gamma-\frac{T_c}{2}\right)\right]^{-1}$$

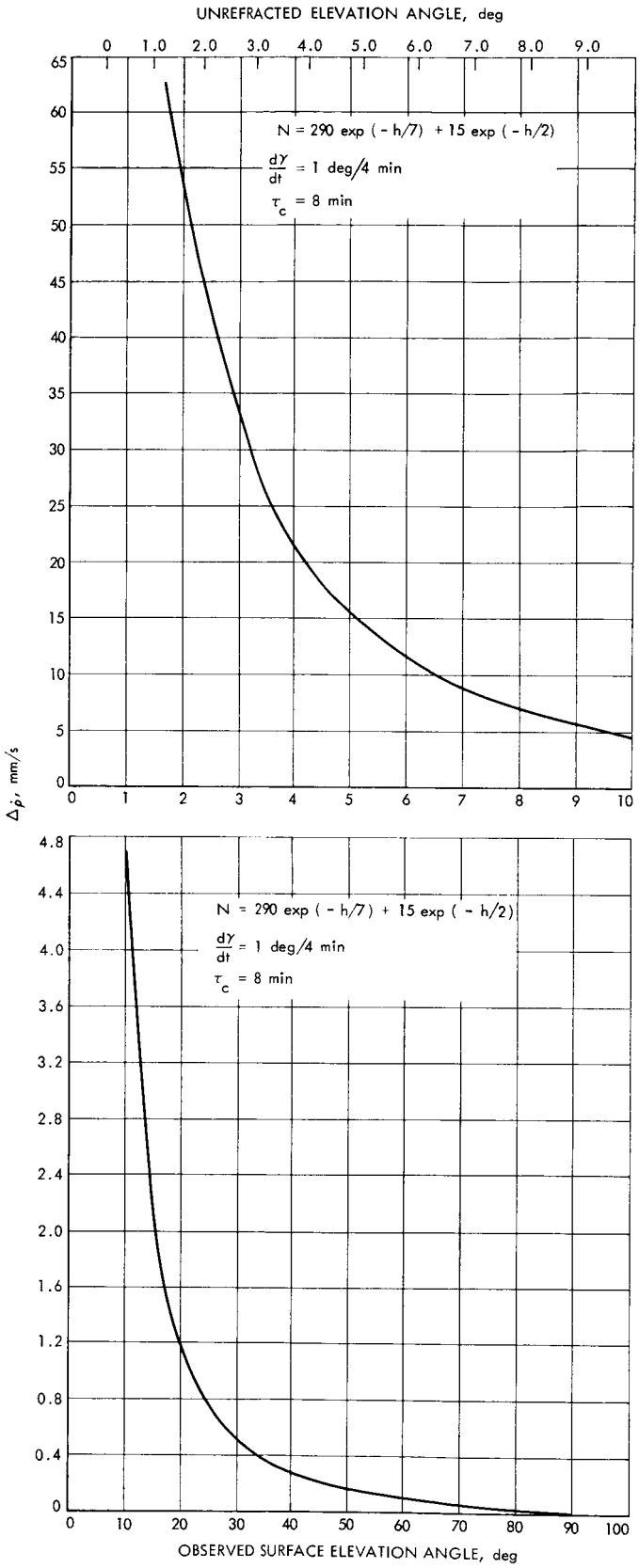


**Fig. 5. Tropospheric doppler effect**

This quantity gives the percentage error of the tropospheric doppler effect induced by mapping with the nominal profile, scaled by the zenith range effects, instead of by mapping with the correct profile.

Table 3 lists the results of computing $\delta\dot{\rho}$ at several elevation angles for the 20 profiles given in Table 1. As was the case for Table 2, if the calculations were performed using the unrefracted elevation angles $\gamma_1$, instead of $\gamma_0$, the changes in the values would only be of the second order. Once more, some idea of the error bound on $\delta\dot{\rho}$ may be found by adding the magnitudes of the largest doppler mapping errors from each of the six groups of profiles in Table 3, for each elevation angle. If the somewhat unrealistic profiles 1 and 2 are ignored, this tentative error bound is 2.6% for elevation angles larger than 10 deg and goes up to 8.3% for elevation angles of 5 deg.

## V. Apparent Changes in Station Locations

A useful artifice for investigating navigational errors, such as the ones produced by the troposphere, is to describe them in terms of equivalent errors in tracking station locations. As described in Ref. 5, an effect which corrupts tracking data can be decomposed into parameters, one of which is the apparent change in distance of the station off the spin axis $\Delta r_s$, and another is the apparent change in the station's longitude $\Delta\lambda$. For a tracking pass which is symmetric about the meridian crossing, a time-independent error source, such as the errors associated with mapping the zenith range effect to lower elevation, which are under consideration here, will not contribute any apparent change to the station longitude. Table 4 gives the apparent changes in distance off the spin axis of a station on the equator viewing a zero-declination spacecraft during a symmetric pass with a given minimum elevation angle, for doppler mapping errors produced by summing the magnitudes of the errors contributed by atmospheres 2, 5, 10, 15, 18, and 20. The result of a 0.2-m change in $r_s$ due to mapping errors for an elevation angle of 10 deg can be put in perspective by noting that the equivalent station location error budget for the *Mariner* Mars 1971 mission is 0.5 m in $r_s$.

## VI. Summary and Discussion

A cursory examination of refractivity profiles computed from EAFB 1967 radiosonde balloon data was made and 21 atmospheres of simple analytical form were chosen which grossly reflected the variability of the profile shapes throughout the year. By investigating how these profiles

**Table 3. Doppler mapping error for various profiles and elevation angles**

| Profile group | Profile number | $\delta\dot{\rho}$, % | | | | | |
|---|---|---|---|---|---|---|---|
| | | Observed surface elevation angle, deg | | | | | |
| | | 3 | 5 | 10 | 19 | 30 | 60 |
| 1a | 1 | 16.78 | 8.41 | 2.70 | 0.82 | 0.34 | 0.09 |
| | 2 | 7.59 | 3.98 | 1.32 | 0.41 | 0.17 | 0.05 |
| | 3 | −6.41 | −3.60 | −1.27 | −0.40 | −0.17 | −0.05 |
| | 4 | −11.90 | −6.87 | −2.50 | −0.80 | −0.34 | −0.09 |
| 1b | 5 | 5.22 | 2.42 | 0.72 | 0.21 | 0.09 | 0.02 |
| | 6 | 1.13 | 0.54 | 0.16 | 0.05 | 0.02 | 0.005 |
| | 7 | −1.10 | −0.53 | −0.16 | −0.05 | −0.02 | −0.005 |
| | 8 | −2.16 | −1.04 | −0.32 | −0.09 | −0.04 | −0.01 |
| | 9 | −4.55 | −2.21 | −0.68 | −0.20 | −0.08 | −0.02 |
| 2a | 10 | −0.04 | −0.07 | −0.03 | −0.009 | −0.004 | −0.001 |
| | 11 | 0.09 | 0.006 | 0.01 | 0.004 | 0.002 | 0.0005 |
| 2b | 12 | −1.20 | −0.52 | −0.15 | −0.04 | −0.02 | −0.005 |
| | 13 | −0.60 | −0.26 | −0.07 | −0.02 | −0.009 | −0.002 |
| | 14 | 0.60 | 0.26 | 0.07 | 0.02 | 0.009 | 0.002 |
| | 15 | 3.05 | 1.30 | 0.37 | 0.10 | 0.04 | 0.01 |
| 3a | 16 | 0.08 | 0.07 | 0.02 | 0.007 | 0.006 | 0.01 |
| | 17 | 0.13 | 0.13 | 0.05 | 0.01 | 0.006 | 0.002 |
| | 18 | 0.14 | 0.20 | 0.08 | 0.02 | 0.01 | 0.003 |
| 3b | 19 | 0.19 | 0.16 | 0.06 | 0.02 | 0.003 | 0.002 |
| | 20 | 0.46 | 0.34 | 0.11 | 0.03 | 0.01 | 0.004 |

**Table 4. Approximate error bounds on apparent change in a station's distance off the spin axis due to errors in *mapping the tropospheric doppler effect*[a]**

| Minimum elevation angle, deg | $\lvert\Delta r_s\rvert$, m |
|---|---|
| 19 | 0.03 |
| 10 | 0.2 |
| 5 | 1.0 |

[a]For zero-degree latitude station viewing, a zero declination spacecraft with doppler error obtained from profiles 2, 5, 10, 15, 18, and 20.

map the zenith range effect down to lower elevation angles, it was shown that the errors induced by performing the mapping with a nominal profile instead of the correct profile may induce errors in the tropospheric range and doppler effects of less than approximately 1.3 and 2.6%, respectively, for an elevation angle of 10 deg. The doppler mapping errors may translate into apparent changes in the station location solution to values on the order of $\Delta r_s = 0.2$ m for symmetric passes with a minimum elevation angle of 10 deg. A much more thorough investigation of refractivity profiles is currently under way to select a nominal mapping procedure for use in the double-precision orbit determination program and to obtain some firm statistics on the errors in the range and doppler produced by mapping of the zenith range effect down to lower elevation angles.

These estimates of the errors produced by mapping the zenith range effect down to lower elevation angles with the wrong profile should not be taken to represent the total tropospheric error. Unfortunately, there are other possible error sources which may contribute significantly to the errors produced by the troposphere. Two such error sources arise from computing the zenith range effect, and from effects produced by the nonhomogeneous structure of the troposphere. These two error sources are currently under investigation.

## References


1. Hamilton, T. W., and Melbourne, W. G., "Information Content of a Single Pass of Doppler Data from a Distant Spacecraft," in *The Deep Space Network*, Space Programs Summary 37-39, Vol. III, pp. 18–23. Jet Propulsion Laboratory, Pasadena, Calif., May 31, 1966.

2. Ondrasik, V. J., and Thuleen, K. L., "Variations in the Zenith Tropospheric Range Effect Computed From Radiosonde Balloon Data," in *The Deep Space Network*, Space Programs Summary 37-65, Vol. II, pp. 25–35. Jet Propulsion Laboratory, Pasadena, Calif., Sep. 30, 1970.

3. Liu, A., "Range & Angle Corrections Due to the Ionosphere," in *The Deep Space Network*, Space Programs Summary 37-41, Vol. III, pp. 38–41. Jet Propulsion Laboratory, Pasadena, Calif., Sep. 30, 1966.

4. Bean, B. R., and Dutton, E. J., *Radio Meteorology*, Monograph 92. National Bureau of Standards, Washington, D. C., 1966.

5. Mulhall, B. D., "Evaluation of the Charged Particle Calibration to Doppler Data by the Hamilton–Melbourne Filter," in *The Deep Space Network*, Space Programs Summary 37-57, Vol. II, pp. 24–29. Jet Propulsion Laboratory, Pasadena, Calif., May 31, 1969.

# Refractivity Influence on DSS Doppler Data

F. B. Winn
Tracking and Orbit Determination Section
R. K. Leavitt
Flight Operations and DSN Programming Section

*Doppler data from deep space missions show terrestrial media contamination influences even after least-square fitting. Cross-correlation between solution parameters and the media-induced errors is large enough to adversely affect parameter least-square adjustments. When a scale factor for Cain's tropospheric refractivity profile is included in the parameter list, the media-induced observed-minus-computed (O − C) structures do not appear above 15-deg elevation. When the scale factor is not included, O − C structures commence to appear at ~25-deg elevation.*

## I. Introduction

Hamilton and Melbourne (Ref. 1) have shown that low-elevation doppler data, from 0- to 15-deg elevation, can essentially double the information extractable from a single pass of doppler data. Thus, the theoretical value of ultra-low-elevation doppler observations for deep space probe navigation is recognized.

## II. Evidence of Terrestrial Media Contamination

Low-elevation observations of extraterrestrial objects are subject to terrestrial media contamination; and indeed, the O − C residuals[1] (after the fit[2]) of *Lunar Orbiter IV*,[3] *Mariner VI*,[4] and *Surveyor VII*[5] exhibit elevation-dependent signatures or structures (Fig. 1). Figure 1 reveals the similarities of the different O − C residuals sets in as far as low-elevation, unmodeled influences are concerned.

[1]Observed-minus-computed residuals (coherent two-way doppler data: CC3).

[2]Recursive least-square fitting to doppler data accomplished by the use of JPL's double-precision orbit determination program (DPODP) (Ref. 2).

[3]*Lunar Orbiter IV* analyses by W. L. Sjogren.

[4]*Mariner VI* analyses by J. W. Zielenbach.

[5]*Surveyor VII* analyses by F. B. Winn.

The high-frequency data noise of the *Lunar Orbiters* masks the finer structure of the residuals; however, even with the limited resolution of the *Lunar Orbiter* data, the elevation dependence of the O − C variation is clear. The *Mariner* and *Surveyor* O − C residuals do not suffer for resolution and they show the "diurnal" signature quite well.

The atmospheric influences, responsible for the O − C variations of Fig. 1, can be attributed to two principal sources: ionosphere and troposphere. The ionosphere is not a specific part of this study although ionospheric charged particle calibrations of the data involved in this study are currently underway and are expected to bring about an improvement of the results.

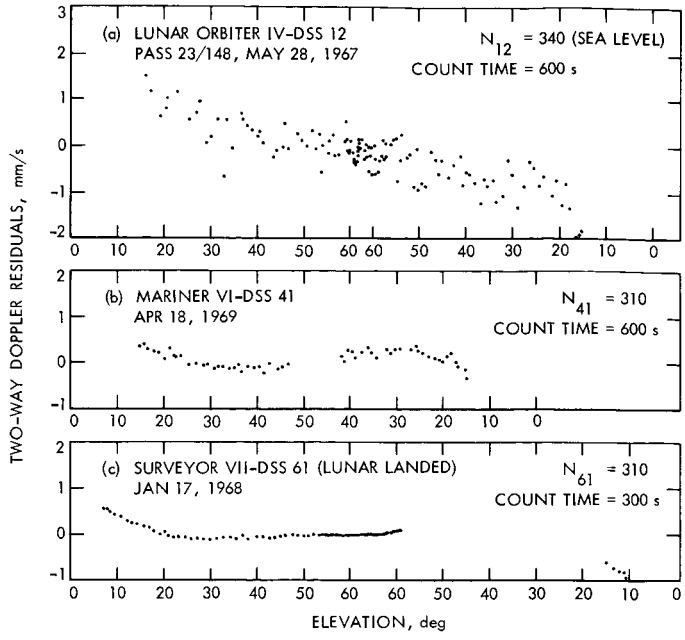


**Fig. 1. Two-way doppler residuals as a function of elevation**

## III. Modelling

Many model atmospheres assume that refractivity decreases exponentially with height above sea level. Formulated, this concept appears as

$$N = N_0 \exp(-Bh) \tag{1}$$

where

$h$ = height above sea level

$N$ = refractivity at height $h$

$N_0$ = refractivity at sea level

$B$ = inverse scale height

The specific model atmosphere which formed the basis of the JPL SPODP[6] and DPODP (Ref. 4) tropospheric model is

$$N = 340 \exp(-0.142\,h) \tag{2}$$

Equation (2) was utilized[7] to compute a set of tabular range corrections as a function of elevation. The tabular arguments were then fitted by the empirical function

$$\Delta\rho_r = C_1\left(\frac{N}{340}\right)[\sin(\gamma) + C_2]^{C_3} \tag{3}$$

where

$\Delta\rho_r$ = range correction due to group velocity retardation, km

$\gamma$ = geometric elevation angle

$N$ = refractivity scaler (340 is the sea level scaler)

and the constants $C_1$, $C_2$, $C_3$ were determined to be

$$C_1 = 1.8958 \times 10^{-3}$$
$$C_2 = 6.483 \times 10^{-2}$$
$$C_3 = -1.4$$

The influence of the troposphere upon the doppler, $\Delta\dot{\rho}_r$, was computed from differenced range corrections normalized per second of time:

$$\Delta\dot{\rho}_r = \frac{\left[\Delta\rho_r\left(\gamma + \frac{\dot{\gamma}\,\tau_c}{2}\right) - \Delta\rho_r\left(\gamma - \frac{\dot{\gamma}\,\tau_c}{2}\right)\right]}{\tau_c} \tag{4}$$

where

$\dot{\gamma}$ = time rate of change of $\gamma$, $\gamma$ units/s

$\tau_c$ = doppler count time, s

[6]SPODP = single-precision orbit determination program (Ref. 3).
[7]By D. L. Cain, JPL Tracking and Orbit Determination Section.

In terms of Eq. (3) variables,

$$\Delta\dot{\rho}_r = \left(\frac{C_1}{\tau_c}\right)\left(\frac{N}{340}\right)\left\{\left[\sin\left(\gamma + \frac{\dot{\gamma}\tau_c}{2}\right) + C^2\right]^{C_3} - \left[\sin\left(\gamma - \frac{\dot{\gamma}\tau_c}{2}\right) + C_2\right]^{C_3}\right\} \quad (5)$$

Equations (3) and (5) constitute the SPODP and DPODP (5.1 versions or earlier) refraction models.

Liu (Ref. 4) scaled Eqs. (3) and (5) in accordance with the findings of a study conducted by Smyth Research Associates. The refractivity scalers were determined to be

$$N_{11}\,(\text{Goldstone}) = 240$$
$$N_{42}\,(\text{Canberra}) = 310$$
$$N_{61}\,(\text{Madrid}) = 300$$

where the subscripts indicate the DSS. If the assumptions behind Eq. (5) are valid, then rescaling of the function can be accomplished by empirically fitting spacecraft tracking data.

Due to the abundance and employment of low-elevation data (below 15 deg) in *Surveyor* mission analysis (Refs. 5–7), coupled with low data noise ($\sigma_{CC3} \simeq$ 0.06 mm/s for a 300-s count time) and the fact that the *Surveyor* data were acquired over large declination ranges, makes *Surveyor* data quite useful in a refractivity study. The abundance of low-elevation data is essential in that the partial of the doppler observable (CC3) with respect to the refractivity scaler $N$ becomes exponentially increasing at low elevation, increasing an order of magnitude from 20 deg down to 5 deg. The large declination sweeps that the *Surveyors* underwent during a lunar day tend to modify the $\partial CC3/\partial N$ profile from pass to pass, thus varying parameter cross-correlations from pass to pass.

The observed fact that the partial of the observable (two-way doppler) with respect to $N$ is unique in signature, particularly at low elevations, when compared to the signature of the partials of the observable with respect to the remaining parameter list (Table 1), demonstrates the separability of $N$ statistically from the other solution parameters (Figs. 2, 3, and 4).

Correlation matrices (Table 2) similarly show the doppler observable sensitivities to the tropospheric refraction parameter $N$ to be unique. The cross-correlations are of sufficient size, however, to indicate that if the tropospheric refraction scaler is variable and not treated as such, or not solved for, the remaining parameter list will be adversely influenced.

In a series of SPODP fits to *Surveyor VII* first-lunar-day tracking data, the "nominal values" of the refractivity scalers for DSSs 11, 42, and 61 were changed with the intent of "brute forcing" the weighted sum of the squares

**Table 1. Parameter list**

| Parameter | Definition |
|---|---|
| $R$ | selenocentric distance of a *Surveyor* |
| $LA$ | selenographic latitude of a *Surveyor* |
| $LO$ | selenographic longitude of a *Surveyor* |
| $r_{s_i}$ | spin-axis distance of $DSS_i$ |
| $LO_i$ | geocentric longitude of $DSS_i$ |
| $\Delta a/a$ | semi-major axis of the lunar orbit[a] |
| $\Delta e$ | eccentricity of the lunar orbit[a] |
| $\Delta L + \Delta r$ | mean lunar longitude[a] |
| $\Delta p$ | rotation around the perigee axis of the lunar orbit[a] |
| $\Delta q$ | rotation around the axis normal to the perigee axis in the plane of the orbit[a] |
| $e\Delta r$ | rotation around the out-of-plane axis completing a right-handed system[a] |

[a]Constitutes set III, two-body osculating elements (Ref. 8).

**Table 2. 2 × 2 cross-correlations[a] of parameter list with respect to $N_{42}$**

| Parameter | Surveyor | | | | |
|---|---|---|---|---|---|
| | I | III | V | VI | VII |
| $R$ | −0.207 | −0.087 | −0.094 | −0.001 | 0.178 |
| $LA$ | 0.352 | −0.097 | −0.147 | −0.009 | −0.318 |
| $LO$ | 0.191 | 0.069 | 0.219 | 0.016 | 0.349 |
| $r_{s_{42}}$ | 0.664[b] | 0.727[b] | 0.777[b] | 0.795[b] | 0.724[b] |
| $LO_{42}$ | 0.187[b] | 0.207[b] | 0.404[b] | 0.510[b] | 0.315[b] |
| $\Delta a/a$ | −0.187 | 0.161 | −0.433 | 0.527 | 0.332 |
| $\Delta e$ | 0.540 | 0.390 | 0.403 | 0.444 | −0.490 |
| $\Delta L + \Delta r$ | −0.187 | −0.167 | 0.455 | −0.590 | −0.335 |
| $\Delta p$ | 0.505 | 0.484 | 0.517 | 0.451 | 0.379 |
| $\Delta q$ | 0.235 | 0.002 | 0.330 | 0.099 | 0.132 |
| $e\Delta r$ | 0.506 | −0.498 | −0.254 | −0.362 | 0.154 |

[a]2 × 2 cross-correlations are derived from the normal equation matrix, and thus express the statistical separability of each parameter with respect to $N$ independent of the other parameters of the list.
[b]DSS 42 spin-axis distances and longitudes were included because DSS 42 is the only station which tracked all *Surveyors*. This is based on all data collected by DSS 42 during the first lunar day of each *Surveyor* mission.

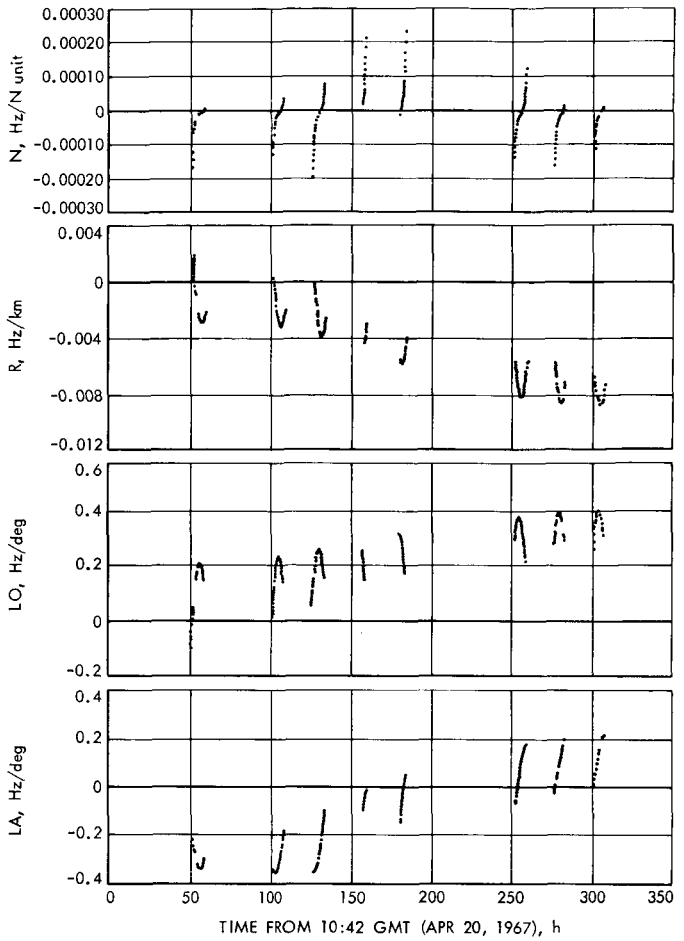


**Fig. 2. Partials of *Surveyor III* two-way doppler with respect to *N*, *R*, *LO*, and *LA***

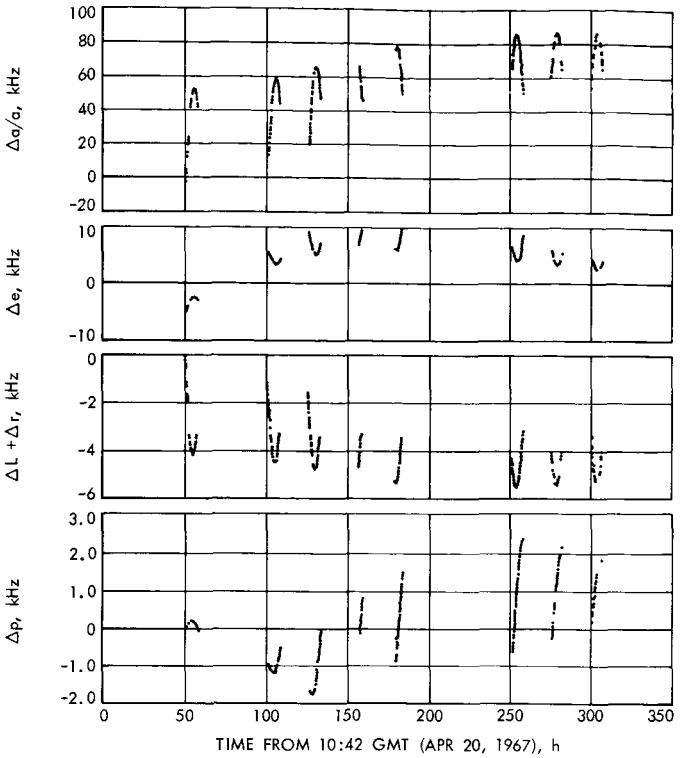


**Fig. 3. Partials of *Surveyor III* two-way doppler with respect to $\Delta a/a$, $\Delta e$, $\Delta L + \Delta r$, and $\Delta p$**

to a new "minimum."[8] The solutions are presented in Table 3, and the response of the spin-axis distance solutions of each DSS to the assigned $N$ values is graphed in Fig. 5.

Once a minimum sum of the squares was achieved as a function of $N$ for each DSS, it was noted that the "mean-best-fit" $N$ for the lunation overcorrected some and undercorrected some of the passes (Ref. 7), that is, the O − C residuals still exhibited $N$-dependent or elevation-dependent signatures (Fig. 6) for some passes. The mean lunar day refractivity scaling factor is not optimum for the individual passes.

Three series of DPODP pass-by-pass fits were made to *Surveyor I*, *III*, *V*, *VI*, and *VII* tracking data sets (only those solutions associated with DSS 11 are presented at this time): the first series of fits solved for $N$, $r_s$, $\lambda$ (DSS refractivity scalers, distance off the spin axis, and longitudes, respectively); the second series of reductions solved for $N$, $r_s$, and $\lambda$, but $N$ was constrained by an *a priori* $\sigma$ equal to 2% of the nominal value of $N$; and, finally, the third series solved for $N$ solely.

[8]The data is off-weighted as a function of elevation; the weighting function is discussed later.

**Table 3. Solution parameter sensitivities to *N***

| $N_{11}$ | 0 | 240 | 240 | 340 |
|---|---|---|---|---|
| $N_{42}$ | 0 | 280 | 310 | 340 |
| $N_{61}$ | 0 | 270 | 300 | 340 |
| $r_{s_{11}}$ | 5206.220 | 5206.209 | 5206.209 | 5206.204 |
| $LO_{11}$ | 243.15090 | 243.15112 | 243.15112 | 243.15112 |
| $r_{s_{42}}$ | 5205.335 | 5205.311 | 5205.308 | 5205.305 |
| $LO_{42}$ | 148.98166 | 148.98192 | 148.98192 | 148.98192 |
| $r_{s_{61}}$ | 4862.527 | 4862.515 | 4862.514 | 4862.512 |
| $LO_{61}$ | 355.75143 | 355.75162 | 355.75161 | 355.75161 |
| $R$ | 1739.302 | 1741.486 | 1741.582 | 1741.687 |
| $LA$ | −40.926 | −40.863 | −40.856 | −40.859 |
| $LO$ | 348.512 | 348.482 | 348.472 | 348.473 |

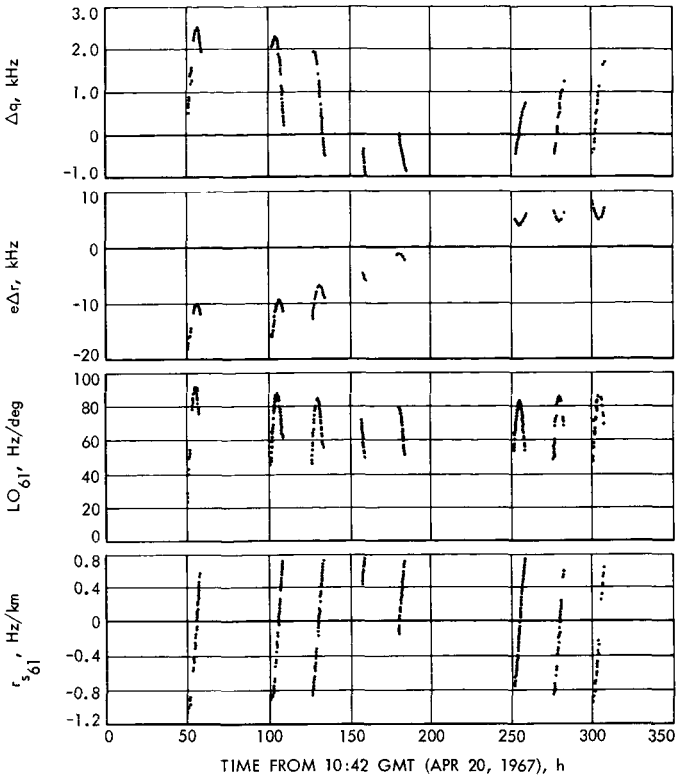


**Fig. 4. Partials of *Surveyor III* two-way doppler with respect to Δq, eΔr, $LO_{61}$, and $r_{s_{61}}$**

## IV. Simultaneous Solutions for $N_{11}$, $r_{s_{11}}$, $\lambda_{11}$

In those solutions in which the *a priori* σ for $N_{11}$, $r_{s_{11}}$, and $\lambda_{11}$ were set to 100 $N$ units, 50 m, and 50 m, respectively, and a unit σ of 0.1 mm/s was applied to all doppler observations, the parameter cross-correlations became the single dominant trait of the fits. That is, the parameter cross-correlations and the variations of the cross-correlations generate a scatter in the parameter solutions (Fig. 7). The variation of the cross-correlations stems from data acquisition patterns and the changing pass-profile of the partial of the doppler observable with respect to the refraction parameter $N_{11}$ (Fig. 8). Thus, it is apparent that $r_s$ and $N$ cannot be simultaneously solved for via a least-square adjustment of doppler data.

## V. Data Fits to $N_{11}$, $r_{s_{11}}$, $\lambda_{11}$ With $N_{11}$ Subjected to *A Priori* Constraint

To diminish the parameter cross-correlation influences responsible for the solution parameter scatter, in the second series of DPODP fits, $N_{11}$ was constrained by an *a priori* σ of 4 $N$ units, that is, the *a priori* σ of $N_{11}$ presumes that

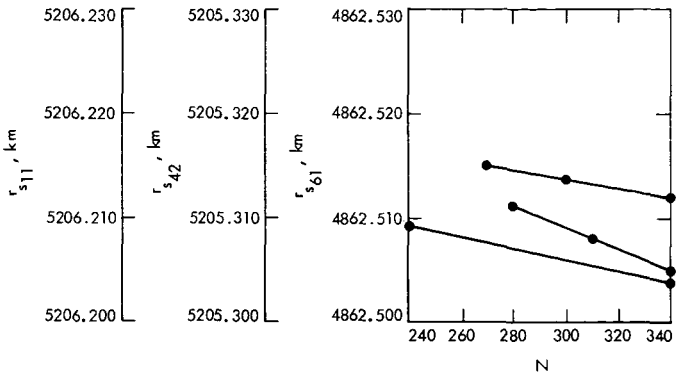


**Fig. 5. DSS $r_s$ solution sensitivity to $N$**

true $N_{11}$ must be within 2% of the nominal value 67% of the time. The assumption is fairly consistent with the radiosonde findings. The radiosonde analysis (Ref. 9) shows the maximum range of the tropospheric doppler error (peak to peak) at 5- to 10-deg elevation to be ~ 16%. Assuming a Gaussian distribution and 8% to be the 3-σ level, then the radiosonde analysis indicates the tropospheric doppler error has a σ of ~ 2.8% of the nominal value.

An additional influence was introduced into the second series of reductions. The doppler observables were weighted (Fig. 9) by the DPODP weighting function (Ref. 2).

$$\sigma_{obs}\,(a\ priori) = 0.1\ \text{mm/s}$$

(~2 times larger than the deduced 1 σ from O − C high-frequency noise)

$$\sigma_{obs}\,(\text{DPODP}) = \sigma_{obs}\,(a\ priori)\left[1 + \frac{18}{(1+\gamma^2)}\right]$$

where γ = elevation in degrees.

$$\omega t_{obs}\,(\text{DPODP}) = \frac{1}{\sigma^2_{obs}\,(\text{DPODP})}$$

where $\omega t$ = weight applied to observable.

Table 4 contains the DPODP estimates of $N_{11}$, pass by pass. From the scatter of $N_{11}$ relative to the nominal value of $N_{11}$, 240 $N$ units, and the "formal" solution σs, it is apparent that the *a priori* σ of $N_{11}$ is too conservative. It is of value to note the characteristics of the pass-by-pass solutions for DSS 11 spin-axis distance and longitude. The spin-axis distance $r_{s_{11}}$ solutions that result when $N_{11}$ is used to exercise a constrained–yet variable scaling of the

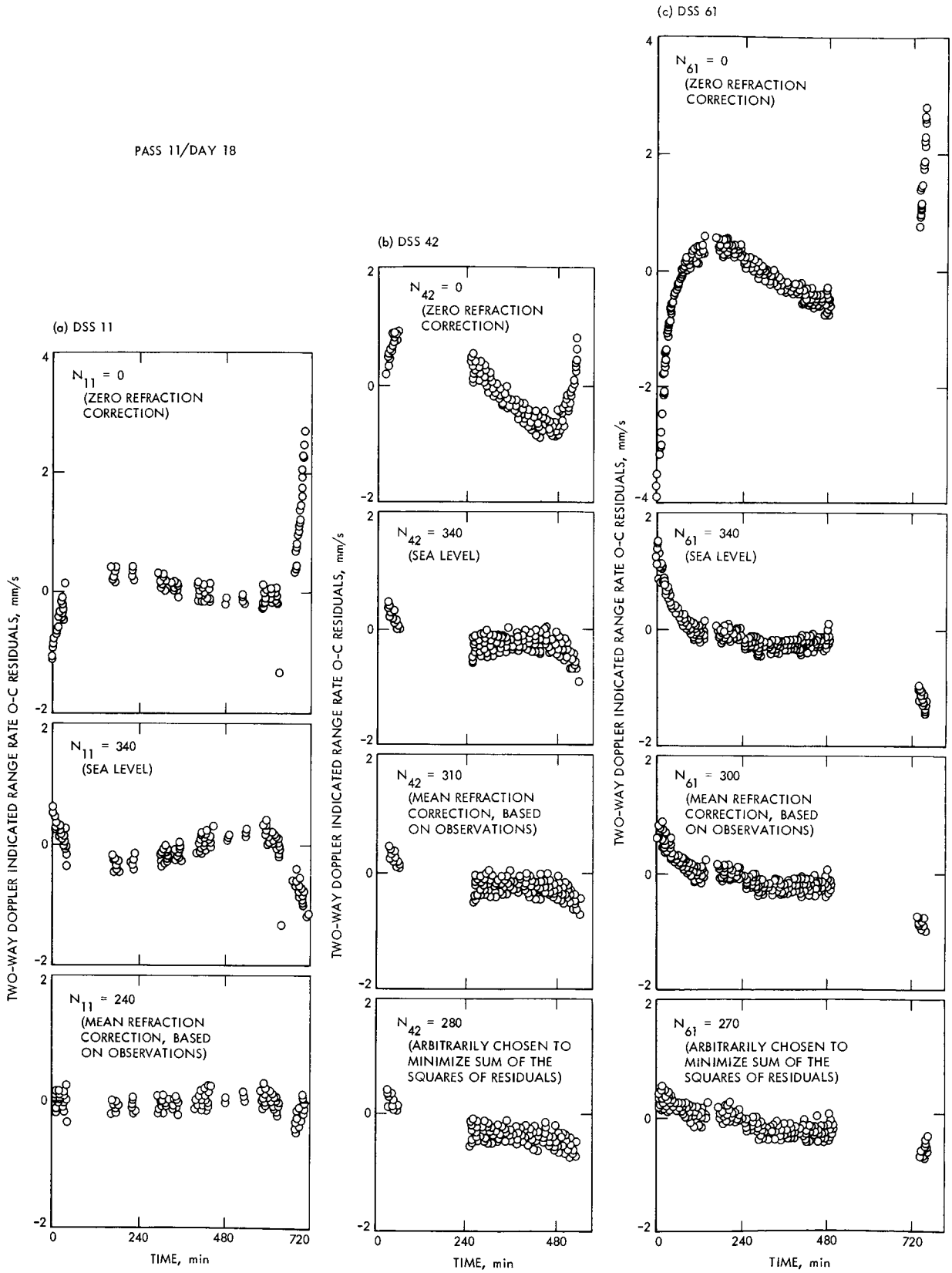


**Fig. 6. Sensitivity of O − C residual profiles to the tropospheric variable *N***

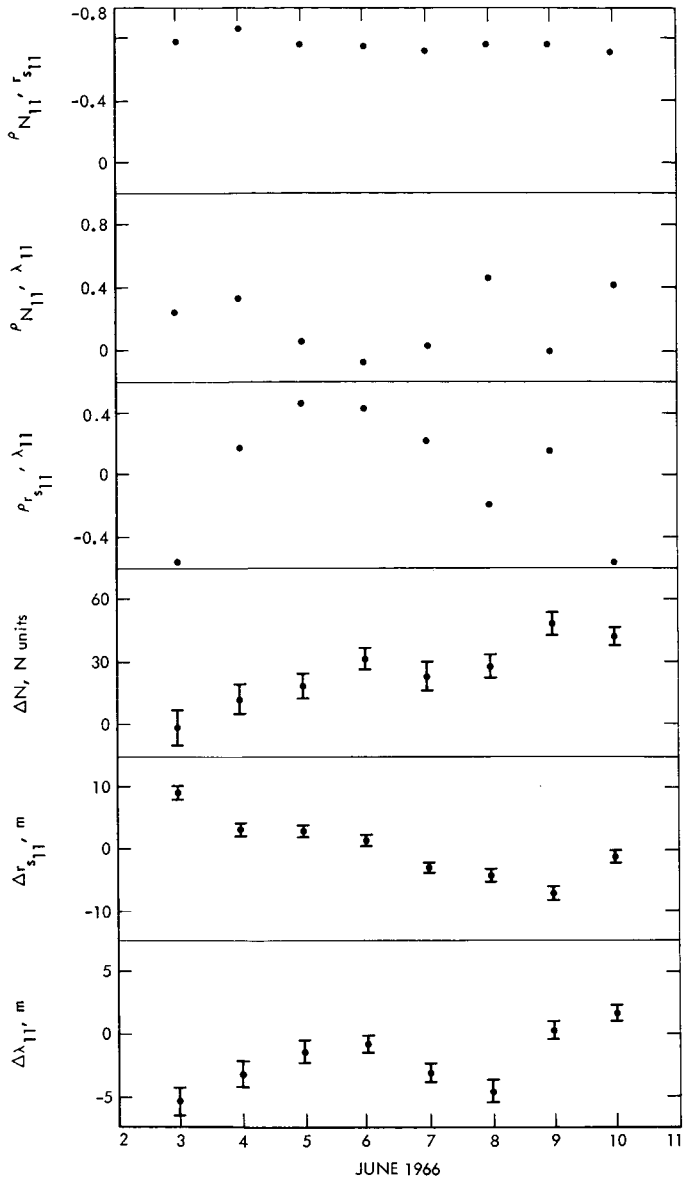


**Fig. 7. DSS 11—*Surveyor VI* tracking data fits (individual passes)**

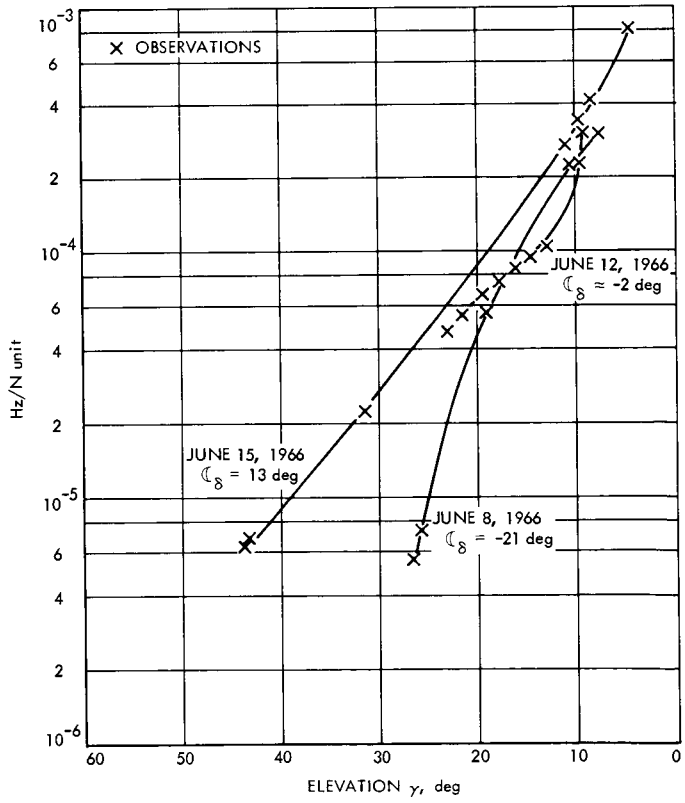


**Fig. 8. Partials of doppler with respect to $N_{11}$**

**Table 4. DSS 11 refractivity scaler estimates[a]**

| Surveyor | Average $N_{11}$ | Pass | | | | | | | | | | | | | | | | | | | | | |
|---|---|---|---|---|---|---|---|---|---|---|---|---|---|---|---|---|---|---|---|---|---|---|---|
| | | 3 | | 4 | | 5 | | 6 | | 7 | | 8 | | 9 | | 10 | | 11 | | 12 | | 13 | |
| | | $N_{11}$ | $\sigma$ | $N_{11}$ | $\sigma$ | $N_{11}$ | $\sigma$ | $N_{11}$ | $\sigma$ | $N_{11}$ | $\sigma$ | $N_{11}$ | $\sigma$ | $N_{11}$ | $\sigma$ | $N_{11}$ | $\sigma$ | $N_{11}$ | $\sigma$ | $N_{11}$ | $\sigma$ | $N_{11}$ | $\sigma$ |
| I | 251 | 244 | 3.7 | 246 | 3.6 | 246 | 3.5 | 253 | 3.1 | 246 | 3.6 | 261 | 2.8 | 250 | 3.6 | 265 | 2.4 | — | — | — | — | — | — |
| III | — | — | — | — | — | — | — | — | — | — | — | — | — | — | — | — | — | — | — | — | — | — | — |
| V | 231 | 234 | 3.6 | 233 | 3.8 | — | — | — | — | 230 | 3.4 | 225 | 3.0 | 236 | 3.8 | 239 | 4.0 | 220 | 2.9 | 234 | 3.2 | — | — |
| VI | 233 | 237 | 3.8 | 225 | 3.0 | 231 | 3.5 | 220 | 2.8 | 231 | 3.6 | 234 | 3.7 | — | — | 240 | 4.0 | 240 | 3.9 | 240 | 4.0 | — | — |
| VII | 229 | — | — | — | — | — | — | — | — | 232 | 3.5 | 226 | 2.9 | 231 | 3.6 | 222 | 2.6 | 225 | 2.7 | 237 | 4.0 | — | — |

[a]Conditions imposed on fit:
(1) the doppler was off-weighted as a function of elevation; (2) the refractivity scaler *a priori* $\sigma$ was 4 *N* units.

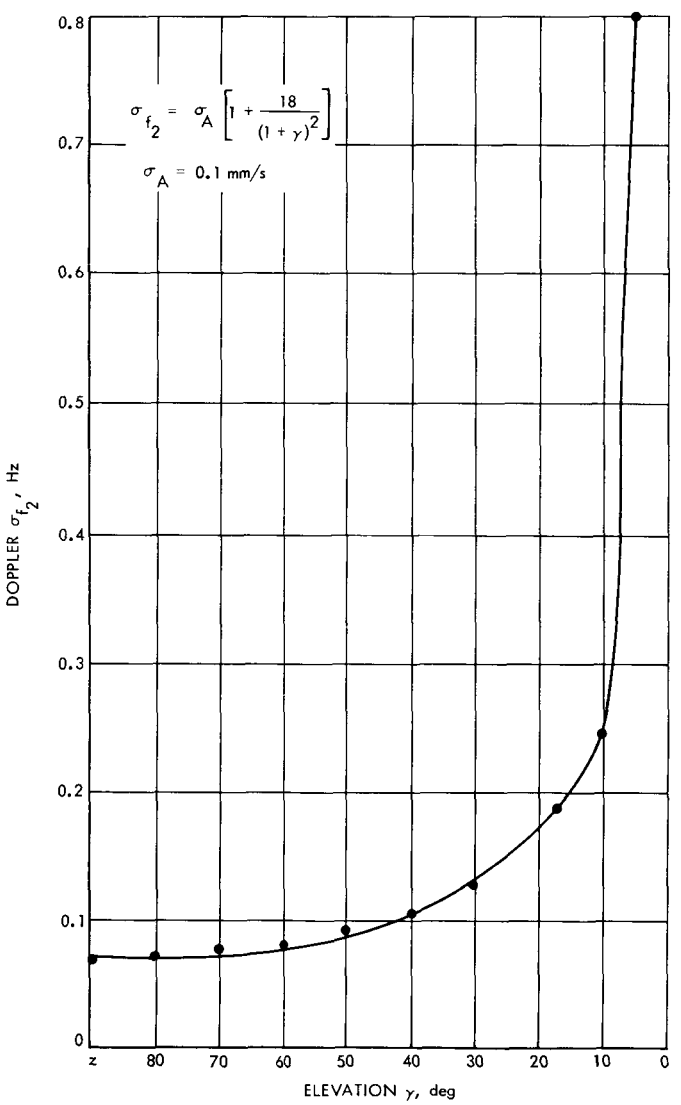


**Fig. 9. DPODP doppler observable weighting as a function of elevation**

tropospheric function—have less scatter than the analogous set of $r_s$ solutions in which $N_{11}$ was held to be a constant (Fig. 10). The sensitivity of $r_s$ to the scaling of the tropospheric corrections (variation in $N$) is shown in Fig. 10. The DSS longitude solutions are only slightly influenced by the inclusion of $N_{11}$ as a parameter.

## VI. Estimates of $N_{11}$ (Pass by Pass)

The first two series of data fits have provided an understanding of parameter cross-correlations and some understanding of the positive value of inclusion of $N_{11}$ into the solution parameter list.

This series presents data fits to the $N_{11}$ parameter. From these estimates of $N_{11}$, formal statistics are generated which reveal the strength of the doppler, pass by pass, to solve for $N_{11}$. The solutions are presented graphically (Fig. 11). It is anticipated that the solutions will change once ionospheric charged particle calibrations are applied to the doppler.

The formal statistics do not reflect the imperfection of the modeler's universe; DSS location errors, polar motion errors, UT1 errors, etc., are assumed non-existent. Thus, the statistics are optimistic and represent some abstract ideal. [This is the reason for weighting the doppler observable with the unit weight of 0.1 mm/s (~2 times the observed high-frequency noise associated with the O − C residuals). Admittedly, the factor of ~2 is subjective.]

The scatter of the $N_{11}$ estimates is ~16–25%. This total percentage variation is the sum of the percentage variation of the estimates over any given lunation (8–10%) and the percentage change from lunation to lunation

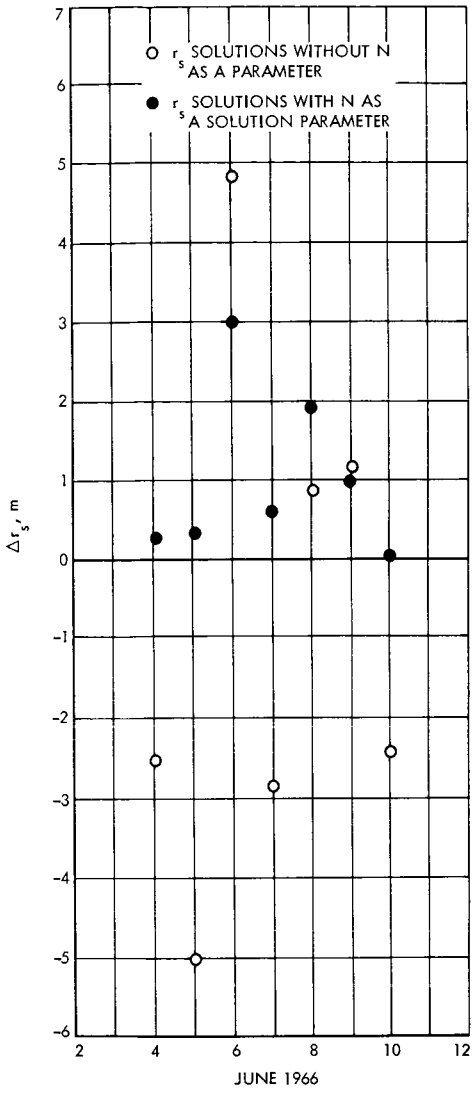


**Fig. 10. *Surveyor I*–DSS 11 $r_s$ solutions**

(~8–15%). Thus, the 16–25% change is the extreme variation.

Radiosonde analysis shows zenith–range errors (tropospheric-induced) to undergo variations of ~8% (Ref. 9). Additionally, the variability of the refractivity versus altitude profile from day to day produces errors of ~8% when a mapping function is used to scale the zenith–range error to 5-deg elevation (L. F. Miller, V. J. Ondrasik, and C. C. Chao in the previous article). Thus, radiosonde analysis shows a 16% variation (in the extreme) for observations taken at 5-deg elevation.

It is the doppler data taken at the very low elevations (5–10 deg) which contain the most information concerning the solution for $N_{11}$. It is not uncommon for the partials of the doppler observable (CC3) with respect to $N_{11}$ to increase an order of magnitude from 20- to 5-deg elevation. The $\partial CC3/\partial N_{11}$ falls off very fast with increasing elevation (Fig. 8). Yet, the high-elevation data do have some influence, and, as a consequence the tracking data estimates $N_{11}$ ideally should have less variation than the radiosonde determinations presented above. It is hoped that once ionospheric effects are included the scatter will diminish. Additionally, the cross-correlations unveiled by the second series of fits indicate that DSS location errors will influence $N_{11}$ estimates as a function of the pass data acquisition pattern.

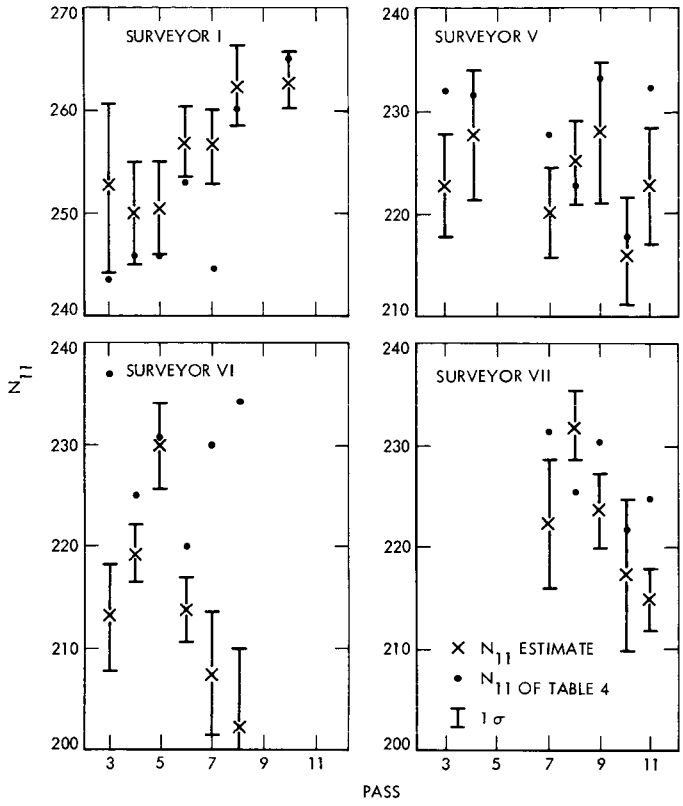


**Fig. 11. $N_{11}$ estimates**

The seasonal variations of the magnitude of the tropospheric influence shown by one year (1967) of radiosonde data (Ref. 9) cannot be seen in the empirical data fits to $N_{11}$ because only two spacecraft (*Surveyors V* and *VI*) functioned during the radiosonde data interval that were tracked at DSS 11. If the radiosonde measures of 1967 were applied to adjacent years, just to deduce the seasonal trends, the doppler fits would not agree.

The response of the O − C residuals to the introduction of $N_{11}$ as a parameter can most easily be shown by a comparison of the second moments $\mu_2$ of the residuals after

the fits. The $\mu_2$ associated with a typical pass are reduced by ~75–80% when $N_{11}$ is estimated. Some elevation-dependent O − C variations are still characteristic of the fits. This is in part due to the ionospheric influences. Figure 12 provides a typical set of O − C residuals after the fit in which $N_{11}$ was and was not estimated.

Elevation-dependent O − C signatures occur in the O − C residuals at elevations as high as 25 deg. When $N_{11}$ is estimated, the quality of the fit is extended to 15-deg elevation, that is, the O − C "diurnal" signature does not appear above 15-deg elevation.

When an entire lunation is fitted solving for DSS spin-axis distance and longitude, with and without $N$ as an accompanying parameter, the quality of the fit is extended very little over the elevation range although the magnitude of the O − C variations are reduced ~18%. Table 5 presents the $\mu_2$ of the lunation fits in which $N$ was and was not estimated.

**Table 5. $\mu_2$ associated with lunation fits**

| Surveyor | Estimated parameters | | Decrease, % |
|---|---|---|---|
| | $N_{11}$, $r_{s_{11}}$, $\lambda_{11}$ | $r_{s_{11}}$, $\lambda_{11}$ | |
| I | 0.0490 | 0.0591 | 17.1 |
| V | 0.0449 | 0.0564 | 20.2 |
| VI | 0.0439 | 0.0502 | 12.6 |
| VII | 0.0391 | 0.0489 | 19.9 |

## VII. Conclusions

In conclusion, the following observations are summarized:

(1) *Mariner*, *Lunar Orbiter*, and *Surveyor* doppler data reveal elevation-dependent O − C residuals which are related to tropospheric refraction effects. (Ionospheric influences are yet to be calibrated.)

(2) The employment of *Surveyor* doppler data to estimate refractivity effects removes all terrestrial media type structures from O − C sets above 15-deg elevation when fit on a pass-by-pass basis. The resultant $\mu_2$ of the fits are reduced ~80%.

(3) If no effort is made to estimate refraction effects, the O − C set exhibits media type variation at ~25-deg elevation, and the amplitude of O − C variations at low elevations (below 10 deg) can be as large as millimeters per second.

(4) Cross-correlations are quite large between the refractivity parameter and some of the parameters on the parameter list. Cross-correlations between $N$ and the parameter list vary according to spacecraft declination and the data acquisition pattern for a pass.

(5) The cross-correlation between the refractivity parameter and the distance off the spin axis for a given station is large enough to preclude simultaneous solution for both. External information concerning the value of one or the other parameter must be available.

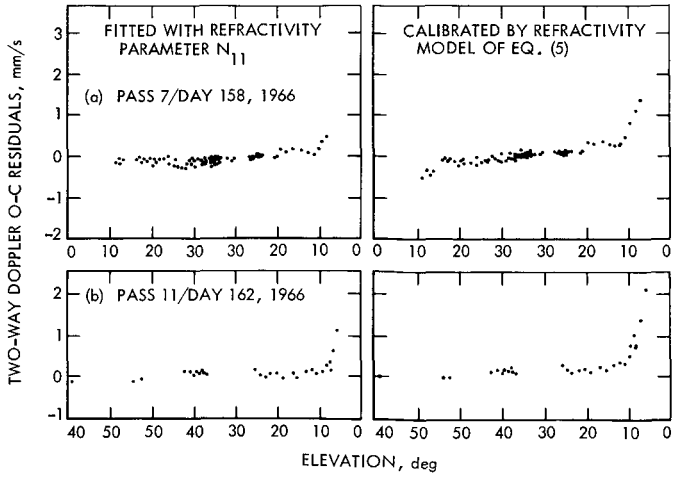


**Fig. 12. Refractivity parameter influence on *Surveyor I*–DSS 11 O − C residuals**

## References


1. Hamilton, T. W., and Melbourne, W. G., "Information Content of a Single Pass of Doppler Data from a Distant Spacecraft," in *The Deep Space Network*, Space Programs Summary 37-39, Vol. III, pp. 18–23. Jet Propulsion Laboratory, Pasadena, Calif., May 31, 1966.

2. Flynn, J. A., et al., *Double Precision Orbit Determination Program, Vol. V, Links Observ., Regres., Parts*, Report 900–298. Jet Propulsion Laboratory, Pasadena, Calif., Sep. 26, 1969.

3. Warner, M. R., and Nead, M. W., *SPODP—Single Precision Orbit Determination Program*, Technical Memorandum 33-204. Jet Propulsion Laboratory, Pasadena, Calif., Feb. 15, 1965.

4. Liu, A., "Recent Changes to the Tropospheric Refraction Model Used in the Reduction of Radio Tracking Data From Deep Space Probes," in *The Deep Space Network*, Space Programs Summary 37-50, Vol. II, pp. 93–97. Jet Propulsion Laboratory, Pasadena, Calif., Mar. 31, 1968.

5. Cary, C., "Spacecraft on the Lunar Surface, Part I—Range-Rate Tracking," in *The Deep Space Network*, Space Programs Summary 37-47, Vol. II, pp. 4–11. Jet Propulsion Laboratory, Pasadena, Calif., Sep. 30, 1967.

6. Winn, F. B., "Preliminary *Surveyor VI* Postlanded Tracking Data Analysis," in *The Deep Space Network*, Space Programs Summary 37-50, Vol. II, pp. 110–125. Jet Propulsion Laboratory, Pasadena, Calif., Mar. 31, 1968.

7. Winn, F. B., "Post-Lunar Touchdown Tracking Data Analysis," in *The Deep Space Network*, Space Programs Summary 37-51, Vol. II, pp. 42–50. Jet Propulsion Laboratory, Pasadena, Calif., May 31, 1968.

8. Brouwer, D., and Clemence, G. M., *Methods of Celestial Mechanics*. Academic Press, New York, 1961.

9. Ondrasik, V. J., and Thuleen, K. L., "Variations in Zenith Tropospheric Range Effect Computed From Radiosonde Balloon Data," in *The Deep Space Network*, Space Programs Summary 37-65, Vol. II, pp. 25–35. Jet Propulsion Laboratory, Pasadena, Calif., Sep. 30, 1970.

# A Second/Third-Order Hybrid Phase-Locked Receiver for Tracking Doppler Rates

R. C. Tausworthe
Telecommunications Division

*This article describes a stable phase-locked receiver configuration for tracking frequency ramp signals. A usual second-order receiver is used for lockup; subsequently a very simple modification is made to the loop filter, altering the loop to one of the third order. The altered loop then tracks the incoming signal with zero static phase error. The receiver bandwidth is practically unchanged; the damping factor lies in the region 0.5 and 0.707, and the design point is 12 dB in gain margin above instability.*

## I. Introduction

The phase-locked loops used in the DSN and spacecraft receivers are severely restricted in design by several requirements relating to their response to dynamic signal conditions. For example, the loop must not oscillate at any signal level above design point. Further, it must be capable of tracking frequency offsets and rates within specifiable static phase error limits.

To rule out oscillations at low signal levels, the accepted practice has been to design second-order phase-lock systems. Such a design, however, limits the doppler-rate tracking capability to spacecraft missions with a very low acceleration profile. Consideration of the spacecraft accelerations expected during a Jupiter flyby (Ref. 1) shows that there is such an excessive static phase error in the loop that lock probably cannot be maintained without operational aid of some sort.

This paper presents a technique which totally relaxes loop stress and thereby eliminates operational problems and any data degradation which might otherwise accompany loop detuning. The method allows the ordinary existing receiver to be used during lock-up. Once locked then, the loop filter is augmented by an integrator to remove any static-phase-error buildup. The analysis presented here shows that the loop bandwidth in this alteration is negligibly changed.

## II. The Second-Order Loop for Acquisition

The design equations for a second-order phase-locked receiver are well documented (Ref. 2) and thus are not to

be derived here. To introduce what follows, however, certain conventions and definitions are in order. We shall assume that the usual loop filter is to be used:

$$F_a(s) = \frac{1 + \tau_2 s}{1 + \tau_1 s}, \qquad \tau_1 >> \tau_2 \tag{1}$$

The rms input signal level and loop gain $K_a$, along with the time constants $\tau_1$ and $\tau_2$ fix the loop bandwidth $w_{L_a}$ and damping factor $\zeta$, by way of the parameter $r$:

$$w_{L_a} = \frac{r+1}{2\tau_2} = \frac{r+1}{r_0+1} w_{L_0}$$

$$\zeta_a = \frac{1}{2}\sqrt{r} = \zeta_0 \sqrt{\frac{r}{r_0}} \tag{2}$$

$$r = \frac{AK_a\tau_2^2}{\tau_1}$$

The zero subscripts here refer to values at design-signal level. We have affixed a subscript $a$ to other loop parameters in this acquisition mode. If the input phase-doppler function relative to the VCO at rest has a frequency offset $\Omega_0$ and rate $\Lambda_0$, i.e.,

$$d(t) = \theta_0 + \Omega_0 t + \frac{1}{2}\Lambda_0 t^2 \tag{3}$$

then there is an ultimate steady-state buildup of loop stress

$$\begin{aligned} \phi_{ss} &\approx \left(\frac{\Omega_0}{AK} + \frac{\Lambda_0\tau_1}{AK}\right) + \frac{\Lambda_0}{AK} t \\ &\approx \left(\frac{\Omega_0}{\beta^2\tau_1} + \frac{\Lambda_0}{\beta^2}\right) + \left(\frac{\Lambda_0}{\beta^2}\right)\left(\frac{t}{\tau_1}\right) \end{aligned} \tag{4}$$

The latter expression gives the stress in terms of the loop natural frequency, $\beta$. The linear buildup in time only becomes of interest when $t$ becomes appreciable to $\tau_1$, but the constant part of the static error is there as soon as the lock-up transient disappears. Control of the VCO tuning can make the $\Omega_0$ term disappear, whereas that with $\Lambda_0$ can only be reduced by sweeping the VCO at the proper rate.

## III. Optimum Doppler-Rate Tracking Loop

Let us suppose that the previous second-order loop has acquired lock by proper sweeping; then at $t = 0$, a new loop filter $F(s)$ is initiated to track, optimized so as to minimize the total phase error by the method of Jaffee and Rechtin (Ref. 3). The optimum loop response is given (Ref. 2) by the Yovits–Jackson formula (Ref. 4).

$$\begin{aligned} L_t(s) &= 1 - \frac{s^3}{\left[-s^6 + \dfrac{A^2\lambda^2}{N_0}\Lambda_0^2\right]^+} \\ &= \frac{2\xi s^2 + 2\xi^2 s + \xi^3}{s^3 + 2\xi s^2 + 2\xi^2 s + \xi^3} \end{aligned} \tag{5}$$

in which the brackets $[\,]^+$ indicate the left-half-plane square root of the enclosed function, and the parameter $\xi$ is

$$\xi = \left(\frac{A^2\lambda^2\Lambda_0^2}{N_0}\right)^{1/6} \tag{6}$$

$\lambda$ is the Jaffee–Rechtin Lagrange multiplier, which sets the loop bandwidth as desired. The new loop filter is

$$F_t(s) = \frac{2\xi^2}{AK_t}\left(\frac{1 + \dfrac{s}{\xi}}{s} + \frac{\xi}{2s^2}\right) \tag{7}$$

By choosing $\xi = 1/\tau_2$ the first term in this new filter resembles the old one, except that there has been a change in level removable by choice of $K_t$

$$\begin{aligned} F_t(s) &= \frac{1 + \tau_2 s}{\tau_1 s} + \frac{1}{2\tau_2\tau_1 s^2} \\ &\approx F_a(s) + \frac{1}{2\tau_2\tau_1 s^2} \end{aligned} \tag{8}$$

The gain value producing this relationship is

$$K_t = \frac{2K_a}{r} \tag{9}$$

In usual practice, the design value of $r$ is taken as $r_0 = 2$, in accordance with the Jaffee–Rechtin optimization for a $\Omega_0$-term only. Hence, we shall also specify that the constants in the acquisition loop be chosen so that $r_0 = 2$. That is, the acquisition loop is identical to the present mechanization. This rationale is a fortunate choice, because it implies that the gains for both the second- and third-order loops are equal:

$$K_t = \left(\frac{2}{r_0}\right)K_a = K_a = K \tag{10}$$

Therefore, the optimum rate-tracking loop merely augments the existing second-order loop used for acquisition by another integration in the loop filter.

The form of the loop filter immediately suggests the synthesis shown in Fig. 1. The isolation amplifiers shown are assumed to have a very high input impedance so as not to degrade $\tau_1$.

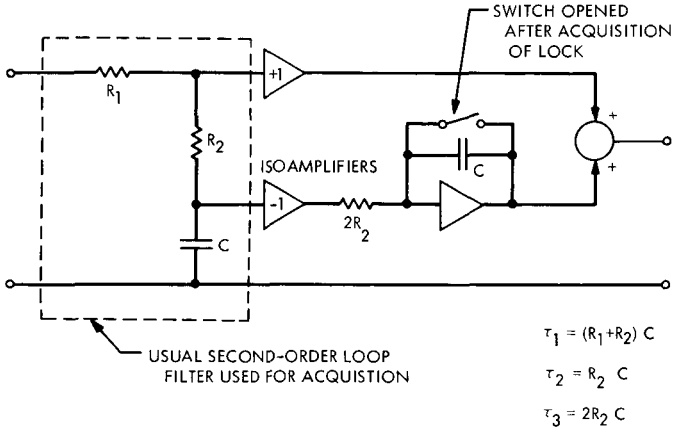


**Fig. 1. The second/third-order system loop filter**

## IV. Performance of the Tracking Loop

At any arbitrary signal level $A$, the rate-tracking loop transfer function, assuming $\tau_1 >> \tau_2$ for the filter shown in Fig. 1, is

$$L_t(s) = \frac{AK\tau_2\left(s^2 + \frac{1}{\tau_2}s + \frac{1}{s\tau_2^2}\right)}{s^3 + AK\tau_2 s^2 + AKs + \frac{AK}{2\tau_2}} \tag{11}$$

and the corresponding loop noise bandwidth is

$$w_{L_t} = \frac{r}{2\tau_2}\left(\frac{2r+1}{2r-1}\right) \tag{12}$$

The ratio of the noise bandwidth during tracking to that of the acquisition loop is

$$\frac{w_{L_t}}{w_{L_a}} = \frac{r}{r+1}\left(\frac{2r+1}{2r-1}\right) \tag{13}$$

As a function of signal margin above design point, as depicted in Fig. 2, this ratio goes from 10/9 to unity. That is, there is a maximum increase in loop bandwidth of 11% at design point, tapering down to only about 1% at 10-dB loop margin, the usual minimum recommended operating level.

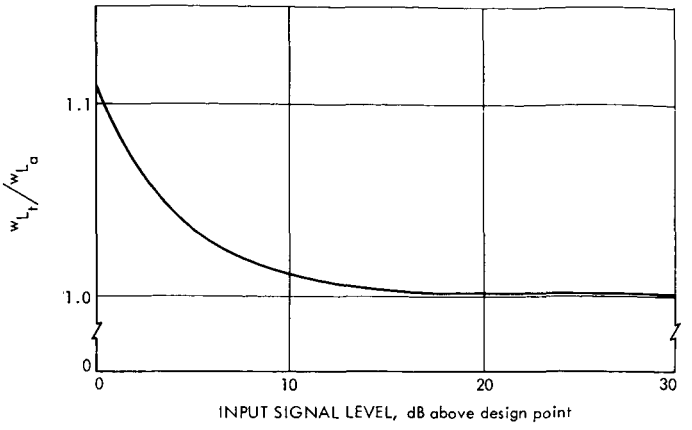


**Fig. 2. Comparison of loop noise bandwidths in the two operating modes versus loop signal margin**

The system has three poles in its response, one on the negative real axis, and the other two, complex. The system response thus exhibits some underdamping. As shown in the root locus of Fig. 3, for margins above design point, the damping coefficient corresponding to these system poles lies in the region

$$0.5 \leq \zeta < 0.707 \tag{14}$$

The voltage gain margin between instability and design point is a factor of 4, i.e., a 12-dB power-gain margin.

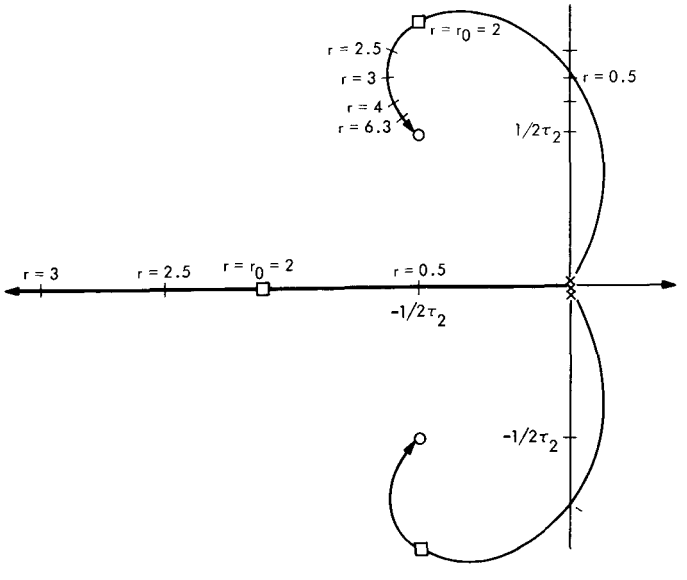


**Fig. 3. Root locus of the third-order loop. System poles at design point ($r_0 = 2$) are shown in squares. Usual minimum recommended operating condition is at $r = 6.3$**

## V. Conclusion

This article shows that a minor modification to presently designed phase-locked receivers can result in a very enhanced doppler-rate tracking capability, without degrading noise performance to any significant degree, especially when operating at or above minimum recommended conditions. The switch from acquisition to tracking mode can be actuated automatically by an AGC sensing relay, if desired.

## References


1. *DSN/Flight Project Interface Design Handbook*, DSN Standard Practice Document 810-5, Rev. A, pp. 2-39 to 2-44, Oct. 1, 1970 (JPL internal document).
2. Tausworthe, R. C., "Theory and Practical Design of Phase-Locked Receivers, Vol. I," Chapts. 5, 6, Technical Report 32-819, Jet Propulsion Laboratory, Pasadena, Calif., February 1966.
3. Jaffee, R. M., and Rechtin, E., "Design and Performance of Phase-Lock Circuits Capable of Near Optimum Performance Over a Wide Range of Input Signals and Noise Levels," *IRE Trans. Info. Theory*, Vol. IT-1, pp. 66–76, March 1955.
4. Yovits, M. C., and Jackson, J. L., "Linear Filter Optimization With Game-Theoretic Considerations," *1955 IRE National Convention Record*, Part 4, pp. 193–199.

# Concatenation of Short Constraint Length Convolutional Codes

D. Erickson

*Communications Systems Research Section*

*Several methods of decoding a concatenated pair of $K = 6, V = 2$ convolutional codes are investigated. It was found that none of the methods provides performance which is suitable for space channel application.*

## I. Convolutional Codes

An encoder for a convolutional code consists of a $K$-bit shift register and $V$ multi-input binary adders, each with some combination of the bits of the shift register as inputs. As each input bit is shifted into the register, the $V$ outputs from the adders are transmitted. The rate of such a code is $1/V$, and $K$ is called its constraint length. Such a code will be referred to as a $K$ by $V$ code. The code may be described by specifying its $V$ by $K$ tap matrix $A = (a_{ij})$ where $a_{ij} = 1$ if the $j$th bit of the shift register is connected to the $i$th binary adder $a_{ij} = 0$ otherwise. If the input to the encoder is $\cdots, \phi_t, \phi_{t+1}, \phi_{t+2}, \cdots$ the output will be $\cdots, (b_{t,1}, b_{t,2}, \cdots, b_{t,V}), (b_{t+1,1}, b_{t+1,2}, \cdots, b_{t+1,V}), \cdots$ where $(b_{t1}, \cdots, b_{tV})^t = A(\phi_t, \phi_{t-1}, \cdots, \phi_{t-K+1})^t$. The tap matrix is often abbreviated by representing its columns in hexadecimal notation if $V \leq 4$. This is accomplished for the $j$th column by representing $a_{V,j} + 2a_{V-1,j} + \cdots + 2^{V-1} a_{1,j}$ as a hexadecimal digit 0, 1, $\cdots$, $F$ (Fig. 1). The signal transmitted is usually $c = \cdots, (c_{t,1}, \cdots, c_{t,V}), \cdots$ where $c_{ij} = (-1)^{b_{ij}}$. Thus we transmit $\pm 1$ instead of 0,1. Notice in Fig. 1 how the response of the encoder to an impulse input is the columns of the tap matrix.

## II. Viterbi Decoding

In the Viterbi algorithm for decoding a convolutional code, one views the encoder as a finite state machine with $2^{K-1}$ possible states corresponding to the contents of the first $K - 1$ bits of the shift register (Ref. 1). As each new bit is shifted in, the encoder generates $V$ output bits and changes states. The encoder 313 pictured in Fig. 1 has the four states 00, 01, 10, and 11. If it is in state 10 and receives a 0 as the next input, it outputs 1, 0 and changes to state 01. If the message $\mathbf{y} = \cdots, y_i, y_{i+1}, \cdots$ is encoded into $\mathbf{x} = \cdots, (x_{i1}, \cdots, x_{iV}), \cdots$ and the channel error is $\mathbf{e} = \cdots, (e_{i1}, \cdots, e_{iV}), \cdots$ then the received signal will be $\mathbf{r} = \mathbf{x} + \mathbf{e}$. The decoder wishes to find y given r. To do this, he must find the message $\Phi$ which encodes into the signal $\mathbf{c} = \mathbf{c}(\Phi)$ such that $\mathbf{e} = \mathbf{e}(\Phi) = \mathbf{r} - \mathbf{c}$ is minimized. We minimize e by minimizing the sum

$$\sum_{t=-\infty}^{\infty} \sum_{j=1}^{V} e_{ij}^2 - \bar{e}_{ij}^2$$

where $e_{ij} = r_{ij} - c_{ij}$ and $\bar{e}_{ij} = r_{ij} - (-c_{ij}) = r_{ij} + c_{ij}$. This sum reduces to

$$\sum_{t=-\infty}^{\infty} \sum_{j=1}^{V} -4 r_{ij} c_{ij}$$

If we define the metric of $\Phi$ at time $t$

$$M(\Phi, t) = \sum_{t=-\infty}^{t} \sum_{j=1}^{V} r_{ij} c_{ij}$$

then our task is to maximize $M(\Phi, \infty)$.

A 3 BY 2 CONVOLUTIONAL CODE

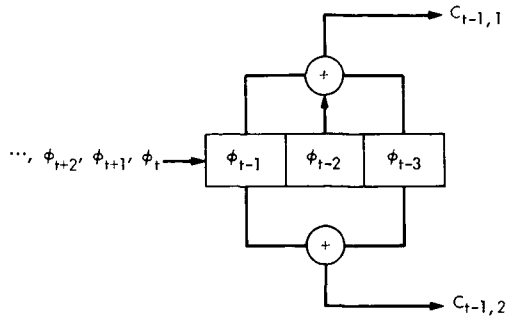


TAP MATRIX $A = \begin{pmatrix} 1 & 1 & 1 \\ 1 & 0 & 1 \end{pmatrix}$

ABBREVIATED REPRESENTATION 323

DECIMAL-TO-HEX CONVERSIONS

| DECIMAL VALUE | 0 | 1 | · · · | 9 | 10 | 11 | 12 | 13 | 14 | 15 |
|---|---|---|---|---|---|---|---|---|---|---|
| HEX DIGIT | 0 | 1 | · · · | 9 | A | B | C | D | E | F |

IMPULSE RESPONSE - ENCODING OF ···0 0 0 1 0 0 0···

| TIME | SHIFT REGISTER | OUTPUT $c_{t,1}$ | OUTPUT $c_{t,2}$ | STATE | SIGNAL |
|---|---|---|---|---|---|
| $t_{0-1}$ | 0 0 0 | 0 | 0 | 0 0 | 1, 1 |
| $t_0$ | 1 0 0 | 1 | 1 | 1 0 | -1, -1 |
| $t_{0+1}$ | 0 1 0 | 1 | 0 | 0 1 | -1, 1 |
| $t_{0+2}$ | 0 0 1 | 1 | 1 | 0 0 | -1, -1 |
| $t_{0+3}$ | 0 0 0 | 0 | 0 | 0 0 | 1, 1 |

**Fig. 1. A 3 by 2 convolutional code**

For each message $\Phi$, we also know $S(\Phi, t)$ the state in which the encoder will be at step $t$. For any states, let the survivor $\Phi(s, t) = \cdots, \phi_{t-1}, \phi_t$ be the message $\Phi$ up to step $t$ which maximizes $M(\Phi, t)$ given $S(\Phi, t) = s$. Let $m(s, t)$ be its metric. If we know for each state $s$, $\Phi(s, t-1)$ and $m(s, t-1)$, we can find $\Phi(s, t)$ and $m(s, t)$ as follows: Each state $s$ can only result from one of two previous states $s_0$ and $s_1$. That is, the state 01 can result from 10 or 11. If we know the present state and the previous state, then we know the contents of the shift register and, hence, the output for the step.

Knowing the step output gives us the change in metric $m_0$ or $m_1$. We compare $m_0 + m(s_0, t-1)$ and $m_1 + m(s_1, t-1)$ and the larger is $m(s, t)$. Its corresponding survivor $\Phi$ becomes $\Phi(s, t)$, the new survivor for $s$ with a 1 or 0 appended, depending on whether $s$ begins with a 1 or 0. These survivors tend to converge after 4 or 5 constraint lengths (Ref. 2, pp. 61–64) so that if $\Phi(s, t) = \cdots, \phi_{t-1}, \phi_t$ and $\Phi(s', t) = \cdots, \phi'_{t-1}, \phi'_t$ then $\phi_{t-5k}$ usually equals $\phi'_{t-5k}$. Thus the survivors need only be saved to a finite depth.

The storage needed is proportional to $K \cdot 2^{K-1}$. Although long constraint length codes perform better, they require so much storage and time or circuitry to decode that they are impractical.

One method of improving performance is careful evaluation of the received signal. If the received signal is hard-limited (resolved into $+1$ or $-1$) performance is 2 dB worse than if it is resolved to 4-bit accuracy $-15/16$, $-13/16$, · · · , $13/16$, $15/16$ (Fig. 2).

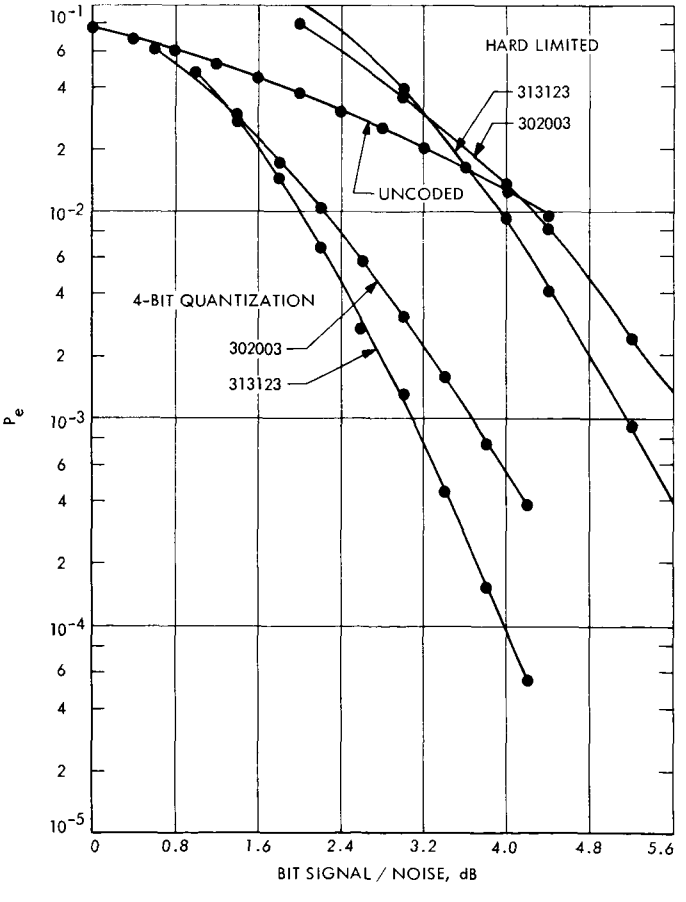


**Fig. 2. Performance of 6 by 2 codes**

## III. Concatenation

Another possible method of improving performance without increasing complexity and storage requirements is to concatenate codes. In encoding, concatenation is accomplished by using the output from one encoder as input to a second encoder (Fig. 3). One way to find the characteristics of the concatenated code is to find its response to an impulse input, $\cdots, 0, 0, 0, 1, 0, 0, \cdots$. If the first encoder is a $K_1$ by $V_1$ code with tap matrix $T = (t_{ij})$, the output from it will be $\cdots, (0, \cdots, 0), (t_{11}, t_{21}, \cdots, t_{V_1}), \cdots, (t_{1K_1}, \cdots, t_{V_1K_1}), (0, \cdots, 0), \cdots$. The output of the pair will be the response of the second encoder to this input. If the second code is $K_2$ by $V_2$, for each of the $t_{ij}$'s it will have $V_2$ outputs. Thus for each input bit, the pair will have $V_1 \cdot V_2$ outputs. The effect of the impulse will be felt by the pair until it has passed through the first encoder $K_1$ steps, and $t_{V_1K_1}$ has passed through the second encoder another $(K_2 - 1)/V_1$ steps. Rounded up, this gives a $K_1 + [(K_2 - 2)/V_1] + 1$ by $V_1V_2$ code. ($[x]$ is the greatest integer $\leq x$.) Thus two 6 by 2 codes can be concatenated to give a 9 by 4 code. If this code could be decoded by two 6 by 2 decoders then the memory requirement would be cut by a factor of more than 4.

Two questions arise:

(1) What form of output from the first decoder is best to use as input to the second decoder?

(2) Can concatenated decoding perform as well as or better than a single decoder of similar complexity?

To pursue these questions, a pair of 6 by 2 Viterbi decoders were simulated on an XDS 930 computer. The program used is an extension of the one described by J. Layland in Ref. 2, pp. 64–66.

## IV. Methods of Linking

Figure 4 contains a block diagram for the three methods of linking described here: direct, differential, and democratic linkage.

Output from the inner decoder, which corresponds to the second encoder, is usually taken to be the oldest bit of the survivor of the most likely state (the $s$ with $m(s, t)$ largest). If this output is $\phi_t$ (0 or 1), we can use $(-1)^{\phi_t}$ as input to the outer decoder. We will call this *direct linkage.*

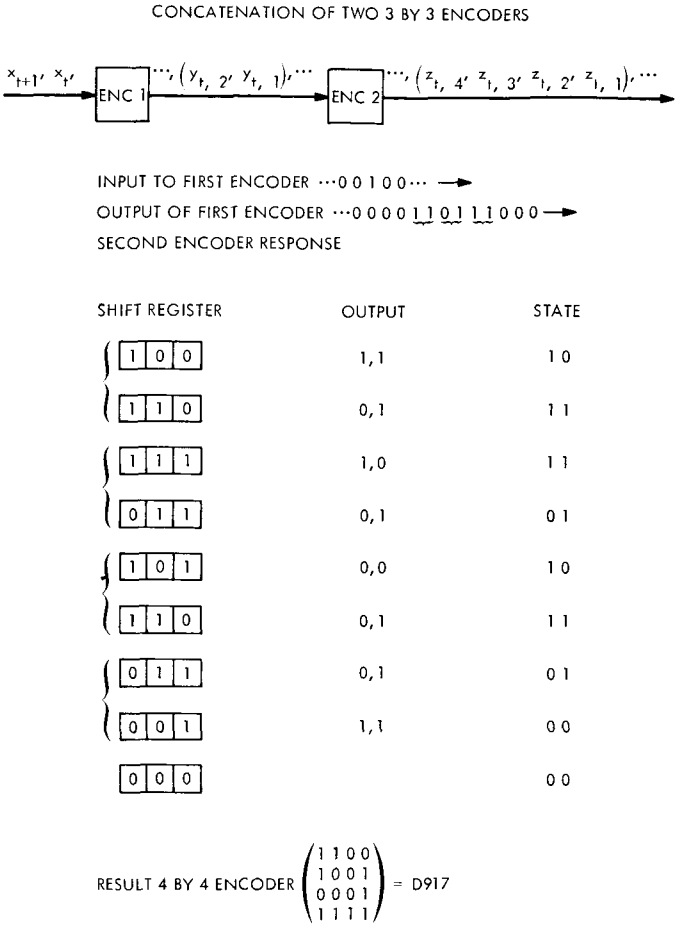


**Fig. 3. Concatenation of two 3 by 2 encoders**

Direct linkage has the disadvantage of providing only hard-limited inputs to the outer decoder which carry no judgments of confidence from the inner decoder. Just as 4-bit quantization improved the performance of a single decoder, we would hope that weighting the inner decoder's decisions would improve performance of the pair.

If the output from the inner decoder is $\Phi$ we can calculate the metric of $\Phi$,

$$M(\Phi, t) = \sum_{i=-\infty}^{t} \sum_{j=1}^{V} r_{ij} c_{ij}$$

We can also calculate the metric of $\Phi'$, the sequence differing from $\Phi$ in the $\ell$th place. Then $M(\Phi, \infty) - M(\Phi', \infty)$ is a measure of the confidence in the $\ell$th bit of $\Phi$. When $(-1)^{\phi_t}[M(\Phi, \infty) - M(\Phi', \infty)]$ is used as input to the second decoder, this is called *differential linkage.* Note that if $\mathbf{c}$ is the signal resulting from message $\Phi$ and $\mathbf{c}'$ is the

signal generated by $\Phi'$, then $\mathbf{c}$ and $\mathbf{c}'$ differ in only $K_2 \cdot V_2$ places at most. Thus

$$M(\Phi, \infty) - M(\Phi', \infty) = \sum_{i=l}^{l+K_2} \sum_{j=1}^{V_2} r_{ij}(c_{ij} - c'_{ij})$$

$$= \sum_{i=1}^{l+K_2} \sum_{j=1}^{V_2} r_{ij} c_{ij} (1 - c_{ij}\, c'_{ij})$$

$$= \sum_{i=1}^{l+K_2} \sum_{j=1}^{V_2} r_{ij} c_{ij} 2t_{j,\,i-l}$$

where $T = (t_{ij})$ is the tap matrix of the outer code.

In the implementation described by the block diagram in Fig. 4, the received signal $\mathbf{r}$ is saved in a shift register. The hard output $\Phi$ from the inner decoder is encoded by a copy of the second encoder (marked ENC 2) and the resulting $\mathbf{c}$ is multiplied by $\mathbf{r}$ with the appropriate alignment so that the products $r_{ij}c_{ij}$ are formed. The linear combination of these corresponding to the tap matrix is then used as a weight for the hard output.

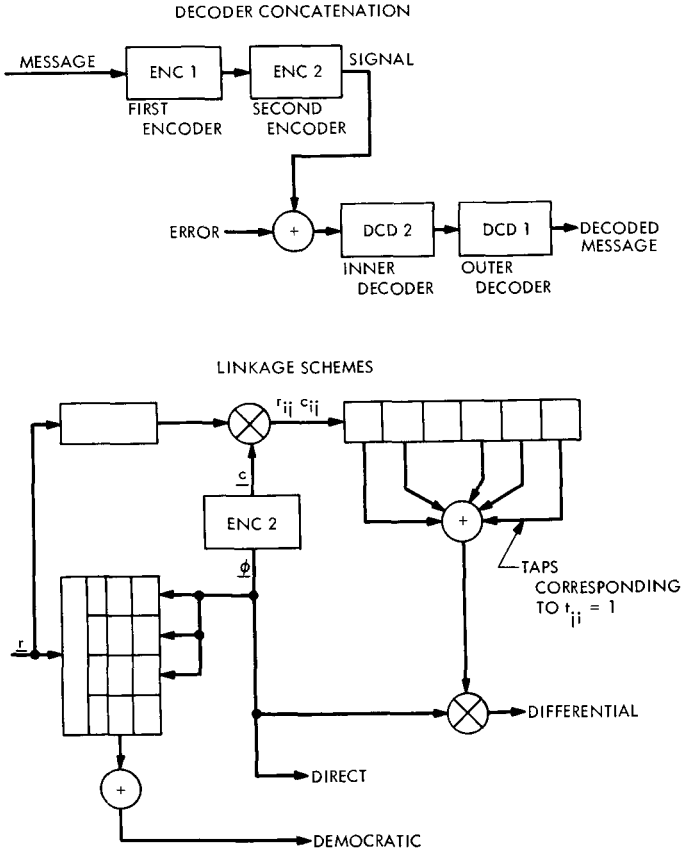


**Fig. 4. Decoder concatenation and linkage schemes**

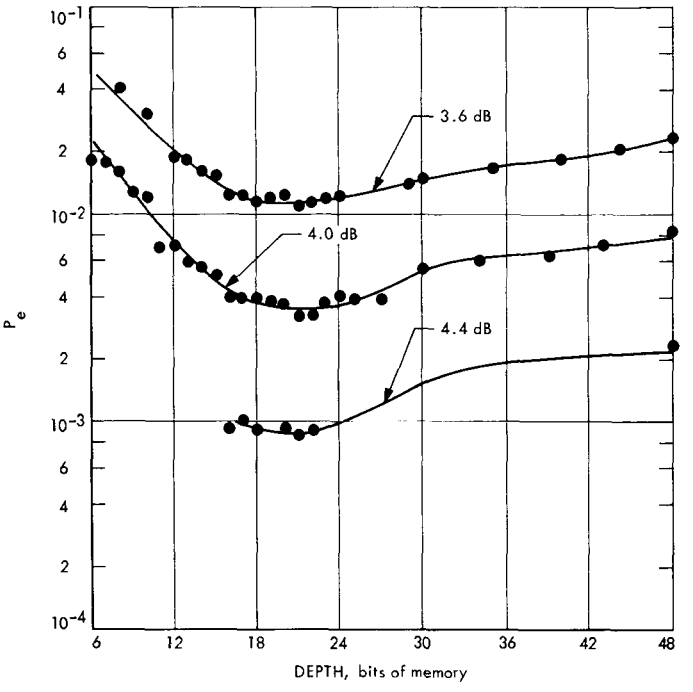


**Fig. 5. Performance of democratic linkage versus depth**

Another method of linkage is to let the bits of the survivors of all the states vote. Let $S_d(s)$ be the $d$th bit of the survivor of state $s$ of the first decoder. When second decoder input is

$$\sum_{s} (-1)^{S_d(s)}$$

this is called *democratic linkage at depth d*. When the depth is too great, the survivors have converged and this is no different from using direct linkage. When $d$ *is too* small, the probability of error is large. Thus, there is an optimal depth which may vary with the signal-to-noise ratio (Fig. 5).

Democratic linkage at this depth performs better than differential or direct linkage (Fig. 6).

## V. Simulation Results

Results indicate that a pair of 6 by 2 decoders could not compete with a single 7 by 3 decoder except at very high signal-to-noise ratios which are not encountered in the planetary program. In fact, for the three methods of linkage tried, the pair did not perform as well as a single 6 by 2 decoder at the same bit signal-to-noise ratio. When the pair is working at noise ratios of interest e.g., $ST_b/N_0 = 3$ dB, the first decoder is operating at half this

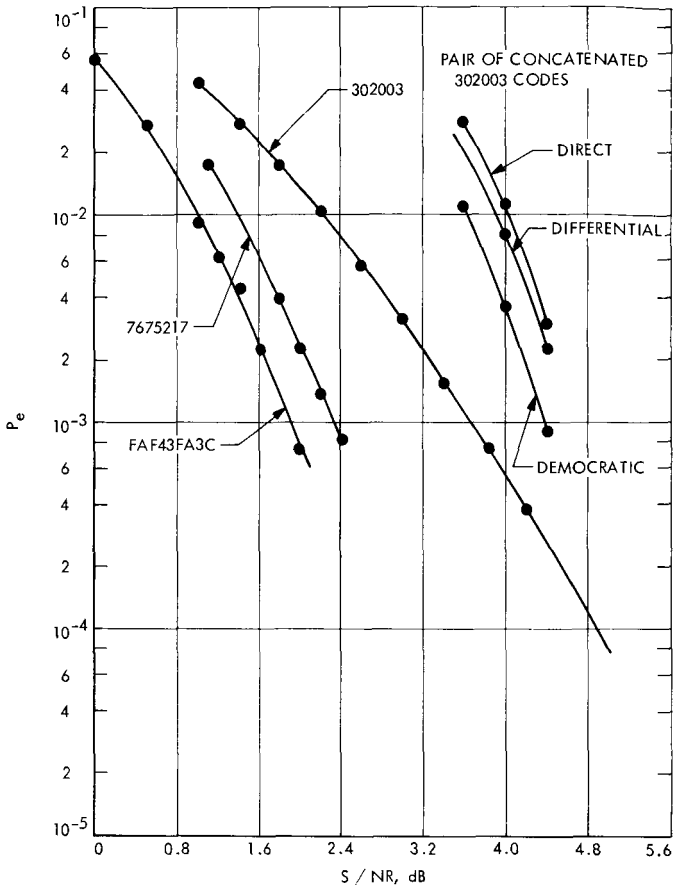


**Fig. 6. Performance of concatenated code**

power or 0 dB. At this power, it does not perform well enough to regain the lost 3 dB. Two $6 \times 2$ codes were studied. One (313123) performs better at higher signal-to-noise ratios, while the other (302003) performs better at low signal-to-noise ratios (Fig. 2). When the concatenated pair is operating at 3.6 to 4.4 dB, the inner decoder runs at 0.6 to 1.4 dB. In this range, it would appear that the sparse code (302003) would work better for the inner decoder. This was borne out by simulation. Although the full code (313123) performed better as the outer code in this range, the sparse code was used for both the inner and outer codes in most of the statistics gathered. Performance of this concatenated code is compared with the single 6 by 2 decoder and a 7 by 3 decoder in Fig. 6.

The codes used in this simulation were found by a hill climbing algorithm described by J. Layland (Ref. 3). This algorithm uses an approximation of the probability of error of the code $P_e'^h$. Let $I_i$ represent the bit sequence that is the binary expansion of the integer $i$, $C * I_i$ represent the coder output sequence corresponding to input $I_i$, and $W_H(x)$ be the Hamming weight of the sequence $x$. Then for a $K$ by $V$ code operating at a signal-to-noise ratio of $E_b/N_0$ define

$$P_e'^h = \sum_{\substack{i=1 \\ i \text{ odd}}}^{2^h-1} W_H(I_i) \exp\left(\frac{-W_H(C * I_i) E_b}{V \cdot N_0}\right)$$

The algorithm starts with a given code, calculates its $P_e'^h$ and compares this with $P_e'^h$ for all codes derived by modifying one bit. If $P_e'^h$ is smaller than for all other codes in this Hamming 1-sphere, it is considered a good code. If not, the code in the sphere with smallest $P_e'^h$ is chosen and the process is repeated. The full code (313123) was the best 6 by 2 code found. The sparse code was found by using the algorithm to search for the best pair of concatenated 6 by 2 codes. It happened that both codes of the pair were the same (302003). The concatenated pair results in a 9 by 4 code (FAF43FA3C). $P_e'^h$ for this code lay between that for the best 9 by 4 code and the best 8 by 4 code. The performance of this code is shown in Fig. 6.

## VI. Conclusion

Concatenation of Viterbi decoders does not appear to be useful in the present context of the planetary program. At higher signal-to-noise ratios, however, this technique might be used to produce the same performance with a small reduction in decoder complexity.

The performance difference between the best linkage scheme and direct connection is only about 0.4 dB, instead of the 2 dB that could exist if the transferred symbols were gaussian and independent. Consequently, it is conjectured that the most appropriate outer code, in any concatenation scheme involving a Viterbi algorithm inner decoder, is a high-rate algebraic block code.

## References


1. Viterbi, A. J., "Decoding and Synchronization Research: Convolutional Codes: The State-Diagram Approach to Optimal Decoding and Performance Analysis for Memoryless Channels," in *Supporting Research and Advanced Development,* Space Programs Summary 37-58, Vol. III, pp. 50–55. Jet Propulsion Laboratory, Pasadena, Calif., Aug. 31, 1969.

2. Layland, J., "Information Systems: Buffer Parameters and Output Computation in an Optimum Convolutional Decoder," in *The Deep Space Network,* Space Programs Summary 37-62, Vol. II. Jet Propulsion Laboratory, Pasadena, Calif., March 31, 1970.

3. Layland, J., "Information Systems: Performance of Short Constraint Length Convolutional Codes and a Heuristic Code-Construction Algorithm," in *The Deep Space Network,* Space Programs Summary 37-64, Vol. II, pp. 44–50. Jet Propulsion Laboratory, Pasadena, Calif., Aug. 31, 1970.

# Matched Filters for Binary Signals

S. Zohar

*Communications Systems Research Section*

*Matched filters for the optimal high-speed detection of binary signals are designed and their performance as a function of their complexity is explored. The range of filters designed extends from a 2-element filter whose performance is about 0.7 dB below the ideal filter, up to a 20-element filter with a degradation of about 0.1 dB.*

## I. Introduction

Let $x(t)$ be a binary signal with the levels $\pm 1$ and let the $k$th bit $(a_k)$ be transmitted during the interval

$$(k-1)T \leqq t < kT \tag{1}$$

In the absence of noise, sampling $x(t)$ at any point in the interval (1) will yield $a_k$. With noise present, the search for an optimal detector leads to the idea of a matched receiver, that is, a receiver whose transfer function is tailored to optimize the detection of a signal having a prescribed spectrum (Ref. 1).

In the simple case considered here, the properties of the matched receiver can be obtained directly without resorting to the general theorem. We adopt this approach here in the interest of completeness.

To determine bit $a_k$ in the presence of noise, we average the signal over the $k$th bit period

$$\bar{x}_k = \frac{1}{T}\int_{(k-1)T}^{kt} x(t)\,dt \tag{2}$$

The average $\bar{x}_k$ is now used to determine $a_k$ according to the following decision rule:

$$\left.\begin{aligned} a_k &= 1 \text{ if } \bar{x}_k \geqq 0 \\ a_k &= -1 \text{ if } \bar{x}_k < 0 \end{aligned}\right\} \tag{3}$$

A straightforward realization of this scheme would call for an integrator that would have to be sampled and reset at the bit rate $1/T$.

Alternatively, recalling that the output of a linear filter is a convolution of its input, it is conceivable that a special type of filter can be designed such that when $x(t)$ is its input, its output $y(t)$ approximates

$$y(kT) \approx \bar{x}_k \tag{4}$$

Thus, the integrator would be replaced by a presumably cheaper passive filter. The main advantage, however, would be in the elimination of periodic resetting. The conceived filter would operate continuously. Sampling its output at $t = kT$ and applying the decision rule in Eq. (3) would yield $a_k$.

## II. The Matched Filter

Our goal in this section is to show that a filter satisfying Eq. (4) is indeed possible.

Anticipating that $\bar{x}_k$ will be proved to be a sample of the filter output, we seek to rephrase Eq. (2) as a convolution. This calls for the "box-car" function $B_T(t)$ defined in terms of the step function $u(t)$ as follows:

$$B_T(t) = \frac{1}{T}[u(t) - u(t-T)] \tag{5}$$

Using Eq. (5), Eq. (2) can be rephrased as follows:

$$\bar{x}_k = \int_0^\infty x(t)\, B_T[t - (k-1)T]\, dt \tag{6}$$

Noting now that $B_T(t)$ satisfies

$$B_T(t+T) = B_T(-t) \tag{7}$$

we get the final form

$$\bar{x}_k = \int_0^\infty x(t)\, B_T(kT - t)\, dt \tag{8}$$

The convolution on the right can be interpreted as the output (at time $kT$) of a filter fed by $x(t)$ and having the impulse response $B_T(t)$.

Denoting the filter output as $y(t)$, Eq. (8) states

$$\bar{x}_k = y(kT) \tag{9}$$

Strictly speaking, such a filter is not realizable in terms of lumped parameters. However, a sufficiently good approximation to it is realizable.

One such realization which approximates $B_T(t)$ while minimizing the integral of the squared error has been described (Ref. 2). It can be shown, however, that the telemetry detection performance of any approximation also depends on a sequence of integrals of the first power of the error. Thus, while elaborate optimization techniques have been used to obtain the networks of (Ref. 2), they are not optimal for the present application.

We shall see that a simple straightforward approximation method due to Guillemin (Ref. 3) yields reasonably good results. For certain parameter values, these are better than the results obtained with the networks of Ref. 2. Guillemin's method is illustrated in Fig. 1. Let $H(s)$, $H_1(s)$, $H_2(s)$ be the Laplace transforms of $h(t)$, $h_1(t)$, $h_2(t)$, respectively. Then $H(s)$, the desired transfer

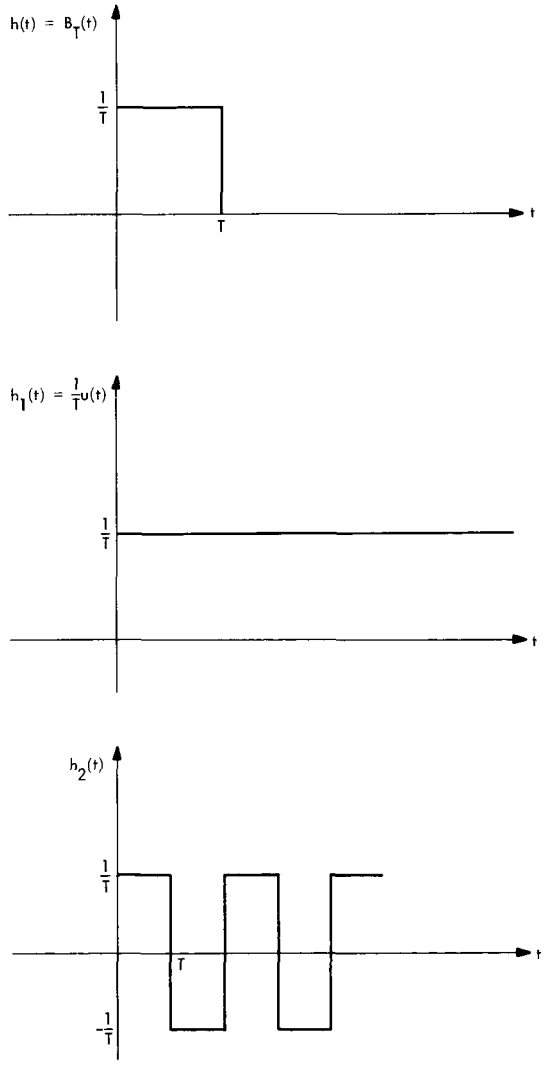


**Fig. 1. Functions generating $B_T(t)$**

function, can be readily expressed in terms of $H_1(s) = 1/sT$, using the shift operator $e^{-sT}$. Thus,

$$H(s) = H_1(s) - e^{-sT} H_1(s) = \frac{1 - e^{-sT}}{sT} \tag{10}$$

Normalizing the complex frequency variable $s$ through

$$\left.\begin{aligned} \gamma &= sT \\ H(s) &= F(\gamma) \\ H_i(s) &= F_i(\gamma) \end{aligned}\right\} \tag{10a}$$

we have

$$H(s) = F(\gamma) = \frac{1 - e^{-\gamma}}{\gamma} \tag{10b}$$

Strictly speaking, $H(s)$, being a transcendental function, is not realizable in terms of lumped circuit elements. We therefore have to settle for a rational approximation to it. Guillemin's approach avoids approximating $e^{-sT}$, introducing instead the approximation inherent in the truncation of a Fourier series. This is effected through the pair $h_2(t)$, $H_2(s)$ as follows: In analogy with Eq. (10) we have

$$F(\gamma) = H(s) = H_2(s) + e^{-sT} H_2(s) = (1 + e^{-\gamma}) F_2(\gamma) \tag{11}$$

Eliminating $e^{-\gamma}$ between Eqs. (10b) and (11), we obtain

$$F(\gamma) = \frac{2 F_2(\gamma)}{1 + \gamma F_2(\gamma)} \tag{12}$$

To get $F_2(\gamma)$ we expand $h_2(t)$ in a Fourier series

$$h_2(t) = u(t) \sum_{k=1}^{\infty} b_k \sin\left(\pi k \frac{t}{T}\right) \tag{13}$$

where

$$b_k = \begin{cases} 0 & (k \text{ even}) \\ \dfrac{4}{\pi k T} & (k \text{ odd}) \end{cases} \tag{14}$$

Taking the Laplace transform of Eq. (13) we get

$$H_2(s) = \frac{\pi}{T} \sum_{k=1}^{\infty} \frac{k b_k}{s^2 + \left(\dfrac{\pi k}{T}\right)^2} \tag{15}$$

Finally, substitution of Eq. (14) in Eq. (15) yields

$$F_2(\gamma) = 4 \sum_{k=1}^{\infty} \frac{1}{\gamma^2 + [(2k-1)\pi]^2} \tag{16}$$

At this point we approximate by truncating the $F_2(\gamma)$ expansion after $N$ terms. Distinguishing approximations by a circumflex we then have

$$\hat{H}_2(s) = \hat{F}_2(\gamma) = 4 \sum_{k=1}^{N} \frac{1}{\gamma^2 + [(2k-1)\pi]^2} \tag{17}$$

$$\hat{H}(s) = \hat{F}(\gamma) = \frac{2 \hat{F}_2(\gamma)}{1 + \gamma \hat{F}_2(\gamma)} \tag{18}$$

We refer to the network realizing $\hat{H}(s)$ as the $N$th order network. As is evident from Eqs. (17) and (18), this transfer function has $2N$ poles.

## III. Performance Criteria

$\hat{H}(s)$, the $N$th order approximation transfer function, approaches the ideal $H(s)$ as $N$ tends to infinity. As we shall presently see, the number of components in the realization of the $N$th order filter is $3N - 1$. We are interested in the performance of $\hat{H}(s)$ as a function of $N$ so that the improved performance associated with a more complex realization can be accurately gauged.

We start with a detailed examination of the effect of the approximation transfer function $\hat{H}(s)$ on the binary signal $x(t)$. In line with the preceding notation, we denote the output of this filter by $\hat{y}(t)$ and its $\delta$-function response by $\hat{B}_T(t)$. Thus we have

$$\hat{y}(t) = \int_0^{\infty} x(\tau) \hat{B}_T(t - \tau)\, d\tau \tag{19}$$

Note that $x(\tau)$ may be expressed in terms of the box-car function as follows

$$x(\tau) = T \sum_{k=1}^{\infty} a_k B_T[\tau - (k-1)T] \tag{20}$$

Substituting in Eq. (19) we get

$$\hat{y}(t) = \sum_{k=1}^{\infty} a_k \hat{\mu}_T(t - kT) \tag{21}$$

where

$$\hat{\mu}_T(t) = T \int_0^T B_T(\tau)\, \hat{B}_T(\tau + t)\, d\tau \tag{22}$$

To see the significance of $\hat{\mu}_T(t)$, note that for the ideal filter $H(s)$, the above procedure yields

$$y(t) = \sum_{k=1}^{\infty} a_k\, \mu_T(t - kT) \tag{23}$$

with

$$\mu_T(t) = T \int_0^T B_T(\tau)\, B_T(\tau + t)\, d\tau \tag{24}$$

Unlike Eq. (22), the two functions here are identical and $\mu_T(t)$ is easily seen to be the simple triangle function displayed in Fig. 2. For arguments which are integral multiples of $T$, the effect of this function is very similar to that of a $\delta$-function. Thus

$$\mu_T(kT) = \delta_{0k} \tag{25}$$

Hence

$$y(kT) = \sum_{i=1}^{\infty} a_i\, \mu_T[(k - i)\, T] = \sum_{i=1}^{\infty} a_i\, \delta_{ik} = a_k \tag{26}$$

The function of interest to us, $\hat{\mu}_T(t)$, is an approximation to $\hat{\mu}_T(t)$. Thus, corresponding to Eq. (25), we have

$$\hat{\mu}_T(kT) = \hat{m}_k \tag{27}$$

with

$$\hat{m}_k \begin{cases} = 0 & (k < 0) \\ \approx 1 & (k = 0) \\ \approx 0 & (k > 0) \end{cases} \tag{28}$$

Note that we are considering here a family of functions, since $\hat{\mu}_T(t)$ is also a function of $N$. As $N$ increases, $\hat{\mu}_T(t)$ approaches $\mu_T(t)$ and $\hat{m}_k$ tends to $\delta_{0k}$. This is evident in Fig. 3 which shows $\hat{\mu}_T(t - T)$ for $N = 3$.

Applying Eqs. (27) and (28) to Eq. (21) we get

$$\hat{y}(kT) = \sum_{i=1}^{k} a_i \hat{m}_{k-i} = \sum_{i=0}^{k-1} a_{k-i}\, \hat{m}_i \tag{29}$$

$$= \hat{m}_0\, a_k + \sum_{i=1}^{k-1} a_{k-i}\, \hat{m}_i$$

We recall now that our objective is to use $\hat{y}(kT)$ to determine $a_k$. Equation (29) shows that in addition to the desired output, $\hat{m}_0 a_k$, we also get small contributions from all preceding bits. This raises the following question: Assuming that $a_k = 1$, what is the probability that application of the decision rule of Eq. (3) would yield $a_k = -1$? The sum in Eq. (29) is one contribution to this probability. The other major contribution is noise. Let us assume that the signal $x(t)$ feeding the filter is accompanied by white gaussian noise yielding the noise output $n(t)$. The filter output is now given by

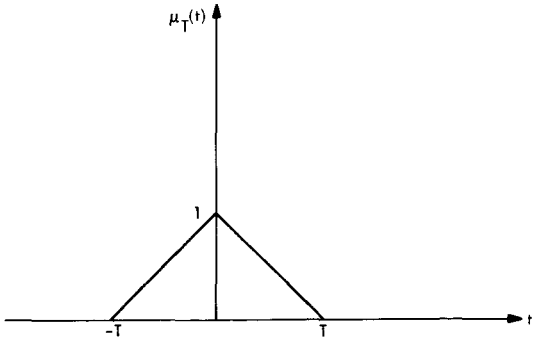


**Fig. 2. Function $\mu_T(t)$**

$$z(t) = n(t) + \hat{y}(t) \tag{30}$$

In particular, for $a_k = 1$

$$z(kT) = \hat{m}_0 + \left\{ n(kT) + \sum_{i=1}^{k-1} \hat{m}_i\, a_{k-i} \right\} \tag{31}$$

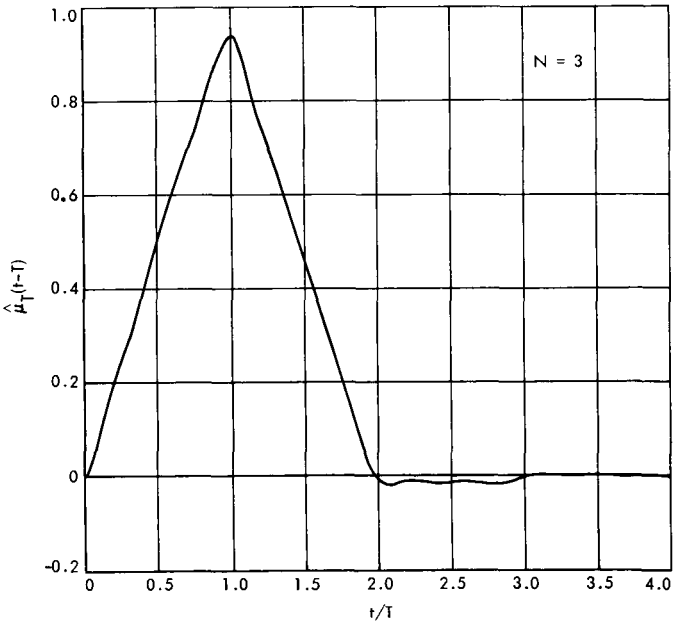


**Fig. 3. Function $\hat{\mu}_T(t - T)$ for $N = 3$**

Assuming now that the bits $a_i$ are totally uncorrelated with themselves as well as with the noise samples, we get for the mean and variance of $z(kT)$

$$\left.\begin{aligned} E[z(kT)] &= \hat{m}_0 \\ \sigma_z^2 &= \sigma_n^2 + \sum_{i=1}^{k-1} \hat{m}_i^2 \end{aligned}\right\} \tag{32}$$

where $\sigma_n^2$ is the variance of the noise output. Finally, applying the law of large numbers we conclude that $z(kt)$ may be reasonably well approximated by a normally distributed random variable with the parameters prescribed in Eq. (32).

Application of the decision rule (3) to $z(kt)$ will yield the wrong answer ($a_k = -1$) when $z(kT) < 0$. Thus, the probability of error is given by the integral of the $z$ distribution over negative $z$. Alternatively, using the normalized entity

$$Q(v) = \frac{1}{\sqrt{2\pi}} \int_v^\infty \exp\left(-\frac{t^2}{2}\right) dt \tag{33}$$

and denoting

$$\xi = \frac{\hat{m}_0}{\sigma_z} \tag{34}$$

we see that

$$\text{probability of error} = Q(\xi) \tag{35}$$

By symmetry, this is also the probability of error when $a_k = -1$.

The parameter $\xi$ is a function of $N$ through $\hat{m}_0$ as well as via $\sigma_z$. To compare the performance of networks of different orders, we need an explicit formulation of $\xi(N)$. To obtain this, let us assume that the input to the filter consists of the signal at levels of $\pm 1$ V (across 1 Ω) and an accompanying white noise with the (two-sided) spectral density $\nu$ (in W/Hz). This means that

$$\sigma_n^2 = \int_{-\infty}^{\infty} |\hat{H}(i\omega)|^2 \nu df = \nu \int_0^\infty \hat{B}_T^2(t)\, dt \qquad (\omega = 2\pi f) \tag{36}$$

It is convenient to express this in terms of the ideal network ($N = \infty$) for which

$$\sigma_n^2 = \nu \int_0^\infty B_T^2(t)\, dt = \frac{\nu}{T} \tag{37}$$

Thus we write for the network of order $N$

$$\sigma_n^2 = p_N \frac{\nu}{T} \tag{38}$$

where $p_N$ is computable from the known $\hat{B}_T(t)$. It is independent of $T$ and varies monotonically from $p_1 = 0.81$ to $p_\infty = 1$.

Applying Eqs. (38) and (32) to Eq. (34), we get

$$\xi^2 = \frac{\hat{m}_0^2}{p_N \frac{\nu}{T} + \sum_{i=1}^{k-1} \hat{m}_i^2} \tag{39}$$

Hence

$$\nu \equiv \nu_N = T \frac{\hat{m}_0^2}{p_N} \left[\frac{1}{\xi^2} - \sum_{i=1}^{k-1} \left(\frac{\hat{m}_i}{\hat{m}_0}\right)^2\right] \tag{40}$$

For $N = \infty$ this simplifies to

$$\nu_\infty = \frac{T}{\xi^2} \tag{41}$$

Hence

$$\frac{\nu_N}{\nu_\infty} = \frac{\hat{m}_0^2}{p_N} \left[1 - \xi^2 \sum_{i=1}^{k-1} \left(\frac{\hat{m}_i}{m_0}\right)^2\right] \tag{42}$$

Equation (42) is an implicit formulation of the desired performance criterion. Given a prescribed error probability $Q(\xi)$, we find $\xi$ from the relevant tables. Now an ideal network ($N = \infty$) would realize the prescribed performance with a noise power density $\nu_\infty$ given by Eq. (41). If, however, we use an $N$th order network, we could still realize the prescribed $Q(\xi)$ provided the noise power density is reduced. Equation (42) computes this reduction.

Table 1 shows $\nu_N/\nu_\infty$ (in dB) as a function of error probability for $1 \leq N \leq 7$.[1] The corresponding plots are shown in Fig. 4. Note that for an error probability of $10^{-3}$, the simplest network ($N = 1$) is 0.69 dB worse than the ideal. The corresponding value for the second order network is 0.33 dB. From here on, however, the rate of improvement diminishes. Essentially the same pattern holds for all other values of the error probability in Fig. 4.

[1]Actually the table values refer to the synthesized networks and thus reflect errors of the synthesis process. These, however, do not exceed 0.001 dB. See *Section IV*.

**Table 1. $\nu_N/\nu_\infty$ in dB, as a function of error probability and network order N**

| NETWORK ORDER / PROBABILITY OF ERROR | 1 | 2 | 3 | 4 | 5 | 6 | 7 |
|---|---|---|---|---|---|---|---|
| 1.-01 | -.673 | -.324 | -.213 | -.158 | -.126 | -.104 | -.089 |
| 1.-02 | -.681 | -.327 | -.214 | -.159 | -.126 | -.105 | -.089 |
| 1.-03 | -.690 | -.329 | -.215 | -.159 | -.127 | -.105 | -.089 |
| 1.-04 | -.699 | -.332 | -.216 | -.160 | -.127 | -.105 | -.089 |
| 1.-05 | -.708 | -.335 | -.218 | -.161 | -.128 | -.106 | -.089 |
| 1.-06 | -.717 | -.338 | -.219 | -.162 | -.128 | -.106 | -.089 |
| 1.-07 | -.726 | -.341 | -.220 | -.162 | -.129 | -.106 | -.089 |
| 1.-08 | -.736 | -.344 | -.222 | -.163 | -.129 | -.107 | -.089 |
| 1.-09 | -.745 | -.346 | -.223 | -.164 | -.130 | -.107 | -.090 |
| 1.-10 | -.754 | -.349 | -.224 | -.165 | -.130 | -.107 | -.090 |

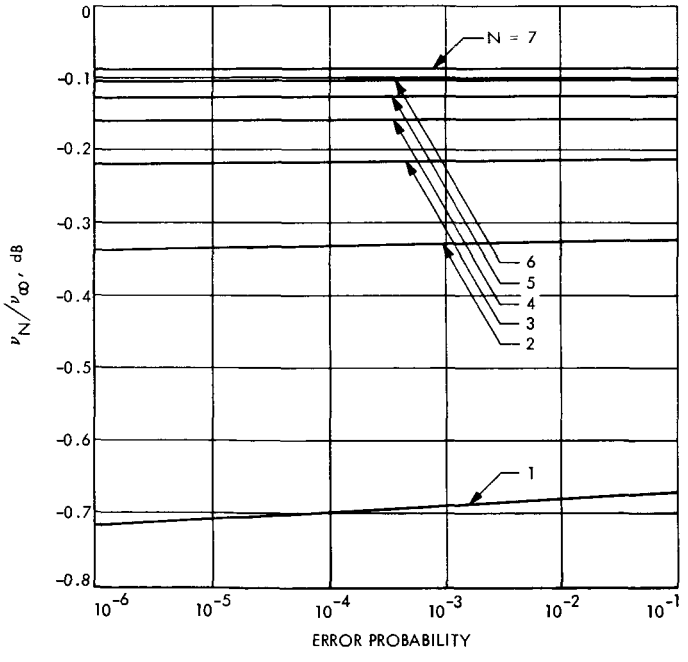


**Fig. 4. $\nu_N/\nu_\infty$ as a function of error probability and network order N**

## IV. The Filter Synthesis

Applying the criteria of the last section, we arrive at the specific $\hat{H}(s)$ that would satisfy the requirements of the problem at hand. It remains now to synthesize a network realizing this $\hat{H}(s)$.

The particular realization considered here is that of a lossless network inserted between a generator having a finite internal resistance and a purely resistive load. In other words, our goal is to design the lossless network indicated in Fig. 5 so as to realize

$$\frac{V_2(s)}{V_g(s)} = \alpha\hat{H}(s) = W(s) \tag{43}$$

The constant multiplier $\alpha$ is necessary to allow arbitrary values of

$$\rho = \frac{R_2}{R_1} \tag{44}$$

(See, however, the discussion associated with Eq. 60). The relationship between $\rho$ and $\alpha$ can be established via the DC behavior of the filter. From Eqs. (17) and (18) we see that

$$\hat{H}(0) = 2\hat{H}_2(0) = \frac{8}{\pi^2} \cdot \sum_{k=1}^{N} (2k-1)^{-2} \neq 0 \tag{45}$$

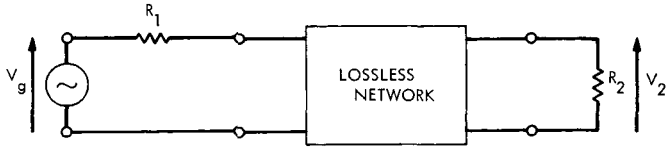


**Fig. 5. Connection of the filter**

But with the network being lossless and $\hat{H}(0) \neq 0$, Fig. 5 prescribes

$$\frac{V_2(0)}{V_g(0)} = \frac{R_2}{R_1 + R_2} = \frac{\rho}{1+\rho} \tag{46}$$

Hence

$$\alpha = \frac{\rho}{\hat{H}(0)(1+\rho)} \tag{47}$$

The synthesis considered will be that of a prototype filter with

$$\left.\begin{aligned} R_1 &= 1\,\Omega \\ \rho &= 1 \\ T &= \pi \text{ sec} \end{aligned}\right\} \tag{48}$$

This particular choice of $T$ allows some of the computations to be carried out with integers, leading to higher precision (see Eqs. 17 and 10a).

Filters realizing any other values of $R_1$ and $T$ are trivially obtained from this prototype filter (see Eq. 65). Modification of $\rho$, however, calls for a new synthesis. Denoting

$$s^2 = q \tag{49}$$

we get for the prototype

$$\hat{H}_2(s) = \frac{4}{\pi^2} \sum_{k=1}^{N} \frac{1}{q + (2k-1)^2} = \frac{4}{\pi^2} \cdot \frac{A(q)}{B(q)} \tag{50}$$

where $A(q)$, $B(q)$ are polynomials of degrees $N-1$, $N$ respectively. $B(q)$ is obtained directly by multiplying out its factors. The simplest way to obtain $A(q)$ is based on the observation that Eq. (50) implies that all residues of $A(q)/B(q)$ are 1. This leads to

$$A(q) = \frac{dB(q)}{dq} \tag{51}$$

Thus, for any finite $N$, $A(q)$, $B(q)$ are easily determined polynomials all of whose coefficients are expressible as sums of products of positive integers. Substituting Eq. (50) in Eq. (18), we express $W(s)$ directly in terms of these polynomials:

$$W(s) = \alpha \hat{H}(s) = \frac{\frac{2}{\pi}\alpha A(q)}{sA(q) + \frac{\pi}{4}B(q)} \tag{52}$$

The actual synthesis is straightforward and follows the standard insertion loss technique (Ref. 4). We are pointing here only highlights of the process.

The subsequent discussion will refer to the following three alternate matrix descriptions of the two port of Fig. 5:

$$\left.\begin{aligned} Z(s) &= \begin{bmatrix} Z_{11}(s) & Z_{12}(s) \\ Z_{21}(s) & Z_{22}(s) \end{bmatrix} \\ Y(s) &= \begin{bmatrix} Y_{11}(s) & Y_{12}(s) \\ Y_{21}(s) & Y_{22}(s) \end{bmatrix} \\ S(s) &= \begin{bmatrix} S_{11}(s) & S_{12}(s) \\ S_{21}(s) & S_{22}(s) \end{bmatrix} \end{aligned}\right\} \tag{53}$$

These are the open-circuit impedance matrix, short-circuit admittance matrix, and scattering matrix, respectively:

The two basic elements in the synthesis procedure are:

(1) The transmission zeros of the network, that is, the zeros of $A(q)$ in our case.

(2) Any one of $Z_{11}(s)$, $Z_{22}(s)$, $Y_{11}(s)$, $Y_{22}(s)$[2]

The transmission zeros are obtained directly from $A(q)$. The immittances mentioned in $b$ are derived from $W(s)$ in an indirect way. First, a scattering matrix satisfying $W(s)$ is determined. The required immittances then follow the application of the standard transformations generating $Z$ and $Y$ from $S$.

In obtaining $S$, use is made of the fact that for a lossless two port and a transfer function whose numerator is an even $s$ polynomial, the scattering matrix has the following form (Ref. 5):

$$S(s) = \frac{1}{g(s)} \begin{bmatrix} h(s) & f(s) \\ f(s) & -h_*(s) \end{bmatrix} \tag{54}$$

where $g$, $h$, $f$ are real polynomials,[3]

$$h_*(s) = h(-s) \tag{55}$$

and

$$gg_* = hh_* + ff_* \tag{56}$$

[2]Strictly speaking, only $Z_{11}(s)$, $Y_{22}(s)$ are capable of generating all the network elements. Referring to Fig. 6, it is obvious that $Y_{11}(s)$ cannot determine $C_N$ while $Z_{22}(s)$ will not determine $L_1$.

[3]The polynomial $h(s)$ should not be confused with the time function $h(t)$ of *Section I*.

To realize $W(s)$ we identify

$$g(s) = sA(q) + \frac{\pi}{4} B(q) \tag{57}$$

$$f(s) = \psi A(q) \tag{58}$$

where

$$\psi = \frac{4\alpha}{\pi\sqrt{\rho}} = \frac{\frac{4}{\pi}}{\hat{H}(0)(\rho^{1/2} + \rho^{-1/2})} \tag{59}$$

To complete the determination of S, $h(s)$ is now obtained from Eq. (56). Note that this equation provides a unique determination only for the product $hh_*$. The determination of $h$ itself is not unique. Generally, a given $hh_*$ is consistent with a number of different $h$ functions leading to different network realizations. In some situations, however, there is no real polynomial $h(s)$ corresponding to the prescribed $hh_*$. This happens to be the case for the first-order network ($N = 1$) where analysis shows a forbidden $\rho$ range given by

$$\frac{1}{1.49} < \rho < 1.49 \tag{60}$$

In view of this, we modify the prototype specifications (48) as follows:

$$\left.\begin{aligned} R_1 &= 1\,\Omega \\ \rho &\begin{cases} = 1.5, & N = 1 \\ = 1, & N > 1 \end{cases} \\ T &= \pi \text{ sec} \end{aligned}\right\} \tag{61}$$

Of the various possible $h(s)$, we examine here only those which satisfy the following constraint

All roots of $h(s)$ are on one side of the imaginary axis (62)

Having determined S, we turn now to the transformation to Z and Y. This is most easily expressed in terms of the even and odd parts of $g$ and $h$. Denoting

$$\left.\begin{aligned} g &= g_e + g_0 \quad [g_e(-s) = g_e(s); \quad g_0(-s) = -g_0(s)] \\ h &= h_e + h_0 \quad [h_e(-s) = h_e(s); \quad h_0(-s) = -h_0(s)] \end{aligned}\right\} \tag{63}$$

the required immittances are expressible as follows:

$$\left.\begin{aligned} \frac{Z_{11}}{R_1} &= \frac{g_e + h_e}{g_0 - h_0} \qquad Y_{11} R_1 = \frac{g_e - h_e}{g_0 + h_0} \\ \frac{Z_{22}}{R_2} &= \frac{g_e - h_e}{g_0 - h_0} \qquad Y_{22} R_2 = \frac{g_e + h_e}{g_0 + h_0} \end{aligned}\right\} \tag{64}$$

The actual synthesis applies the method of Fujisawa (Ref. 6) which yields a transformerless ladder configuration. We have chosen the synthesis realizing the transmission zeros as parallel resonance circuits as shown in Fig. 6. The combination of this configuration constraint and the roots constraint (62), limits the various possibilities so that there is only one prototype for each $N$ value.[4]

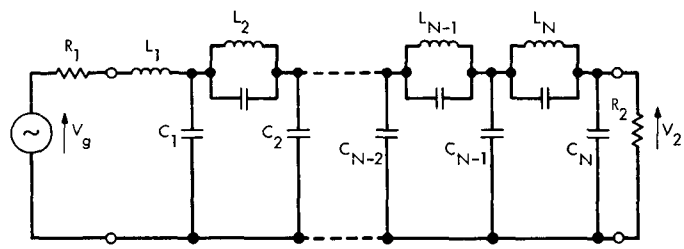


**Fig. 6. Filter configuration**

The computed parameter values of networks up to order 7 are shown in Table 1, which is directly related to Fig. 6, and is mostly self-explanatory (RGEN = $R1$; RLOAD = $R2$; capacitor $CR(I)$ resonates coil $L(I)$ at frequency $FR(I)$). A new entity introduced here is the "sample gain" which is defined as the ratio (in the absence of noise) of the filter output voltage at time $kT$ to the generator voltage representing bit $a_k$.

To illustrate the use of this table assume that we wish to construct a matched filter for bit time $T'$ and generator resistance $R_1'$. Assigning primes to all the parameters of this filter, we obtain them according to the following

[4]It should be borne in mind, though, that given a network such as that in Fig. 6, one could alter the connections, feeding the input in series with $R_2$ and taking the output across $R_1$, realizing a transfer function which is a constant multiple of the original transfer function.

transformations applicable to inductances, capacities, and frequencies, respectively:

$$\left.\begin{aligned} \frac{L'}{L} &= \frac{T'}{T}\frac{R_1'}{R_1} \\ \frac{C'}{C} &= \frac{T'}{T}\frac{R_1}{R_1'} \\ \frac{f'}{f} &= \frac{T}{T'} \end{aligned}\right\} \qquad (65)$$

With $T = \pi$ sec and $R_1 = 1\ \Omega$, Table 2 provides all the information necessary to determine the "primed" filter.

A specific example is shown in Table 3 which refers to filters associated with a 10-$\mu$s bit time and a 50-$\Omega$ generator.

## V. Reliability of Element Values

To check the reliability of the computed element values we compute the performance of the synthesized network and compare it to the design goal. Since we are dealing here with a ladder configuration, it is relatively easy to obtain the transfer function of the synthesized network by multiplying out the ABCD matrices of the individual network sections. Note that this computation is quite precise since it involves the multiplication and summation of positive quantities only. Having thus obtained the "synthesized transfer functions" we compute from them $v_N/v_\infty$, the performance criteria described in *Section III*.

Comparing these to the values obtained from $\hat{H}(s)$ directly, we found that the discrepancies for all the networks shown in Table 2 do not exceed 0.001 dB. Furthermore, the values appearing in Table 1 are those of the synthesized networks so that even the above minor discrepancies should not be of concern to the user.

**Table 2. Network elements for $T = \pi$ sec, $R_1 = 1\ \Omega$**

***UNITS*** SECOND,HERTZ,OHM,HENRY,FARAD
T= 3.1415927+00
RGEN= 1.000+00

| NET. ORDER | 1 | 2 | 3 | 4 | 5 | 6 | 7 |
|---|---|---|---|---|---|---|---|
| RLOAD | 1.500+00 | 1.000+00 | 1.000+00 | 1.000+00 | 1.000+00 | 1.000+00 | 1.000+00 |
| SAMPLE GAIN | 6.170-01 | 5.076-01 | 5.051-01 | 5.039-01 | 5.031-01 | 5.033-01 | 0.000 |
| L (1) | 1.410+00 | 5.006-01 | 2.991-01 | 2.157-01 | 1.689-01 | 1.562-01 | 2.126-01 |
| CR(1) | 0.000 | 0.000 | 0.000 | 0.000 | 0.000 | 0.000 | 0.000 |
| C (1) | 1.182+00 | 8.890-02 | 2.271-02 | 1.041-02 | 6.647-03 | 1.088-03 | 4.996-02 |
| L (2) | | 4.908-01 | 7.719-02 | 2.869-02 | 1.459-02 | 9.807-03 | -2.434-02 |
| CR(2) | | 4.075-01 | 6.920-01 | 8.563-01 | 9.680-01 | 9.352-01 | -2.645-01 |
| FR(2) | | 3.559-01 | 3.418-01 | 3.354-01 | 3.318-01 | 3.295-01 | 3.278-01 |
| C (2) | | 1.749+00 | 6.944-02 | 1.306-02 | 3.645-03 | -4.937-02 | 8.556-02 |
| L (3) | | | 4.672-01 | 8.518-02 | 3.310-02 | 8.140-03 | -1.746-02 |
| CR(3) | | | 4.642-01 | 6.573-01 | 7.667-01 | 1.777+00 | -5.353-01 |
| FR(3) | | | 6.886-01 | 6.726-01 | 6.645-01 | 6.594-01 | 6.559-01 |
| C (3) | | | 1.995+00 | 7.011-02 | 1.335-02 | 3.031-02 | -1.681-02 |
| L (4) | | | | 4.597-01 | 8.799-02 | 2.798-02 | -1.994-01 |
| CR(4) | | | | 4.897-01 | 6.520-01 | 9.230-01 | -7.354-02 |
| FR(4) | | | | 1.015+00 | 9.991-01 | 9.903-01 | 9.846-01 |
| C (4) | | | | 2.100+00 | 7.066-02 | 2.844-02 | -3.459-02 |
| L (5) | | | | | 4.557-01 | 8.750-02 | 1.866-01 |
| CR(5) | | | | | 5.049-01 | 6.658-01 | 1.400-01 |
| FR(5) | | | | | 1.339+00 | 1.323+00 | 1.314+00 |
| C (5) | | | | | 2.160+00 | 1.378-02 | -4.917-02 |
| L (6) | | | | | | 4.525-01 | 1.130-01 |
| CR(6) | | | | | | 5.157-01 | 5.209-01 |
| FR(6) | | | | | | 1.662+00 | 1.646+00 |
| C (6) | | | | | | 2.199+00 | 4.209-02 |
| L (7) | | | | | | | 4.587-01 |
| CR(7) | | | | | | | 5.138-01 |
| FR(7) | | | | | | | 1.983+00 |
| C (7) | | | | | | | 2.220+00 |

Table 3. Network elements for $T = 10\ \mu s$, $R_1 = 50\ \Omega$

***UNITS*** MICROSECOND,MEGAHERTZ,OHM,MICROHENRY,MICROFARAD
T= 1.0000000+01
RGEN= 5.000+01

| NET. ORDER | 1 | 2 | 3 | 4 | 5 | 6 | 7 |
|---|---|---|---|---|---|---|---|
| RLOAD | 7.500+01 | 5.000+01 | 5.000+01 | 5.000+01 | 5.000+01 | 5.000+01 | 5.000+01 |
| SAMPLE GAIN | 6.170-01 | 5.076-01 | 5.051-01 | 5.039-01 | 5.031-01 | 5.033-01 | 0.000 |
| L (1) | 2.244+02 | 7.967+01 | 4.769+01 | 3.434+01 | 2.688+01 | 2.487+01 | 3.384+01 |
| CR(1) | 0.000 | 0.000 | 0.000 | 0.000 | 0.000 | 0.000 | 0.000 |
| C (1) | 7.526-02 | 5.660-03 | 1.446-03 | 6.624-04 | 4.232-04 | 6.925-05 | 3.181-03 |
| L (2) | | 3.812+01 | 1.228+01 | 4.567+00 | 2.322+00 | 1.561+00 | -3.874+00 |
| CR(2) | | 2.594-02 | 4.405-02 | 5.452-02 | 6.162-02 | 5.954-02 | -1.684-02 |
| FR(2) | | 1.118-01 | 1.074-01 | 1.054-01 | 1.042-01 | 1.035-01 | 1.030-01 |
| C (2) | | 1.114-01 | 4.421-03 | 8.317-04 | 2.321-04 | -3.143-03 | 5.447-03 |
| L (3) | | | 7.435+01 | 1.356+01 | 5.268+00 | 1.296+00 | -2.779+00 |
| CR(3) | | | 2.955-02 | 4.185-02 | 4.881-02 | 1.131-01 | -3.408-02 |
| FR(3) | | | 2.163-01 | 2.113-01 | 2.087-01 | 2.072-01 | 2.061-01 |
| C (3) | | | 1.270-01 | 4.463-03 | 8.496-04 | 1.929-03 | -1.070-03 |
| L (4) | | | | 7.316+01 | 1.400+01 | 4.453+00 | -3.173+01 |
| CR(4) | | | | 3.117-02 | 4.151-02 | 5.876-02 | -4.682-03 |
| FR(4) | | | | 3.190-01 | 3.139-01 | 3.111-01 | 3.093-01 |
| C (4) | | | | 1.337-01 | 4.498-03 | 1.831-03 | -2.202-03 |
| L (5) | | | | | 7.252+01 | 1.393+01 | 2.970+01 |
| CR(5) | | | | | 3.214-02 | 4.239-02 | 8.915-03 |
| FR(5) | | | | | 4.208-01 | 4.158-01 | 4.129-01 |
| C (5) | | | | | 1.375-01 | 4.697-03 | -3.130-03 |
| L (6) | | | | | | 7.201+01 | 1.799+01 |
| CR(6) | | | | | | 3.283-02 | 3.316-02 |
| FR(6) | | | | | | 5.221-01 | 5.172-01 |
| C (6) | | | | | | 1.400-01 | 2.679-03 |
| L (7) | | | | | | | 7.301+01 |
| CR(7) | | | | | | | 3.271-02 |
| FR(7) | | | | | | | 6.231-01 |
| C (7) | | | | | | | 1.413-01 |

## VI. Concluding Remarks

The element values appearing in the example of Table 3 are quite reasonable. Thus, the main goal of synthesizing the matched filter has been achieved. However, if one is to apply this design in practice, various questions have to be answered, whether through computer simulation or with actually built filters. We briefly mention some of these here.

We start with the effects of stray capacities. Examination of Fig. 6 shows that most stray capacities could be incorporated into the circuit elements. An exception is the first section, that is, the section realizing the transmission zero at infinity. As the self-resonance of a physical coil occurs at a finite frequency, we have here a factor which might be prominent in limiting the applicability of this design for very small $T$, i.e., very high symbol rates. Another unknown factor is the effect of losses in the elements, particularly in the coils.

Regarding the sensitivity of the performance criteria to deviations from the prescribed element values, we have some indirect evidence that as long as the transmission zero frequencies are adjusted to their correct values, the performance is relatively immune to slight deviations. Finally, it has been assumed at the outset that the sampling instants ($t = kT$) are precisely known. The effect of slight shifts in the sampling times merits further study.

## References


1. Viterbi, A. J., *Principles of Coherent Communication,* Sect. 7.1. McGraw-Hill Book Co., Inc., 1966.

2. Meyer, R. A., "Filters with an Approximately Rectangular Impulse Response," *NTZ Commun. J.*, Vol. 5, No. 3, 1966.

3. Guillemin, E. A., *Synthesis of Passive Networks.* Sect. 6, Chapt. 15. John Wiley & Sons, 1957.

4. Saal, R., and Ulbrich, E., "On the Design of Filters by Synthesis," *IRE Trans. PGCT,* Vol. CT-5, No. 4, pp. 284–327, December 1958.

5. Belevitch, V., "Topics in the Design of Insertion Loss Filters," *IRE Trans. PGCT,* Vol. CT-2, No. 4, pp. 337–346, December 1955.

6. Fujisawa, T., "Realizability Theorem for Mid-Series or Mid-Shunt Low-pass Ladders Without Mutual Induction," *IRE Trans. PGCT,* Vol. CT-2, No. 4, pp. 320–325, December 1955.

# Digital Modulator

R. Winkelstein
Communications Systems Research Section

*Utilization of the increased capability of the DSS 14 transmitter and antenna for planetary radar transmission has been made possible by the design, construction, and installation of a digital modulator at DSS 14. This device reshapes the digital modulating waveform generated at DSS 13 and received over the microwave link at DSS 14. The digital modulator output is an accurately adjustable 2-level waveform used to biphase-modulate the transmitter frequency. During precalibration setup, the digital modulator provides selectable frequency square waves used in correctly adjusting the waveform amplitude to obtain carrier suppression greater than 40 dB. The capability that this technique provides has been demonstrated in planetary radar experiments. By this method, one station's processor can be used to generate commands to be sent to a spacecraft from another station at the same complex, thus increasing the reliability of the DSN command system.*

## I. Introduction

A digital modulator was constructed and installed in the pedestal room at DSS 14. Its function is to reshape a partially degraded digital waveform received over the microwave link. The modulator output is an accurately controlled 2-level digital waveform used to biphase modulate the transmitter frequency. Thus it is now possible to modulate the Mars Deep Space Station transmitter (DSS 14) from digital coders being operated at the Venus Deep Space Station (DSS 13).

## II. System Operation

Since the transmitter phase modulator has a linear phase modulation characteristic versus input voltage, it is necessary to accurately set the amplitude of the digital modulating signal in order to obtain the required 180-deg biphase modulation of the transmitter output frequency. To assist in this precalibration adjustment, the digital modulator can be switched to produce precise square waves at selected frequencies between 0.5 and 100 kHz.

Figure 1, the transmitter modulation block diagram, illustrates the calibration technique. A front panel mode switch on the digital modulator disconnects the normal microwave link signal and introduces a DC signal into the transmitter phase modulator. During this procedure the transmitter power amplifier is not energized. The receiver input is connected to the ambient load and the 455-kHz IF frequency output is connected to the wave analyzer. The

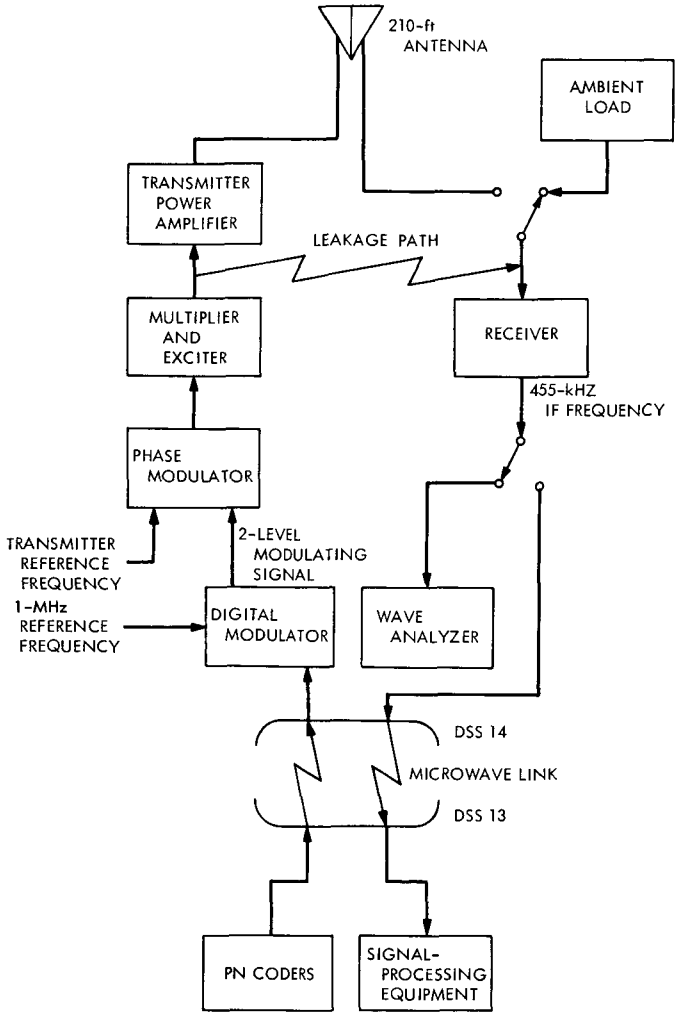


**Fig. 1. Transmitter modulation block diagram**

wave analyzer is tuned to the 455-kHz signal obtained from the leakage path between the transmitter exciter output and the receiver input. After noting the wave analyzer reading, the operator selects a frequency on the digital modulator close to half the scheduled clock frequency of the pseudonoise (PN) coders. He then switches the digital modulator mode switch to the square wave position, which is the output of a digital circuit counting down the 1-MHz reference frequency. A 10-turn output level control potentiometer on the digital modulator panel is then adjusted for a minimum reading on the wave analyzer. This denotes 180-deg biphase modulation and the resultant high degree of carrier suppression.

The mode switch is then turned to the microwave position, the receiver connected to the antenna and microwave link, and the system is ready for operation.

## III. Digital Modulator Block Diagram

Figure 2 shows a block diagram of the digital modulator. The 1-V peak-to-peak microwave input signal is amplified to 2 V peak-to-peak and then passed to a capacitance-diode clamping circuit. This stabilizes the trigger point of the Schmitt trigger on the PN waveform with minimum sensitivity to the changing PN code duty cycle. The reshaped PN code is then available to the output circuit when the mode switch is in the microwave position.

Also available to the output circuit is a square wave counted down from an external 1-MHz reference frequency. The multi-frequency countdown circuit is controlled by a front panel frequency selector switch which can select one of the following 8 frequencies: 0.5, 1, 2, 5, 10, 20, 50, or 100 kHz.

The output circuit produces a stable, accurate 2-level waveform at 50 Ω internal impedance for both the microwave and square wave mode switch positions. Figure 3 shows some details of the output circuit. $Q_1$ provides a constant current whose value is adjusted by means of the resistance programmed power supply. This current is steered into either $Q_2$ when $Q_2$ is in the conducting state, or into the 50-Ω source resistor and output load when $Q_2$

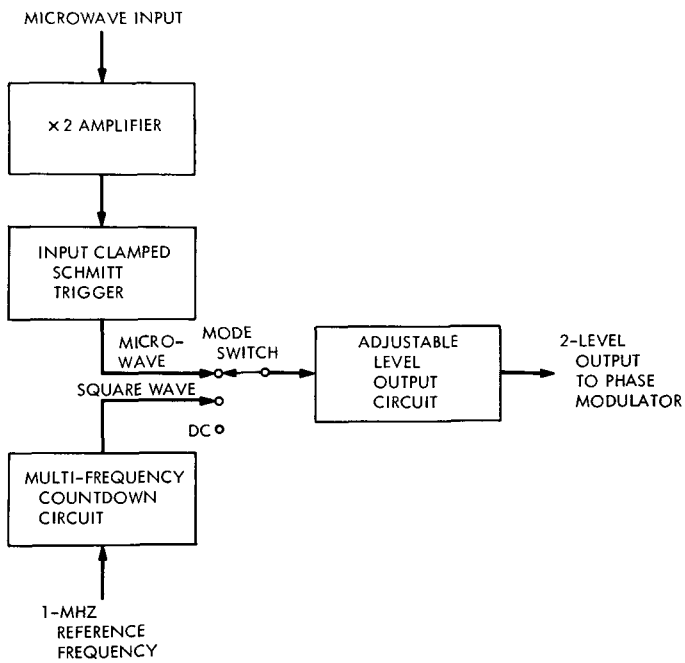


**Fig. 2. Digital modulator block diagram**

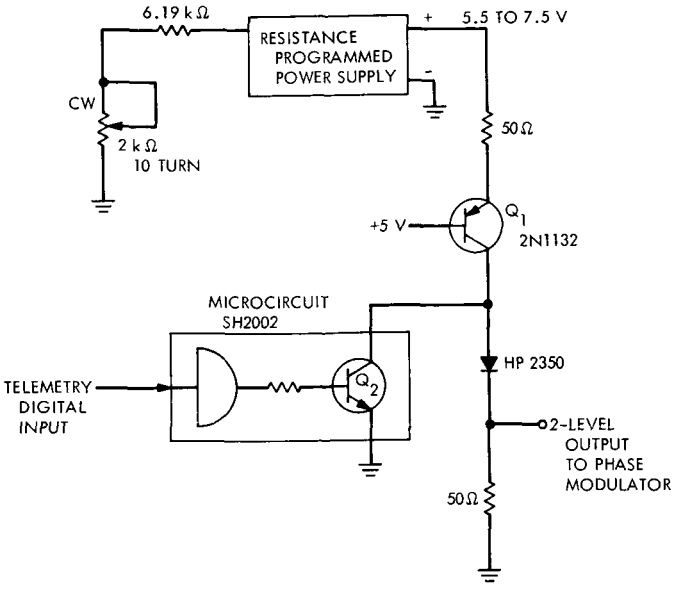


**Fig. 3. Output circuit**

is not conducting. Thus one level of the output is at ground potential, and the other level is adjustable from 0 V to +1 V when the output is loaded with 50 Ω. Current steering results in an extremely flat stable waveform with transition times less than 100 ns.

## IV. Conclusion

The described digital modulator has been successfully utilized in the planetary radar program. The DSS 14 antenna has been used in the monostatic radar mode while the controlling waveforms have been generated and data processing carried out at DSS 13. Thus advantage has been taken of the high transmitter power capability and high antenna gain at DSS 14 during the radar transmission cycle. In the precalibration setup, the stability and purity of the digital modulator output waveform has permitted carrier suppression adjustments typically greater than 40 dB for square-wave modulation.

# Tracking and Data Acquisition Elements Research: Polarization Diverse S-Band Feed Cone

D. E. Neff and A. J. Freiley
Communications Elements Research Section

*Development of the polarization diverse S-band (PDS) feed cone that is used on the DSS 14 210-ft-diam antenna tricone is described. The PDS system integrates the knowledge gained in two previous feed system developments and provides a highly flexible microwave front end. Right-handed circular polarization, left-handed circular polarization, and orthogonal linear polarizations are available on low-noise listen-only or diplexed channels. Additionally, a research and development radar capability for 500-kW continuous-wave power is provided. The system further provides manual or automatic servo tracking of the position angle of received linear polarization, which will be used for radio science purposes.*

## I. Introduction

The polarization diverse S-band (PDS) feed cone is a radio-frequency front-end system for the DSIF reflector antennas (85- or 210-ft diam) that provides a flexible polarization capability, low-noise temperature performance, and a high-power transmission capability. Use of improved techniques and field-tested equipment insured an operational system that has very flexible high performance and reliability.

The PDS feed cone uses the fundamental configuration of the S-band multi-frequency (SMF) feed cone previously reported in Refs. 1–3. However, several significant changes include (1) reduction of waveguide circuitry, (2) modification of RF components from 20- to 500-kW power levels, (3) reduction of total operating noise temperatures $T_{op}$ in all modes, (4) a wide-band feed horn with improved illumination efficiency at the DSIF transmission frequency (Ref. 4), and (5) 500-kW radar capability at the 2388-MHz research and development (R&D) frequency.

The SMF feed cone has been used to support DSS 14 operations since the 1966 station turnon, with only two brief interruptions for *Mariner* planetary encounters. These encounters were characterized by the need for ultra-low-noise receive-only performance in 25°K at the 25-deg

elevation class, which could not be provided by the SMF configuration (Ref. 5). The decision was made to merge, insofar as was possible, the flexible SMF configuration with the ultra-low-noise listen capability and, in May 1970, planning began for installation of the new system as a part of the DSS 14 tricone installation. The new system was to serve, primarily, the multifaceted polarization requirements of the *Pioneer* and *Mariner* families of spacecraft, including occultation and other radio science. Secondary goals were to develop a system capable of reproduction and introduction into the overseas 210-ft-diam antennas, and to provide the future capability of high-power diplexed (500-kW) operations. R&D radar requirements (2388 MHz) and the 500-kW power level were included to reduce costs and the total number of feed cones required for the tricone configuration.

## II. Feed Cone Description

The PDS feed cone (Fig. 1) was developed to provide the lowest loss and best physical RF layout with the planned waveguide components. Transmission from the cone is allowed only through the lower orthomode junction port, thus simplifying power handling and isolation problems with the upper "low-noise port." The single transmitter select switch (SW 3) that combines the DSIF and R&D transmitter outputs further reduces the number of components. Placing the megawatt cassegrain diplexer in the cone provides diplexed modes comparable with the original SMF cone in operation, i.e., either the cone maser or the tricone module III maser can be diplexed. The waveguide switch controller (Fig. 2) is used to position the PDS cone waveguide switches required for the various operating modes. The waveguide paths and polarization selection are presented by an illuminated status display to reduce possible ambiguities with a complex system. All cone operating modes (Table 1) have been carefully safety-interlocked and inhibited through the tricone RF switch controller subsystem. Table 1 includes typical zenith $T_{op}$ values of 18.5 and 23.5°K for the listen-only and diplexed modes, the primary operating modes.

## III. Polarization Diversity Operation

The polarization diversity components (Fig. 1) consist of the upper and lower quarterwave plates with three WC504 cylindrical waveguide rotary joints and two drive

**Table 1. Operating modes**

| Mode | Description | Remarks | Switch positions | | | Polarizer position | Approximate zenith $T_{op}$, °K (PDS/mod. III traveling wave maser) |
|---|---|---|---|---|---|---|---|
| | | | SW 1 | SW 2 | SW 3 | | |
| DSIF | | | | | | | |
| I | Prime linear listen, ortho transmitter | Ortho linear at mod. III traveling wave maser | 2 | 3 | 2 | 4 | 18.5/29 |
| II | Prime linear, colinear transmitter | Ortho linear at mod. III traveling wave maser | 2 | 1 | 2 | 3 | 23.5/26 |
| III | RCP listen only (star track calibration) | LCP at mod. III traveling wave maser | 2 | 3 | 2 | 2 | 18.5/26 |
| IV | RCP diplex | LCP at mod. III traveling wave maser | 2 | 1 | 2 | 1 | 23.5/26 |
| V | LCP listen only | RCP at mod. III traveling wave maser | 2 | 3 | 2 | 1 | 18.5/29 |
| VI | LCP diplex | RCP at mod. III traveling wave maser | 2 | 1 | 2 | 2 | 23.5/26 |
| VII | Prime linear listen only | Ortho linear at mod. III traveling wave maser | 2 | 3 | 2 | 4 | 18.5/29 |
| R&D | | | | | | | |
| A | Bistatic radar, DSS 14 receiver | LCP to PDS traveling wave maser, RCP to mod. III traveling wave maser | 2 | 3 | 2 | 1 | 20.6/26 |
| B | Bistatic radar, DSS 14 transmitter | RCP radiated | 2 | 2 | 3 | 1 | — |
| C | Monostatic radar | RCP radiated, LCP to PDS traveling wave maser, RCP to mod. III traveling wave maser | 2 | transmit 2, receive 3 | 3 | 1 | 20.6/26 |
| D | Standby, other cone operative | 400-kW transmitter from other cone permitted | 2 | 2 | 1 | any | — |

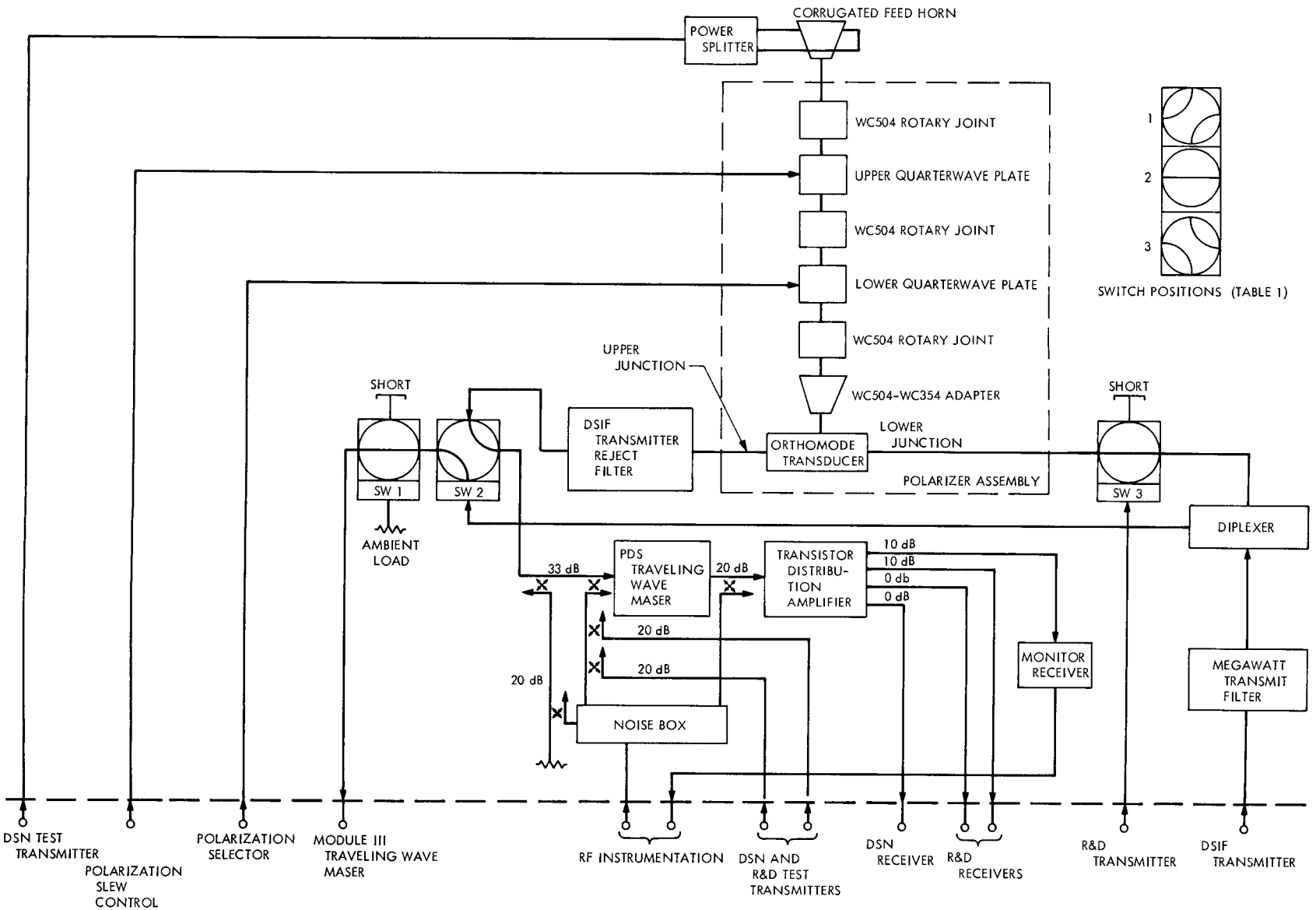


**Fig. 1. PDS feedcone block diagram**

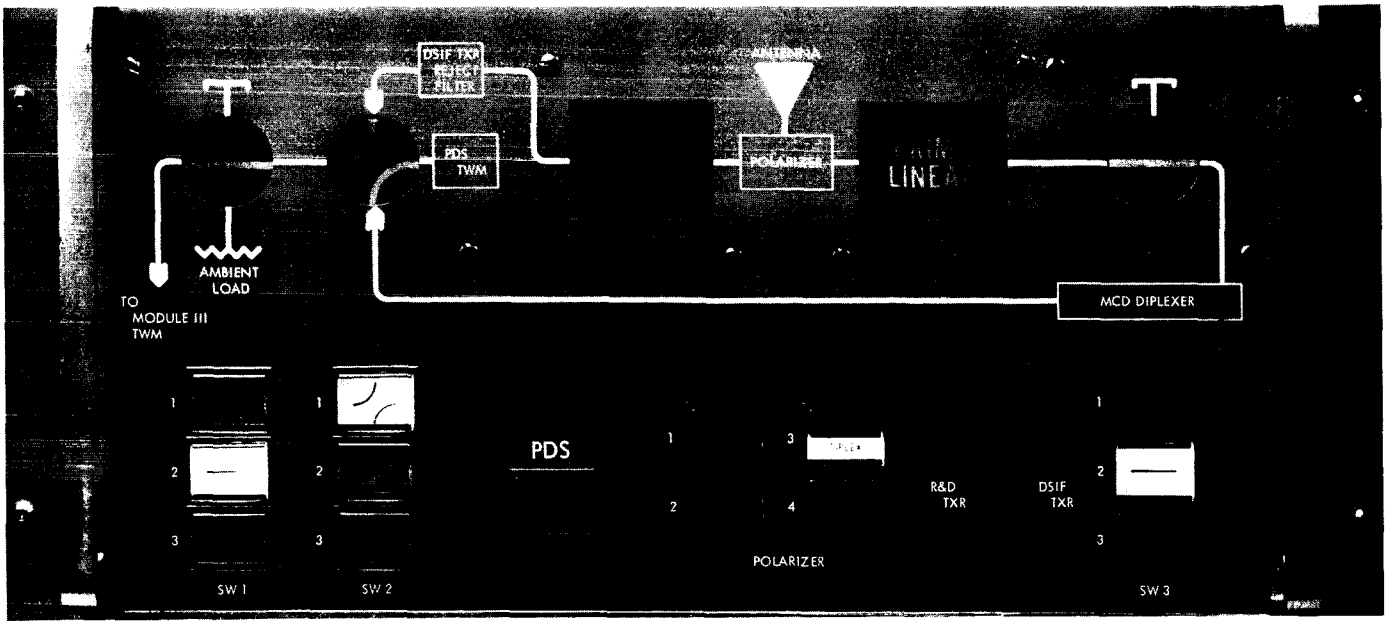


**Fig. 2. Control panel, PDS feedcone**

motors. Polarization control is accomplished by rotating the quarterwave plates with respect to the orthomode transducer immediately below.

Circular polarizations (CP) are generated by aligning the lower quarterwave plate with the transmitter input port, such that no polarization change is produced; the upper plate is then rotated ±45 deg to generate the required right-hand circular polarization (RCP) or left-hand circular polarization (LCP) at the horn mouth. Ellipticities of (2.2 ±0.4), (0.28 ±0.28), and (0.40 ±0.40) dB are achieved at 2115, 2295, and 2388 MHz, respectively.

The rotating linear polarizations (LP) are generated by aligning the lower quarterwave plate ±45 deg with respect to the transmitter input port, such that CP signals are produced at the center rotary joint. The upper quarterwave plate then reconverts the CP signals back into linearly polarized waves at the horn mouth. The angular position of these LP waves may be controlled by rotating the upper quarterwave plate. The LP vectors may also be rotated an exact 90 deg by changing the sense of the CP signals from the lower quarterwave plate. This last effect is taken advantage of and used to eliminate a waveguide switch to transfer the signals between the orthomode transducer ports. Ellipticities of (12.5 ±1.5), 20.5 (minimum), and approximately 15 dB are achieved at (2100–2120), (2270–2300), and 2388 MHz, respectively.

The polarization changes are implemented with the waveguide switch controller (Fig. 2). Four modes, diplexed RCP, LCP, PRIME LINEAR, and ORTHO LINEAR, are selectable with front panel pushbutton switches. PRIME LINEAR is used to denote the indicated polarization angle (IEEE standard) as readout on a digital display, which is available at a given port. The opposite port will then provide ORTHO LINEAR, i.e., 90-deg spatially oriented from the PRIME. The control of the upper quarterwave plate is switched to the polarization tracking servo unit (Fig. 3) when a linear mode is selected. The polarization tracking servo unit either provides a manual slew mode or polarization autotrack on received position angle of an incoming LP signal, and this is, of course, the prime mode of operation for radio occultation studies of the solar corona transients. Provision within the polarization tracking servo for possible future computer drive is made.

The physical complexity of the original SMF polarization tracking servo unit was vastly simplified by redesign. Two coaxial probes were installed in the feed horn (Fig. 4) to enable alignment of the polarization tracker. The probes provide a receive-band test signal with accurately known position angle. The probes have a coupling coefficient of (−46 to −53) and (−41 to −51) dB at (2100–2120) and (2270–2300) MHz, respectively.

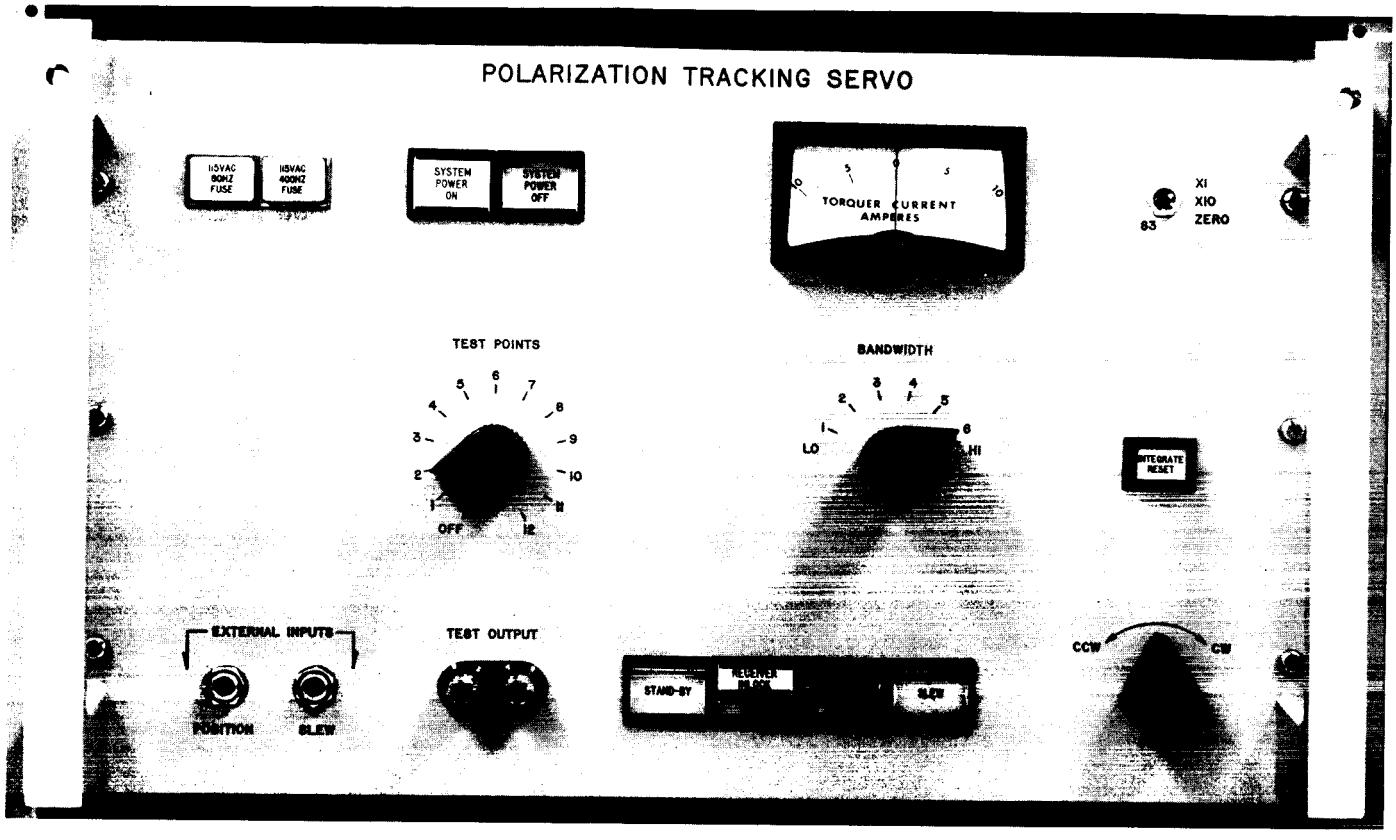


**Fig. 3. Polarization tracking servo control unit, PDS feedcone**

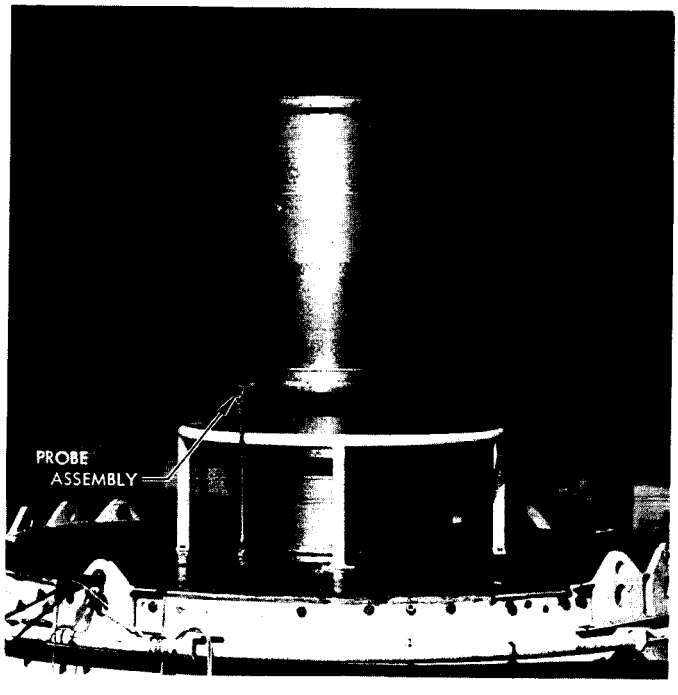


**Fig. 4. Alignment probe assembly, PDS feedcone**

## IV. Waveguide Component Description

Development of the high-power components (Fig. 1) required redesign and high-power testing to insure proper operation. A full description of this work is given in Ref. 6. Basically, all critical parts were made in copper of one-piece construction and liberally water-cooled.

The quarterwave plates are air-cooled because of the difficulty of water cooling continuously rotating equipment reliably. Maximum heat dissipation in this area is approximately 900 W at a 500-kW power level; the air flow is sensed and the transmitters are interlocked OFF in event of an air failure.

Improved choking is utilized in SW 1 and SW 2 to achieve lower insertion loss and improved isolation and match (Ref. 7). SW 3, which handles both high-power transmitter levels, is uniquely water-cooled such that no chance of coolant leakage to the internal waveguides is possible. All waveguide switches use larger rotor-to-stator gaps than previously used, and employ conductive grease on the ball bearings. These measures are thought to

provide improved noise characteristics for waveguide switches.

Figure 5 shows the PDS cone interior, including the orthomode, the diplexer, the transmitter filter, and the lower quarterwave plate drive assembly, and shows the major part of the high-power cooled transmission lines.

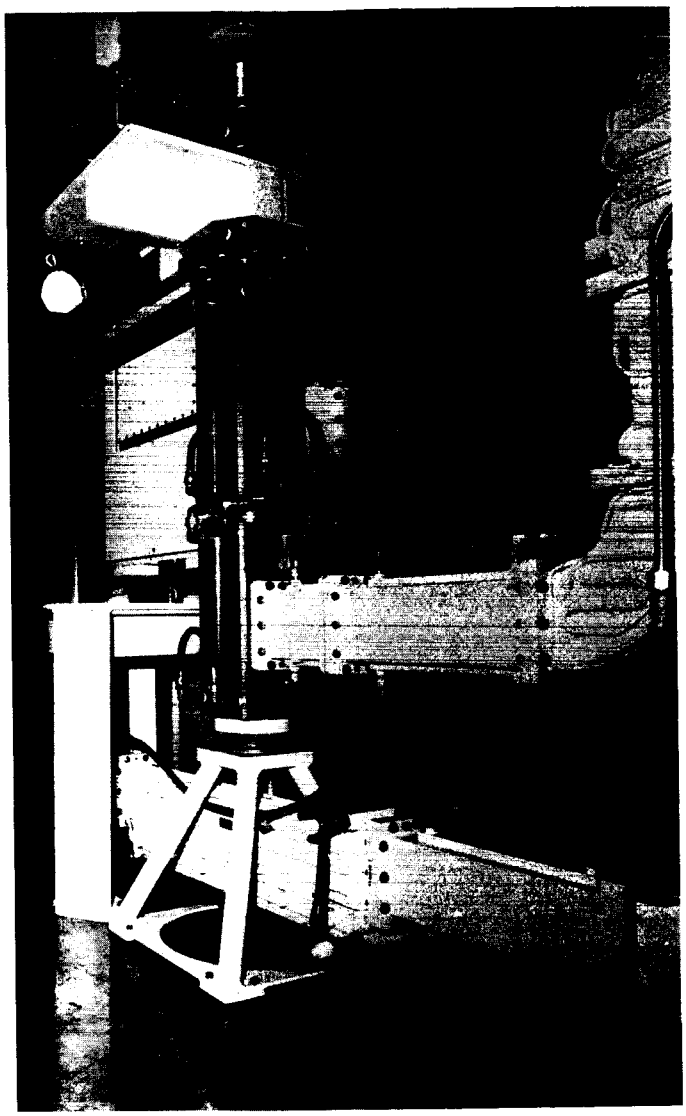

Fig. 5. PDS feedcone interior

The PDS cone construction and initial system measurements were accomplished at JPL on the roof of Building 238. Figure 6 shows the system being readied for shipment to Goldstone.

## V. Evaluation

Installation of the PDS cone was made on September 15, 1970. Since that time, the cone has been successfully operated with 200 kW at 2115 MHz, 400 kW at 2388 MHz, and the polarization tracker has been routinely used with the *Pioneer* spacecraft.

Preliminary test results indicate the PDS cone can fulfill the flexible DSN front-end requirements in the S-band range for the near future.

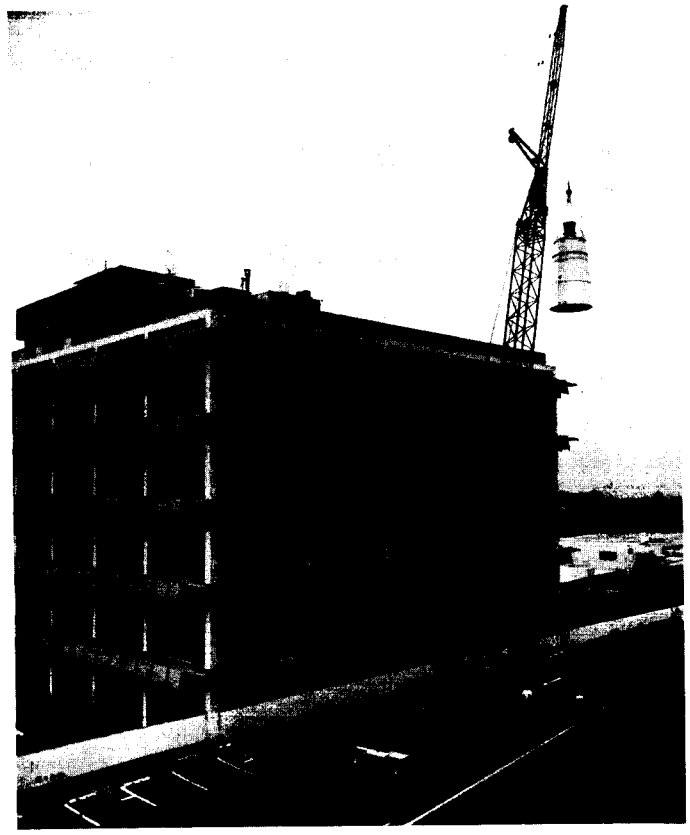

Fig. 6. PDS feedcone shipment

## References


1. Cormack, R. E., "R&D Listening Cone for AAS," in *Supporting Research and Advanced Development*, Space Programs Summary 37-35, Vol. IV, pp. 268–270. Jet Propulsion Laboratory, Pasadena, Calif., Oct. 31, 1965.

2. Levy, G. S., Stelzried, C. T., and Seidel, B., *"Pioneer VI* Faraday Rotation Solar Occultation Experiment," in *The Deep Space Network*, Space Programs Summary 37-53, Vol. II, pp. 69–71. Jet Propulsion Laboratory, Pasadena, Calif., Sep. 30, 1968.

3. Stelzried, C. T., Otoshi, T. Y., and Wallace, K. B., "JPL System Checkout of S-Band Multifrequency Cone (SMF SN1 Mod 1)," in *The Deep Space Network*, Space Programs Summary 37-54, Vol. II, pp. 48–55. Jet Propulsion Laboratory, Pasadena, Calif., Nov. 30, 1968.

4. Brunstein, S. A., "A New Wideband Feed Horn with Equal E- and H-Plane Beamwidths and Suppressed Sidelobes," in *The Deep Space Network*, Space Programs Summary 37-58, Vol. II, pp. 61–64. Jet Propulsion Laboratory, Pasadena, Calif., Jul. 31, 1969.

5. Neff, D. E., and McCrea, F. E., "S-Band Cassegrain Ultra Cone Modification," in *The Deep Space Network*, Space Programs Summary 37-58, Vol. II, pp. 59–61. Jet Propulsion Laboratory, Pasadena, Calif., Jul. 31, 1969.

6. McCrea, F. E., Reilly, H. F., Jr., and Neff, D. E., "High-Power Feed Component Development," in *The Deep Space Network*, Space Programs Summary 37-66, Vol. II, pp. 64–69. Jet Propulsion Laboratory, Pasadena, Calif., Nov. 30, 1970.

7. Cormack, R. E., "Improved S-Band Waveguide Switch Measurements," in *The Deep Space Network*, Space Programs Summary 37-58, Vol. II, pp. 64–65. Jet Propulsion Laboratory, Pasadena, Calif., Jul. 31, 1969.

# Frequency Generation and Control: Atomic Hydrogen Maser Frequency Standard

C. Finnie

Communications Elements Research Section

*System considerations are described for a prototype hydrogen maser cavity tuner for use with the atomic hydrogen maser frequency standard developed at the Jet Propulsion Laboratory.*

The long-term frequency stability of a hydrogen maser oscillator is determined by the stability of the microwave cavity resonant frequency. Temperature controller drifts, mechanical shocks, and relaxation cause cavity frequency displacements which must be periodically corrected. To maintain long-term maser frequency stabilities of $10^{-14}$, the frequency of the 1420-MHz maser RF cavity must be maintained within 0.5 Hz. If a periodic cavity retuning scheme were not employed, a $10^{-14}$ maser stability requirement would dictate that cavity dimensions must be maintained within $10^{-10}$ and cavity temperature must be controlled within 0.003°C. In the long term (days), these tolerances on dimensional and thermal stability are not practical. Therefore, an automatic cavity tuner has been developed which removes long-term drift.

The quantitative effect of cavity pulling of the maser output frequency is given by (Ref. 1)

$$f_n - f_o \approx (f_n - f_c)\frac{Q_c}{Q_l}$$

where

$f_n$ = the atomic hydrogen transition frequency ($\approx 1.420 \times 10^9$ Hz)

$f_o$ = the maser oscillation frequency

$f_c$ = the cavity resonance frequency

$Q_c$ = the cavity frequency divided by its bandwidth ($\approx 45{,}000$)

$Q_l$ = the atomic hydrogen transition frequency divided by its line width ($\approx 1.4 \times 10^9$)

Therefore, the maser output frequency is pulled by the cavity resonance frequency by the ratio of $Q_c/Q_l$ ($3 \times 10^{-5}$). The most acceptable maser cavity tuning method (Ref. 2), and the one used at JPL, is to increment the transition line width and adjust the cavity frequency $f_c$ such that this increment in line width does not change the output frequency.

Manual cavity tuning is accomplished by plotting the oscillation frequency as a function of transition line width for large cavity frequency offsets and extrapolating to the tuning point which is insensitive to transition line width variations. Manual tuning has these disadvantages:

(1) Is time consuming (several hours).

(2) Requires a fair degree of operator skill.

(3) Requires two hydrogen masers for practical tuning times.

(4) Does not remove the spin-spin interaction frequency shift (Ref. 3).

(5) Requires surveillance of tuning accuracy.

(6) Requires system down time for cavity tuning.

The design of an automatic maser cavity tuner obviously must meet operational constraints of the frequency and timing system. The author has considered the following modes:

(1) *Two* masers at each antenna site, for redundancy and rapid tuner response times. The role of each maser will be separated into a long-term and short-term standard. The long-term standard will be controlled by the automatic tuning servo and will have a degradation in short-term stability to achieve high-gain, short response time cavity tuning. The second maser will be maintained at a constant offset from the first; it will not be tuned and its adjustable physical parameters will be set to optimize short-term stability.

(2) *One* maser at each site. The automatic tuner would use an auxiliary tuning reference such as the site rubidium standard. This allows the maser to be an independent standard with a degradation in tuning accuracy and tuner response time (several days). Automatic tuning would have to be performed at non-critical use times, since tuner modulation would degrade short-term stability substantially more than for the case of two masers at each site.

The hydrogen maser frequency stability is independent of the measurement time for times greater than approximately 100 s and less than the time dictated by the cavity frequency stability. For measurement periods less than 100 s, receiver noise degrades the maser frequency stability.

Signal-to-noise ratio restrictions require tuning integration times of several days, where a reference source other than a second hydrogen maser is used. As previously noted, delay of 100 s is required to make an accurate output frequency determination. These two factors necessitate the "ideal" integrator of a characteristic digital servo design. A block diagram of the tuning servo system presently in use on the research masers at the Goldstone DSCC is shown in Fig. 1. The maser tuner modulates the hydrogen transition line width by limiting the dissociator power and, therefore, the supply of hydrogen atoms to the oscillator. This increases the life time of excited atoms within the storage bulb, and decreases the transition line width. The cavity is tuned by a varactor connected through a directional coupler to the cavity coupling loop. The period of the beat frequency between the hydrogen maser and a frequency reference is measured to determine incremental frequency change produced by a flux change.

Figure 2 shows the timing sequence of the tuner operation. The upper sinusoid is the beat between the reference oscillator and the maser of an approximately 100-s period. The counter up-counts an internal clock for the first beat

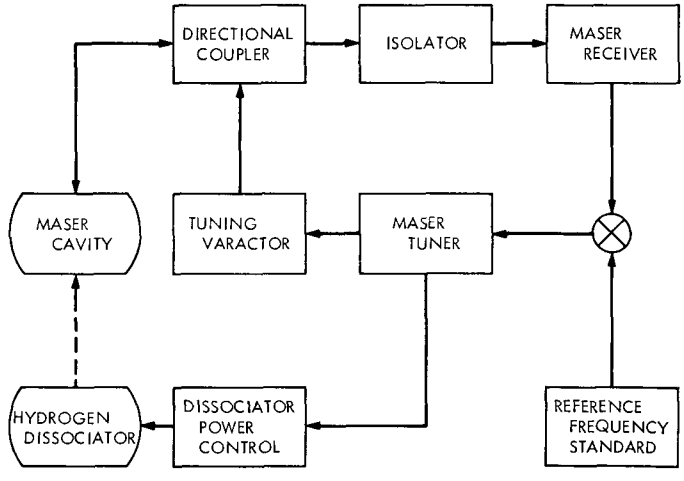


**Fig. 1. Maser tuner system block diagram**

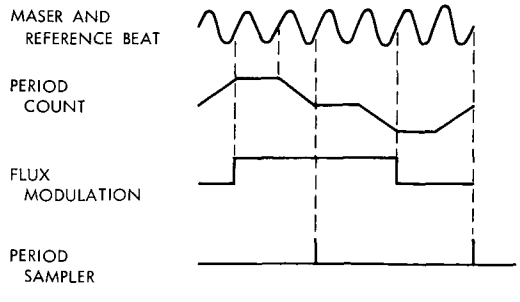


**Fig. 2. Tuner operation sequence**

period. The flux is increased and the counter down-counts for one period after a one-period delay to allow the physical system of the dissociator to reach equilibrium at the new flux level. At the end of the down count, the residual in the counter is transferred to a buffer supplying a digital-to-analog converter. The tuning varactor voltage is taken from the digital-to-analog converter. The next count cycle is reversed, the high-flux down count is taken first and the low-flux up count is second. The latter averages any linear drift term longer than 800 s in the reference oscillator.

## References


1. Gordon, J. P., Zeiger, H. J., and Townes, C. H., "The Maser—New Type of Microwave Amplifier, Frequency Standard, and Spectrometer," *Phys. Rev.*, Vol. 99, pp. 1264–1274, 1955.
2. Risley, A. S., and Halford, D., *Feasibility of Two Cavity Tuning Servo Methods for the Atomic Hydrogen Maser*, Technical Report prepared for JPL. National Bureau of Standards, Boulder, Colo., Aug. 11, 1969.
3. Hellwig, H., *Hydrogen Spin Exchange Frequency Shifts*, Technical Report 387. National Bureau of Standards, Boulder, Colo., Mar. 1970.

# Antenna Structures: Evaluation of Reflector Surface Distortions

M. S. Katow
DSIF Engineering Section

*The reflector surface distortions of the 210-ft antenna as evaluated by the linearized formulation of the RMS paraboloid best-fitting computer program has provided sufficient significant digits in its answers for meaningful results. This article presents a clearer documentation as well as the error bounds of the formulation. Since basically the solution is a non-linear problem, improved formulation would be desirable. However, the program should be useful for evaluating larger than 210-ft antennas with about the same degree of distortion.*

## I. Introduction

Reflector surface distortions of antennas and their effects on the RF performance may be evaluated by best fitting to the distortions, in a least-squares pathlength sense, a paraboloid. The resulting value

$$\text{rms} = \sqrt{\frac{\Sigma\,(\Delta PL_j)^2\,A_i}{\Sigma\,A_i}}$$

is applicable in Ruze equation for computing the RF gain.

A computer program for this purpose was described earlier (Refs. 1 and 2). Results of its use with analytically computed distortions and with field measurements of the 210-ft antenna in calculating its RF performance have been reported (Refs. 3 and 4). Comparisons to RF performance measurements were made by Bathker (Ref. 5).

With the use of positional data of the best-fit paraboloid and the deflected positions of the RF feeds, the RF boresight directions may be calculated (Ref. 6).

To date, the best fitting of the analytical 210-ft antenna data using the linearized solution formulation has provided sufficient significant digits for meaningful results. Comparisons between analytical solutions and RF field tests have shown close correlations.

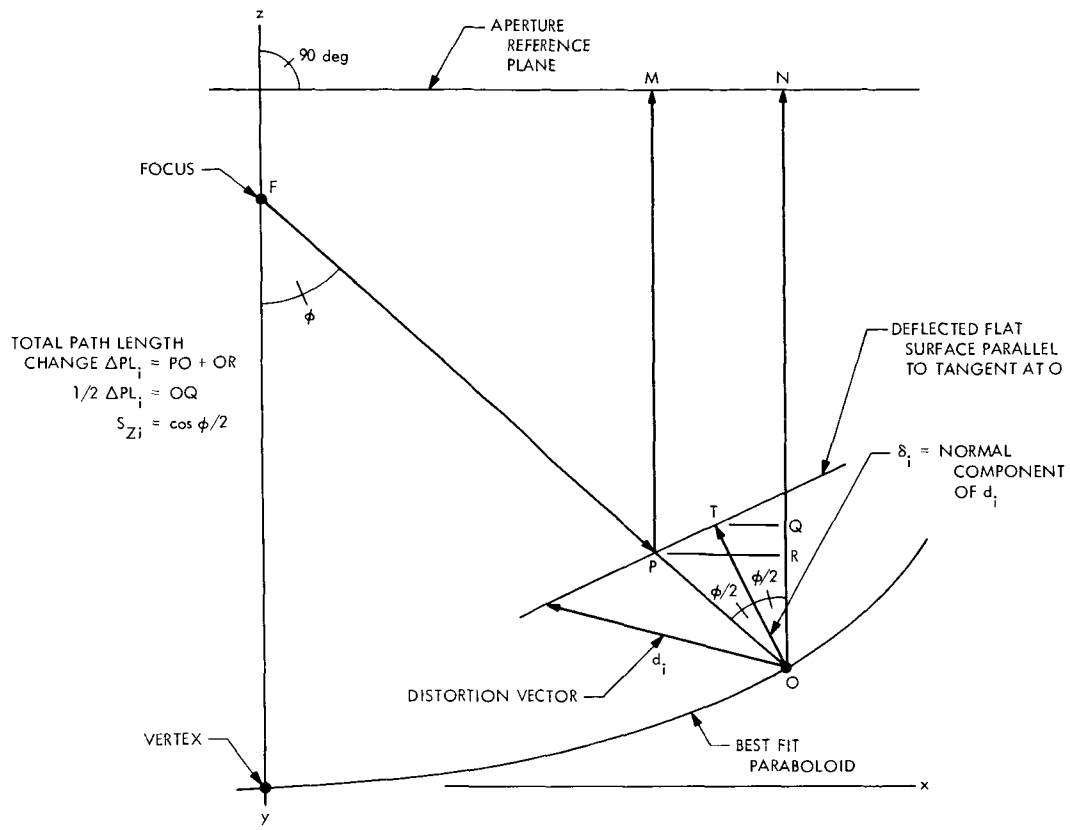


**Fig. 1. RF path-length change**

This article presents the results of studies made to determine the accuracy bounds of the best-fitting program and to present a clearer description of the formulation.

The documentation is presented as follows:

(1) The modifications, as well as the complete formulations, are graphically and algebraically delineated.

(2) Data manipulations to improve the accuracy of field measurements using the angle-measuring theodolite method will be described in a following article. The method combines the direction vectors from the analytical analysis with the direction lacking field measurements.

(3) The output has been converted to show SI (metric) units in addition to English units values.

## II. Formulation Modifications

From Refs. 1 and 2 the ½-path-length change or error may be denoted by

$$\Delta PL_i = -\delta_i \cdot \delta_{zi} \qquad (1)$$

Fig. 1 shows the graphical definition of the equation. The basic assumption is made that the deflected surface is flat and has moved parallel to the tangent at the node O.

The error due to this assumption is illustrated in Fig. 2. A sample calculation using a point on the outer edge of the 210-ft dish results in a negligible error. For

$$\frac{\phi}{2} = 15 \text{ deg}$$

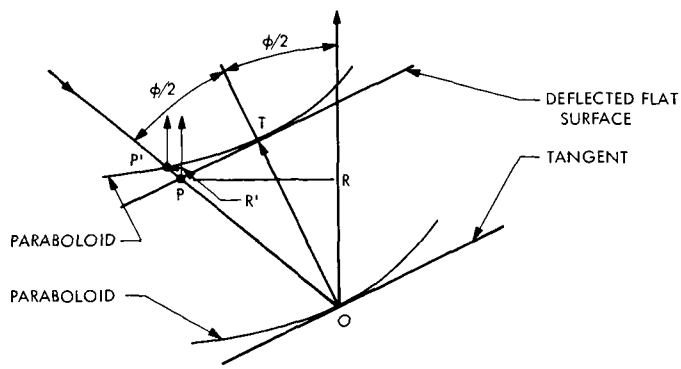


**Fig. 2. Assumption error**

and assuming a normal error (OT of Fig. 2) = 1.0 in., and an approximate radius of curvature = 2000 in., the path-length error ($P'P + PR'$) = 0.00004 in.

The total normal distortion at a node on the surface of a reflector from the best-fit paraboloid is the sum of four types of normal errors:

$$S_i = S_{ia} + S_{ib} + S_{ic} + S_{id} \tag{2}$$

The first,

$S_{ia}$ = surface distortions normal error

$$= n_i Sx_i + v_i Sy_i + w_i Sz_i \tag{3}$$

The second,

$S_{ib}$ = normal error due to change in focal length from the original paraboloid

$$= -K(x_i^2 + y_i^2) S_{zi} \tag{4}$$

where

$$K = \frac{1}{4}\left(\frac{1}{F} - \frac{1}{F_n}\right)$$

$F$ = focal length of original paraboloid

$F_N$ = focal length of best fit paraboloid

Equation (4) is derived from the equation of the paraboloid

$$z_i = \frac{x_i^2 + y_i^2}{4F} \tag{5}$$

The change in $z$ from a change in $F$ results in

$$\Delta z_i = \frac{x_i^2 + y_i^2}{4}\left(\frac{1}{F} - \frac{1}{F_N}\right)$$

which is equivalent to

$$\Delta z_i = \frac{x_i^2 + y_i^2}{4F}\left(1 - \frac{F}{F_N}\right) \tag{6}$$

substituting Eqs. (5) into (6) and defining

$$K^1 = \left(1 - \frac{F}{F_N}\right)$$

yields

$$S_{ib} = -K^1 z_i s_{zi} \text{ (Fig. 3)} \tag{7}$$

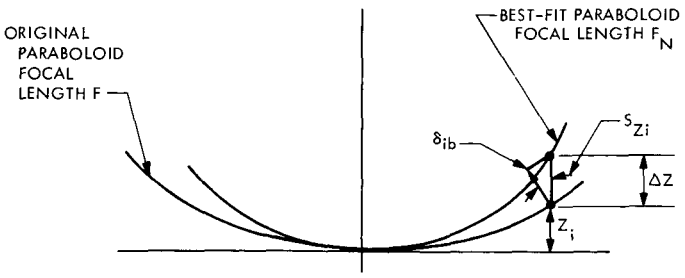


**Fig. 3. Normal error from focal length change**

Equation (7) is equivalent to Eq. (4) and is used in the coding of the program.

The third,

$S_{ic}$ = normal error due to rigid body translations of the paraboloid

$$= -U_0 S_{zi} - V_0 S_{yi} - W_0 S_{zi} \tag{8}$$

The fourth,

$S_{id}$ = normal error due to rigid body rotations of the best-fit paraboloid

$$= (z_i S_{yi} - y_i S_{zi}) + \beta (x_i S_{zi} - z_i S_{xi}) \tag{9}$$

The normal error due to positive (right-hand rule) rotation about the $Y$ axis is graphically defined in Fig. 4.

From Fig. 4, the normal error due to rigid body rotation is

$$-\delta = -\beta x_i S_{zi} + \beta z_i S_{xi}$$

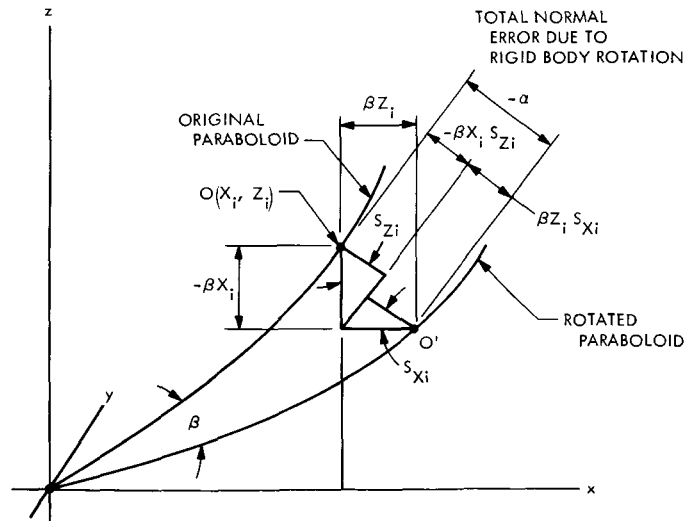


**Fig. 4. Normal error due to rotation about y axis**

which transposes to

$$\delta = \beta\,(x_i S_{zi} - z_i S_{xi})$$

The linear type of calculations for offsets due to rotation is defined in Ref. 2 and, as stated therein, rotations are limited to small angles.

In summing, the ½-path-length change

$$\begin{aligned}\Delta PL_i = [&u_i S_{xi} + v_i S_{zi} + w_i S_{zi} - K^1 z_i S_{zi} - U_0 S_{xi} \\ &- V_0 S_{yi} - W_0 S_{zi} + \alpha\,(z_i S_{yi} - y_i S_{zi}) \\ &+ \beta\,(x_i S_{zi} - z_i S_{xi})]\, S_{zi} \qquad (10)\end{aligned}$$

Equation (10) is equivalent to the corrected Eq. (8) of Ref. 1, with the exception that $\Delta PL$ now is referenced to ½-path-length change, and as shown in the reference, the best-fit paraboloid is found by minimizing $R$, the sum of the squares of the residuals (i.e., path-length change) where

$$R = \Sigma_i\,(\Delta PL_i)^2\, A_i$$

and where $A_i$ is a weighting factor (usually the area of the surface panel associated with the measured point when a uniform RF illumination density is assumed).

The minimization and the best-fit data of the new paraboloid then result from a solution of a set of six linear normal equations derived from setting the partials of $R$ with respect to the six parameters of motions equal to zero.

A new double-precision subroutine identified in the JPL Fortran V Subroutine Library as DVANAS3—Singular Value Analysis of a Linear Least Squares Problem (Ref. 7) replaces the MATINV subroutine used for the solution of the resulting matrix equation $Ax = b$, where

$$A = \Sigma\, A_i S_{zi}\,\{D\}\,\{D\}^T, \qquad x = C, \qquad b = \Sigma\, A_i S_{zi}^2 y_i\,\{D\}$$

$$D = \begin{Bmatrix} S_{xi} \\ S_{yi} \\ S_{zi} \\ S_{zi}\,(x_i^2 + y_i^2) \\ (S_{yi} y_i - S_{zi} z_i) \\ (S_{xi} z_i - S_{yi} x_i) \end{Bmatrix} \qquad C = \begin{Bmatrix} U_0 \\ V_0 \\ W_0 \\ K \\ \alpha \\ \beta \end{Bmatrix}$$

$$y_i = S_{xi} m_i + S_{zi} v_i + S_{yi} w_i$$

The DVANA3 subroutine computes and prints a sequence of candidate solutions with their singular values, the sum of the squares of the residuals, and other quantities useful in analyzing a least squares problem.

Preliminary evaluation, based on these quantities, indicates that the matrix is well conditioned for accurate answers of $W_0$ ($z$ offset), $K$ (focal length), $\alpha$ (rotation about $x$ axis) and $\beta$ (rotation about $y$ axis).

It follows that the RMS value is accurately determined. However, the $U_0$ ($x$ offset) and $V_0$ ($y$ offset) answers results from large ratios of singular values, and this requires precise input deflection values ($u_i, v_i, w_i$) in order for $U_0$ and $V_0$ answers to be meaningful. The present interpretation is that the analytically computed deflections provide useful $U_0$ and $V_0$ answers for determining the RF boresight directions and the existing Theodolite-type field measurements produce marginal answers.

Test problems were formulated to determine the linearized formulation error which occurs only for rotations $\alpha$ and $\beta$. For the 210-ft case, where the rotation about the $x$ axis ($\alpha$) was less than 0.003 rad, the rms error was 0.001 in. and $V_0$ displaced 0.004 in. For only translations and focal length changes, the formulation is exact.

**Definition of terms**

| | |
|---|---|
| $u_i, v_i, w_i = x, y, z$ | Components of the distortion vector of point or node $i$ from the original paraboloid |
| $S_{xi}, S_{yi}, S_{zi} = x, y, z$ | Direction cosines of the normal to the original paraboloid |
| $S_{xj}, S_{yj}, S_{zj} = x, y, z$ | Direction cosines of the normal to the best-fit paraboloid. |
| $U_0, V_0, W_0$ | Rigid body translations or vertex offsets of the best-fit paraboloid |

$S_i$ = normal component of the distortion vector of point $i$.

$\Delta PL_i$ = ½-path-length change at point $i$.

$A_i$ = RF weighting function of point $i$.

## References


1. Katow, S. M., and Schmele, L. W., "Antenna Structures: Evaluation Techniques of Reflector Distortions," in *Supporting Research and Advanced Development,* Space Programs Summary 37-40, Vol. IV, p. 176. Jet Propulsion Laboratory, Pasadena, Calif., August 31, 1966.

2. Utku, S., and Barondess, S. M., *Computation of Weighted Root-Mean-Square of Path Length Changes Caused by the Deformations and Imperfections of Rotational Paraboloidal Antennas,* Technical Memorandum 33-118, Jet Propulsion Laboratory, Pasadena, Calif., March 1963.

3. Bathker, D. A., "Efficient Antenna Systems: X-Band Gain Measurements, 210-ft Antenna System," in *The Deep Space Network,* Space Programs Summary 37-52, Vol. II, pp. 78–86. Jet Propulsion Laboratory, Pasadena, Calif., July 31, 1968.

4. Katow, M. S., "Techniques used to Evaluate the Performance of the NASA/JPL 210-ft Reflector Structure under Environmental Loads," in *Structures Technology for Large Radio and Radar Telescope Systems.* Edited by J. W. Mar and H. Liebowitz, The M.I.T. Press, Cambridge, Mass., 1969.

5. Bathker, D. A., *Radio Frequency Performance of a 210-ft Ground Antenna: X-Band,* Technical Report 32-1417, Jet Propulsion Laboratory, Pasadena, Calif., Dec. 15, 1969.

6. Katow, M. S., "210-ft Antenna Quadripod Structural Analysis, II," in *The Deep Space Network,*" Space Programs Summary 37-53, Vol. II, pp. 73–76. Jet Propulsion Laboratory, Pasadena, Calif., Sept. 30, 1968.

7. Forsythe, G., and Moler, C. B., *Computer Solution of Linear Algebraic Systems,* Prentice-Hall, Inc., Englewood Cliffs, N.J., 1967.

# Antenna Rigging Angle Optimization Within Structural Member Size Design Optimization

*R. Levy*
*DSIF Engineering Section*

*It is shown that the horizon rms deviation of the antenna from the best-fitting paraboloid is a representative measure of the cosine-weighted average rms for the complete elevation attitude range. Therefore, the horizon rms can be used as a substitute merit function in a structural redesign program that generates improved member size distributions to reduce the weighted-average rms. Validity of the substitution follows because: (1) the optimal rigging angle is a slowly changing function of changes in member size distributions; (2) the weighted average rms is not sensitive to small rigging angle changes; (3) at rigging angles near the optimal, ranking according to the minimum horizon rms is equivalent to ranking according to the minimum cosine-weighted average for alternative designs with different member size distributions.*

## I. Introduction

An appropriate choice of the antenna rigging angle, which is the elevation attitude of the antenna used in the field for setting the surface panels to the ideal paraboloid, provides a simple way to improve antenna gain by reducing the gravity contribution to the rms distortion of the surface. In accordance with convention, the distortion is considered with respect to the best-fitting paraboloid. The mathematical relationships entailed in rigging angle selection and illustrations of the effectiveness for the alternative objectives of either reducing the maximum rms distortion at the most unfavorable elevation attitude, or

minimizing the average weighted rms distortion over the entire elevation range have been given previously (Ref. 1). For the first objective, it was found that the maximum rms distortion was minimized by choosing a rigging angle to make the rms at the horizon attitude equal to the rms at the zenith attitude. For the second objective, the weighting function was equal to the cosine of the elevation angle attitude. Cosine weighting minimizes the mathematical expectation of rms distortion when the antenna follows targets that are uniformly distributed within the observation space.

## II. Incorporation of Rigging Angle Optimization Within Member Size Optimization Procedure

The present discussion describes additional numerical examples and parameter studies. The studies were performed to explore how the advantages of rms reduction via the choice of rigging angle can most simply be incorporated within a structural-optimization design procedure that seeks to reduce rms via the choice of member properties. The optimization design procedure currently being developed (Ref. 2) operates iteratively through successive stages by generating improved vectors of member property distributions that reduce the rms found for the size distribution vector that existed at the start of the stage. RMS for reduction in the present context is taken to be the average cosine-weighted rms for a 90-deg elevation attitude range. Since the structural deformations at every elevation attitude depend upon the changes in gravity loading and these depend upon the rigging angle, the following considerations are entailed in each stage:

(1) Computation of the starting rms requires the rigging angle of the structure with the current distribution of member properties. This implies a parameter study to determine the optimum rigging angle at the start of each stage.

(2) To generate the vectors of improved member properties, it is impractical to perform sequences of parameter studies to find the optimum rigging angles associated with all the alternative member size distributions. Therefore, it is preferable to have a single measure of performance that will serve as a valid guide in selecting the new sizes for each of the members.

The first consideration above does not entail a major computational difficulty, since the parameter study to determine the optimum rigging angle for a single structural design can be executed rapidly. Nevertheless, it would be useful to know whether or not there are significant changes in the rigging angle from the initial stage to subsequent redesign stages. Then if these changes are small, some computational advantage could be obtained by performing the parameter study only at the start of the procedure.

The simplest performance measure for the second consideration is the rms of some particular elevation attitude, e.g., the horizon (or nearest attitude to the horizon within the practical range), determined for the rigging angle that was optimal at the start of the stage. However, if this measure is to be used as an indicator of the weighted-average rms in judging the relative merits of alternative member property distributions, the following three assumptions are required to be true:

(1) *The optimal rigging angle is a slowly changing function of changes in member size distributions.* Therefore, the rigging angle at the end of each cycle (after a new distribution of member properties has been generated) will not differ significantly from the rigging angle at the beginning of the cycle.

(2) *The weighted-average rms distortion is not sensitive to small differences in rigging angle from the optimal.* Consequently, in conjunction with the first assumption, the weighted-average rms size computed for a new member property distribution will be reliable even though it is based upon the optimal rigging angle for the size distribution of the beginning of the cycle.

(3) *At the optimal or near optimal rigging angle, the ranking of alternative designs (different member-property distributions) according to the minimum horizon rms is the same as the ranking of these designs according to the minimum weighted-average rms.* Validity of this assumption permits the substitution of the horizon rms for the weighted-average rms as the merit function to be used in developing or evaluating improved member-property distributions.

The validity of the first assumption has been tested and confirmed by examining over 100 cases of alternative designs for the same antenna. The optimal rigging angle appears to be almost independent of the design. Furthermore, additional results tend to show that all antennas with the same focal length-to-diameter ratio ($f/D$) will have about the same optimal rigging angle with respect to an average, cosine-weighted rms. The angle is between

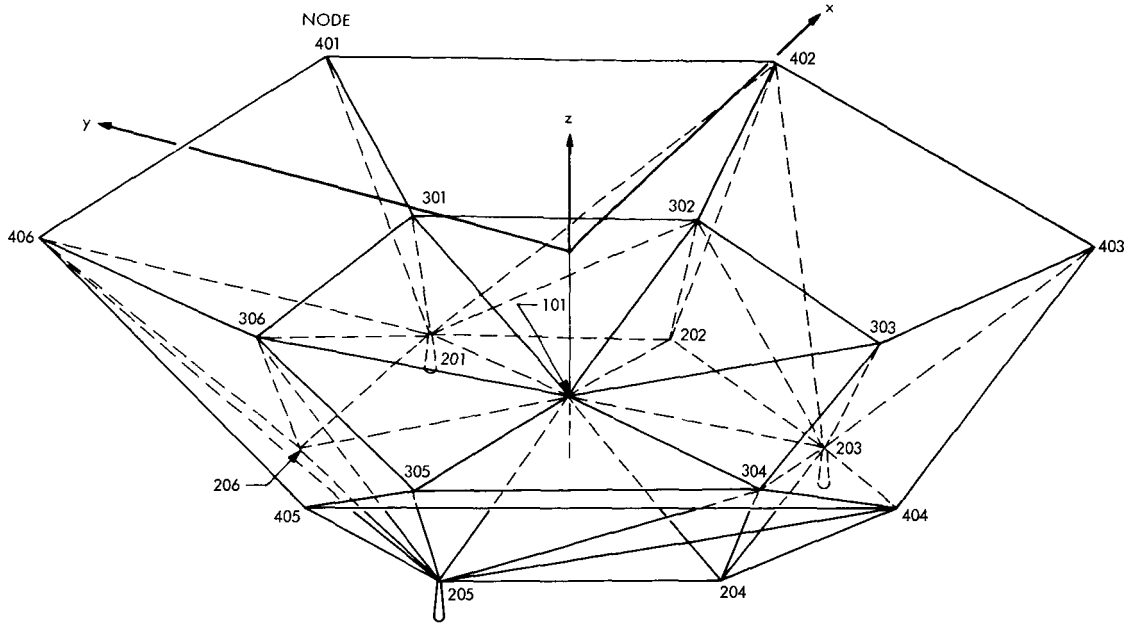


**Fig. 1. Model of baseline structure**

25 deg and 30 deg for an $f/D$ ratio equal to 0.424. The examples and data that follow will present data to show that the second and third assumptions also are true.

## III. Antenna Model

The hypothetical model reflector structure shown in Fig. 1 was used as the basis for the parameter studies. This is called the "baseline structure" and represents a simplified model of a practical reflector. It contains most of the essential features of typical reflector frameworks, notwithstanding that the surface and structure have been subdivided into a relatively coarse grid to expedite the computations. There are six identical ribs spaced at 60-deg increments, which are interconnected by the customary hoop and diagonal members. Three supports are shown at nodes 201, 203, and 205. The plane of the supports is taken to be capable of being rotated about the X-axis to vary the antenna elevation attitude. The Z-axis is the focal axis, and the Y–Z plane is a plane of symmetry. There are a total of 19 nodes, with three translational degrees of freedom permitted for each node. Therefore, excluding supports, there are 48 degrees of freedom in the model. Surface target nodes are 101, 301–306, 401–406, which provide 13 points for rms computation. There are six framing members of identical topology and similar structural function in each of ten different groups (five-rib member, three-hoop member, two-diagonal member), resulting in a total of 60 members.

## IV. Rigging Angle Studies

The initial rms analysis was made for a basic model in which all the framing members were assigned identical cross-sectional area properties. Subsequently, additional designs were generated by means of new property distributions in which the areas common to all six members within each of the ten groups were changed relative to the areas for the remaining nine groups.

Studies to find the optimal rigging angle with respect to the minimum cosine-weighted average rms were performed for each of 21 designs. These consisted of a basic design and 20 additional designs in which the member areas for each of the ten groups were relatively one-half and twice the areas for the remaining nine groups. The results were plotted to show the weighted average rms as a function of the rigging angle for each structure of the 21 cases. It was found that several curves for individual cases were quite similar so that only five distinct curves, which are shown in Fig. 2, were sufficient to represent all of these cases, each curve representing possibly more than one case.

Figure 3 shows the results of the rigging angle parameter studies that were based upon the analytical models of the 210-ft antenna and three additional 85-ft antenna models. These are considerably more complex in that

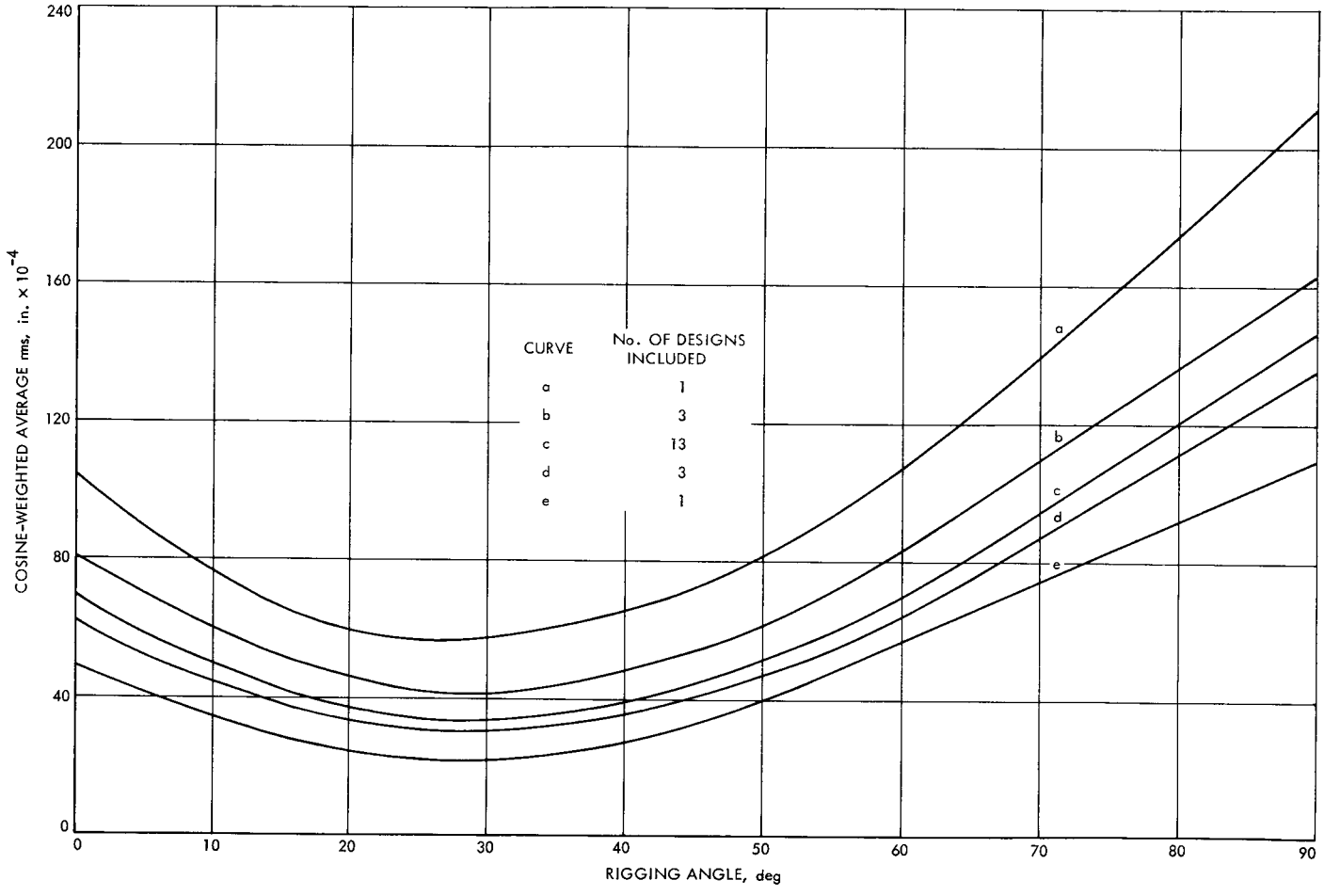


**Fig. 2. Weighted average rms versus rigging angle, baseline structure**

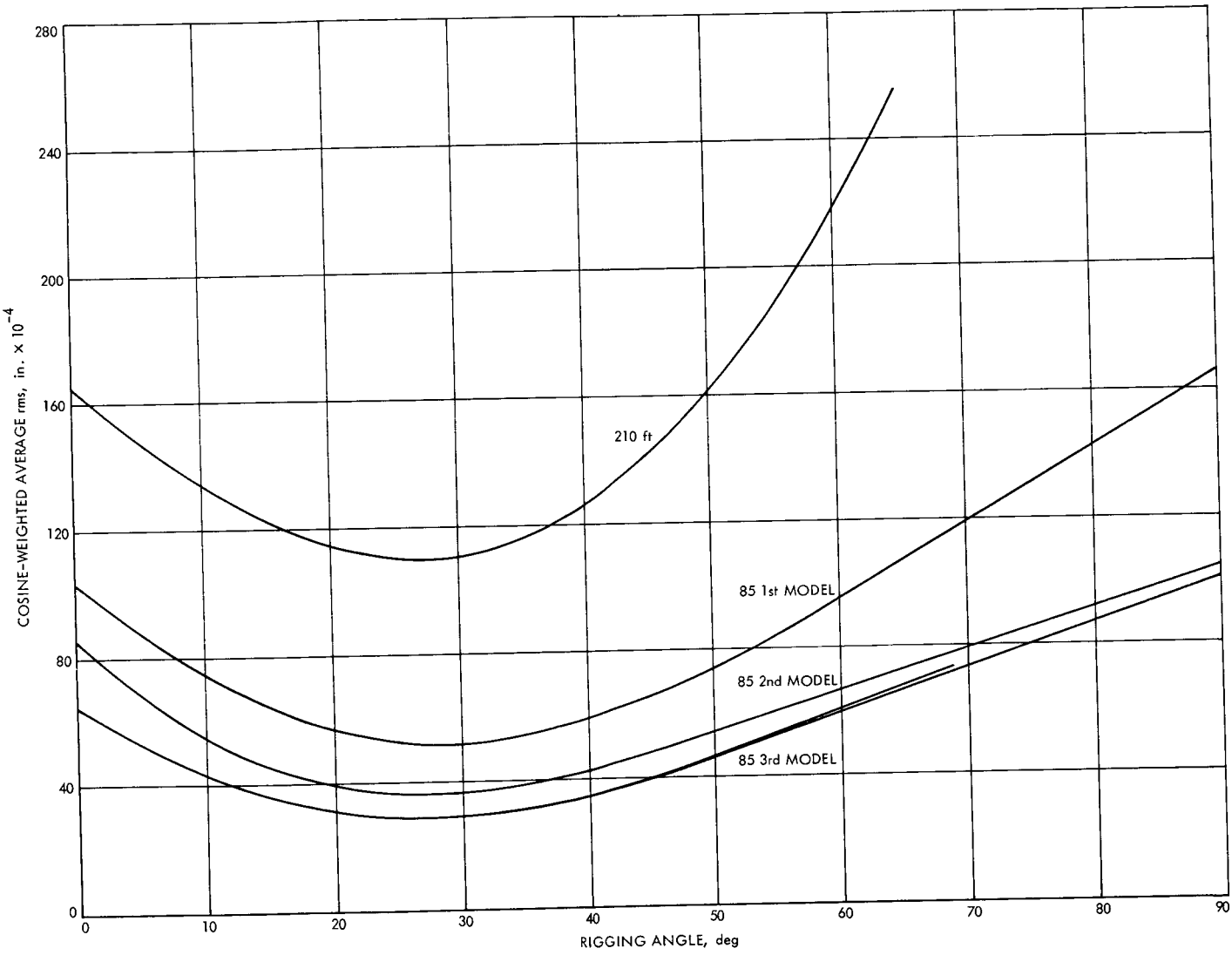


**Fig. 3. Weighted average rms versus rigging angle, 210- and 85-ft antennas**

much finer subdivisions were used in defining the structural grids for the framework idealization, each framework consisting of more than 1000 members and degrees of freedom, and over 100 surface target nodes. In all cases, it can be seen that the optimal rigging angle is always close to 30 deg and that the weighted average does not vary by more than a few percent for rigging angles between 25 and 35 deg. Therefore, these figures confirm the validity of the first two assumptions.

In Fig. 4 the cosine-weighted rms for the antenna rigged at 30 deg is plotted as a function of the elevation attitude for the 21 structural variations of the baseline structure. As in Fig. 2, similarity of some of the curves permitted grouping so that all cases could be represented by a relatively smaller number of curves. The figure shows that none of the curves cross each other. Therefore, it can be concluded that in comparing any two curves the one that has a relatively lower 0-deg (horizon attitude) rms value also has a relatively lower weighted rms value at all elevation attitudes, resulting in a relatively smaller area under the entire curve. Since the area under the curve is a measure of the weighted-average rms value, it follows that the horizon rms is also a measure of the weighted average. Therefore, this confirms the third assumption.

## V. Conclusion

It has been shown that with the optimal rigging angle, the horizon rms deviation of the antenna from the best-fitting paraboloid is a representative measure of the cosine-weighted average rms for the complete elevation attitude range. Therefore, the horizon rms can be used as a simplified substitute merit function in a structural redesign program that generates improved member size distributions to reduce the weighted-average rms. Validity of the substitution follows because: (1) the optimal rigging angle is a slowly changing function of changes in member size distributions; (2) the weighted-average rms is not sensitive to small rigging angle changes; and (3) at rigging angles near the optimal, ranking according to the minimum horizon rms is equivalent to ranking according to the minimum cosine-weighted average for alternative designs with different member size distributions.

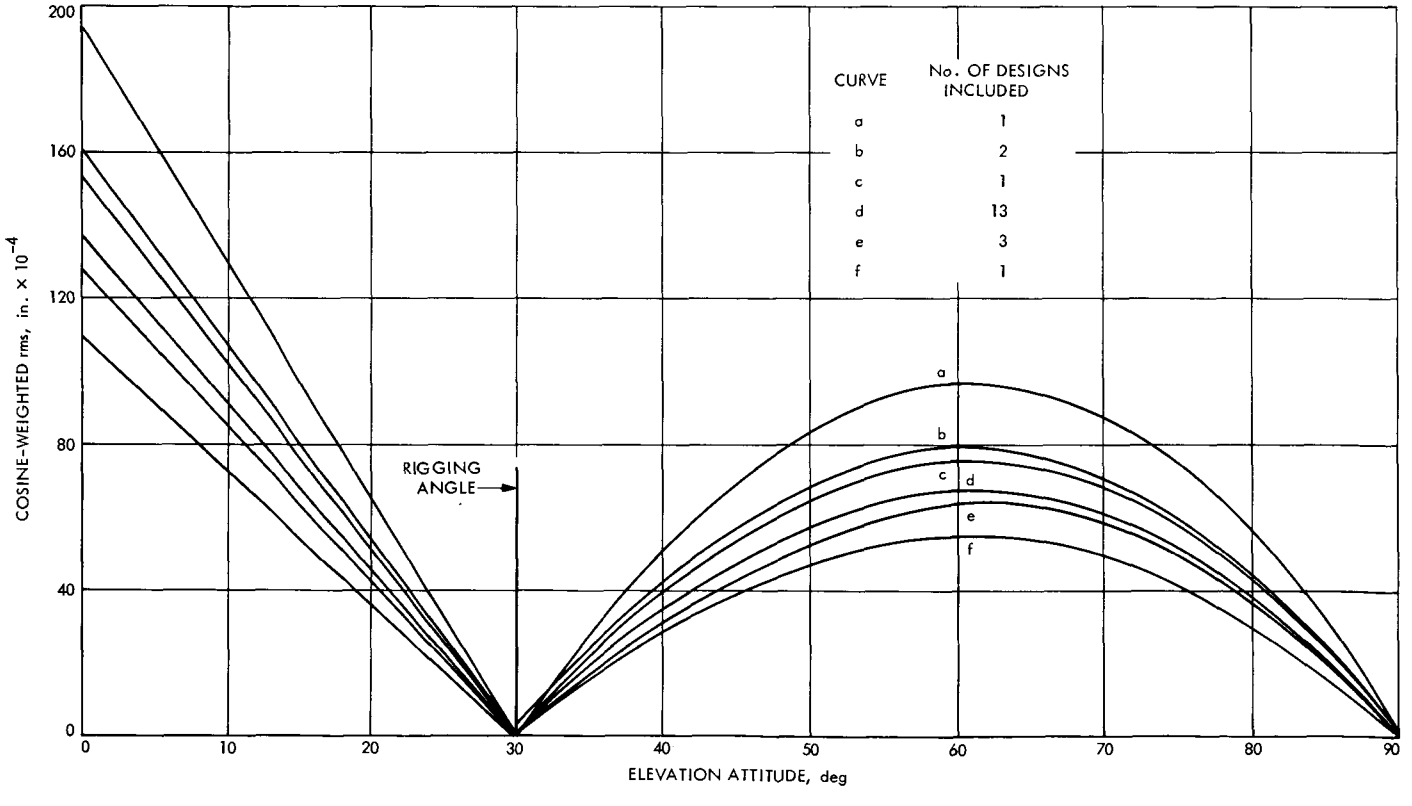


**Fig. 4. Weighted rms versus elevation attitude, baseline structure**

## References


1. Levy, R., "A Method for Selecting Antenna Rigging Angles to Improve Performance," in *The Deep Space Network*, Space Programs Summary 37-65, Vol. II, pp. 72–76. Jet Propulsion Laboratory, Pasadena, Calif., Sept. 30, 1970.
2. *Antenna Reflector Design Optimization*, Philco-Ford Corp., WDL Div., March 1970.

# Mark IIIA Simulation Center EMR 6050–Univac 1108 Computer Interface

C. F. Leahey
SFOF/GCF Development Section

*The Mark IIIA simulation center is capable of simultaneously simulating two spacecraft and three deep space stations using the Univac 1108 and EMR 6050 computers. The EMR 6050 and the Univac 1108 were interfaced using Bell System 303C modems and a JPL-designed interface adapter. The design of the interface was constrained by two factors: (1) the final location of the Univac 1108 was undetermined at the time of finalization of the interface assembly design, and (2) the EMR 6050 and the Univac 1108 have different word lengths. The hardware and software approaches used to satisfactorily mate the two computers are explained.*

## I. Introduction

The purpose of this article is to describe the development, capabilities, and operation of the EMR 6050–Univac 1108 interface. This equipment configuration is an assembly of the DSN simulation center (designated the Mark IIIA Simcen), which is located in the SFOF.

The interfacing of the EMR 6050 and the Univac 1108 computers is part of the current development activity that is taking place in the DSN Simcen in preparation for *Mariner* Mars 1971 and *Pioneer F* support. This activity is described in Ref. 1.

The Mark II Simcen configuration was capable of simulating one spacecraft and one DSS. The Simcen computer, the EMR 6050, had minimal spacecraft modeling capability—the bulk of the data being constructed of fixed data values and ramp functions.

The Mark IIIA configuration is capable of simultaneously simulating two separate spacecraft and three DSSs. The Univac 1108 contains command responsive spacecraft mathematical models, which dynamically change spacecraft commutator parameters. The EMR 6050 accesses model parameters from the Univac 1108 and provides

input/output processing, formatting, and control of displays.

The overall design of the interface between the EMR 6050 and the Univac 1108 was constrained by two major factors: (1) the uncertainty of the location of the Univac 1108, and (2) the different word lengths of the two computers. At the time of finalizing the design of the interface assembly, the location of the Univac 1108 was not finalized. To assure that the interface assembly would be compatible with the location of the Univac 1108, the interface was designed using Bell System 303C modems to provide the coupling between the interface assembly and the Univac 1108.

The different word lengths of the computers provided a constraining influence on the interface assembly design, since the data could not be exchanged on a word for word basis. The methods used to provide a satisfactory mating of the computers are described herein.

## II. Description

The general configuration of the EMR 6050–Univac 1108 interface is shown in Fig. 1. The interface assembly was designed and implemented at JPL. The Bell System 303C modems provide the coupling between the interface assembly and the 1108. The interface assembly is connected to the EMR 6050 through a buffered input/output channel. An interface assembly block diagram is shown in Fig. 2. The interface assembly consists of a 24-bit data register, two 8-bit shift registers (one input and one output register), parity generation and detection, failure detection, timing, and control logic.

### A. Word Formats

The word length is 24 bits in the 6050 computer and 36 bits in the 1108 computer. Since the computer word lengths are different and since the computers are coupled via modems, which are serial transmission devices, a parallel transfer of information on a word for word basis is not feasible. Instead, the information is processed in 6-bit bytes.

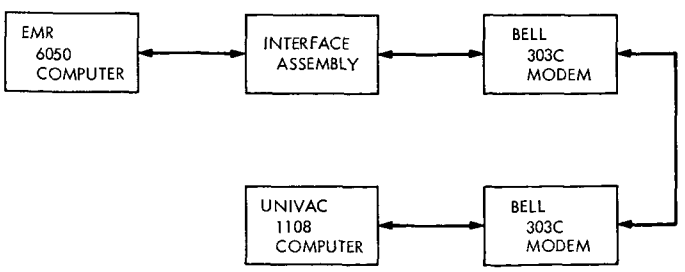


**Fig. 1. EMR 6050–Univac 1108 interface configuration**

### B. EMR 6050 to Univac 1108 Format

The 6050 word format in its standard form and processed for transmission to the 1108 is shown in Fig. 3. The 24 bits are divided into four 6-bit bytes. The interface assembly adds two additional bits to each 6-bit byte. The two bits are a control bit C and a parity bit P. A zero "0" in the control bit position signifies that the byte is a control byte, whereas a one "1" signifies that the byte is a data byte. The parity generator generates even parity for the 8-bit byte.

The words are then transmitted in this 8-bit format least significant bit of the least significant byte first, which results in an unpacked 1108 word.

### C. Univac 1108 to EMR 6050 Format

The words transmitted from the 1108 to the 6050 are transmitted in the same 8-bit format. The function and use of the control and parity bits are exactly the same.

The control and parity bits are stripped off of the word in the interface assembly, yielding a 6-bit byte. These 6-bit bytes are packed four to a 6050 word; therefore, $4n$ bytes of data must be sent to the 6050 from the 1108, since the 6050 requires a completely filled word.

### D. Control Bytes

Transmission of data between the two computers is activated by the START control bytes, and ended by the STOP control byte. The START control bytes consist of two sync codes ($26_8$, $26_8$) and the STOP control byte consists of one end-of-text (ETX) code ($03_8$). These control bytes are illustrated in Fig. 4 in the packed 6050 word format. These bytes are stripped off of the data messages in the interface assembly for messages going to the 6050. The communications terminal module in the 1108 performs the same function for messages going to the 1108.

### E. Error Detection

Five error conditions are detected and indicated by the interface assembly. These conditions are: (1) collision, (2) parity, (3) data set, (4) underflow, and (5) overflow. These error conditions cause an interrupt to be set in the computer. The response of the system to this interrupt is explained in *Subsection F.*

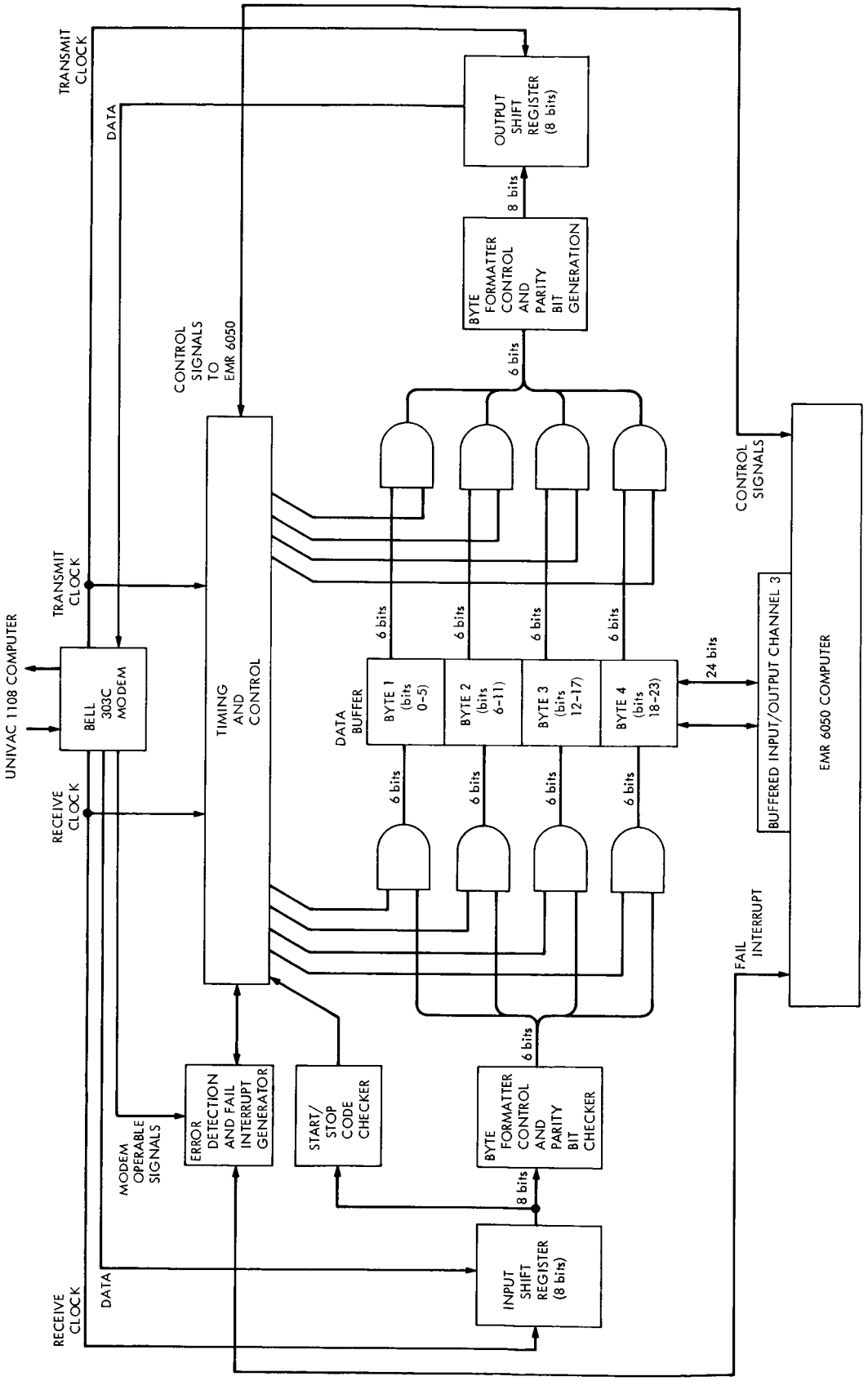


**Fig. 2. Interface assembly block diagram**

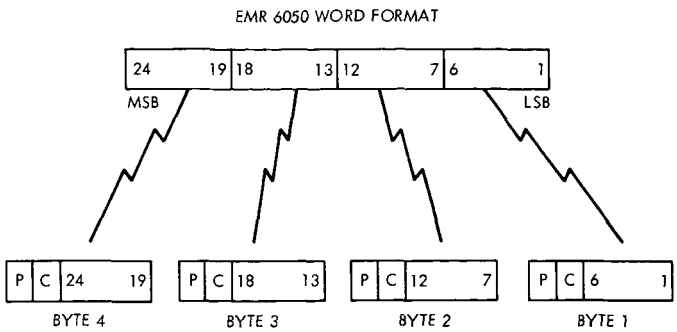


**Fig. 3. EMR 6050–Univac 1108 word format**

*1. Collision.* The collision error condition arises when an attempt is made to transmit data to the 6050 by the 1108 during the time that data is being transmitted to the 1108 by the 6050.

*2. Parity.* The parity error message arises when incorrect parity exists in the message received at the interface assembly from the 1108.

*3. Data set.* The data set error message arises when the 6050 attempts to transmit data to the 1108 at a time when:

(1) The DATA SET READY signal from the modem is false, indicating that the modem is in the test mode.

(2) The AGC (automatic gain control) LOCK signal from the modem is false, indicating noisy data transmission conditions.

(3) The modem fails to respond to a SEND REQUEST from the 6050 by not setting CLEAR TO SEND true.

*4. Underflow.* The underflow error message arises when the number of words transferred to the 6050 is less than the number expected, i.e., the number determined by the setting of the memory address and limit registers in the 6050 buffered channel.

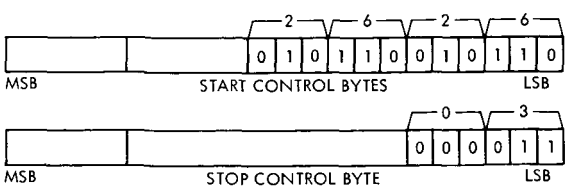


**Fig. 4. EMR 6050 START, STOP control bytes**

*5. Overflow.* The overflow error message arises when the number of words transferred to the 6050 is greater than the number expected.

### F. Trap or Normal Mode

The interface operates in either the trap or normal mode, the choice of which is determined by a switch on the front panel of the interface assembly. In the normal mode, if an error is detected, the error interrupt is initiated, and as soon as a response is received from the computer, the error flag and the interrupt are reset and the interface is ready for further operation. The cause of the interrupt cannot be determined.

In the trap mode, a detected error causes an interrupt which cannot be reset by the computer. The interface adapter will "hang up," i.e., respond "busy" on this interrupt condition until manually reset by the operator. In this mode, the error condition is stored and indicated on the front panel of the interface assembly. To restore the interface to operation, the mode control switch must be put in normal momentarily.

### G. Data Transfer

When a block of data has been completely transferred to the interface assembly or received from the interface assembly, an interrupt is activated in the 6050 to signify the completion of the operation.

### H. Communication Sequence

Due to the design of the executive software in the 1108 system, a definite sequence of events must occur when communicating with the 1108. This communication sequence consists of the following information blocks:

(A) "Request to Send" block (6050 → 1108)

(B) Data block (6050 → 1108)

(C) Data block(s) (1108 → 6050)

### I. Communication Rules

There must be at least 10 ms between block A and block B. There may be only one block B after an A block.

There may be many C blocks following an A, B sequence. There must be at least one C block before another A block can be sent. All data blocks sent in either direction must be separated by at least 1 ms.

### J. Block Formats

The block formats of blocks A, B, and C are illustrated in Fig. 5.

Although the 1108 precedes each C block with two sync codes ($26_8$, $26_8$) and follows each C block with one ETX code ($03_8$), the hardware will strip these characters off and only data will arrive at the 6050.

If the 1108 user tries to send more than 250 words, the data will be segmented by the 1108 system into 250-word blocks and more than one C block will be sent.

### K. Software Constraints

Due to the complexity of the 1108 software system, it had been decided that the 6050/1108 interface diagnostic routine would remain in the 1108 system at all times. The way the system is mechanized calls for the first word after the sync word in a B block to be interpreted by the 1108 as a control word to bring in various diagnostic routines in the 1108. This word, designated XYXYXYXY in the B block illustration, is used in the following configuration to control the diagnostic:

| | |
|---|---|
| 77777777 | Multiple-block diagnostic |
| 01010101 | Single-block diagnostic |
| 77770000 | Last diagnostic to be sent (causes job to dump in the 1108) |

If these control words are used, the 1108 automatically brings in the diagnostic system and returns the data block sent to the 6050.

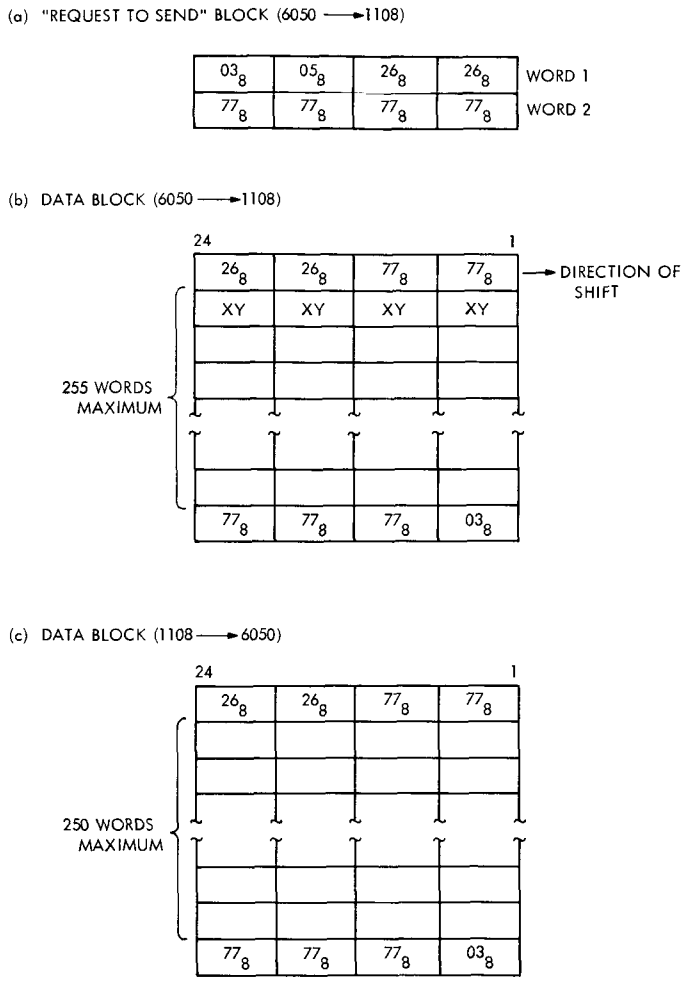


**Fig. 5. Data block formats**

## III. Summary

The need to interface one computer with another is becoming more commonplace in the data processing world of today. The constraining factors in this design—the uncertainty of the location of the Univac 1108 and the different word lengths of the two computers—are typical of the constraining factors which would be encountered in the interfacing of other types of computers. These factors were successfully integrated into the design for this system. The approach used here, if not the actual design, may be usable in the interfacing of other computer systems.

The successful completion of this project will further enable the DSN Mark IIIA simulation center to simultaneously simulate two spacecraft and three DSSs in support of *Mariner* Mars 1971 and *Pioneer F* missions.

## Reference


1. Polansky, R. G., "DSN Mark IIIA Simulation Center Development," in *The Deep Space Network*, Space Programs Summary 37-65, Vol. II, pp. 94–96. Jet Propulsion Laboratory, Pasadena, Calif., Sep. 30, 1970.

# Inbound High-Speed and Wideband Data Synchronizers

P. F. Peavler
SFOF/GCF Development Section

*The SFOF high-speed and wideband data synchronizers accept serial, blocked, digital data from the GCF. These synchronizers establish synchronization, detect and delete filler blocks, perform serial-to-parallel conversion, and output this data to two IBM 360/75 computers.*

## I. Introduction

The SFOF Mark IIIA computer configuration, as part of the DSN, includes inbound high-speed and wideband data capability. Outbound high-speed data conversion is described in Ref. 1. High-speed circuits will be used to handle tracking, telemetry, command, and monitor and operations control data. Wideband circuits will handle video information.

High-speed data is transmitted at a rate of 4800 bits/s; wideband data at 50,000 bits/s. High-speed and wideband data synchronizers are functionally identical except for speed of operation and input interface requirements.

## II. Functional Characteristics

The high-speed and wideband data synchronizers (Fig. 1) were developed to perform the following functions:

(1) Accept serial-blocked digital data and control signals.

(2) Synchronize the incoming data by utilizing a sync word imbedded in each data block.

(3) Convert the serial data into computer words.

(4) Present these words to two digital computers.

In addition to the four basic functions, the synchronizers also detect and delete filler blocks. These filler blocks are not transmitted to the computer to minimize processing overhead because their prime function is to keep ground communication equipment in lock when data are not present.

## III. Input

These synchronizers accept control and data signals at the terminator and receiver section. The terminators and receivers in the high-speed data synchronizers conform to Electronic Industries Association Standard RS-232-C. The wideband data unit conforms to characteristics outlined in JPL Service Specification LS 505391, Ground Communications Facility, Standard Wideband Data Interface.

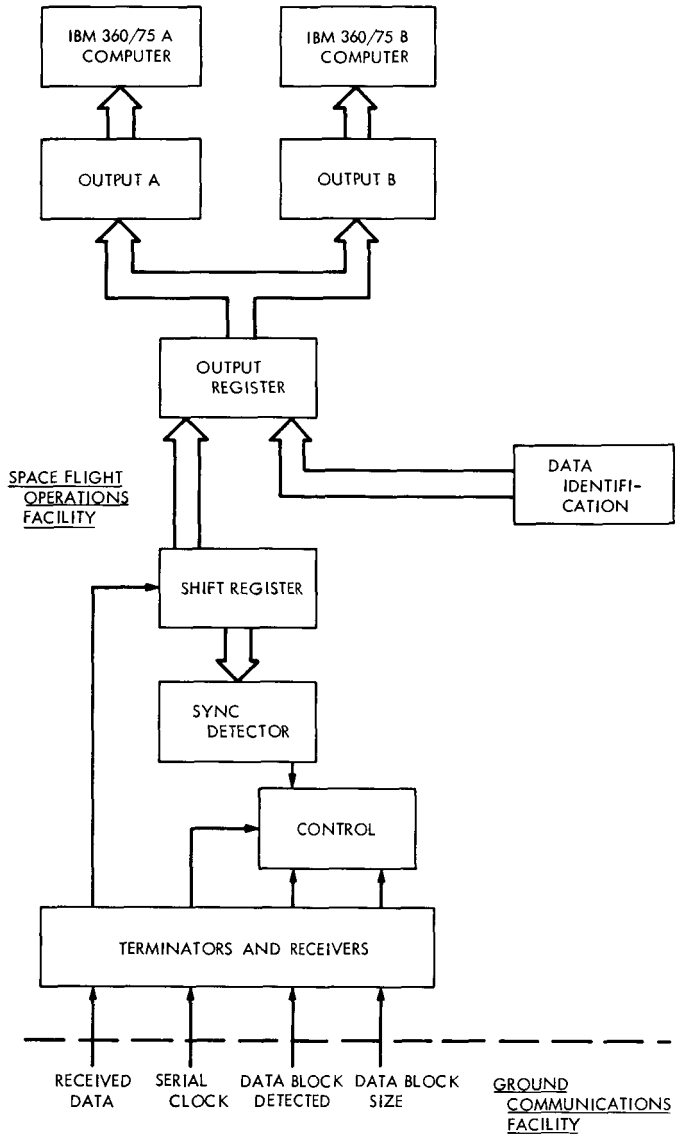


**Fig. 1. Synchronizer block diagram**

## IV. Synchronization

Synchronization, or framing of the data blocks, is attempted in two ways: (1) by examining the serial data moving through a shift register for the standard sync word of 24 bits, and (2) by monitoring a control circuit supplied by the GCF. Data to the computer will be tagged by the addition of an extra word to indicate how synchronization was accomplished. These two methods are employed to provide synchronization of data blocks during conditions when bit errors would not otherwise allow synchronization. The sync detector connected to the shift register can be preset to allow 0-, 1-, 2-, or 3-bit errors. These errors may occur in any position within the sync word.

## V. Conversion

Conversion of serial data to computer words is accomplished by use of a shift register of computer word length (32-bits) and an output register of the same size.

## VI. Output

Presentation to the computer employs a modified demand response technique. The data demand indicates to the computer that a data word is ready for transfer. The technique is modified in the case of the computer response. This is done because the output is presented to two computers simultaneously.

The presentation to the computer includes a data identification word transferred after the last word of the block. This word identifies the synchronizer, the data circuit to which the synchronizer is connected, the number of bit errors allowed in the sync word by the sync detector, and the method of synchronization by which the block was framed.

## VII. Conclusion

This equipment, as part of the SFOF, enables inbound communication. The synchronizers, with the capability of framing data that may have bit errors, enhance the synchronization ability of the inbound data path. These units also relieve the computer of the task of editing filler blocks.

## Reference

1. Mullen, P. G., "High-Speed Data, SFOF Outbound Communication," in *The Deep Space Network*, Space Programs Summary 37-65, Vol. II, p. 101. Jet Propulsion Laboratory, Pasadena, Calif., Sep. 30, 1970.

# SFOF Mark IIIA Central Processing System Model Development

H. S. Simon
SFOF/GCF Development Section

*Simulation models are currently being used for SFOF development at the Jet Propulsion Laboratory. The results of two modeling studies are described that were performed during the early stages of the SFOF Mark IIIA Central Processing System development.*

## I. Introduction

Simulation models are currently being developed to support the design and implementation of the SFOF Mark IIIA Central Processing System (CPS). See Ref. 1 for a functional description of the SFOF.

SFOF Mark IIIA modeling studies began in May 1969 when it was learned that NASA would be providing JPL with IBM 360 model 75 digital computers to form the nucleus of the SFOF Mark IIIA CPS.

The IBM computer system simulator program was selected for model development activities since it runs on the IBM 360/75 and the program itself applies specifically to computer systems.

This article describes the results of two modeling studies that were performed during the early stages of SFOF Mark IIIA development. The first study, completed in August 1969, evaluated the performance of two real-time operating systems. The second study, completed in November 1969, provided information on central processing unit (CPU) utilization and response times during a simulated 24-h time segment in the orbital phase of the *Mariner* Mars 1971 dual spacecraft mission.

## II. Performance Evaluation of Two Real-Time Operating Systems

To meet the requirement to provide test and flight support for the *Mariner* Mars 1971 mission, within the time allotted for the SFOF Mark IIIA CPS development cycle, it was deemed necessary to use an existing operating system with real-time data handling capabilities. The two systems selected for consideration were:

(1) The Goddard Real-Time System (GRTS).

(2) The Houston Real-Time Operating System (RTOS).

The objective of this study was to evaluate the relative performance of the two operating systems using simulation models, each being subjected to similar loading conditions.

### A. Hardware Configuration

The final SFOF Mark IIIA CPS hardware configuration had not been established at the time of this study. Therefore, the preliminary configuration, shown in Fig. 1, was defined in both models.

### B. Software Configuration

The model routines represented the capabilities within each operating system at the time the study was performed. Timings for the execution of each of the RTOS model elements were derived from the Statistics Gathering System measurements provided by NASA, Houston. Timings for the GRTS model were derived from instruction counts with an assumed execution speed of 1 $\mu$s per instruction.

Additionally, real-time data processors and analysis programs were included in each model.

### C. Sequence of Events

To exercise the models, a script was developed defining the inputs that were applied in a time-sequenced manner. The script simulated real-time data from four missions using assumed data loading conditions. It also simulated requests from user area inquiry devices to turn on non-real-time programs.

Telemetry and tracking data for each mission were routed to the system as messages of 600 and 1600 bits, respectively, at a simulated real-time input rate of 40,800 bits/s.

Two streams of high-rate video data were input to the system for processing. The resulting full frame of TV data was made available for outputting to the Mission Test and Video System at a rate of 2,496,000 bits/s.

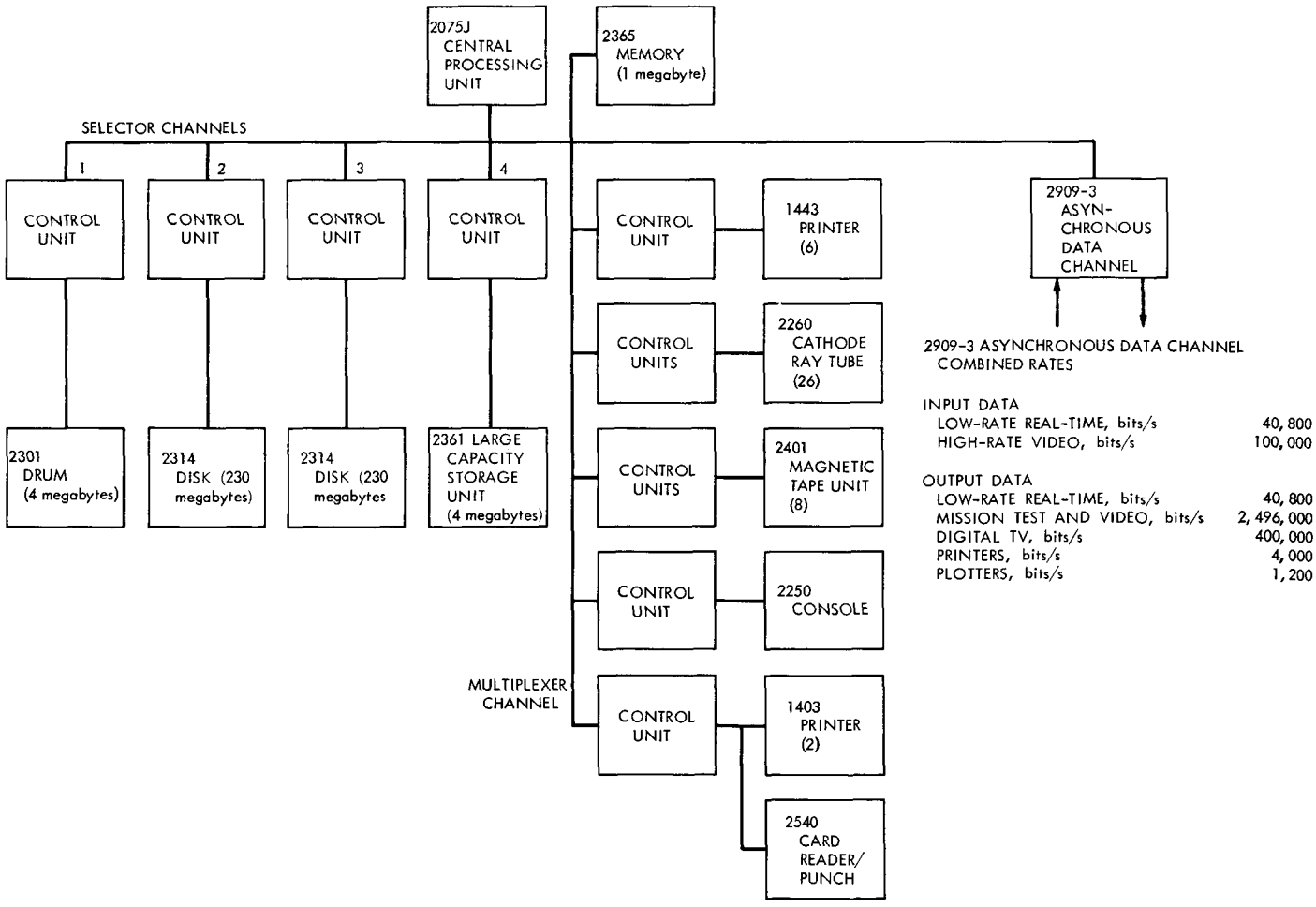


**Fig. 1. Hardware configuration for performance evaluation of real-time operating systems**

To realistically exercise the models, the script was written to impose a heavier than normal load on the systems. This was accomplished by turning on the following three large-scale computation-bound programs:

(1) Double-precision orbit determination program (DPODP).

(2) Star identification program (SIPM).

(3) Monitor criteria data program (MCDM).

These programs ran concurrently with the real-time data processors.

Additionally, the models were initialized to cause the following computation-bound programs to operate shortly after the start of the simulation runs:

(1) Orbit data generator program (ODGX).

(2) Engineering data records program (RECM).

(3) Communications measurements program (CMPM).

### D. Results

Statistics obtained from two simulation runs are shown in Table 1. The statistics were derived from a 10-min computer run on the RTOS model and a 6-min run on the GRTS model. The script was deliberately set to give high CPU utilization to measure the effectiveness of each operating system.

**Table 1. RTOS–GRTS comparison statistics**

| Utilization summary and task breakdown | RTOS | GRTS |
|---|---|---|
| CPU utilization summary (max values) | | |
| Applications, % | 87.2 | 69.0 |
| Defined system tasks, % | 0.5 | 12.6 |
| GRTS supervisor service, % | — | 12.6 |
| Supervisor/mission and test video service, % | 7.7 | 4.6 |
| Memory interference, % | 4.4 | 1.1 |
| Total | 99.8% | 99.9% |
| Task breakdown | | |
| System CPU utilization | | |
| Interrupt input/output supervisor, % | 2.0 | 5.3 |
| Task management, % | 2.8 | 4.4 |
| Data management, % | 2.7 | 25.2 |
| Supervisor state CPU utilization (includes supervisor service requested by, and charged to, the application), % | 10.2 | 35.0 |
| Application | | |
| Average response time for real-time task, ms | 140 | 756 |
| CPU utilization for real-time task (max value), % | 2.4 | 6.3 |
| DPODP CPU utilization (max value), % | 75.8 | 58.2 |

### E. Observations

In the RTOS model, approximately 88% of the available CPU time was spent processing application programs compared with 69% for the GRTS model.

RTOS required 8.2% of the available time to process system supervisor calls and to define system tasks compared to 29.8% for GRTS.

The most significant divergence between the two systems was in the area of data management. Here, RTOS required 2.7% of CPU time compared to 25.2% for GRTS. This significant difference was attributed to the data management concepts for each operating system.

The average task response time for the tracking and telemetry data was 140 ms for RTOS compared to 756 ms for GRTS. The major difference in response times between the two systems is the input/output time required by GRTS. In GRTS, real-time data is queued to a disk resident string before processing, while RTOS holds real-time input data in main memory until it is processed.

During the simulation runs, DPODP plus the system services that it calls received 75.8% of the CPU time under RTOS and 58.2% of the CPU time under GRTS. This means that DPODP would run approximately one-third faster under RTOS.

The total supervisor state utilization provides a measure of the total overhead of the system. For RTOS, the total system utilization was 10.2% compared to 35.0% for GRTS.

### F. Conclusion

Based upon the assumptions made for these simulation runs, data was processed more efficiently under RTOS than under GRTS:

(1) Data management services required 9 times as much CPU time for the GRTS run.

(2) GRTS required 3.5 times more CPU time than RTOS to process system supervisor calls and to define system tasks.

(3) The navigation program (DPODP) ran 3 times faster under RTOS than under GRTS.

(4) The average real-time task response time was faster under RTOS by a factor of nearly 5.5.

## III. *Mariner* Mars 1971 Simulation Study

The objective of this study, performed in November 1969, was to obtain CPU utilization and real-time task response time information from a simulation model that defined a preliminary SFOF Mark IIIA configuration. This information was obtained from several runs that exercised the model during a simulated 24-h segment of the orbital phase of the *Mariner* Mars 1971 dual spacecraft mission.

### A. Hardware Configuration

The simulation model defined the preliminary hardware configuration shown in Fig. 2. The IBM 360 model 75J digital computer with 1 megabyte of main memory formed the nucleus of the hardware system. The configuration also included the following units:

(1) A multiplexer channel with nine control units for servicing the following set of assumed input/output devices: two 1443 line printers, two 1403-N1 line printers, eight 2401-1 magnetic tape units, 26 CRTs with keyboards, a 2250 console, and a 2540 card reader/punch.

(2) A selector channel with two control units for servicing two 2314 disk units (230 megabytes each), a 2361 large capacity storage unit (4 megabytes), and an electrical interface with the Univac 1108 computer.

(3) An asynchronous data channel with seven subchannels.

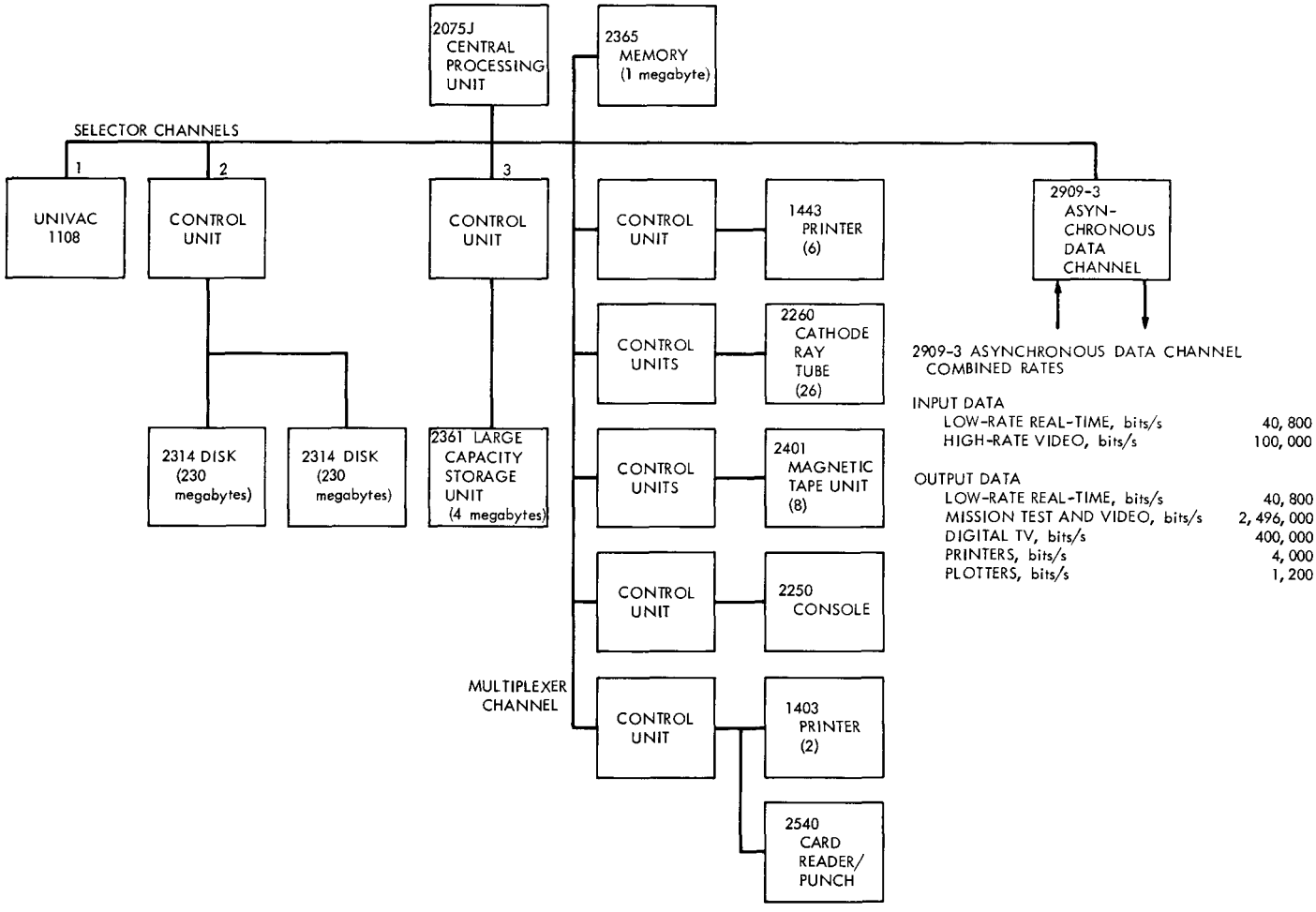


**Fig. 2. Hardware configuration for *Mariner* Mars 1971 simulation study**

### B. Software Configuration

The model of the software system defined the capabilities of five functional software subsystems:

(1) Master control and user interface.

(2) SFOF command data.

(3) SFOF telemetry data.

(4) SFOF tracking data.

(5) SFOF monitor and operations control data.

The master control, or operating system portion of the master control and user interface, utilized the capabilities of Houston's RTOS version 11.0.

The user interface capabilities enabled each SFOF data software subsystem to interface with the operating system. In the model, all input data was routed directly by the operating system to the appropriate task and module for processing. Each task used the display formatting language for data conversion to the output device and the operating system's real-time access method to output the converted data.

The processing capabilities included in the model for the four remaining software subsystems (command, telemetry, tracking, and monitor and operations control data) are listed in Table 2.

### C. Sequence of Events

The scripts used for this study were derived from a *Mariner* Mars 1971 project memorandum that described a suggested strategy to be used during the orbital phase of the mission. The period chosen was from 16:00 GMT, December 2, 1971, to 16:00 GMT, December 3, 1971. A mission profile corresponding to this 24-h period is shown in Fig. 3.

System utilization and response time information was obtained from two runs. All functions were performed in accordance with the scheduled, time-sequenced events as shown on the mission profile (Fig. 3).

*Run 1.* The entire 24-h period was simulated during which time all real-time data, including high-rate video, was logged and processed in the IBM 360/75 and distributed for display. Raw data was passed to the Univac 1108 as it was received.

**Table 2. Processing capabilities of software subsystems**

| Type of data | Processing performed |
|---|---|
| Tracking | Data conversion<br>Residual computation<br>Store data for later use<br>Display converted data<br>Display residuals |
| Engineering telemetry | Frame synchronization<br>Decommutation<br>Data conversion<br>Store data for recall<br>Display frame synchronized data |
| Spectral science telemetry | Frame synchronization<br>Decommutation<br>Data conversion<br>Store data for recall<br>Display frame synchronized data |
| Video | Frame synchronization<br>Decommutation<br>Store data for recall<br>Display video frame and/or plots |
| Monitor | Data conversion<br>Store data for recall<br>Display data |

A peak utilization of the IBM 360/75 occurred at approximately 04:30 hours. During this time, the following streams of data were input to the IBM 360/75:

(1) Recorded science (8,100 bits/s).

(2) High-rate video (16,200 bits/s).

(3) Low-rate telemetry and tracking.

*Run 2.* The same 24-h period was simulated with identical input data streams as in Run 1. All processing was done in the IBM 360/75. In addition to the processing of all real-time data, the following science and navigation programs were turned on during the run:

(1) Spacecraft command generation program (COMGEN).

(2) Double-precision orbit determination program (DPODP).

(3) Planetary observation geometry and science instrument sequence program (POGASIS).

(4) Infrared interferometer spectrometer program (IRIS).

(5) Predicts (PRDX).

(6) Central computer and sequencer (CC&S) update.

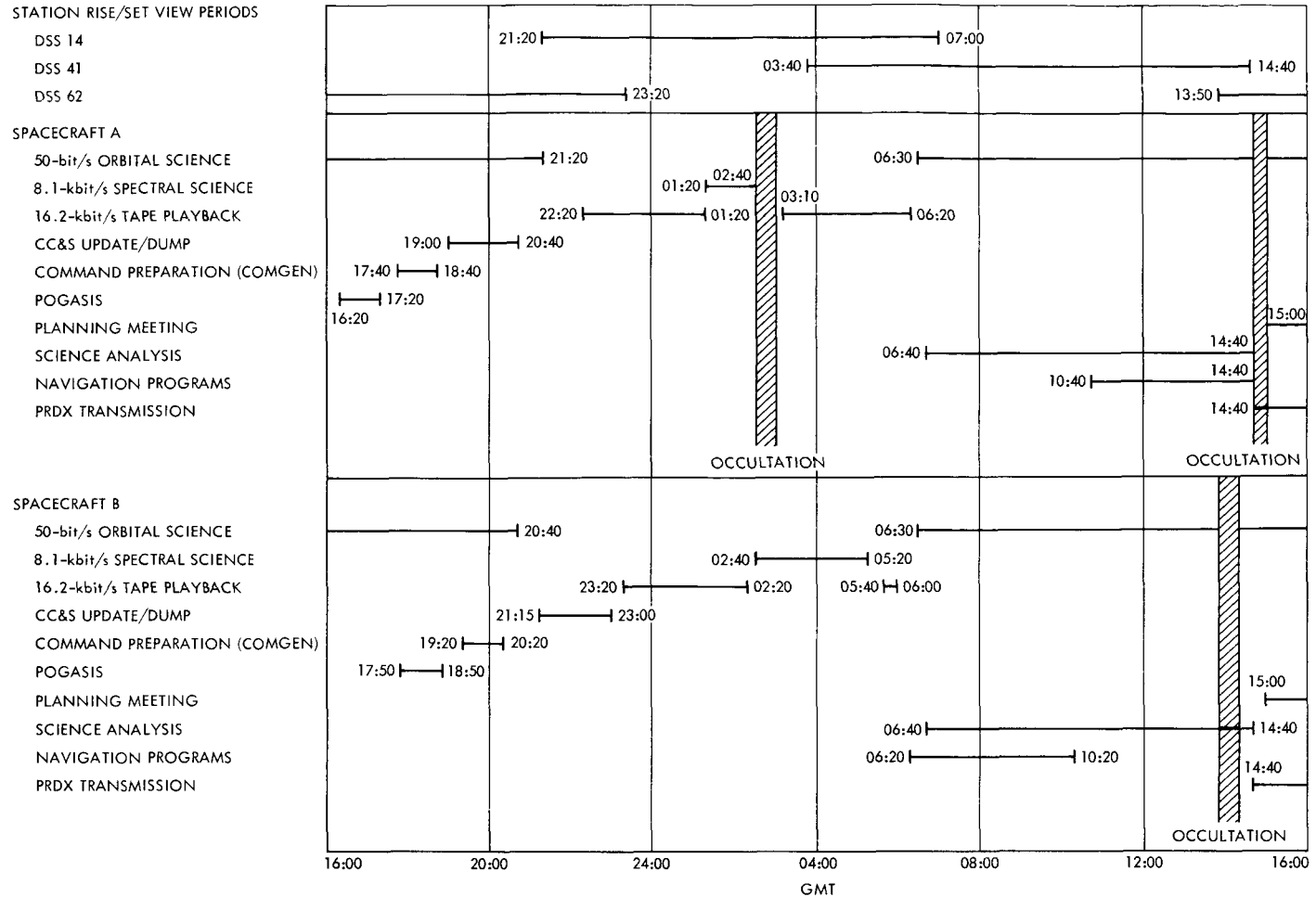


**Fig. 3. Dual-mission profile (orbital phase)**

Two scripts were utilized during Run 2 to evaluate segments of the orbital phase.

Script 1 covered the period from 16:00 to 23:00 hours, following the one-hour daily planning meeting. During the first three hours (16:00–19:00), POGASIS was run for each spacecraft. COMGEN was run for spacecraft A. During the next two hours, COMGEN was run for spacecraft B and the CC&S updates for Spacecraft A were transmitted to the site. During the final two hours (21:00 to 23:00), CC&S updates for spacecraft B were transmitted to the site.

Script 2 covered the period from 06:00 to 15:00 hours, prior to the planning meeting. During this time, the computation-bound navigation and science analysis programs for both spacecraft were turned on.

### D. Results

The results of each run are shown graphically in Figs. 4 and 5. A summary of the utilization and response time statistics, for each run, is presented in Table 3.

### E. Observations

During Run 1, the CPU utilization reached a peak value of 30.36% when the IBM 360/75 was required to simultaneously process (1) a stream of 8,100-bits/s science data, (2) a stream of 16,200-bits/s video data, and (3) streams of low-rate engineering telemetry and tracking data. The average CPU utilization over the 24-h period for all processing was 6.39%, while the average utilization required for processing low-rate, real-time data only was 2.45%.

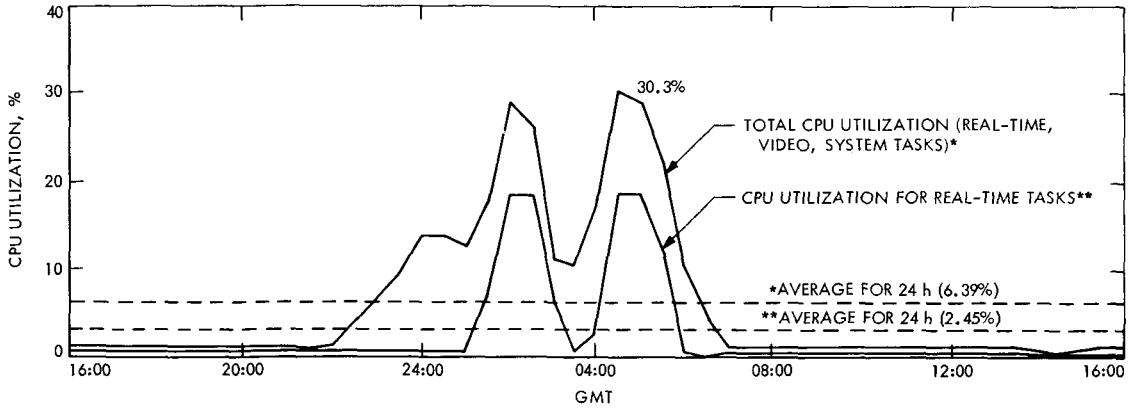


**Fig. 4. CPU utilization during Run 1**

During Run 2, the average CPU utilization for all jobs, over the 24-h period was 24.05%. An examination of average CPU utilization for various segments of the orbital phase reveals the following figures:

| | | |
|---|---|---|
| Post-planning meeting period | 16:00–23:00 | 12.72% |
| Video and high-rate science playback period | 23:00–06:00 | 14.88% |
| Science–navigation analysis program period | 06:00–15:00 | 40.77% |

The peak CPU utilization, which reached essentially 100%, occurred during the running of the computation-bound, science and navigation analysis programs for both spacecraft.

The average real-time task response time is defined as "the period of time starting with a real-time attach statement and ending when the task exits." This includes queue time, input/output time, and execution of the task. For this study, real-time tasks included telemetry processing, tracking residuals, and monitor data processing. Video data was excluded.

During the 9-h period that the science and navigation programs were running, the average real-time task response time was 58.680 ms. This relatively fast time demonstrated the efficiency of the operating system's task management function.

### F. Conclusion

The results of this study showed that, during the orbital phase of the mission, the average CPU utilization over a 24-h period was 24.05%, leaving an average of 75.95% of the CPU for background processing. Assuming that DPODP will not be run in the IBM 360/75, the average CPU utilization should drop to less than 20%.

**Table 3. Summary of utilization and response time statistics**

| Utilization and response time | Run 1 | Run 2 | | | Summary of all tasks (24-h period) |
|---|---|---|---|---|---|
| | Real-time and video processing (24-h period) | Post-planning meeting period (16:00–23:00) | Playback period (23:00–06:00) | Science–navigation period (06:00–15:00) | |
| Average CPU utilization, % | 6.39 | 12.72 | 14.88 | 40.77 | 24.05 |
| Real-time processing, % | 2.95 | 1.01 | 6.80 | 1.06 | 2.97 |
| Video processing, % | 1.81 | — | 5.42 | — | 1.81 |
| Total non-real-time processing, % | — | 10.87 | — | 39.44 | 17.96 |
| Navigation programs, % | — | 10.87 | — | 15.80 | 9.09 |
| Science programs, % | — | — | — | 23.64 | 8.87 |
| System, % | 2.53 | 0.88 | 6.15 | 0.92 | 2.57 |
| Average response time for real-time task, ms | 79.779 | 42.615 | 164.165 | 58.680 | 82.316 |

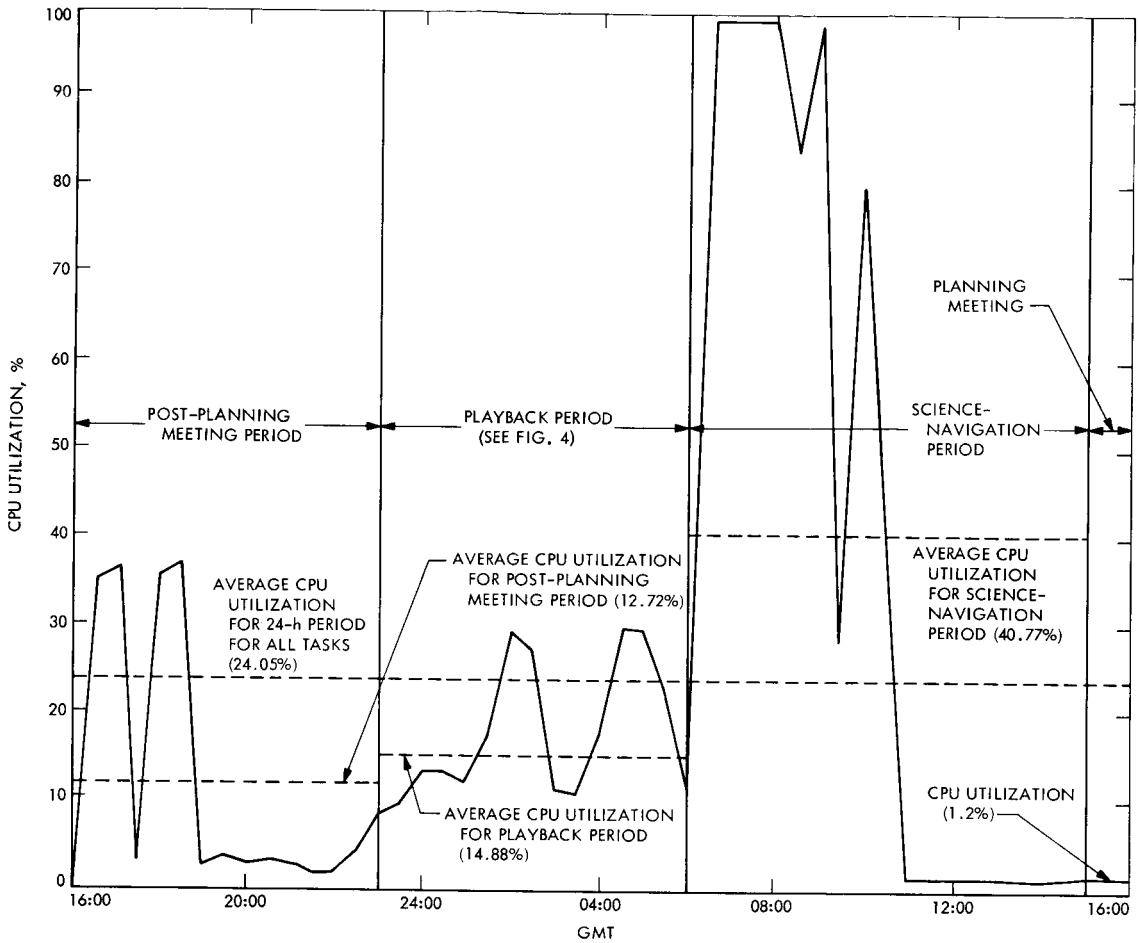


**Fig. 5. CPU utilization during Run 2**

## Reference

1. Simon, H. S., "Functional Design of the Space Flight Operations Facility for the 1970–1972 Era," in *The Deep Space Network*, Space Programs Summary 37-66, Vol. II, pp. 90–94. Jet Propulsion Laboratory, Pasadena, Calif., Nov. 30, 1970.

# Diagnostics for the Mark IIIA Central Processing System: IBM 360/75 Computer On-Line Test Routines

R. A. Wells
SFOF/GCF Development Section

*A family of real-time on-line diagnostics was developed to check out all IBM 360/75-related components of the SFOF Mark IIIA Central Processing System. Diagnostic requests are entered from a cathode-ray-tube display station, initiating concurrent tests of assorted user devices and communications links. A supervisory software monitor program coordinates execution and, where necessary, draws on the facilities of the JPL Operating System in each IBM 360/75 computer.*

## I. Introduction

This article describes the *real-time, on-line* diagnostic routines which have been developed for IBM 360/75 computer-related hardware: channels, subchannels, control units, devices, input/output lines, attached processors, and special features. Reference 1 describes the independent or standalone diagnostics developed for JPL-unique subsystems and devices in the SFOF Central Processing System (CPS).

## II. Implementation

Figure 1 shows the current Mark IIIA SFOF CPS equipment configuration, all elements of which are supported by on-line test routines insofar as they relate to the IBM 360/75 processors. Reference 2 gives specific interconnection details, model numbers, and equipment complement for this configuration.

These real-time, on-line diagnostic routines are resident under the JPL Operating System (JPLOS) and execute under the control of the *Dia*gnostic *Mon*itor (DIAMON), which recognizes the requests and coordinates the test(s). DIAMON also generates the necessary test patterns, checks those which are returned, and issues error messages and statistics. If requested, DIAMON will also generate diagnostic summary displays and printouts.

As presently implemented, the DIAMON system (when initialized) becomes the one and only real-time job step under JPLOS; no other concurrent real-time data processing is possible. (Work is underway to permit DIAMON to operate as one of several independent tasks under the real-time job step, allowing simultaneous testing and mission data processing on disparate parts of the system.)

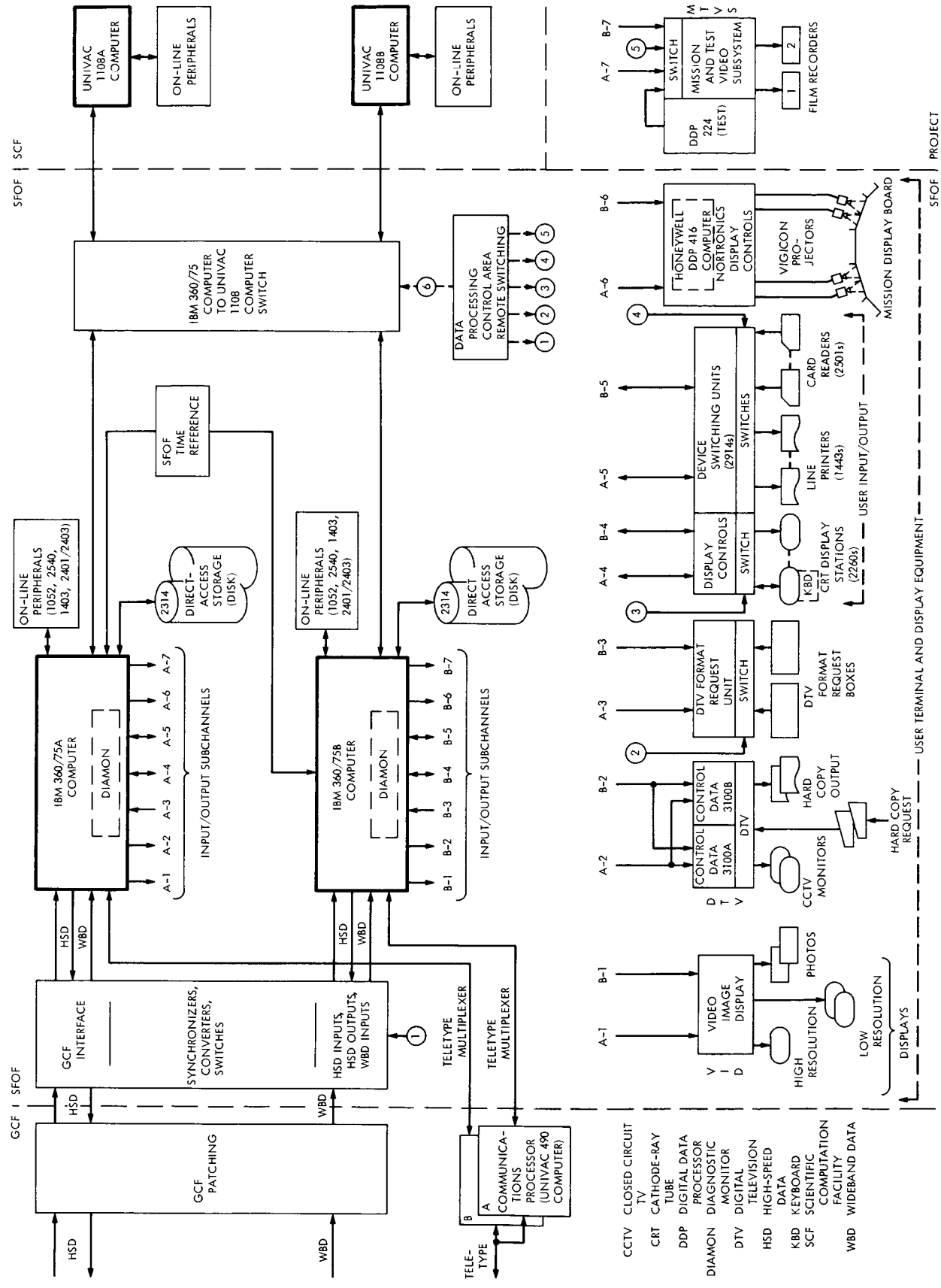


**Fig. 1. SFOF Mark IIIA CPS diagnostic configuration**

## III. Operation

Equipment to be tested is identified at time of initialization so as to be reserved by JPLOS for the exclusive use of DIAMON, thus preventing the conflicts which would result from competition for the same resources.

Diagnostic requests are made from a cathode-ray-tube display station keyboard (Fig. 2) designated for this purpose. Test durations are variable at the discretion of the diagnostic operator. Runs on different devices and/or subchannels may be made concurrently and compatibly, with the sole exception of the diagnostic which tests the GMT (Greenwich Mean Time) register and the interval timer (IT) register in the central processing unit (CPU). The GMT/IT diagnostic must be run on a drained (empty) system so as not to jeopardize other programs which may attempt to access these registers. Diagnostic requests for the console-assigned peripherals (1052 typewriter, 2540 card read/punch, 1403 bulk printer) are accessed by DIAMON through the HASP[1] priority scheduler/queuer since these operator devices are reserved for system (JPLOS) usage.

Diagnostics which communicate with remotely situated processors in the SFOF (Univac 1108s, communications processors, control data 3100s, mission display board) are not automatically operable but require voice communication and coordination between operators to set up the desired test.

DIAMON has been so structured as to be extensible for the accommodation of future equipment additions. This

[1]HASP = Houston automatic spooling priority.

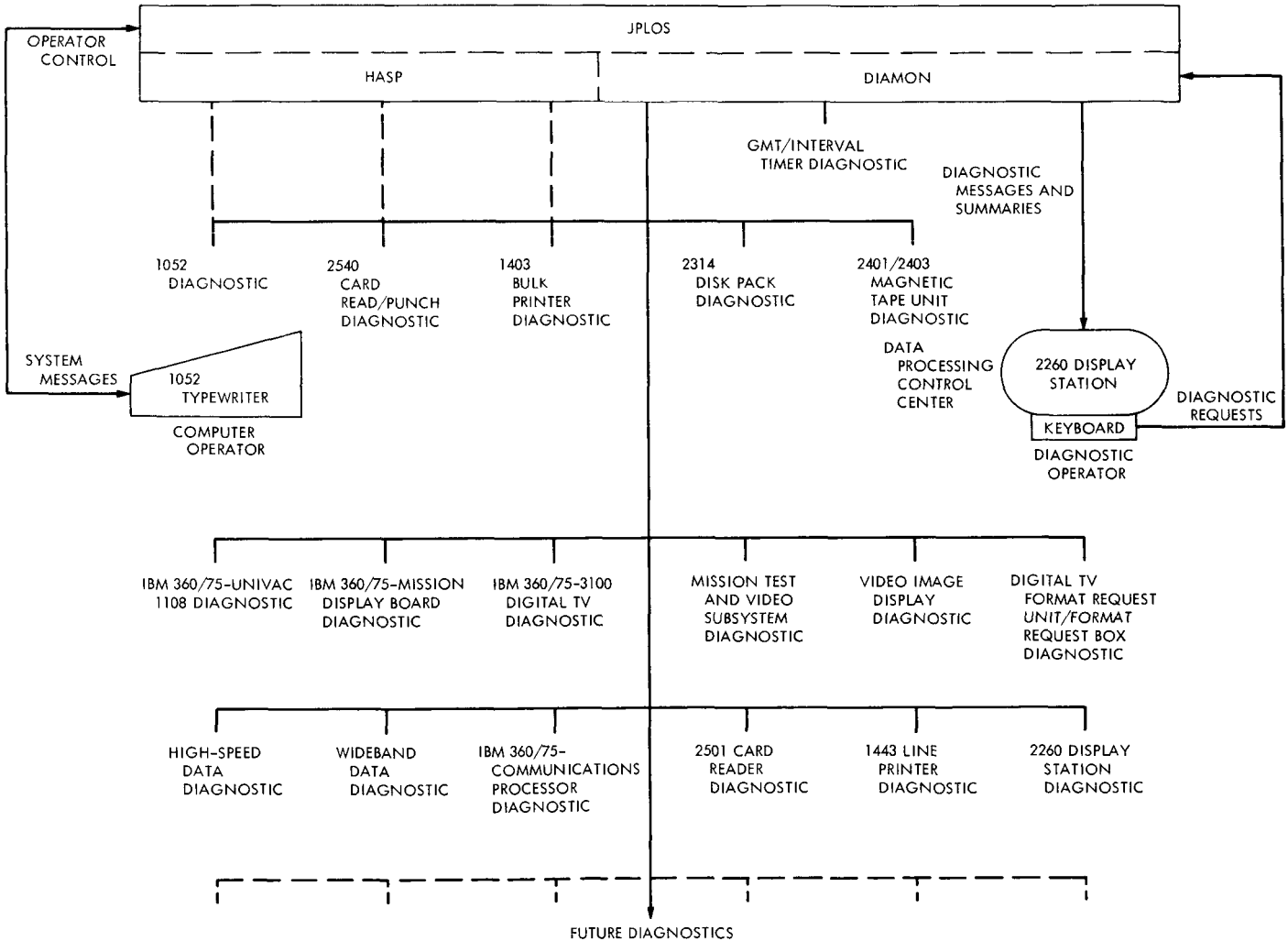


**Fig. 2. SFOF CPS on-line diagnostics for the IBM 360/75 computer**

open-ended modular approach also simplifies documentation, maintenance, and modifications.

## IV. Conclusion

All of the DIAMON diagnostics referenced in this article have been fully developed and documented, and are in daily use to verify the operational integrity and performance of the various hardware components. Periodic full-scale facility-level tests are conducted using a preestablished script to assess and attest the current performance of all IBM-360/75-related equipments, in order that the continuing demands of spaceflight data processing may be satisfied.

## References


1. Wells, R. A., "Diagnostics for the SFOF Mark IIIA Central Processing System: Standalone Acceptance and Maintenance Routines," in *The Deep Space Network*, Space Programs Summary 37-65, Vol. II, pp. 97–99. Jet Propulsion Laboratory, Pasadena, Calif., Sep. 30, 1970.
2. Stiver, R. A., "Mark IIIA IBM 360/75 Computer Configuration," in *The Deep Space Network*, Space Programs Summary 37-66, Vol. II, pp. 71–75. Jet Propulsion Laboratory, Pasadena, Calif., Nov. 30, 1970.

# IBM 360/75 Computer Time Interface

C. Zandell
SFOF/GCF Development Section

*The IBM 360/75 computer time interface and the capabilities of two custom-feature modifications of the IBM 360/75 are described. The modified IBM 360/75 accepts signals from an existing time reference, provides GMT with 10-μs resolution, includes an interval timer, and provides programmable interrupts.*

## I. Introduction

The inclusion of a GMT clock interface in the Mark IIIA central processing system (CPS) (Ref. 1) is a direct continuation of Mark II CPS support. Mark II programs that utilized the GMT reference have been converted for Mark IIIA use. The current GMT clock also is an improvement, requiring significantly fewer memory cycles to make its data available to the programmer.

The implementation technique for the GMT clock was influenced by the existing configuration of the first IBM 360/75 computer transferred to JPL. It included a custom-feature modification, an interval timer, which satisfied all the Mark IIIA requirements but one—the number of lines for the GMT day limited the day of the year to 39.

To take advantage of the large investment represented by the interval timer feature, a second modification was added. This increased the number of lines for the GMT day to 10, allowing the full range of 366 days. Both modifications were added to the second IBM 360/75 computer to provide the capabilities described below.

## II. Timer

The GMT timer is a real-time clock that specifies Greenwich Mean Time. The clock is composed of two parts: (1) GMT expressed in days, hours, minutes, and seconds in BCD format as received from the SFOF time reference, and (2) the fractional part of a second in binary format (to 10-μs resolution). The central processing unit (CPU) may sample the GMT (including the fractional part) whenever the GMT is valid. The fractional part is incremented at a 100-kpps rate from the time reference and is reset to *one* every second by a 1-pps signal from the time reference. The 1-pps signal is also used to start a blocking pulse in the CPU which inhibits the GMT from being sampled while the GMT is changing. Figure 1 shows the double word (64-bit) format of the GMT clock.

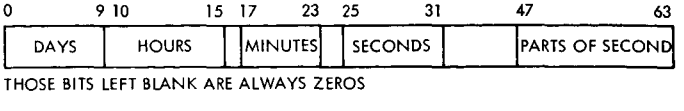


**Fig. 1. GMT clock word format**

The interval timer is a one-word, 32-bit, binary register that is decremented at a 100-kpps rate by a signal from the time reference or from an internal 100-kpps source. The interval timer runs continually and requests an external interrupt every time it changes from all *zeros* to all *ones*. In addition, the interval timer may be loaded by a load timer instruction, providing the ability to request external interrupts at predetermined times. The timer contents may be stored by a store timer instruction.

## III. One-Second Interrupt

A 1-pps signal is furnished to the CPU from the time reference, providing an external interrupt every second, under program control.

## IV. Interface

The first word of the GMT clock is obtained by sensing the state of 30 lines from the time reference. The 30 lines are used as follows:

| | |
|---|---|
| 2 lines | hundreds of days of the year |
| 4 lines | tens of days of the year |
| 4 lines | units of days of the year |
| 2 lines | tens of hours |
| 4 lines | units of hours |
| 3 lines | tens of minutes |
| 4 lines | units of minutes |
| 3 lines | tens of seconds |
| 4 lines | units of seconds |

The second word of the GMT clock represents the contents of a 17-bit binary counter that is incremented by a 100-kpps signal from the time reference. The 15 high-order bits of this word are always *zeros*.

The 30 lines of GMT from the time reference will be updated once each second. Immediately prior to the GMT being updated, a 1-pps signal (pulse width of 100 ms) is received from the time reference. This signal will lead the change of the GMT lines by 0.75 $\mu$s (nominal).

The 1-pps signal blocks the model 75 CPU from sampling the GMT lines while the GMT is changing. This is done by initiating a 10.0-$\mu$s delay. During this 10.0-$\mu$s period, the CPU is inhibited from performing a store timer 1 (store GMT) instruction. The time reference should start changing the GMT lines 0.75 $\mu$s from the leading edge of the 1-pps signal. Figure 2 shows the timing relationship between the 1-pps reset pulse and the GMT lines.

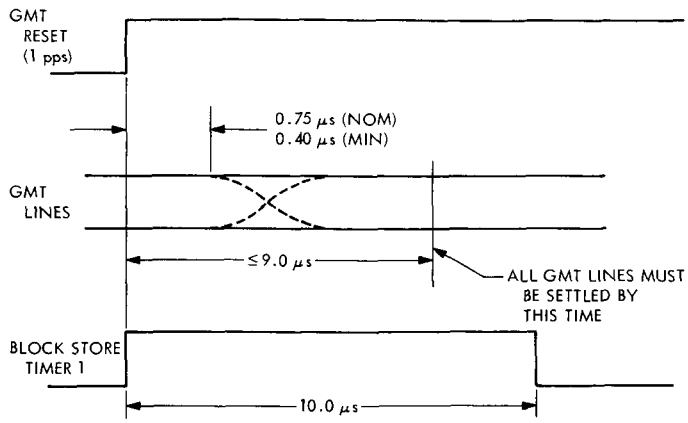


**Fig. 2. Timing relationship**

The 32-bit interval timer is decremented by *one* every 10 $\mu$s by a 100-kpps signal (pulse width = 2.5 $\mu$s) from the time reference or from an internal oscillator; this is selectable by switch setting. Facilities are also provided to disable the interval timer so that it will not step.

The interval timer will request an external interrupt when it rolls over from *zeros* to *ones*. A bit in the program status word will enable this interrupt. The timer interrupt is also requested if a load timer instruction is issued when the timer is disabled (by switch setting) or is in the maintenance mode.

An external interrupt is requested at a rate of 1-pps (pulse width of 100 ms) by a signal from the time reference. A bit in the program status word will enable this interrupt.

## V. Conclusion

With the inclusion of the modified features in the IBM 360/75, GMT and a variety of timing and interrupt techniques are available to programmers. Since the lines are sampled only when requested versus loading a core location every millisecond, few memory cycles are required. Using IBM designs also allows continued customer engineer support for the CPU. This approach is technically feasible for other IBM 360 models, in particular models 65, 67, and 85.

## Reference

1. Stiver, R. A., "Mark IIIA IBM 360/75 Computer Configuration," in *The Deep Space Network*, Space Programs Summary 37-66, Vol. II, pp. 71–75. Jet Propulsion Laboratory, Pasadena, Calif., Nov. 30, 1970.

# IBM 360/75–Univac 1108 Computer Interface

C. Zandell
SFOF/GCF Development Section

*A serial synchronous communication method for short distances without the use of modems is described. Reducing the total resistance between the current mode drivers and receivers makes transmission lengths of 400 ft possible. External timing replaces the modem function, allowing the direct connection of serial synchronous devices.*

## I. Introduction

Reference 1 describes the functional design of the SFOF for the 1970–1972 era. As described therein, a capability for interfacing the Central Processing System with the Scientific Computing Facility will exist. This interface is required to implement the transfer of orbital and trajectory data between programs in the IBM 360/75 and the Univac 1108 computers for the *Mariner* Mars 1971 and *Pioneer F* missions. An electrical interface has been designed for this purpose. This interface will provide for the transmission of $10^7$ bits of data from computer to computer in a time span of 10 min. This article describes the interface design which provides a method of synchronous communication for short distances without the use of modems.

## II. Required Capabilities

The required capabilities for the interface were:

(1) A data transmission length between machines of 400 ft.

(2) A data path from each IBM 360/75 to both Univac 1108s.

(3) Actual data rates of 17 kbps or greater.

It was decided to switch single lines from each computer rather than having dedicated lines from each IBM 360/75 to each Univac 1108 (Fig. 1). This minimized the hardware costs and kept the address requirements to one

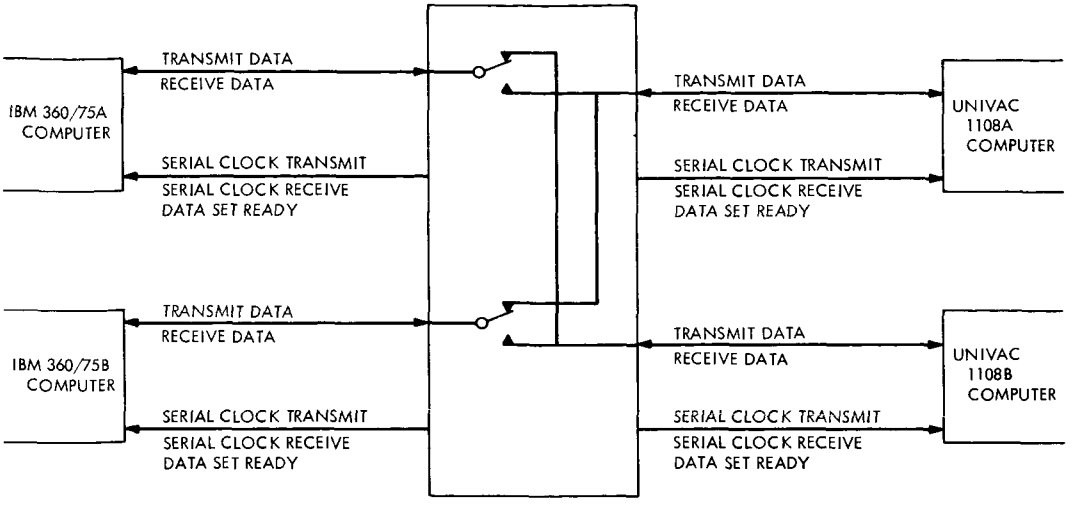


**Fig. 1. IBM 360/75–Univac 1108 coupler interfaces**

per machine. The decision also eliminated the possibility of a direct channel-to-channel connection because of the complexity of the related switch and the high cost.

A serial interface using modems offered the most direct method to meet the required capabilities. All other choices would require additional hardware for driving and receiving the signal lines. Additionally, modem communications were already supported on the Univac 1108.

Past experience with the current drivers of devices connected to modems suggested a modification: use low-resistance coaxial cable in place of the normal high-resistance cable. Since the length of the transmission path is limited by the total resistance between the driver and receiver, longer than normal lengths are feasible. Tests confirmed that the IBM and Univac drivers could drive in excess of 400 ft. Eliminating the modems would require additional logic to provide timing and enabling signals but would allow the use of JPL-owned lines and switch versus leased modems, lines, and switch.

## III. Implementation

The 75–1108 coupler provides the signals normally supplied by a modem (Fig. 2). Logic within the coupler divides and squares a 100-kHz crystal clock for input to current mode drivers. Clock is sent to all serial devices at all times while DATA SET READY (DSR) is included in the switching. DSR at the serial device then is true only if the device is connected.

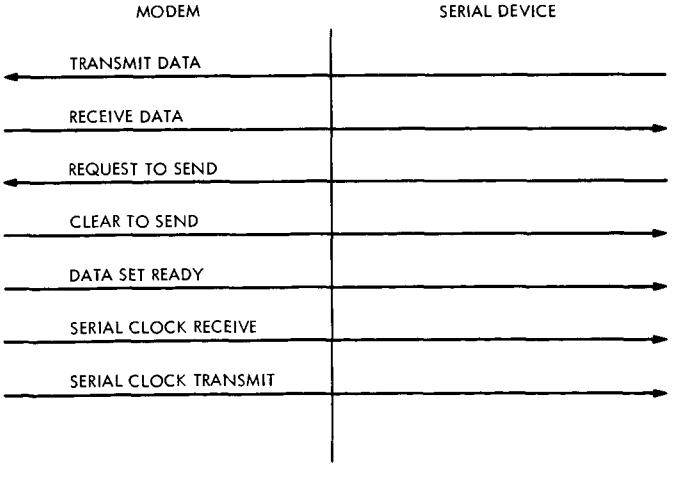


**Fig. 2. Modem interface signals**

Data lines, TRANSMIT DATA (TD), and RECEIVE DATA (RD) are connected within the switch (TD and RD to RD and TD, respectively, for the two connected devices). REQUEST TO SEND (RS) and CLEAR TO SEND (CS) are connected at each serial device. This is possible since RS can be raised only if DSR is valid, which means the line is either clear or the device is receiving. If the device is receiving, it will not raise RS.

An added advantage was the simplified switching problem since the number of lines was reduced when compared to a switch between a modem and two serial devices. Also, the difficulties of switching the modem-to-modem lines were avoided.

## IV. Conclusion

The use of the coupler permitted a direct solution of the electrical interface requirement using serial synchronous devices. Design problems were simplified by using the coupler. Initial costs were comparable to using modems but with no further lease expenses for modems, lines, or switch.

## Reference

1. Simon, H. S., "Functional Design of the Space Flight Operations Facility for the 1970–1972 Era," in *The Deep Space Network,* Space Programs Summary 37-66, Vol. II, pp. 90–94. Jet Propulsion Laboratory, Pasadena, Calif., Nov. 30, 1970.

# Communications Control Group Assembly: Teletype Line Switching Equipment

D. W. Passell
SFOF/GCF Development Section

*This article describes the teletype portion of the communications control group assembly installed in the GCF's deep space station communications equipment subsystem. The functions, developmental status, and operational features of the teletype switching equipment are discussed; and the necessity for interfacing with a variety of communications common carriers is explained.*

## I. Introduction

This article describes the teletype (TTY) line switching equipment which is a part of the communications control group assembly (CCGA) installed at each of the deep space stations. The CCGA is, in turn a part of the GCF's deep space station communications equipment subsystem (DCE). This teletype switching equipment functions as a component of the GCF teletype system as described in Space Programs Summary 37-66, Vol. II, pp. 111–113. This article considers the purpose, developmental status, and configurations of this teletype switching equipment.

## II. Purpose of CCGA

The CCGA installed at each station interfaces with the communications common carrier who, with other carriers, provides the teletype transmission circuits between the stations and the SFOF. The station side of this teletype equipment is connected to the teletype machines and computers which generate and receive teletype data. The teletype switching equipment performs several functions:

(1) Accepts the widely varying teletype signals used by the various common carriers around the world and transforms these variable signals into a common logic level.

(2) Regenerates incoming teletype signal to reduce errors.

(3) Provides the switching necessary to distribute teletype signals to the various computers and teletype machines in the DSS.

(4) Provides standardized electrical levels to all of the equipment in the DSS.

(5) Provides, in some cases, the tone transmission equipment necessary for economical transmission of teletype signals over long distances between stations.

As noted, the various international communications common carriers (telephone companies) around the world utilize substantially different electrical interface levels for teletype transmission. The teletype switching equipment is specifically tailored to accommodate the interface used nationally at each station. Specifically the CCGA teletype equipment can accommodate the following external interfaces:

(1) Direct current; 60 mA neutral: the remote end supplies current on receive and transmit lines. (This is also the standard used with on-site equipment with CCGA supplying the current.)

(2) Direct current; 40 mA inverted polar: the CCGA supplies the transmit current.

(3) Direct current; 20 mA polar: the CCGA supplies the transmit current.

(4) Voice frequency shift keying. An audio carrier is shifted by the signal; used between DSS 11, DSS 14 and the Goldstone Area Communication Terminal (ACT), and between ACT and SFOF via microwave carrier.

## III. Development and Status of the CCGA

Along with other systems and assemblies of the Ground Communications Facility, the CCGA has undergone evolutionary development. Development has been evolutionary because service must be maintained for current operations simultaneously with upgrading the overall facility to meet ever-increasing requirements for data volume and data rates. Multimission commitments of the DSN have dictated standardization of the communications configurations at all of the tracking stations. Operational standardization was achieved at all ten of the DSSs in 1969 when the CCGA equipment became operational.

The teletype portions of the CCGAs at the various stations are sized to meet the station needs. The size of the switching matrices, and other data, are shown in Table 1.

The CCGA is capable of expansion to ten external lines and twenty users, switched by matrix. The capability shown in Table 1 currently exists.

## IV. Operational Features

The CCGA has the capability to terminate, regenerate, and distribute external teletype lines to on-site teletype machines and computers. The incoming and outgoing line signals conform to one of the four standards described previously. Internal routing and switching within the CCGA is in inverted-voltage mode and the interfaces to machines and computers at the station is standard 60 mA neutral.

Figure 1 shows the distribution of teletype signals performed by the CCGA. Two distribution paths are used:

### A. Non-switched

Each of the computer teletype input and output ports and specific TTY machines are permanently connected through the CCGA to each of the external teletype lines. These computer ports and TTY circuit configurations can be rearranged only by patching.

**Table 1. CCGA teletype input/output capabilities**

| DSS | Line access jacks | Line conditioning equipment | Receive matrix size | | Transmit matrix size | | Tone keyer shelves (6 lines each) |
|---|---|---|---|---|---|---|---|
| | | | Horizontal | Vertical | Horizontal | Vertical | |
| 11 | 5 | 5 | 5 L | 10 U[a] | 10 U | 5 L | 1 |
| 12 | 6 | 10 | 10 L | 10 U | 10 U | 10 L | 0 |
| 14 | 6 | 10 | 10 L | 10 U | 10 U | 10 L | 2 |
| 21 | 5 | 5 | 5 L | 10 U | 10 U | 5 L | 1 |
| 41 | 5 | 10 | 10 L | 10 U | 10 U | 10 L | 0 |
| 42 | 7 | 10 | 10 L | 20 U | 20 U | 10 L | 0 |
| 51 | 10 | 10 | 10 L | 10 U | 10 U | 10 L | 0 |
| 61 | 6 | 10 | 10 L | 10 L | 10 U | 10 L | 0 |
| 62 | 6 | 10 | 10 L | 10 L | 10 U | 10 L | 0 |
| 71 | 5 | 10 | 10 L | 20 L | 20 U | 10 L | 0 |

[a]L = External line. Lines 6–10 on receive matrix are internally connected to lines 1–4 of transmit matrix.
U = Switched user (TTY machine).

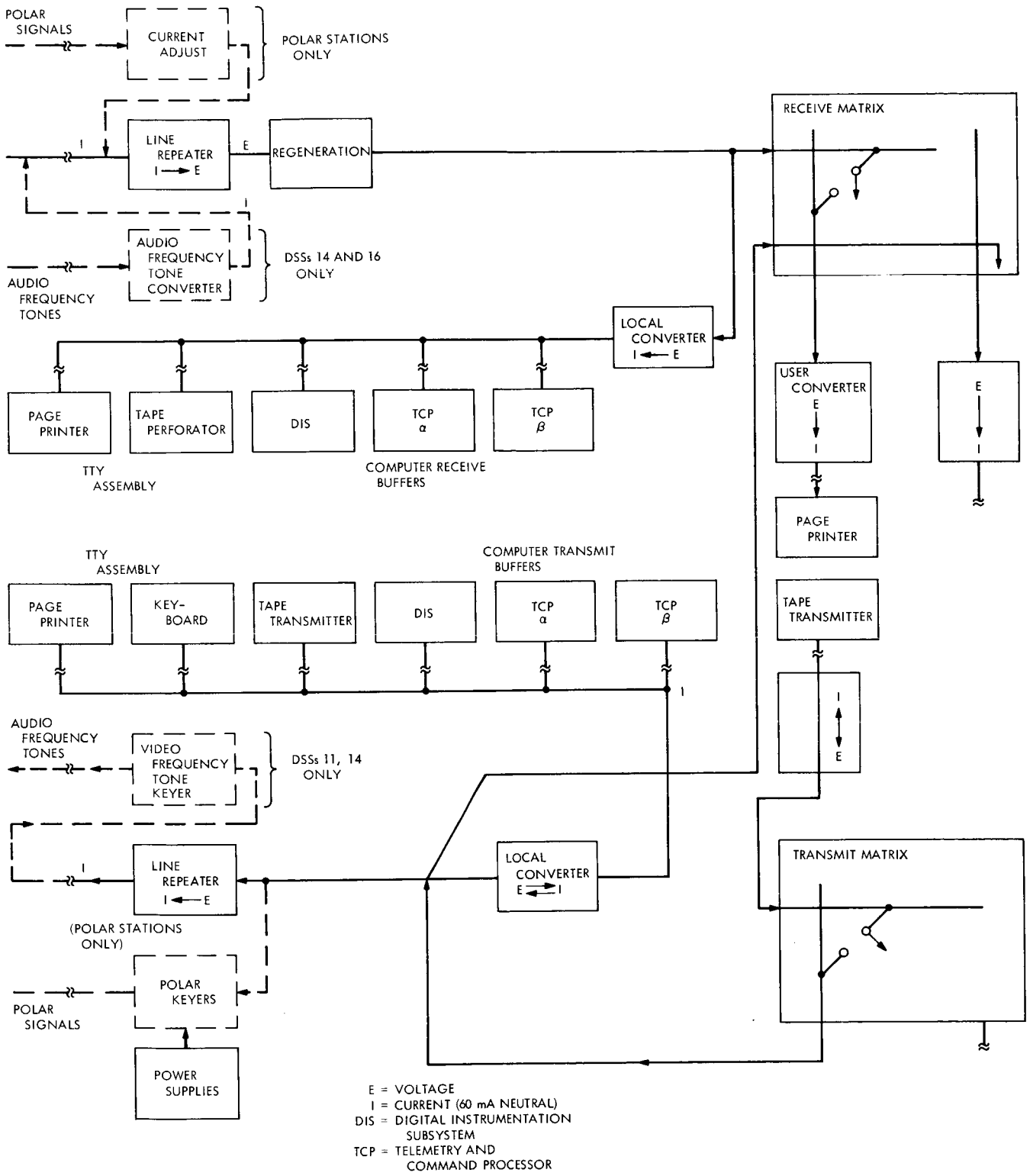


**Fig. 1. Simplified signal flow**

### B. Matrix-switched

The incoming TTY signal is converted to a voltage mode signal and fed to the horizontal ($X$) of a receive matrix switch. Crosspoint switches route the signals to vertical ($Y$) outputs. These outputs are reconverted to 60 mA neutral and sent to user machines. The primary use of the receive matrix is to switch monitoring machines for the DSS control room. Conversely, in the opposite direction the TTY signals originating at the station are converted to voltage mode and then fed to a transmit matrix. The signals from the transmit matrix are converted to the appropriate station transmission standard and forwarded to the SFOF.

A complete monitoring and alarm system is incorporated into the CCGA. Flashing lamps indicate activity on the receive and transmit circuits; the matrix crosspoint switches are illuminated when a user line is selected.

## V. Conclusion

The TTY CCGA is expected to provide a reliable means of controlling, conditioning, and distributing TTY signals at the DSSs.

# Choice of Integrators for Use With a Variation-of-Parameters Formulation

*T. D. Talbot and E. A. Rinderle*
*Flight Operations and DSN Programming Section*

*A comparison of three integrators is made in an effort to choose the one best suited for variations-of-parameters computations of the orbits of satellites.*

## I. Introduction

In searching for better methods of computing the orbit of a satellite over many revolutions, a special perturbations theory using a variation-of-parameters formulation has been developed (Ref. 1). As a prelude to obtaining valid comparisons with the Cowell technique currently in use, a study of various integrators was made in an effort to find the integrator best suited to a variation-of-parameters formulation. This study was initiated in response to suggestions (Ref. 2) that for a given set of differential equations, there exists an optimum integrator.

This study considered three integrators. One of these is a variable-order integrator, DVDQ[1] (Ref. 3). The second is another polynomial-type integrator which has a fixed order. The third integrator, termed "Fourier" by Sheffield (Ref. 2), integrates trigonometric functions exactly.

[1]Double-precision variable-order differential equation solver.

These integrators were compared by the execution of two sets of test cases. The integrators were first compared in the predict-only mode, then in the predict-correct mode. The numerical results of these studies and the conclusions reached are presented in the following section.

## II. Numerical Results of Comparing the Integrators

### A. Test Problem

The test problem for this study was a Mars orbiter with a semimajor axis of about 12,000 km, an eccentricity of about 0.6, and a period of about 12 h. The perturbing forces included were the gravitational attraction of the sun and the Mars zonal harmonics $J_2$, $J_3$, $J_4$, and $J_5$. Integration was carried out for five days (ten orbits).

A classical variation-of-parameters formulation was used. The orbital elements that were integrated consisted of the following:

$a$ = semimajor axis

$e$ = eccentricity

$i$ = inclination

$M_0$ = mean anomaly at epoch

$\omega$ = argument of periapsis

$\Omega$ = longitude of the ascending node

The trajectory was started at about 2 h past periapsis. Print was obtained at both apoapsis and periapsis for each orbit.

To obtain an "exact" solution to this problem, the variable-order integrator DVDQ was used with very tight local integration tolerances ($10^{-8}$ to $10^{-11}$). The resulting step sizes chosen varied from 900 sec at apoapsis down to less than 60 sec at periapsis. All of the other runs made were compared to this run to determine their accuracies.

### B. Comparison of Predict-Only Cases

Table 1 contains the apoapsis and periapsis errors on each orbit for several predict-only cases. The left column contains a brief description of each case. The errors in six of the ten orbits are tabulated. The right column contains the total number of integration steps.

The description of the DVDQ case contains the maximum, minimum, and average step sizes and integration orders. In the other variable-step cases, the maximum step size was $4/3\ h_0$, the minimum was $1/3\ h_0$, and the average was slightly less than $h_0$, where $h_0$ is the initial integration

**Table 1. Comparison of predict-only cases**

| Case number | Integrator | Apsis | Error = max {\|δx\|, \|δy\|, \|δz\|}, m | | | | | | Number of steps |
|---|---|---|---|---|---|---|---|---|---|
| | | | Orbit number | | | | | | |
| | | | 1 | 2 | 4 | 6 | 8 | 10 | |
| 1 | DVDQ, maximum order 10, minimum order 5, maximum step 2400, minimum step 75, average order 8, average step 380 | Apoapsis | 0.00124 | 0.200 | 1.87 | 2.95 | 4.32 | 5.57 | 1130 |
| | | Periapsis | 0.0810 | 2.65 | 4.24 | 6.43 | 9.36 | 12.14 | |
| 2 | Fourier, fourth order Variable step $h_0 = 300$ | Apoapsis | 0.0540 | 0.951 | 3.59 | 7.08 | 11.3 | 16.4 | 1711 |
| | | Periapsis | 0.324 | 2.08 | 7.57 | 16.2 | 26.5 | 39.9 | |
| 3 | Polynomial, fourth order Variable step $h_0 = 300$ | Apoapsis | 0.0447 | 0.824 | 2.81 | 5.10 | 7.54 | 10.4 | 1711 |
| | | Periapsis | 0.304 | 1.54 | 4.55 | 8.91 | 13.3 | 19.2 | |
| 4 | Fourier, sixth order Variable step $h_0 = 300$ | Apoapsis | 0.0143 | 0.474 | 3.25 | 8.32 | 15.7 | 25.4 | 1712 |
| | | Periapsis | 0.0793 | 1.88 | 11.9 | 29.7 | 54.5 | 88.0 | |
| 5 | Polynomial, sixth order Variable step $h_0 = 300$ | Apoapsis | 0.0123 | 0.484 | 3.26 | 8.29 | 15.6 | 25.2 | 1712 |
| | | Periapsis | 0.0682 | 1.89 | 11.8 | 29.4 | 54.0 | 85.2 | |
| 6 | Polynomial, fourth order Fixed step $h = 300$ | Apoapsis | 0.0402 | 0.178 | 1.00 | 2.55 | 4.79 | 7.73 | 1417 |
| | | Periapsis | 1.77 | 4.21 | 9.37 | 14.2 | 18.3 | 21.9 | |
| 7 | DVDQ, maximum order 9, minimum order 4, maximum step 2400, minimum step 150, average order 7, average step 430 $E = E_0K$ (Footnote a) | Apoapsis | 0.00194 | 0.0149 | 1.52 | 2.16 | 2.78 | 3.13 | 982 |
| | | Periapsis | 0.259 | 2.40 | 2.88 | 3.52 | 4.15 | 4.15 | |

[a] $E$ = local error

$E_0$ = initial local error

$K = \frac{a(1+e)}{r}$

step size. In each case, the minimum step occurred at periapsis and the maximum occurred at apoapsis. The maximum orders for DVDQ occurred near periapsis and the minimum orders occurred near apoapsis. The errors tabulated are the maximums of the absolute errors in the components of position (the error in $z$ in each instance).

Two main results are evident from these studies. First, it does not appear to be very advantageous to use higher orders or variable step sizes. Further investigation is necessary to explain these results. Second, there seems to be little difference between the Fourier and polynomial integrators. This result becomes more apparent when the integration coefficients are examined. Table 2 contains these coefficients for both fourth and sixth orders with a starting step size $h_0 = 300$ sec.

**Table 2. Polynomial and Fourier Integration Coefficients**

| Fourth order | | |
|---|---|---|
| | Polynomial | Fourier |
| $\beta_{40}$ | 792.0833333333333 | 791.1839790650130 |
| $\beta_{41}$ | −1155.833333333333 | −1153.177337110016 |
| $\beta_{42}$ | 1190.000000000000 | 1087.425341026402 |
| $\beta_{43}$ | −530.833333333333 | −530.0560158768241 |
| $\beta_{44}$ | 104.5833333333333 | 104.6240328954251 |
| **Sixth order** | | |
| | Polynomial | Fourier |
| $\beta_{60}$ | 985.7192460317460 | 983.3672331781959 |
| $\beta_{61}$ | −2218.690476190476 | −2207.020820533816 |
| $\beta_{62}$ | 3499.747023809523 | 3476.647150904269 |
| $\beta_{63}$ | −3413.968253968254 | −3391.241259327214 |
| $\beta_{64}$ | 2019.538690476190 | 2008.540513368117 |
| $\beta_{65}$ | −667.0238095238095 | −665.0451712873998 |
| $\beta_{66}$ | 94.67757936507936 | 94.75235369784858 |

Table 2 reveals that the Fourier and polynomial integration coefficients are very similar. These results prompted further theoretical investigation which led to the following equivalence theorem for Fourier and polynomial integrators:

**THEOREM.** *Let $N$ be any positive integer. Let $n$ be any positive real number and let $h$ be any fixed positive step size such that $Nh < 2\pi/n$. Let $t_k = -kh$ for $k = 0, 1, \cdots, N$. Define the Fourier integration coefficients $\beta_j(n)$ as follows:*

$$\beta_j(n) = \int_0^h T_j(n, s)\, ds, \qquad j = 0, 1, \cdots, N$$

where

$$T_j(n,t) = \frac{\prod_{\substack{k=0 \\ k\neq j}}^{N} \sin\frac{1}{2}n(t - t_k)}{\prod_{\substack{k=0 \\ k\neq j}}^{N} \sin\frac{1}{2}n(t_j - t_k)}$$

Note that the inequality constraint on $h$ prevents the denominator from being zero. Define the polynomial integration coefficients $\gamma_j$ as follows:

$$\gamma_j = \int_0^h P_j(s)\, ds, 0, 1, \cdots, N$$

where

$$P_j(t) = \frac{\prod_{\substack{k=0 \\ k\neq j}}^{N} (t - t_k)}{\prod_{\substack{k=0 \\ k\neq j}}^{N} (t_j - t_k)}$$

Then

$$\lim_{n\to 0} \beta_j(n)\, \gamma_j$$

A proof of this theorem, which was previously established by Gautschi (Ref. 4), is given in Ref. 5. The theorem states that the Fourier integrator approaches the polynomial integrator as the mean motion $n$ approaches zero.

Several test runs were made with values of $n$ that varied from $10^{-2}$ sec$^{-1}$ to $10^{-4}$ sec$^{-1}$. This range includes the largest values of $n$ possible in current celestial mechanics applications. In every case, the two sets of coefficients agreed to two or three digits. Therefore, one may conclude that the Fourier method offers no advantage over the polynomial method in the integration of the differential equations of celestial mechanics. The Fourier integration coefficients also have the disadvantage of depending on both $n$ and the step size $h$.

### C. Comparison of Predictor-Corrector Cases

Table 3 contains a comparison of several predictor-corrector cases. This table has the same format as Table 1. The remarks in *Subsection B* regarding the maximum, minimum, and average step sizes in Table 1 also apply to Table 3.

## Table 3. Comparison of predictor-corrector cases

| Case number | Integrator | Apsis | Error = max {\|δx\|, \|δy\|, \|δz\|}, m | | | | | | Number of steps |
|---|---|---|---|---|---|---|---|---|---|
| | | | Orbit number | | | | | | |
| | | | 1 | 2 | 4 | 6 | 8 | 10 | |
| 1 | DVDQ, maximum order 10, minimum order 5, maximum step 2400, minimum step 75, average order 8, average step 380 | Apoapsis | 0.00124 | 0.200 | 1.85 | 2.93 | 4.30 | 5.56 | 1135 |
| | | Periapsis | 0.0809 | 2.60 | 4.17 | 6.36 | 9.31 | 12.08 | |
| 2 | Polynomial, fourth order Variable step $h_0 = 300$ | Apoapsis | 0.00183 | 0.0594 | 0.311 | 0.731 | 1.31 | 2.06 | 1711 |
| | | Periapsis | 0.0126 | 0.198 | 1.00 | 2.37 | 4.22 | 6.56 | |
| 3 | Polynomial, sixth order Variable step $h_0 = 400$ | Apoapsis | 0.00330 | 0.134 | 0.870 | 2.21 | 4.16 | 6.72 | 1286 |
| | | Periapsis | 0.0180 | 0.513 | 3.18 | 7.84 | 14.4 | 22.7 | |
| 4 | Polynomial, tenth order Variable step $h_0 = 400$ | Apoapsis | 0.0000644 | 0.0961 | 0.845 | 2.22 | 4.35 | 7.14 | 1288 |
| | | Periapsis | 0.00279 | 0.644 | 3.85 | 9.10 | 16.8 | 26.2 | |
| 5 | Polynomial, fourth order Fixed step $h = 300$ | Apoapsis | 0.00162 | 0.112 | 0.819 | 2.24 | 4.15 | 6.77 | 1417 |
| | | Periapsis | 0.0614 | 0.554 | 3.36 | 8.49 | 15.8 | 25.0 | |
| 6 | Polynomial, sixth order Fixed step $h = 300$ | Apoapsis | 0.000286 | 0.00639 | 0.0672 | 0.190 | 0.373 | 0.613 | 1418 |
| | | Periapsis | 0.146 | 0.279 | 0.234 | 0.253 | 1.15 | 2.36 | |
| 7 | Polynomial, sixth order Fixed step $h = 400$ | Apoapsis | 0.00313 | 0.222 | 1.48 | 3.84 | 7.32 | 12.0 | 1064 |
| | | Periapsis | 0.603 | 2.94 | 9.29 | 17.8 | 28.6 | 41.7 | |
| 8 | Polynomial, tenth order Fixed step $h = 400$ | Apoapsis | 0.000235 | 0.168 | 1.16 | 3.07 | 5.97 | 9.91 | 1066 |
| | | Periapsis | 0.728 | 0.428 | 5.86 | 19.0 | 38.3 | 61.5 | |
| 9 | Polynomial, tenth order Variable step $h_0 = 300$ | Apoapsis | 0.152E-4 | 0.226E-2 | 0.976E-2 | 0.205E-1 | 0.346E-1 | 0.527E-1 | 1714 |
| | | Periapsis | 0.107E-3 | 0.445E-2 | 0.219E-1 | 0.573E-1 | 0.900E-1 | 0.142 | |
| 10 | DVDQ, $E = E_0K$ (Footnote a) | Apoapsis | 0.00193 | 0.0140 | 1.51 | 2.11 | 3.20 | 3.27 | 987 |
| | | Periapsis | 0.279 | 2.38 | 2.79 | 3.38 | 4.12 | 4.46 | |
| 11 | DVDQ, $E = E_0K$ | Apoapsis | 0.00173 | 1.35 | 5.16 | 4.75 | 3.84 | 2.84 | 893 |
| | | Periapsis | 0.184 | 7.61 | 7.20 | 3.91 | 0.476 | 8.25 | |
| 12 | DVDQ, $E = E_0K$ | Apoapsis | 0.0107 | 0.566 | 2.54 | 1.56 | 0.624 | 0.00193 | 872 |
| | | Periapsis | 0.248 | 1.57 | 7.43 | 13.2 | 17.3 | 23.3 | |

[a] $E$ = local error

$E_0$ = initial local error

$K = \frac{a(1+e)}{r}$

Several conclusions may be made from these studies. For instance, cases 1 through 9 again indicate that taking fixed steps requires less work (fewer steps) to achieve a given accuracy than taking variable steps. Hence, it seems that more error can be introduced at periapsis than at apoapsis without increasing the total error in the computed solution. Cases 10 through 12 were run as a check on this hypothesis. Case 10, in particular, tends to substantiate the hypothesis.

These studies also indicate that higher order (tenth order) integration formulas are not necessarily more efficient for this type of problem. Also, a comparison of Tables 1 and 3 indicates that the predict-only mode is perhaps more efficient (that is, takes fewer derivative evaluations to achieve a given accuracy) than the predict-correct mode. But further study is needed in these areas.

Finally, it appears from these studies that DVDQ is approximately fifteen to 20% more efficient than the fixed-order polynomial type integrator. Therefore, since the Fourier method is essentially equivalent to the polynomial method, DVDQ seems to be the most efficient of the integrators studied for use in a variation-of-parameters formulation. These studies indicate that for maximum integrator efficiency DVDQ should be run in the predict-only mode, with the error introduced at each step proportional to $1/r$.

## References


1. Dallas, S., and Rinderle, E., *A Special Perturbations Theory Using the Variation of Parameters Formulation,* April 1, 1970 (JPL internal document).
2. Sheffield, C., "Generalized Multi-Step Method With an Application to Orbit Computations," *Celest. Mech.*, Vol. I, pp. 46–58, 1969.
3. Krogh, F., *On Testing a Subroutine for the Numerical Integration of Ordinary Differential Equations,* May 9, 1969 (JPL internal document).
4. Gautschi, W., "Numerical Integration of Ordinary Differential Equations Based on Trigonometric Polynomials," *Numer. Math.*, Vol. 3, pp. 381–397, 1961.
5. Talbot, T., and Rinderle, E., *The Choice of Integrators for Use in the Variation of Parameters Formulation for DPTRAJ Research,* October 16, 1970 (JPL internal document).

# SFOF Configuration Control

K. R. Carter
SFOF/GCF Operations Section

*This article describes the need for and design of a Space Flight Operations Facility Configuration Control System based on the highly dynamic nature of the facility and the unique, critical requirements levied upon it by multiple and simultaneous flight projects supported by various JPL functional organizations.*

## I. Introduction

The Space Flight Operations Facility (SFOF) provides capabilities which make it possible to carry out the network control and analysis functions of the Deep Space Network (DSN) and the mission control function for the Flight Projects. Generally, the facility provides equipment and space for network operations down to the facility control level; i.e., station controllers, communications controllers, computer operations chief, and support operations chief. Also for the network, it houses the control center for the Ground Communications Facility and its interfaces with the NASCOM for all external communications required to operate the network, and internal communications to support the network and mission control functions.

The network is configured to support many flight projects simultaneously. The demands of these multi-users, both in a functional and in a line organization sense, have required that the management of this facility design and implement a configuration control system to encompass all changes required. The SFOF configuration control system is concerned mainly with network equipment, but it is also used for mission-dependent hardware housed in this facility such that its interfaces with network equipment would affect the conduct of flight operations.

The article discusses hardware changes only. A parallel control system for all operational software in the many computers in this facility is under development.

## II. Purpose

The purpose of the configuration control system is to allow management to have control over the detail configuration of the SFOF. This can be accomplished only through a system that requires management review of all changes, irrespective of their complexity.

Changes to the SFOF are accomplished by many functional organizations. Engineering modifications are performed by the SFOF/GCF Development Section; equipment configuration changes by the SFOF/GCF Operations Section; and physical plant modifications and configuration changes by the Plant Engineering Division. Most changes involve several agencies.

The configuration control system provides a vehicle for requesting changes to the configuration or engineering capabilities of the SFOF. It allows examination for technical feasibility and costing and funding by appropriate organizations, reviewing and commenting upon by all affected organizations, and final approval or disapproval by appropriate management.

Following the above approval cycle, the system provides the authority for accomplishment of the change and subsequent documentation requirement.

## III. Background

The configuration control system for the SFOF was first implemented in October 1965. From that time until the present, more than 5000 change requests have been initiated and accomplished or cancelled through this system.

The system operation is handled by a relatively small staff of contractor personnel under the cognizance of the SFOF/GCF Operations Section configuration control engineer.

The existing design for the operation of the system has been in effect for over 1 yr and is the direct result of continuing modification and improvement.

## IV. Implementation

The vehicle for the configuration control system is a two-page SFOF change request (Form 18). The requester is required to identify the request in detail on the first page and to gain the concurrence of the cognizant operations engineer from the SFOF/GCF Operations Section, and of the cognizant development engineer from the SFOF/GCF Development Section, for each system or subsystem involved in the request. This avoids interference with other planning or with existing capability and ensures completeness and technical feasibility of the request.

The request is then submitted to the configuration control office where it is numbered and becomes an official change request. It is then routed through steps to secure costing, funding, concurrence or comment by involved parties, and is subsequently approved or disapproved by the managers of the SFOF/GCF Development Section and the SFOF/GCF Operations Section. Any disagreement in final approval is arbitrated and decided upon by the Data Systems Division SFOF manager.

After a request has been authorized, a change order is issued by the configuration control engineer to the appropriate agencies for action. They advise the configuration control office when the changes have been accomplished, and documentation of the affected portions of the SFOF is updated.

All concerned parties are advised of disapproved requests. Negotiation may be initiated at this point, if appropriate. A disapproved request is cancelled if no further advice is received.

## V. Feasibility

Frequent emergencies develop wherein a change is required on short notice to meet an unexpected demand on this highly diverse facility. In such cases, the change control engineer may issue an emergency change order under the authority of the SFOF manager, and the work can be accomplished in real-time. The Form 18 is initiated simultaneously, and after-the-fact approval is secured for documentation and notification to all concerned parties.

## VI. Summary

The design of the configuration control system for the SFOF provides an orderly system to gain approval of a requested change to the facility and to ensure that no ramification of a request is overlooked. This system has become a valuable tool in the evolution of the SFOF.



NASA — JPL — Coml., L.A., Calif.